UNIVERSITÀ DEGLI STUDI DI NAPOLI
"FEDERICO II"

Ph.D. Program in Physics
XXXV Cycle
Chairman : prof. Vincenzo Canale
Thesis for the Degree of Doctor of Philosophy

Targeted search and ensemble analysis for the detection of gravitational waves from known pulsars

Advisors:
Prof. Rosario De Rosa
Dott. Cristiano Palomba

Candidate:
Luca D'Onofrio

A.Y. 2019-2022

Abstract

Continuous gravitational waves (CWs) are promising signals targeted by the LIGO and Virgo detectors; possible sources of this type of signals are spinning neutron stars with a non-axisymmetric mass distribution. The "strength" of the signal depends on the ellipticity, the physical parameter that quantifies the mass distribution asymmetry respect to the rotation axis. According to the assumption and the knowledge of the source parameters (sky position, rotation frequency parameters), different strategies can be adopted to search for a CW signal. The simplest, but also the most sensitive strategy, is the targeted search: measuring the electromagnetic emission of the source, as in the case of pulsars, it is possible to infer with high accuracy the sky position and the rotation parameters.

So far, there is no evidence of a CW signal in LIGO and Virgo data. In this thesis, I describe the last targeted search from the LIGO and Virgo Collaborations, using the data from the observing run O3 and analyzing 236 known pulsars with three independent analysis pipelines: the Bayesian pipeline, the F-statistic and the 5n-vector method. Since there was no evidence of a CW signal, it has been possible to set 95% credible upper limit on the amplitude and also on the ellipticity. For this Collaboration paper, I contributed as analysts and in the editorial team.

Ensemble procedures can improve the detection probability for CW signals. In this thesis, I describe and test the *5n-vector ensemble method*, a multiple test for the targeted search of CW signals from a collection of known pulsars. This method significantly improves the detection probability combining the results from individually undetectable pulsars if few signals are near the detection threshold. I apply this procedure to the O3 dataset from the LIGO and Virgo detectors considering an ensemble of 223 known pulsars. I find no evidence of a signal from the ensemble and set 95% credible upper limit on a global parameter for the ensemble and, assuming a common exponential distribution for the pulsars' ellipticitites, 95% credible upper limit on the mean ellipticity. Using two independent hierarchical Bayesian procedures, I find 95% upper limit of 2.7×10^{-9} and 1.8×10^{-9} on the mean of the assumed exponential distribution for the 223 pulsars. This results are more than one order of magnitude below the upper limit of a different ensemble search where the authors considered a Bayesian procedure on an ensemble of 92 pulsars and data from the LIGO V6 science run.

Application of the 5n-vector ensemble method on the next observing runs will improve the possibility to detect a CW signal from rotating neutron stars for the first time.

Contents

Introduction

The LIGO and Virgo gravitational wave detectors have achieved historical discoveries over the last seven years reaching the experimental detection of gravitational waves by ground-based interferometers and initiating the new era of the gravitational wave astronomy.

The first detection, GW150914 - on September 14, 2015 by the LIGO Hanford and LIGO Livingston observatories - demonstrated the existence of binary stellar-mass black hole systems and was also the first observation of a binary black hole merger.

The first confirmed multi-messenger counterpart to a gravitational wave observation came instead with GW170817, a signal from a binary neutron star coalescence which was accompanied by detection across the electromagnetic spectrum.

So far, the LIGO and Virgo detectors have detected 90 gravitational wave signals from compact binary coalescences across the first three observing runs. These observations, described in the third Gravitational-wave Transient Catalog (GWTC-3), explore the most extreme conditions of spacetime and of matter testing the General Relativity at the relativistic, strong-field regime and providing insights into the formation and evolution of black holes and neutron stars.

This thesis deals with a quite different and as-yet-undiscovered gravitational wave signal type, defined by persistence and near-monochromaticity over long time scales, namely *continuous gravitational waves* (CWs).

CWs are promising signals targeted by the LIGO and Virgo detectors; possible sources of this type of signals are spinning neutron stars with a non-axisymmetric mass distribution. The "strength" of the signal depends on the ellipticity, the physical parameter that quantifies the mass distribution asymmetry respect to the rotation axis.

According to the assumption and the knowledge of the source parameters (sky position, rotation frequency parameters), different strategies can be adopted to search for a CW signal. The simplest, but also the most sensitive strategy, is the *targeted search*: measuring the electromagnetic emission of the source, as in the case of pulsars, it is possible to infer with high accuracy the sky position and the rotation parameters, which include the source rotation frequency and the spin-down. The spin-down is the decrease of the rotation frequency induced by the electromagnetic, and possibly gravitational wave, emission. Given the long-lived nature of CW signals, the signal can be integrated over a long time duration to improve the signal-to-noise ratio.

At the source, the CW signal is almost monochromatic with the CW frequency that, according to the considered emission model, is proportional to the rotation frequency. At the detector, the CW signal has a frequency phase modulation due to the Doppler effect for the relative motion between the source and the Earth (and other minor effects, like the Einstein and Shapiro effect).

De-modulation techniques, as the heterodyne method, are useful for correcting pulsar signals for the phase modulation caused by the spin-down/Doppler shift and hence to precisely unwind the apparent phase evolution of the source. Once this correction has been applied, a CW signal would become monochromatic except for the sidereal modulation due to the antenna patterns. This depends on the detector position on the Earth and it is used by the *5n-vector method* to define a detection statistic as well as to estimate the signal parameters.

So far, there is no evidence of a CW signal in LIGO and Virgo data. The last targeted search from the LIGO and Virgo Collaborations, using the data from the observing run O3 analyzed 236 known pulsars using three independent analysis pipeline: the Bayesian pipeline, the F-statistic and the 5n-vector method. Since there was no evidence of a CW signal, it has been possible to set 95% credible upper limit on the amplitude and also on the ellipticity.

This thesis tries to improve the detection probability for the targeted search of CWs considering an ensemble of individually undetectable pulsars. In order to improve the detection probability, since few signals are expected near the detection threshold, it may be more desirable to consider the combined evidence for subsets of hypotheses. Indeed, the proposed ensemble procedure, *the 5n-vector ensemble method*, defines a statistic of ensemble $T(k)$ as the partial sum of the statistics of single pulsar ranked for increasing p-values. To control the look-elsewhere effect, the statistics $T(k)$ must be considered as the partial sum of order statistics; a Monte Carlo procedure is needed to reconstruct both the noise and the signal distributions for each value of k.

Since the classical definition of the 5n-vector statistic follows a noise distribution that depends on the analyzed pulsar, I propose a normalized definition of this statistic that allows to rank pulsars according to the p-values. The proposed ensemble procedure is a rank truncation method that selects the top ranking sources according to the significance of the corresponding individual test.

Using the statistics $T(k)$, I define a p-value for the ensemble as a function of k, that is a p-value for the overall hypothesis of the presence of CWs from an ensemble of known pulsars.

In case of no detection, I describe a Bayesian procedure to set 95% credible upper limit on a global parameter that describes the ensemble, and two independent hierarchical procedures to return information about the population properties.

The goal of this PhD thesis is the design, implementation, test and application to O3 data of the 5n-vector ensemble method. The thesis is organized as follows.

Chapter 1 is divided in two parts. In the first part, I briefly introduce the General Relativity theory and describe the generation and emission mechanism of the CW radiation. In the second part, I review the astrophysical and observational properties of neutron stars, the possible sources of CWs, focusing on the theoretical reasons for a non-axisymmetric mass distribution.

In Chapter 2, I introduce the general idea and the main features of the ground-based interferometric detectors that allowed the first gravitational wave detection. In the last Sections, I focus on the searches for CWs describing in detail the targeted search from known pulsars. I review the main pipelines used for this search describing the latest results by the LIGO and Virgo Collaborations.

In Chapter 3, I describe extensively the 5n-vector pipeline composed by the Band Sample Data framework - an optimized data framework for the CW search - and by the 5n-vector method. This pipeline has been developed in the last decade by the Rome Virgo group; the contribution to this pipeline due to my research is the implementation of the Doppler correction for sources in binary system and the characterization of a different multi-detector extension that takes into account the different detectors' noise level.

Chapter 4 describes the 5n-vector ensemble method and the rank truncation method introduced in this thesis to improve the detection probability. In the last Section, I describe how to set upper limits on a global parameter of ensemble and also two independent hierarchical procedures to return information about the population properties.

Chapter 5 shows the validation tests of the method and it is divided in three parts. In the first part, I present different tests for the analysis of single pulsar using the 5-vector pipeline. In the second part, I validate the ensemble procedure using a theoretical test and also real data, considering hardware and software injections and highlighting weaknesses and strengths of the method. In the last part, analyzing different sets of injected signals, I validate and test the upper limit procedures.

Finally, Chapter 6 shows the application and the results of the analysis of O3 data for 223 known pulsars considering three different ensembles. Since there is no evidence of a CW signal, I report the results of the upper limits on the mean of the assumed exponential distribution for the ellipticities. Different applications and future prospects are also presented.

Chapter 1

Gravitational waves and pulsars

In this Chapter, I introduce the gravitational wave (GW) formalism and describe the astrophysical properties of pulsars - spinning neutron stars detected mainly in the radio band - that could be sources of a periodic GW radiation.

First, I start introducing the general concepts of General Relativity focusing on the linearized formulation of the Einstein equations that entails a wave equations and a relatively simple solution in a certain gauge condition.

Then, exploring the possible sources of GWs for ground-based detectors, I analyze how non-axisymmetric spinning neutron stars can emit a GW radiation. Briefly reviewing the astrophysical properties of neutron stars and pulsars, I analyze the theoretical sources of the neutron stars' non-axisymmetry and a theoretical upper limit for the amplitude of the expected GW radiation.

1.1 Einstein field equations

In 1907, Albert Einstein realized that, as a consequence of the equality of inertial and gravitational mass[1], it is not possible to detect an external homogeneous constant gravitational field in a freely falling system [1] and suggested that gravity is a property of the space itself. In his paper of 1916 [2], Einstein showed that the gravitational field, the distribution of matter/energy and the geometry of spacetime are intimately linked and ruled by field equations.

This idea could be summarized with the words of the American physicist John Wheeler: "Space acts on matter, telling it how to move. In turn, matter reacts back on space, telling it how to curve" [3].

---

[1] This is the historical formulation of the equivalence principle, already present in the *Philosophae naturalis principia matematica* written by Isaac Newton in 1686.

The equations describing how matter generates gravity must have form [4]:

$$O(g_{\mu\nu}) = kT_{\mu\nu}\,, \tag{1.1}$$

where O is a differential operator on the metric tensor $g_{\mu\nu}$, k is a proportionality factor and $T_{\mu\nu}$ is the stress-energy tensor, that is the "geometric object" that must act as the source of gravity [3, 5]. As a consequence of the equivalence principle, if there is a local law of physics that is expressed in tensor notation in special relativity (SR), then its mathematical form should be the same in a locally inertial frame of a curved spacetime. It is the so called "comma goes to semicolon law"[2] because if a law contains derivatives in its special-relativistic form ("commas"), then it has these same derivatives in the local inertial frame. To generalize to a curved spacetime, you need to replace the partial derivatives with covariant ones ("semicolons") [4].

For this reason, since in SR the law of local energy-momentum conservation implies that ${T^{\alpha\beta}}_{,\beta} = 0$, in a curved spacetime and for any reference frame it reads [3]:

$${T^{\mu\nu}}_{;\nu} = 0. \tag{1.2}$$

The stress-energy tensor, on the right-hand side of the equation (1.1), is a symmetric, divergence-free tensor. On the left-hand side of the equation (1.1), there is the "geometric object" that characterizes gravity and accordingly it must be:

- a second rank, symmetric, divergence-free tensor;
- it must vanish when spacetime is flat;
- it must be a measure of curvature, that is linear in the Riemann curvature tensor;

It can be demonstrated [1, 4] that the Einstein curvature tensor $G_{\mu\nu}$,

$$O(g_{\mu\nu}) \equiv G_{\mu\nu} = R_{\mu\nu} - \frac{1}{2}g_{\mu\nu}R, \tag{1.3}$$

is the only tensor that satisfies these conditions. $R_{\mu\nu}$ is the Ricci tensor defined as:

$$R_{\mu\nu} = R^{\alpha}_{\mu\alpha\nu} \tag{1.4}$$

that is by contraction of the Riemann tensor,

$$R^{\alpha}_{\beta\mu\nu} = \Gamma^{\alpha}_{\beta\nu,\mu} - \Gamma^{\alpha}_{\beta\mu,\nu} + \Gamma^{\sigma}_{\beta\nu}\Gamma^{\alpha}_{\sigma\mu} - \Gamma^{\sigma}_{\beta\mu}\Gamma^{\alpha}_{\sigma\nu} \tag{1.5}$$

---

[2] For the factor ordering problems in the application of "comma goes to semicolon law" see [3].

where $\Gamma^{\lambda}_{\mu\nu}$ is the Christoffel symbol defined as:

$$\Gamma^{\lambda}_{\mu\nu} = \frac{1}{2} g^{\lambda\alpha} [g_{\alpha\mu,\nu} + g_{\alpha\nu,\mu} - g_{\mu\nu,\alpha}] \,, \tag{1.6}$$

whereas R is the scalar curvature,

$$R \equiv R^{\mu}_{\mu} \,. \tag{1.7}$$

In component notation, the Einstein field equations, describing the generation of curvature by mass-energy, are[3]:

$$G_{\mu\nu} = kT_{\mu\nu}. \tag{1.8}$$

The field equations in (1.8) are a system of ten coupled differential equations that have to be solved for the ten components $g_{\mu\nu}$ when the source is given. These equations are nonlinear, but from given initial data they determine future values of $g_{\mu\nu}$, that is the evolution of geometry. However, the ten components are not all independent.
The Bianchi identities,

$$G^{\mu\nu}{}_{;\nu} = 0, \tag{1.9}$$

are four constraints that reduce to six the independent components of $g_{\mu\nu}$, that characterize the geometry independently of the coordinates [4].
For the sake of completeness, in the following I describe the equation of motion for a falling body [6]. For SR, the action for a free particle is given by:

$$A = -mc \int ds = -mc \int \sqrt{\eta_{\mu\nu} dx^{\mu} dx^{\nu}} \tag{1.10}$$

where ds is the line element that is the simplest scalar on the table. Using the variational principle $\delta A = 0$, the equation of motion for a free particle in SR - that is the geodesic equation in a flat spacetime - can be obtained. Because of the equivalence principle, the generalized action becomes:

$$S = -mc \int ds = -mc \int \sqrt{g_{\mu\nu} dx^{\mu} dx^{\nu}} \tag{1.11}$$

and the equation of motion derived from the principle of least action is

$$\frac{d^2 x^{\lambda}}{ds^2} + \Gamma^{\lambda}_{\mu\nu} \frac{dx^{\mu}}{ds} \frac{dx^{\nu}}{ds} = 0 \,. \tag{1.12}$$

---

[3] In this work, it is used the "Landau-Lifshitz Spacelike Convention", as in [3].

For a flat spacetime, the Christoffel symbols vanish and the equation corresponds to the equation for the geodesics in the Minkowski space. Indeed, the gravitational field is in the second term of the equation (1.12), that is in the components of the metric tensor, as has been said. The equation (1.12) is the geodesic equation for a curved spacetime and, given the initial conditions on x^μ and $\frac{dx^\mu}{ds}$, its solution is uniquely determined.

1.2 Correspondence structure of General Relativity

When a new physical theory gives a better description or a more accurate explanation of the same domain than an older theory - as in the case of GR - the unity of physics is preserved by a network of correspondence principles. These principles link simpler and older theory to more accurate and more sophisticated ones [3].

For example, Newtonian mechanics is recovered from SR when the considered velocities are negligible[4] compared to the speed of light c.

Einstein's GR theory has different limiting cases that depend on the chosen approximations. For example, the Newtonian limit is the limit of GR in the approximation of weak field, low velocities and small pressures.

In the next Section, I describe in detail the weak-field limit, the so-called "linearized theory of gravity".

1.2.1 The Linearized theory of Gravity

The Linearized theory of Gravity (LG) is the limit of GR for weak gravitational fields [3], that is

$$g_{\mu\nu} = \eta_{\mu\nu} + h_{\mu\nu} \qquad |h_{\mu\nu}| \ll 1\,. \tag{1.13}$$

Note that the condition $|h_{\mu\nu}| \ll 1$ requires both the gravitational field to be weak and in addition constrains the coordinate system to be approximately Cartesian. $h_{\mu\nu}$ is the metric perturbation and, as it will be seen, entails the propagation of GWs.

In LG, the "smallness" of the perturbation means that only terms which are linear in $h_{\mu\nu}$ are significant. As a consequence, indices are raised and lowered using the flat metric $\eta_{\mu\nu}$. The metric perturbation $h_{\mu\nu}$ transforms as a tensor under Lorentz transformations, but not under general coordinate transformations [7]. Before proceeding, it is important to focus on the gauge symmetry of GR. In facts, Einstein's field equations are invariant under general coordinate transformations. More precisely, given an arbitrary

---

[4] Specifically, the Galileo transformation laws are obtained from Lorentz transformation laws in the limit $c \to +\infty$ rather than in the limit $v \ll c$ (for a limit of small velocities but not newtonian, see [6]).

diffeomorphism:

$$x^\mu \longrightarrow x'^\mu(x) \tag{1.14}$$

the Einstein field equations do not change their form if the metric tensor transforms as:

$$g_{\mu\nu}(x) \longrightarrow g'_{\mu\nu}(x') = \frac{\partial x^\rho}{\partial x'^\mu}\frac{\partial x^\sigma}{\partial x'^\nu} g_{\rho\sigma}(x). \tag{1.15}$$

The group of general coordinate transformations is a symmetry group for Einstein's field equations, and it is said that GR is diffeomorphism-invariant [5].
Choosing a reference frame where the equation (1.13) holds, the invariance of GR is broken. From a transformation of coordinates:

$$x^\mu \longrightarrow x'^\mu(x) = x^\mu + \xi^\mu(x) \tag{1.18}$$

using the equation (1.15), it follows that:

$$h_{\mu\nu}(x) \longrightarrow h'_{\mu\nu}(x') = h_{\mu\nu}(x) - (\partial_\mu \xi_\nu + \partial_\nu \xi_\mu)\,. \tag{1.19}$$

If the derivatives $|\partial_\nu \xi(x)_\mu|$ are of the same order of "smallness" as $|h_{\mu\nu}|$ (see equation (1.13)), these slowly varying diffeomorphisms are a symmetry of linearized theory [9]. In the chosen reference frame, the Einstein equations can be analyzed by expanding in the metric (1.13) and keeping terms to first order in $h_{\mu\nu}$ [7]. Because of the equation (1.6), the Christoffel symbols are given by:

$$\Gamma^\mu_{\nu\gamma} = \frac{1}{2}\eta^{\mu\delta}(\partial_\gamma h_{\delta\nu} + \partial_\nu h_{\delta\gamma} - \partial_\delta h_{\nu\gamma})\,, \tag{1.20}$$

and the Ricci tensor is

$$R_{\mu\nu} = R^\gamma_{\mu\gamma\nu} = \frac{1}{2}(\partial_\gamma \partial_\nu h^\gamma_\mu + \partial^\gamma \partial_\mu h_{\nu\gamma} - \Box h_{\mu\nu} - \partial_\mu \partial_\nu h) \tag{1.21}$$

---

[5] It is important to underline the difference between invariance (a symmetry property of a set of equations) and covariance (a property of the formal apparatus used in a physical theory) [8]. For example, the wave equation

$$\frac{\partial^2\Phi}{\partial(x^0)^2} + \frac{\partial^2\Phi}{\partial(x^1)^2} + \frac{\partial^2\Phi}{\partial(x^2)^2} + \frac{\partial^2\Phi}{\partial(x^3)^2} = 0 \tag{1.16}$$

is invariant under Lorentz transformations but not under general transformations. The equation (1.16) can be rewritten in covariant form,

$$\eta^{\mu\nu}\partial_\mu\partial_\nu\Phi = 0. \tag{1.17}$$

but, by no means has this cosmetics enlarged the invariance group of the equation (1.16) [8]. The possibility to write the wave equation in the form (1.17) does not automatically imply an invariance group larger than the Lorentz one."Hence, GR invariance is not a fictitious property of Einstein's equations, due to the fact that they are usually written using tensors. On the contrary, it is a precise symmetry that shows up most clearly when the equations are written down explicitly in coordinates" [8].

where $h = \eta^{\mu\nu}h_{\mu\nu}$ and $\Box = \partial^\gamma\partial_\gamma$. Since the curvature scalar is now defined as $R = \eta^{\mu\nu}R_{\mu\nu}$, the Einstein tensor can be written as

$$G_{\mu\nu} = R_{\mu\nu} - \frac{1}{2}\eta_{\mu\nu}R = \frac{1}{2}(\partial_\gamma\partial_\nu h^\gamma_\mu + \partial^\gamma\partial_\mu h_{\nu\gamma} - \Box h_{\mu\nu} - \partial_\mu\partial_\nu h - \eta_{\mu\nu}\partial_\gamma\partial^\delta h^\gamma_\delta + \eta_{\mu\nu}\Box h)\,. \tag{1.22}$$

This expression can be reduced defining a new perturbation tensor $\bar{h}_{\mu\nu}$ as

$$\bar{h}_{\mu\nu} = h_{\mu\nu} - \frac{1}{2}\eta_{\mu\nu}h \tag{1.23}$$

whose trace is $\bar{h} \equiv \eta^{\mu\nu}\bar{h}_{\mu\nu} = h - 2h = -h$ (*trace-reversed* perturbation). In this way, the equation (1.23) can be inverted to give:

$$h_{\mu\nu} = \bar{h}_{\mu\nu} - \frac{1}{2}\eta_{\mu\nu}\bar{h}. \tag{1.24}$$

Using the equation (1.24), all terms with the trace h are canceled in the Einstein tensor $G_{\mu\nu}$ and the Einstein field equations in LG become:

$$\partial_\gamma\partial_\nu\bar{h}^\gamma_\mu + \partial^\gamma\partial_\mu\bar{h}_{\nu\gamma} - \Box\bar{h}_{\mu\nu} - \eta_{\mu\nu}\partial_\gamma\partial^\delta\bar{h}^\gamma_\delta = +\frac{16\pi G}{c^4}T_{\mu\nu}\,. \tag{1.25}$$

Choosing an appropriate coordinate system (or *gauge*) this expression can be simplified further[6]. Using the gauge freedom (1.19), it could be chosen the reference frame where the Lorentz gauge condition[7]

$$\partial^\nu\bar{h}_{\mu\nu} = 0\,, \tag{1.26}$$

is verified. To prove that it is possible to use this gauge, suppose that our metric perturbation is not in Lorentz gauge. In terms of the trace-reversed perturbation, the equation (1.19) becomes:

$$\begin{aligned}\bar{h}'_{\mu\nu} &= h_{\mu\nu} - (\partial_\mu\xi_\nu + \partial_\nu\xi_\mu) - \frac{\eta_{\mu\nu}}{2}(h - 2\partial^\gamma\xi_\gamma)\\ &= \bar{h}_{\mu\nu} - (\partial_\mu\xi_\nu + \partial_\nu\xi_\mu - \eta_{\mu\nu}\partial^\gamma\xi_\gamma)\end{aligned} \tag{1.27}$$

where $h' \equiv \eta_{\mu\nu}h'_{\mu\nu} = h - 2\partial^\gamma\xi_\gamma$ and therefore

$$\begin{aligned}\partial^\nu\bar{h}_{\mu\nu} \Longrightarrow \partial^\nu\bar{h}'_{\mu\nu} &= \partial^\nu\bar{h}_{\mu\nu} - (\partial^\nu\partial_\mu\xi_\nu + \partial^\nu\partial_\nu\xi_\mu - \partial_\mu\partial^\gamma\xi_\gamma)\\ &= \partial^\nu\bar{h}_{\mu\nu} - \Box\xi_\mu\,.\end{aligned} \tag{1.28}$$

---

[6] Gauge transformations in GR are just coordinate transformations [7].

[7] "Lorentz gauge" derives its name from the electromagnetism, but it is a misprint because in electromagnetism, there is the "Lorenz gauge". However this misprint is universally into use [9].

Any metric perturbation $h_{\mu\nu}$ can be put into a Lorentz gauge by making an infinitesimal coordinate transformation that satisfies:[8]

$$\Box\xi_\mu = \partial^\nu \bar{h}_{\mu\nu} \tag{1.29}$$

In the Lorentz gauge, the Einstein field equations in LG are:

$$\Box\bar{h}_{\mu\nu} = -\frac{16\pi G}{c^4} T_{\mu\nu}. \tag{1.30}$$

In vacuum, where $T_{\mu\nu} = 0$ this equation admits a class of homogeneous solutions which are superposition of plane waves [7]:

$$\bar{h}_{\mu\nu} = \mathit{Re}\left\{\int d^3k\, A_{\mu\nu}(\mathbf{k})\exp^{(ik\cdot x)}\right\} \tag{1.31}$$

with $k = (\omega/c, \mathbf{k})$, where $\mathbf{k}$ is the wave vector and $\omega/c = |\mathbf{k}|$.
Physically, the approximations implicit in the LG implies that the sources of GWs are taken to move in flat spacetime, along the trajectories described by Newtonian gravity. The response of test masses to the GWs generated is rather computed using the relation (1.13) and neglecting terms not linear in the perturbation metric when evaluating the Christoffel symbols or the Riemann tensor [9].

1.3 The transverse-traceless gauge

To study the propagation and the interaction of GWs, it is useful to analyze the equation (1.30) in vacuum [9].
In the last Section, I used the Lorentz gauge to simplify the Einstein field equations in LG. For the coordinate transformation in (1.15), the components $\bar{h}_{\mu\nu}$ transform according to the equation (1.19), but there could be another coordinate transformation (or residual gauge freedom)

$$x^\mu \longrightarrow x'^\mu(x) = x^\mu + p^\mu(x) \tag{1.32}$$

with the condition:

$$\Box p_\mu = 0\,. \tag{1.33}$$

---

[8] Since $\Box$ is an invertible operator, the equation (1.29) always admits solutions using the Green function method.

If this condition holds, then $\Box p_{\mu\nu} = 0$ where

$$p_{\mu\nu} = \partial_\mu p_\nu + \partial_\nu p_\mu - \eta_{\mu\nu}\partial^\gamma p_\gamma \tag{1.34}$$

Subtracting the functions $p_{\mu\nu}$ from the six independent components $h_{\mu\nu}$, the Einstein field equations in vacuum

$$\Box \bar{h}_{\mu\nu} = 0 \tag{1.35}$$

do not change. It means that, choosing opportunely the four functions p_μ, there are only two independent components as in the case of the Electromagnetic Theory.

In the *transverse-traceless* (TT) gauge the p^μ are chosen to have $\bar{h} = 0$ and $\bar{h}_{0i} = 0$. For these conditions, it follows that $\bar{h}_{\mu\nu} = h_{\mu\nu}$. In conclusion, in the TT gauge the following relations hold considering also the Lorentz gauge:

$$h_{0\mu} = 0 \qquad h^i_i = 0 \qquad \partial^j h_{ij} = 0. \tag{1.36}$$

Considering a single plane wave[9], the components of the metric in the TT gauge h^{TT}_{ij} can be written as:

$$h^{TT}_{ij}(t,z) = \begin{pmatrix} h_+ & h_\times & 0 \\ h_\times & -h_+ & 0 \\ 0 & 0 & 0 \end{pmatrix}_{ij} cos[\omega(t - z/c)] \tag{1.37}$$

where $\mathbf{n} = \mathbf{k}/|\mathbf{k}|$ is the direction of propagation that it is chosen along the z axis.

h_+ and $h_\times$ are called the amplitude of the "plus" and the "cross" polarization and are two independent waveforms of the GW [7].

The TT gauge conditions fix completely all the local gauge freedom, simplify greatly the Einstein equation and lead to a transverse and traceless metric tensor.

1.4 The generation of GWs

Since the Einstein equations in the Lorentz gauge in (1.30) are linear in the $h_{\mu\nu}$ components, it can be solved using the method of Green's function [9]. As in the case of the Electromagnetic Theory, using a retarded Green's function, the appropriate solution is:

$$\bar{h}_{\mu\nu}(t,\mathbf{x}) = \frac{4G}{c^4}\int d^3x' \, \frac{T_{\mu\nu}(t - \frac{|\mathbf{x}-\mathbf{x}'|}{c}, \mathbf{x}')}{|\mathbf{x}-\mathbf{x}'|} \,. \tag{1.38}$$

---

[9] The TT gauge works only in vacuum, not for example inside the source of GWs.

This solution can be evaluated in vacuum and also in the TT gauge, using the Lambda tensor.
The GW in the TT gauge is defined in terms of the spatial components of the $h_{\mu\nu}$:

$$h_{ij}^{TT} = \Lambda_{ij,kl} h^{kl} \tag{1.39}$$

where the components of the Lambda tensor are defined as ($\hat{\mathbf{n}}$ is the propagation versor):

$$\Lambda_{ij,kl}(\hat{\mathbf{n}}) = P_{ik}P_{jl} - P_{ij}P_{kl} \qquad \text{with} \qquad P_{ij}(\hat{\mathbf{n}}) = \delta_{ij} - n_i n_j \tag{1.40}$$

If the detector is at distance r, much larger than the typical dimension d of the source and in the case of a non relativistic source, the following approximations hold:

$$|\mathbf{x} - \mathbf{x}'| \simeq r - \mathbf{x}' \cdot \hat{\mathbf{x}} \qquad \text{with} \qquad \hat{\mathbf{x}} = \frac{\mathbf{x}}{r} \equiv \frac{\mathbf{x}}{|\mathbf{x}|}\,, \tag{1.41}$$

$$\bar{\lambda} \equiv \frac{c}{\omega} \sim \frac{c}{v} d \gg d \tag{1.42}$$

where v is the typical velocity within the system [1] and ω the GW frequency. The relation (1.42) implies that the typical velocities inside the source are small compared to the speed of light. In this limit of "small velocities" and large distance from the source, it is possible to perform a multipole expansion for the stress-energy tensor [7]. This expansion can be written in terms of the momenta of the T_{00} energy density using the energy-momentum conservation [9].
The emission of radiation is governed by the lowest multipole moments and at the leading order,

$$h_{ij}^{TT}(t, \mathbf{x}) = \frac{2G}{c^4} \frac{\Lambda_{ij,kl}(\hat{\mathbf{n}})}{r} \ddot{M}^{kl}(t - r/c)\,. \tag{1.43}$$

where M^{kl} is:

$$M^{kl}(t, \mathbf{x}) = \frac{1}{c^2} \int d^3x\, T^{00}(t, \mathbf{x}) x^k x^l \tag{1.44}$$

In the non relativistic limit, the mass density is $\rho(t, \mathbf{x}) = T_{00}/c^2$ and in terms of the quadrupole tensor[10]

$$Q^{ij} \equiv M^{ij} - \frac{1}{3}\delta^{ij} M_{kk} = \int d^3x\, \rho(t, \mathbf{x}) \left(x^i x^j - \frac{1}{3} r^2 \delta^{ij} \right)\,. \tag{1.46}$$

---

[10] More precisely, Q^{ij} is the reduced quadrupole moment linked to the quadrupole moment,

$$q^{ij} = \int dx^3\, \rho x^i x^j\,, \qquad \text{by the relation:} \qquad Q^{ij} = q^{ij} - \frac{1}{3}\delta^{ij} q\,. \tag{1.45}$$

It follows that the equation (1.43) is:

$$h_{ij}^{TT}(t,\mathbf{x}) = \frac{2G}{c^4}\frac{\Lambda_{ij,kl}(\hat{\mathbf{n}})}{r}\ddot{Q}^{kl}(t-r/c)\,, \tag{1.47}$$

since $\Lambda_{ij,kl}M^{kl} = \Lambda_{ij,kl}Q^{kl}$. Considering $\hat{\mathbf{n}} \equiv \hat{\mathbf{z}}$ and therefore the consequent expression for the Lambda tensor, the two polarization amplitudes are:

$$h_{+}(t,\mathbf{x}) = \frac{G}{c^4}\frac{\ddot{Q}_{11}-\ddot{Q}_{22}}{r} \tag{1.48}$$

$$h_{\times}(t,\mathbf{x}) = \frac{2G}{c^4}\frac{\ddot{Q}_{12}}{r}\,. \tag{1.49}$$

where the right-hand side is computed at the retarded time $t - r/c$.
The factor $2G/c^4 \sim 8 \cdot 10^{-50} s^2/g\,cm$ in the equation (1.43), entails that the amplitude of GWs is very weak unless the quadrupole deformation is very strong. The only interesting sources of GWs will be those which have very large masses undergoing extremely rapid variation; even in this case, the expected strain from typical sources is tiny. The smallness of GWs reflects the fact that gravity is the weakest of the fundamental interactions [7].

1.5 GWs sources overview

As previously mentioned, asymmetries in the shape and/or in the motion of the source are necessary conditions for generating a GW radiation. Specifically, in the equation (1.47), the second time derivative of the quadrupole tensor components of the stress-energy tensor must be non-zero.
According to Figure 1.1, it is useful to categorize GW sources (and the methods for detecting the emitted waves) by the frequency band in which they radiate [7]. Broadly speaking, the GW spectrum can be divided in different frequency bands: a very low frequency band $10^{-18}\,\mathrm{Hz} < f < 10^{-7}\,\mathrm{Hz}$, a low frequency band $10^{-7}\,\mathrm{Hz} < f < 1\,\mathrm{Hz}$ and a high frequency band $1\,\mathrm{Hz} < f < 10^{4}\,\mathrm{Hz}$.
In this Section, I describe briefly the "high frequency" band that is targeted by the ground-based laser interferometric detectors. The interferometric method is described in Section 2.2.
The lower limit of the "high frequency" band is set due to the gravitational coupling of ground vibrations, human activity, and atmospheric motions with the test masses [7, 11] of the interferometric detectors while the high end is set by astrophysical reasons. Indeed, it is unlikely that any interesting GW source radiates at frequencies higher than

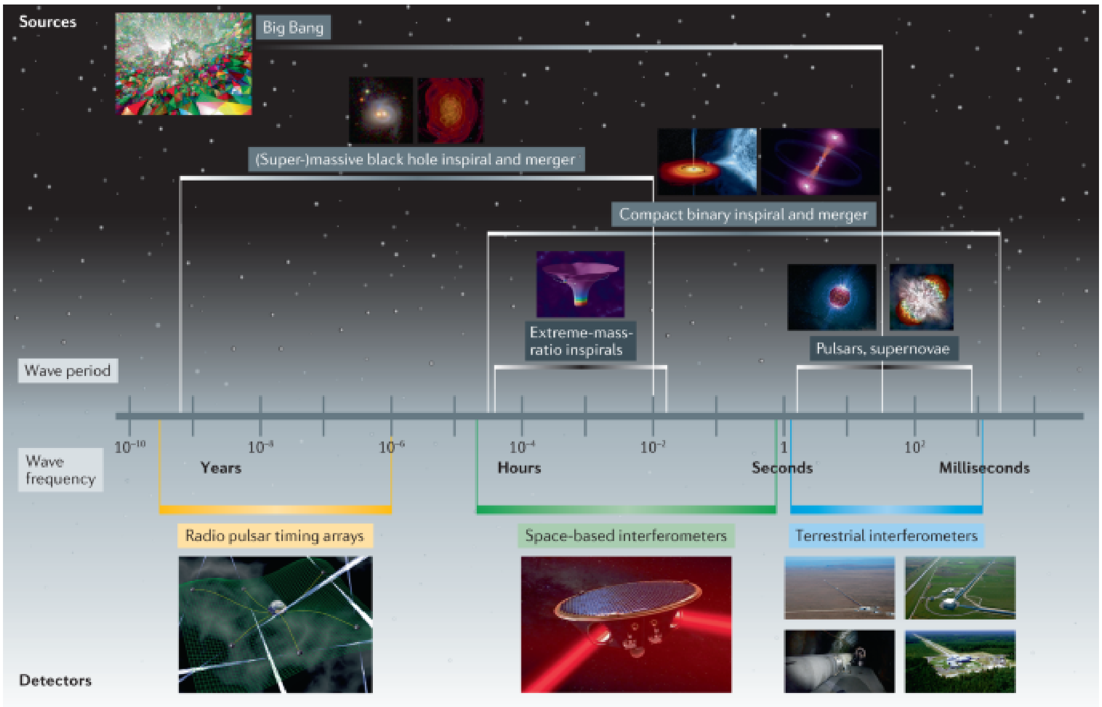

Figure 1.1: A review of potential sources linked to the frequency (in Hz) of the GW emitted and to the relevant detectors. *Credit to [10].*

a few kHz that means relatively low masses ($\lesssim M_{\odot}$, solar masses). In this mass range, there are no known theoretical or observational indications of gravitationally collapsed objects [7].

In the next paragraphs, I briefly describe the possible sources of GW radiation for ground-based detectors.

Coalescing compact binaries Binary stars systems in which each member is a neutron star or black hole are referred as compact binaries. The coalescences of compact binaries are currently the best known sources of GWs. This kind of signal has short duration (fraction of second) and a well defined signature [12] that can be divided in three different phases.

The *inspiral phase* is the first phase of the coalescence; over thousand years, the binary system progressively move to smaller and closer orbits, increasing their speed. The signal looks like an oscillating function, whose amplitude and frequency oscillation are increasing with time, dissipating orbital energy.

The *merger phase* is characterized by the strongest GW emission, because the collision of the two objects, once they get close enough, occurs. As a result, the newly-forming object experiences a large distortion in its own shape, which gradually vanishes during the *ringdown phase*.

The typical strain amplitude of a GW from a compact binary, estimating the quadrupolar moment for a binary system [13] and assuming typical values for the masses and distance from the Earth, is of order of 10^{-21} at a frequency of 100 Hz.
The first detection of GWs by ground-based detectors, GW150914 [14], was the detection of a binary black holes merger at a luminosity distance of 410 Mpc with estimated black hole masses, in the source frame, of 36 $\mathrm{M}_{\odot}$ and 29 $\mathrm{M}_{\odot}$, and the final black hole mass of 62 $\mathrm{M}_{\odot}$. The era of GW astronomy began with this detection.

Burst GWs Burst GWs come from short-duration unknown or unanticipated sources with a not so well defined signature. Likely sources could be supernovae or γ ray burst, which are transient astrophysical events [15].
Stellar collapse certainly exhibits all of the necessary conditions for strong GWs generation, that is large amounts of mass flowing in a compact region at relativistic speeds. However, these conditions are not sufficient to guarantee strong emission since the degree of asymmetry in collapse is not particularly well understood. Too little information about these systems are available up to now, but instabilities occurring during the collapse of the inner core of the star could lead to fragmentation of the stellar material in numerous components, which might reveal as a strong source of GWs.

Stochastic GWs Stochastic backgrounds are "random" GWs, arising from a large number of independent, uncorrelated sources that are not individually resolvable. A particularly interesting source of stochastic waves is the dynamics of the early Universe, which could produce an all-sky GWs background, similar to the cosmic microwave background even if with amplitude relatively small. These waves can extend over a wide range of frequencies; waves from inflation in particular span all bands, from very low frequency to high frequency [7] (see Figure 1.1).
Because of their random nature, stochastic GWs look just like noise. Supposing stationary, isotropic and homogeneous stochastic GWs, ground-based detectors measure stochastic backgrounds by comparing data at multiple sites and looking for "noise" that is correlated.

Continuous GWs Periodic sources of GWs radiate at constant or nearly constant frequency. The prototypical source of continuous GW (CW) is a spinning neutron star. The search of CW radiation is the main topic of this thesis.
In the next Subsection, I analyze how a spinning triaxial body can generate GW radiation if non-axisymmetric respect to the rotation axis. In the remaining Sections of the Chapter, I review the neutron stars as astrophysical objects focusing on pulsars and on

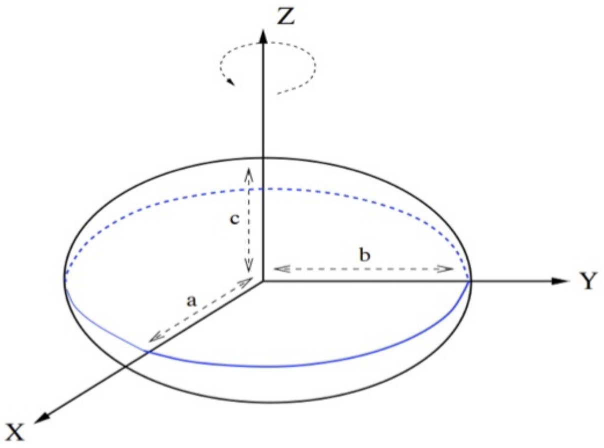

Figure 1.2: A representation of an ellipsoid with semi-axes a, b and c, rotating around the z axis.

the physical mechanisms that allow a GW emission.

1.5.1 Generation of GWs from a triaxial body

As previously mentioned, spinning neutron stars could be interesting sources of periodic GW radiation.

The production of GWs of these astrophysical objects can be deduced by using the equations (1.48) and (1.49). In this Section, I describe the approximated but illustrative case of a rigid body which rotates around one of its principal axes.

Considering the constant density ellipsoid in Figure 1.2; a, b and c are the semi-axes, ρ the density, $V = 4/3\pi abc$ the volume whereas $\hat{\mathbf{z}} = \hat{\mathbf{x}}^3$ is the direction of rotation with angular velocity $\omega = (0, 0, \Omega)$.

In the reference frame $\{x'_i\}$ co-rotating with the ellipsoid, the inertial tensor is diagonal:

$$I'_{ij} = \begin{pmatrix} I_1 & 0 & 0 \\ 0 & I_2 & 0 \\ 0 & 0 & I_3 \end{pmatrix} = \frac{M}{5} \begin{pmatrix} b^2 + c^2 & 0 & 0 \\ 0 & c^2 + a^2 & 0 \\ 0 & 0 & a^2 + b^2 \end{pmatrix} \tag{1.50}$$

since the inertial tensor is defined as:

$$I'_{ij} = \int_V d^3x\, \rho(\vec{x})(r^2\delta_{ij} - x_i x_j) \qquad \text{with} \qquad r^2 = (x'_1)^2 + (x'_2)^2 + (x'_3)^2\,. \tag{1.51}$$

In the inertial frame $\{x_i\}$, the inertial tensor components are:

$$I_{ij} = \begin{pmatrix} I_1\cos^2(\Omega t) + I_2\sin^2(\Omega t) & -\sin(\Omega t)\cos(\Omega t)(I_2 - I_1) & 0 \\ -\sin(\Omega t)\cos(\Omega t)(I_2 - I_1) & I_1\cos^2(\Omega t) + I_2\sin^2(\Omega t) & 0 \\ 0 & 0 & I_3 \end{pmatrix} \tag{1.52}$$

because the two frame are related by the rotation matrix

$$R_{ij} = \begin{pmatrix} \cos(\Omega t) & -\sin(\Omega t) & 0 \\ \sin(\Omega t) & \cos(\Omega t) & 0 \\ 0 & 0 & 1 \end{pmatrix} \tag{1.53}$$

and the following relations hold:

$$x_i = R_{ij}x'_j\,, \qquad I_{ij} = R_{ik}R_{jl}I'_{kl}\,. \tag{1.54}$$

The quadrupolar moment is linked to the inertial tensor by the relation:

$$Q_{ij} = -(I_{ij} - \frac{1}{3}\delta_{ij}Tr(I)) = -I_{ij} + const \tag{1.55}$$

since the trace of a tensor is invariant under rotation, that is $Tr(I) = I_1 + I_2 + I_3 = const$. For this reason, the components Q_{ij} can be written as:

$$Q_{ij}(t,\mathbf{x}) = \frac{I_2 - I_1}{2}\begin{pmatrix} \cos(2\Omega t) & \sin(2\Omega t) & 0 \\ \sin(2\Omega t) & -\cos(2\Omega t) & 0 \\ 0 & 0 & 0 \end{pmatrix} + const \tag{1.56}$$

using the relation $\cos(2\Omega t) = 2\cos^2(2\Omega t) - 1$ where all the constant terms are included in $const$. Using equations (1.48) and (1.49), it is easy to show that the GW polarization amplitudes received by an observer at a distance r, whose line-of-sight makes an angle[11] i with the direction of rotation of the star, is[12]:

$$h_+(t,\mathbf{x}) = \frac{1}{r}\frac{4G\Omega^2}{c^4}(I_1 - I_2)\frac{1+\cos^2(i)}{2}\cos[2\Omega(t - r/c)] \tag{1.57}$$

---

[11] Equations (1.48) and (1.49) are obtained in a frame where the GW propagates in the $\hat{\mathbf{z}} = \hat{\mathbf{x}}^3$ direction. In a general frame, the component Q'_{ij} are linked to the components in (1.46) by the general relation $Q'_{ij} = R_{ik}R_{jl}Q_{kl}$ where the rotation matrix R is completely defined when the usual transformation angles ϑ, ϕ are known (in (1.57), $\vartheta = i$ and $\phi = 0$) .

[12] "Recall that h_+ and h_x are defined in terms of the components of h_{ij} in the plane transverse to the propagation direction. Therefore these are "the" polarization amplitudes, and are denoted by h_+ and h_x , rather than h'_+ and h'_x" [9].

$$h_\times(t,\mathbf{x}) = \frac{1}{r}\frac{4G\Omega^2}{c^4}(I_1 - I_2)\cos(i)\sin[2\Omega(t - r/c)]\,. \tag{1.58}$$

It is useful to introduce the ellipticity $\epsilon = (I_2 - I_1)/I_3$, that in the limit of small asymmetry $a \simeq b$ becomes:

$$\epsilon \simeq \frac{b-a}{a}\,, \tag{1.59}$$

and the GW frequency $f_{gw} = \Omega/\pi$.
The polarization amplitudes can be rewritten as:

$$h_+(t,\mathbf{x}) = h_0\frac{1+\cos^2(i)}{2}\cos[2\pi f_{gw}(t - r/c)] \tag{1.60}$$

$$h_\times(t,\mathbf{x}) = h_0\cos(i)\sin[2\pi f_{gw}(t - r/c)]\,. \tag{1.61}$$

where h_0 is:

$$h_0 = \frac{16\pi^2 G}{c^4}\frac{f_{rot}^2\epsilon I_3}{r} \tag{1.62}$$

and $f_{rot} = \Omega/2\pi$ is the rotation frequency.
The analyzed model entails a periodic GW radiation with frequency that is twice the rotation frequency of the star $f_{gw} = 2f_{rot}$.
Different models [16], for example considering a precessing rigid body ("wobbling" stars), imply a dual-harmonic emission, i.e a GW radiation both at once and twice the rotation frequency. A different mechanism described in [17] that entails a dual-harmonic emission without a modulation of the observed radio emission, assumes a pinned superfluid component with a misaligned rotation axis within the star.
More complex emission models exist (see [18] for a complete discussion) and the emission may happen on more than two harmonics. In general, it can be assumed that the GW frequency f_{gw} is proportional to the rotation frequency f_{rot} and also to the precession frequency f_{prec} by

$$f_{gw} = k(f_{rot} + f_{prec}) \tag{1.63}$$

(as shown in this Section, if $f_{prec} = 0$, $k = 2$). Typically, the complex models discussed above are not considered in real searches since the relation in (1.63) dramatically complicates the signal waveform to be searched for.

1.6 Spinning neutron stars as possible CW sources

As shown in Section 1.5.1, non-axisymmetric spinning rigid body can generate a continuous GW radiation. This kind of signal is referred as "continuous waves" since their lifespan is expected to be longer than the observation period of experiments.

Canonical CW sources for ground-based detectors are Galactic, non-axisymmetric, spinning neutron stars both in accreting systems or as isolated sources. Different exotic scenarios, as bosons clouds surrounding a fast spinning black hole [19], or CW-like signals potentially induced by dark matter candidates [20], will not be discussed here.

First theorized by Baade and Zwicky [21] in 1934, the observational evidence of a neutron star came with the discovery of the first radio pulsar in 1967 [22] by Hewish and Bell. They observed a very regular, clock-like, pulsing radio signal - from which the name *pulsar* - at a particular sky position. The identification of pulsars with neutron stars is due to Pacini and Gold [23]; rotating neutron stars are responsible for the observed pulsating radio signals. This explanation was confirmed by the discovery of the Crab and Vela pulsar in 1968 at the heart of supernova remnants.

The analysis of the time of arrivals of the pulses in the Hulse-Taylor binary system, discovered in 1974 [24], showed that neutron star binary system looses energy due to GW emission [9]. This was the first indirect evidence of the existence of GWs.

In general, isolated neutron stars can emit GWs due to two main processes: normal modes of oscillation of the fluid core or crustal deformations of the star. In this Section, I consider only the second process of emission where the neutron star is not a simple fluid (see [16] for a review of normal modes emission) but can instead support some sort of strain (see Subsection 1.6.2).

The relation in (1.62) for the expected amplitude can be used to estimate the typical CWs amplitude. Most of the parameters in (1.62) can be constrained by astronomical observations (for example, measuring the radio signal from pulsars), except for the ellipticity ϵ that characterizes the degree to which the star is distorted. For example, for a Galactic source (distant from Earth a few kpc) assuming a rotation period of the order of a few ms, a typical value of the neutron star moment of inertia[13] of $10^{38}\,\mathrm{kg}\cdot\mathrm{m}^2$ and ellipticity as small as 10^{-6}, h_0 in (1.62) can be parametrized as:

$$h_0 \simeq 10^{-27}\left[\frac{f_{gw}}{100\,\mathrm{Hz}}\right]^2\left[\frac{10\,\mathrm{kpc}}{r}\right]\left[\frac{I}{10^{38}\,\mathrm{kg}\cdot\mathrm{m}^2}\right]\left[\frac{\epsilon}{10^{-6}}\right]. \tag{1.64}$$

The expected amplitude is several orders of magnitude lower than the one expected by binary coalescences. Measuring CW radiation requires coherently tracking the signal for a large number of wave cycles since they are periodic sources.

It is clear the the expected amplitude depends on the parameter ϵ, that is poorly understood and linked to the unknown neutron star equation of state. As described in Section 2.7, CWs searches by ground-based detectors can constrain the value of ϵ for known

---

[13] Neutron stars have typically a radius $R \sim 10$ km and a mass $\mathrm{M} \sim 1.4\mathrm{M}_\odot$; it follows that $I \sim 2MR^2/5 \sim 10^{38}\mathrm{Kg}\cdot\mathrm{m}^2$.

pulsars.

In the next Sections, I briefly describe the neutron star formation, structure and population analyzing also the theoretical reasons for a non-axisymmetric structure that could generate a CW emission.

1.6.1 Neutron star observables, structure and population

Neutron stars are the final states of stars with mass between 10 and $25\ M_{\odot}$, too massive to form white dwarfs and too light to form black holes upon collapse after fuel consumption. The formation of a neutron star could happen mainly [25] due to core-collapse supernova explosions but also after a binary neutron star merger.

It is thought that neutron stars have a crust with outer radius between 10 and 15 km and a thickness of almost 1 km [16], composed near the top of a tight lattice of neutron-rich heavy nuclei, permeated by neutron superfluid. Deeper in the star, as pressure and density increase, the nuclei may become distorted and elongated, forming a “nuclear pasta” of ordered nuclei and gaps [26]. Still deeper, the pasta gives way to a hyperdense neutron fluid and perhaps undergoes phase transitions.

As a result of the collapse with the reduction of the outer surface of the star, it is expected that neutron stars have strong magnetic fields ranging from 10^{8} G to 10^{15} G [27]. The strongest magnetic fields can be observed in some young neutron stars, the so-called magnetars.

The neutron star matter equation of state (EOS) [28] directly reflects on the star’s observable global parameters such as the mass and the radius. To set constraints on the EOS of isolated neutron stars, both mass and radius should be measured, and some assumptions on the pulse profiles should be made. Indeed, due to the high density and the strong conditions, the EOS is not experimentally accessible in terrestrial laboratories.

Neutron star masses are typically measured from pulsar observations, while radius measurements are more challenging and strongly depend on the X-ray emission model assumed. The neutron star measured masses lie in the range $1 \div 2\ M_{\odot}$ [29]. Estimates of the radius can be made only indirectly, for instance, by combining the measured flux and temperature with the source distance. According to latest results [29, 30], neutron star radii should be in the range $9 \div 13$ km.

The detection of the first neutron star merger event GW170817 by LIGO and Virgo [31], followed by the gamma-ray burst GRB170817 [32], and the optical transient signal of a kilonova AT 2017gfo [33], provided a new tool for neutron star mass and radius estimates [34] and hence, for the EOS analysis. Future detection of neutron star merger in the coming observing runs will provide new constraints on the neutron star EOS.

Form supernovae observations, the expected number [35] of neutron stars in our galaxy is up to $10^{8\div9}$; only a small fraction, almost 10^3, has been detected as pulsars (see Section 1.7). Other neutron stars can be detected [36] from X-ray thermal emission or from accretion in binary system, as in the case of low-mass X-ray binary.

1.6.2 Potential sources of neutron star non-axisymmetry

As shown in Subsection 1.5.1, if a neutron star is not perfectly axisymmetric it emits GWs, with the GW frequency proportional to the rotation frequency.

If the GW emission mechanisms are well understood (see e.g. [37]), the actual factors that cause the asymmetry in neutron stars are still under debate. The asymmetry respect to the rotation axis is traditionally [38] ascribed to crustal deformations or to the presence of a strong inner magnetic field not aligned with the star's rotation axis.

Crustal deformations, or in other words "mountains" on the neutron stars surface, can create a time-varying quadrupole on a neutron star. "The idea is that the crust can sustain a “mountain” on the neutron star in much the same way as the terrestrial crust sustains mountains on Earth" [39].

Models of the neutron stars crust [16] provide evidence for a maximum value of the ellipticity that the crust can support:

$$\epsilon < 2 \times 10^{-5} \left(\frac{\mu_{break}}{0.1}\right) \tag{1.65}$$

where μ_{break} is the maximum stress that the crust can support, normalized to the shear modulus (value of 0.1 is much larger of any terrestrial material). It is clear that the obtained maximum value strongly depends on the assumed EOS and on the breaking strain of the crust.

It is known, already in [40] by Chandrasekhar and Fermi, that magnetic fields induce quadrupolar deformations on spherically symmetric stars. In other words, mountains can also be supported by the strong magnetic field of the neutron star, which deforms the spherical shape of the star.

The expected deformation due to magnetic field strongly depends on the magnetic field morphology and on the assumed EOS (see e.g. [39]). For example, if the magnetic field is purely poloidal [16],

$$\epsilon \approx 10^{-12} \left(\frac{\hat{B}}{10^{12} G}\right)^2 \tag{1.66}$$

where $\hat{B}$ is the average magnetic field. In contrast, a toroidal magnetic field induces a smaller value and also a prolate deformation. The estimated ellepticity depends again by the EOS used and can vary almost one order of magnitude [41] among the different proposed models.

In binary systems, quadrupolar deformations can be present in accreting neutron stars also due to temperature gradients in the accreted crust (the so-called "thermal mountains"). Indeed, as the matter accretes, it is buried and compressed until nuclear reactions occur (electron capture, neutron emission, etc.). These reactions heat the crust, and since the accreted matter is expected to be asymmetric, the temperature gradient produced by nuclear reactions is also asymmetric, giving rise to quadrupolar deformations in the neutron star [37].

As described in [16], a possible value for the typical ellipticity in young neutron star should be of the order of 10^{-7}; since $\epsilon \approx \Delta R/R$ (see (1.59)) detecting a GW radiation due to $\epsilon \approx 10^{-7}$ means to detect the effect of a deformation, or mountain, with a height of few millimeters for radius $R = 10$ km.

1.7 Pulsars: lighthouses in space

Most of the neutron stars in the Galaxy has been detected as pulsar, spinning neutron stars characterized by a periodic radio emission (but also detected in the X-ray and gamma-ray band) and a strong dipole magnetic field. Even though the word pulsar is a combination of "pulse" and "star," pulsars are not pulsating stars; their radio emission is actually continuous but the magnetic axis is tilted respect to the rotation axis.

During the rotation, the pulsating radiation is detectable every time one of the conical beams produced by the magnetic field crosses the field of view of the observer. Since the pulse periods (typically from a few milliseconds up to ten seconds) equal the rotation periods of spinning neutron stars, they are quite stable. This is the lighthouse (or rotating dipole) model for the electromagnetic pulsar emission (see Figure 1.3).

To date (ATNF Catalogue v1.67[14]), more than 3000 pulsars are known in our Galaxy. This is expected to be a small part of the pulsar population due to strong selection effects. First, the flux density can not be detected beyond few kpc for the current radio telescope sensitivities. Then, there is also a beaming effect since we can detect pulsars only if the radio beam intercept our line of sight. It is estimated that, with the SKA (Square Kilometer Array) project fully operational, the current known population of pulsars will grow tenfold [42].

The radio emission originates in the magnetosphere and can be explained by the polar cap model. Since the Lorentz force vastly exceeds the gravitational force, charged par-

---

[14] http://www.atnf.csiro.au/research/pulsar

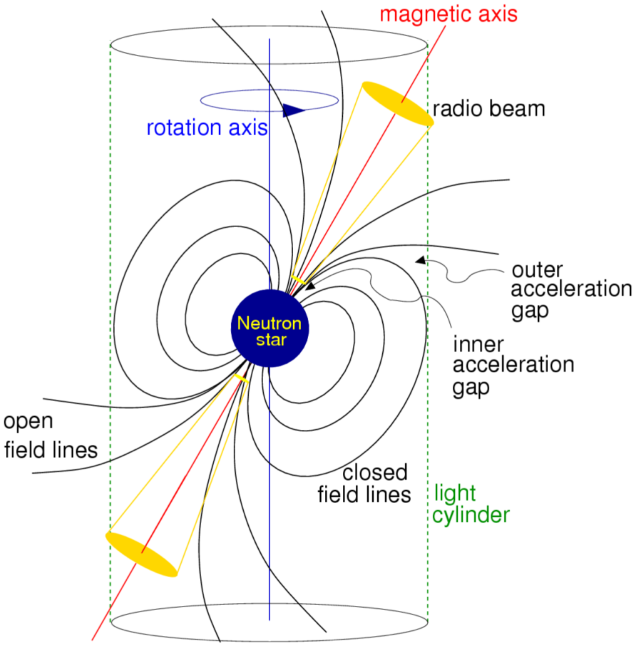

Figure 1.3: Representation of the dipole magnetic field configuration around a pulsar. The magnetic axis is not aligned with the rotation axis and thus electromagnetic beams can be observed as pulses with regular rotation periods. The light cylinder, outlined in dashed green, is the radius out to which the co-rotation speed of the magnetic field approaches the speed of light. *Credit to [43].*

ticles flow freely along the magnetic field lines, forming a magnetosphere co-rotating with the neutron stars. Co-rotation is limited by relativity to the light cylinder (Figure 1.3), where the field lines are closed. Modelling of the magnetosphere is difficult, but charges should flow until the Lorentz force is balanced by an electric force. Regions in the magnetosphere where this force-free state cannot be maintained are called ‘gaps’. One of these is above the (magnetic) polar cap, where a depleted concentration of charges results in a net force on a charge. Gamma ray photons from these accelerating charges interact with the magnetic field to generate electron/positron pairs and a cascade of radiation and particles close to the surface of the neutron star. The pair cascade is thought to generate the coherent[15] emission detected as radio waves.

Radio pulsars can exhibit several timing irregularities, as in the case of the so-called *glitches*. While most objects are observed to steadily spin-down due to the emission of electromagnetic waves (and, possibly, also GWs), many pulsars show glitches, that

---

[15] The particles emit coherently at low frequencies, in the sense that N particles radiate N^2 times the power per individual particle. Coherent emission explains the much greater apparent brightness pulsar temperature respect to what is achieved by random processes.

is sudden, impulsive increases in their spin in some cases followed by an increase in their spin-down rate [44]. The exact mechanism driving a glitch is not fully understood, although it is clear that a sudden transfer of angular momentum occurs between the rapidly rotating superfluid interior and the outer crust.

1.7.1 The spin-down and the $P - \dot{P}$ diagram

It is observed that the pulse period (and hence, the rotation period) from known pulsars increases. For example, in 1969 using few months of data, it was already observed the uniform increase of the period P for the Crab pulsar at a rate of about 34 ns/day, i.e. $\dot{P} \approx 4.2 \times 10^{-13}$.

A phenomelogical model for the pulsar spin-down is a power law:

$$\dot{f} = K f^{n} \tag{1.67}$$

where f is the rotation (or gravitational) frequency, $\dot{f}$ the first time derivative and K, a negative constant. The exponent n is the braking index and can be deduced assuming a certain spin-down mechanism. For example, if the spin-down is entirely due to the magnetic dipole radiation, it follows that $n = 3$ while if the increase in the rotation period is due to the emission of GWs, $n = 5$.

From the power-law model (1.67), the second derivative is:

$$\ddot{f} = -nK f^{n-1} \dot{f} \tag{1.68}$$

and from this relation, it follows that:

$$n = \frac{f \ddot{f}}{\dot{f}^{2}} \tag{1.69}$$

The measurement of the spin-down parameters for known pulsars can be used to constrain the braking index.

Assuming the same power law has applied since the birth of the star, the characteristic age τ of the star can be related to its birth rotation frequency f_0 and current frequency f by:

$$\tau = -\left[\frac{f}{(n-1)\dot{f}}\right]\left[1 - \left(\frac{f}{f_0}\right)\right] \tag{1.70}$$

and in the limit $f \ll f_0$,

$$\tau \approx -\left[\frac{f}{(n-1)\dot{f}}\right] \tag{1.71}$$

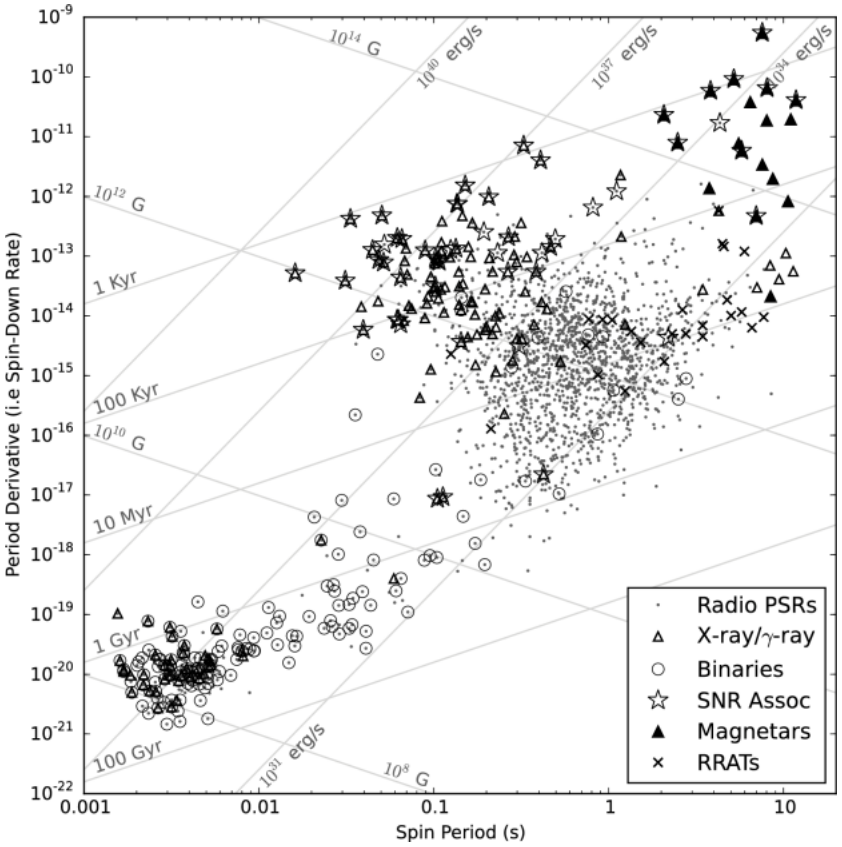

Figure 1.4: $P - \dot{P}$ scatter plot for known pulsars with counter plots for constant values of the characteristic age, magnetic field strength and spin-down luminosity. Rotating Radio Transients (RRATs) are pulsars that sporadically emit single pulses instead of continuous pulse trains. *Credit to [47].*

For the Crab pulsar, the characteristic age τ assuming a magnetic dipole radiation ($n = 3$) is $\tau \approx 1240$ yr since $P \simeq 33$ ms and $\dot{P} \simeq 4.2 \times 10^{-13}$; while considering the measured [45] breaking index $n \simeq 2.515$, $\tau \approx 1600$ yr. These estimates are in agreement with the supernova explosions associated to the Crab pulsar of AD 1054.

Measured braking indices inferred from frequency derivatives of known pulsars are typically ranging between 2 and 3, although several have large uncertainties. These measurements suggest that the model of a neutron star spinning down with constant magnetic field is, most often, inaccurate.

Several mechanisms that entail braking indices below 3 have been proposed [46]. However, it is also clear that for many pulsars a phenomenological model with time-independent K and n is not realistic due to possible magnetic field decay or glitches.

The properties of pulsars population are well summarized in the scatter diagram (Figure 1.4) of all known pulsars in the $P - \dot{P}$ (period-period derivative) plane [47]. Indeed, P and $\dot{P}$ return some indication of the age, magnetic field and luminosity of the pulsar.

From (1.71), the characteristic age $\tau \propto P/\dot{P}$, while it can be shown [16] that the magnetic field $B \propto (P\dot{P})^{1/2}$ and the spin-down luminosity $L \propto \dot{P}/P^3$.

Young pulsar, born on supernova explosion as the Crab pulsar, appears in the upper-left corner (short period) of the $P - \dot{P}$ diagram. Then, they gradually move to the right and down (for the spin-down), along lines of constant magnetic field and crossing lines of constant characteristic age.

Pulsars with characteristic ages $< 10^5$ yr are often found in or near recognizable supernova remnants while older pulsars are not, either because their supernova remnants have faded to invisibility or because they escaped for high kick velocities.

Most of the pulsars are in the region of periods between 0.1 and few seconds and $\dot{P}$ values between 10^{-13} and 10^{-17}.

A clear separate population is in the lower left corner, for the so-called millisecond (or recycled) pulsars, and in the upper right corner for the magnetars. Millisecond pulsars are old pulsars with short rotation periods spun-up by accretion from a binary companion.

There is a clear absence of pulsars in the lower right of the diagram, to the left of the "death line" where the radio emission is predicted to shut off. Indeed, due to the low rotation and/or magnetic field, the curvature radiation near the polar surface is no longer capable of generating particle cascades.

1.7.2 The spin-down amplitude limit

In this Subsection, I describe how to set a theoretical limit for the expected GW amplitude assuming that the spin-down of the pulsar is entirely due to the GWs emission.

GWs carry energy and cause a deformation of spacetime. The stress-energy carried by GWs can not be localized within a wavelength. Instead, one can say that a certain amount of stress-energy is contained in a region of the space which extends over several wavelengths. The energy flux has all the properties one would anticipate by analogy with electromagnetic waves: it is conserved, it can be absorbed by detectors, and it can generate curvature like any other energy source in Einstein's formulation of relativity [48].

It can be possible to derive [9, 48] in the TT gauge of the linearized theory, the gravitational luminosity as a function of the third-order time derivative of the quadrupole moment tensor:

$$L_{gw} = -\frac{dE}{dt} = \frac{G}{5c^5}\left\langle \frac{\partial^3 Q_{ij}}{dt^3}\frac{\partial^3 Q_{ij}}{dt^3} \right\rangle \tag{1.72}$$

where the brackets represent the average over several wavelengths.
Using the expressions (1.46), the gravitational luminosity of a rotating compact star is:

$$L_{gw} = \frac{32G}{5c^2}\epsilon^2 I_3^2 \Omega^6 \,. \tag{1.73}$$

As showed in the previous Section, pulsars slow down mainly because, having a time varying magnetic dipole moment, they radiate electromagnetic waves. A further braking mechanism is provided by GW emission.
Supposed that the pulsar radiates its rotation energy entirely in GWs, it is possible to infer a theoretical limit on the emitted GW amplitude.
The rotation kinetic energy, in the Newtonian approximation, is:

$$E_{rot} = \frac{1}{2} I \Omega^2 \tag{1.74}$$

where $I = I_{ij}\hat{\omega}_i\hat{\omega}_j$. The kinetic energy lost as the pulsar slows down is:

$$\frac{dE_{rot}}{dt} = 4\pi^2 I f_{rot} |\dot{f}_{rot}| \tag{1.75}$$

with $\dot{f}_{rot}$, the derivative of the star's rotation frequency.
Equating the gravitational luminosity with the expression (1.75), it follows that:

$$|\dot{f}_{rot}| \propto f_{rot}^5 \tag{1.76}$$

that is the breaking index is $n = 5$ if the neutron stars loses energy via GW emission. Rewriting the equality in terms of an expected strain amplitude [49], the spin-down limit is:

$$h_0^{SD} = \left(\frac{5GI|\dot{f}_{rot}|}{2c^3 d^2 f_{rot}} \right)^{1/2} \,. \tag{1.77}$$

The spin-down limit on the signal amplitude corresponds to an upper limit on the star's ellipticity. Setting an upper limit on the amplitude of a CW below the spin-down limit is an important achievement and indication for the detectors sensitivity.
It is important to note that spin-down limits on the GW luminosity are plausible, but model dependent. They assume a model for the structure of the neutron star (for instance, that it is not accreting and is rigidly rotating, in addition to assumptions about its EOS), and they take dispersion measure distance as a consistently good measure of true distance. There is some considerable uncertainty associated with all of these assumptions.

Chapter 2

Gravitational wave detectors and the CW search

In the years after the GR formulation, there was strong skepticism about the physical reality of GWs. It was Einstein himself to doubt and to consider GWs as "pure gauge". In 1956, Felix Pirani published a paper, *“On the physical significance of the Riemann tensor”*, showing that GWs "move particles back and forth as they pass by" [50]. The results were presented at the Chapel Hill Conference[1] in 1957 that might be considered the starting point and the inspiration for the entire GW detection program[2] [51].
In the first part of this Chapter, I analyze how GWs interact with test masses and describe the interferometric method that allows the LIGO and Virgo Collaboration to detect the first GW signal from a binary black hole merger. Then, I focus on the actual detectors describing briefly the main instrumental features and the observational results achieved so far.
In the second part, I focus on the searches for CW signals describing in detail the targeted search from known pulsars. I review the main pipelines used for this analysis describing the results of the last observing runs.

2.1 Interaction of GWs with test masses

As described in the previous Chapter, the notion of “gravitational force” disappears in GR, replaced instead by the idea that freely falling bodies follow geodesics in spacetime described by the geodesic equation inferred in (1.12). The linearized Einstein equations

---

[1] Chapel Hill conference, at the University of North Carolina in Chapel Hill, played a central role in the future development of classical and quantum gravity. In addition to the questions linked to GWs, during the conference many questions were formulated, including ideas that are topical even today, like the Everett’s parallel universes interpretation of quantum physics.

[2] See Appendix A for a brief history of GW detectors.

allow GWs to propagate through spacetime at the speed of light, and using an appropriate system of coordinates - the TT gauge - it is possible to infer the expression for the components of the perturbation tensor.

The geodesic equation has a simple expression in the TT gauge. If a test mass is at rest at $\tau = 0$, the equation for the coordinate acceleration is:

$$\frac{d^2x^i}{d\tau^2} = 0 \tag{2.1}$$

since the Christoffel symbols (see (1.6)), related to the first derivatives of $h_{\mu\nu}$, are all null to the first order in the component $h_{\mu\nu}$. This means that in the TT gauge for non-relativistic motion the coordinate location of freely falling body is unaffected by the GW. It follows that also the coordinate separation remain constant.

The TT gauge shows that the physical effects of GWs are not described in the coordinate system since the theory is invariant under coordinate transformation [9]. The physical effect of GW can be described in terms of proper distance that is a coordinate-invariant observable [52].

Let us consider two spatial freely falling particles, located at $z = 0$ and separated on the x axis by a coordinate distance L_c. Consider a GW in TT gauge that propagates down the z axis (see (1.37)), $h^{TT}_{\mu\nu}(t, z)$.

The proper distance L between the two particles in the presence of the GW is given by:

$$L = \int_0^{L_c} \sqrt{g_{xx}} dx = \int_0^{L_c} \sqrt{1 + h^{TT}_{xx}(t, z = 0)} dx \tag{2.2}$$

$$\simeq \int_0^{L_c} \left(1 + \frac{1}{2} h^{TT}_{xx}(t, z = 0)\right) dx = L_c \left(1 + \frac{1}{2} h^{TT}_{xx}(t, z = 0)\right) \tag{2.3}$$

that is the proper separation of the two particles oscillates with a fractional length change,

$$\frac{\delta L}{L} \approx \frac{1}{2} h^{TT}_{xx}(t, z = 0) \tag{2.4}$$

This expression is obtained in the TT gauge but the results is gauge independent.

Let us consider the reference frame of the laboratory - the proper detector frame - where the distance between two free-falling test masses is measured. In this reference frame, the study of the effects of GWs is easier considering the geodesic deviation equation [3]. To first order in $h_{\mu\nu}$ and assuming that the coordinate time and proper time are equivalent (i.e. test-masses that are slowing moving):

$$\frac{d^2\xi^i}{d\tau^2} = \frac{d^2\xi^i}{dt^2} = R^i_{\mu\nu\beta} U^\mu U^\nu \xi^\beta \tag{2.5}$$

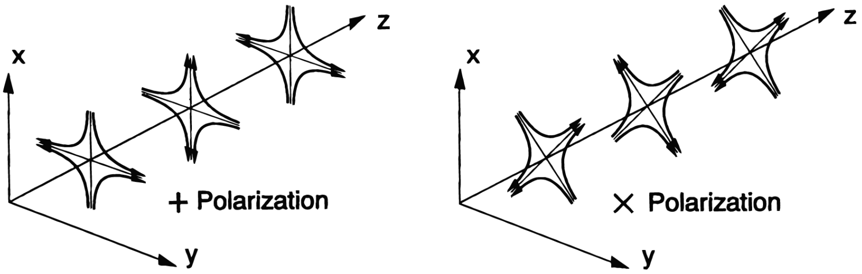

Figure 2.1: The line of forces on the x- and y-axis corresponding to a plus and cross polarized GW that propagates along the z-axis.

where ξ^i is the vector connecting two geodesics and U^μ is the four-velocity vector ($U^\mu = dx^\mu/d\tau$) of the free-falling test-masses.

Considering two test-masses separated along the x-axis by L, the geodesic deviation equation becomes:

$$\frac{d\xi^i}{dt^2} \equiv \ddot{\xi}^i = R^i_{00x} L \tag{2.6}$$

The Riemann tensor can be evaluated in the TT gauge since it is invariant. It follows that:

$$\ddot{\xi}^i = \frac{1}{2}\ddot{h}^{TT}_{ij}\xi^j \tag{2.7}$$

that is, the effect of GW in the proper detector frame can be described in terms of a Newtonian force applied to the mass m: $F_i = m\ddot{\xi}^i$. This expression is valid as long as the distance L is small compared to the GW reduced wavelength.

The relative length change is thus defined at first order:

$$\frac{\delta L}{L} \approx \frac{1}{2}h^{TT}_{xx} \tag{2.8}$$

The important result is that the effect of a GW on the spacetime metric has an intrinsic differential nature. This means that the distance between two nearby test masses in the metric generated by a GW is modulated at the wave frequency in the direction perpendicular to the propagation direction. Indeed, GWs are "transverse" waves since the effect is in the plane perpendicular to the direction of propagation, and also "traceless" waves since the effect is equal and opposite in the two perpendicular directions, as in Figure 2.1. The relative change in the distance is given by the amplitude of the GW, usually called strain amplitude.

2.2 Interferometric method

A Michelson interferometer is designed to be highly sensitive to changes in the path length of two arms that are orthogonal to each other (see Figure 2.2). A light source is sent into a beam splitter, which divides the beam in half. At the end of each arm, there is a mirror that reflects the light back to the beam splitter. At the beam splitter, the light from each arm is split again, such that half of the light is sent back towards to input, while the other half is sent to the output.

Choosing a coordinates system such that the interferometer's two arms lie along the x- and y-axes, with the beam splitter at the origin, the input beam to the interferometer is characterized by the electric field:

$$E_{in} = E_0 e^{i(2\pi ft - k_L x)} \tag{2.9}$$

where $k_L = 2\pi/\lambda$ is the wave vector and λ the laser wavelength. This input field encounters a 50/50 beam splitter with reflection and transmission amplitude coefficients of $r_B = 1/\sqrt{2}$ and $t_B = 1/\sqrt{2}$; the light transmitted down the x and y-axes is described as

$$E_x = \frac{E_0}{\sqrt{2}} e^{-i(2\pi ft - k_L x)} \qquad E_y = \frac{E_0}{\sqrt{2}} e^{-i(2\pi ft - k_L y)} \tag{2.10}$$

After travelling down the length of each arm, and reflecting on the end mirrors, each field picks up a factor of -1. Reflecting back to the beam splitter and recombining, the final output field is [9]:

$$E_{out} = -\frac{E_0}{2} e^{-i(2\pi ft - 2k_L L_x)} + \frac{E_0}{2} e^{-i(2\pi ft - 2k_L L_y)} = -iE_0 e^{-i(2\pi ft - k_L [L_x + L_y])} \sin(k_L \Delta L) \tag{2.11}$$

where $\Delta L = L_y - L_x$. The total power output, i.e. the measurable quantity, is:

$$P_{out} = \frac{P_{in}}{2}(1 + \cos(2k_L \Delta L)) \tag{2.12}$$

where $P_{in} = E_0^2$ is the input power.

At the output port, either constructive or destructive interference can occur based on the path distance along each arm. If the path length differs by an integer number of wavelengths, constructive interference occurs, while a difference of a half wavelength results in destructive interference.

In a more realistic case, for generic values r_b/t_b of the reflectivity/transmissivity of the beam splitter and values r_1 and r_2 for the reflectivities of the mirrors at the end of each

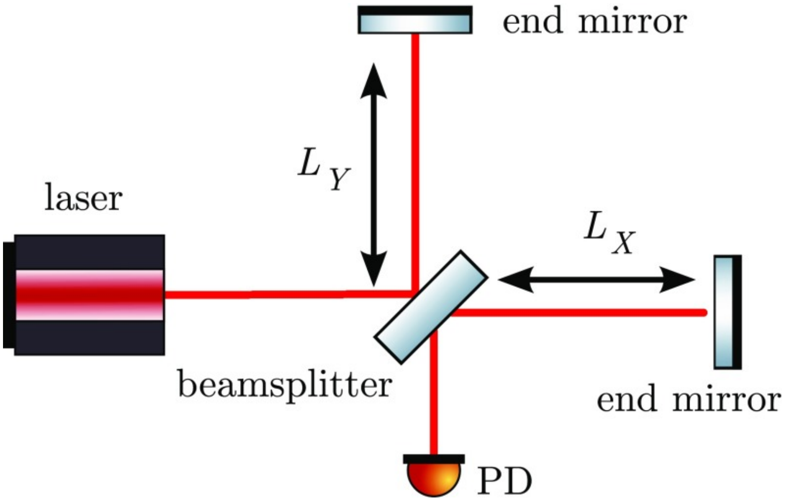

Figure 2.2: Sketch of a simple Michelson interferometer. *Credit to [53].*

arm, the power output is:

$$P_{out} = P_{in} r_b^2 t_b^2 (r_1^2 + r_2^2)(1 + C\cos(2k_L \Delta L)) \tag{2.13}$$

where C is the contrast $C = (2r_1 r_2)/(r_1^2 + r_2^2)$ that quantifies the asymmetries in reflectivities of the two arms.
Let us assume, for example, in the TT gauge a GW with a plus polarization propagating along the z-axis,

$$h_+(t, z = 0) = h_0 \cos(\omega_{gw} t) \tag{2.14}$$

The GW strain shortens one arm while lengthening the other as it passes the detector, resulting in a slight difference in round-trip travel time for the laser light due to the mirrors displacement ΔL. The mirrors' displacement leads to a phase shift of the light in one arm of the detector relative to the other, creating a change in light intensity at the photodetector of the output port. The time-dependent intensity recorded by the photodetector reconstructs the propagating GW.
The phase shift $\Delta\Phi$ induced by a passing GW in an interferometer is:

$$\Delta\Phi = \Phi_0 + \delta\Phi_{GW} = \Phi_0 + 2k_L h_0 L \mathrm{sinc}(\omega_{gw} L/c) \cos\omega_{gw}(t - L/c) \tag{2.15}$$

with k_L the laser wave vector, $L = (L_x + L_y)/2$ and $\Phi_0 = k_L \Delta L$.
The effect is a variation of the power detected at the output port which can be expressed at first order in the GW amplitude:

$$P_{out} = P_0 \sin^2(\Phi_0 + \delta\Phi_{GW}) = \frac{P_0}{2}[1 - \cos(2\Phi_0 + \delta\Phi_{GW})] \tag{2.16}$$

In the limit $\omega_{gw}L/c \ll 1$, the phase shift due to the GW is:

$$\delta\Phi_{GW} \approx h_+(t - L/c)k_L L \tag{2.17}$$

and it follows that:

$$\frac{\Delta L}{L} \approx h_0 \tag{2.18}$$

The phase Φ_0 is a parameter that can be chosen by the experimenter to fix the best working point of the interferometer. Since the effect to be observed is small, the interferometer must work as a null instrument that when there is no signal, records a zero output. The working point is the dark fringe[3].

Expanding to the first order in h_0 the expression for the electric field, the effect of the GW on the laser light is to generate sidebands in the light propagating in each of the two arms. To the laser carrier at frequency ω_L, the GW signal adds two sidebands at the frequencies $\omega_L \pm \omega_{gw}$.

2.2.1 Fabry-Perot cavities

The optimal arms' length L is given by computing which is the length that maximizes the phase shift in (2.15), i.e. when $\omega_{gw}L/c = \pi/2$ and

$$L \sim 750\,\mathrm{km}\left(\frac{100\,\mathrm{Hz}}{f_{gw}}\right) \tag{2.19}$$

Since it is not technically (and also financially) easy to have arms longer than 3 - 4 km, one way to increase the effective length of the arms is to substitute them with resonant cavities. In this way, the light is stored for a longer time inside the arms, being reflected multiple times back and forth, and therefore enhancing the dephasing due to GWs. The cavity is on resonance when its length is tuned in order to have constructive interference between the field transmitted by the input mirror and the one which has done a round trip inside the cavity. In this condition, the power stored inside the cavity can be enhanced by a large factor, which depends on the finesse $\mathcal{F}$ of the cavity that depends on the mirrors reflectivities r_1 and r_2:

$$\mathcal{F} = \frac{\pi\sqrt{r_1 r_2}}{1 - r_1 r_2} \tag{2.20}$$

---

[3] There is actually a small DC offset since at the dark fringe $dP/d\Delta L = 0$, and the interferometer would detect effect $O(h^2)$.

The finesse defines the storage time τ_s, that is the average time spent by a photon inside the cavity:

$$\tau_s \simeq \frac{L}{c}\frac{\mathcal{F}}{\pi} \tag{2.21}$$

For example, considering LIGO detectors, a Finesse of 450 with 4 km-long arms results in a light storage time of $\tau_s \approx 2$ ms and an effective arm length of $\tau_s c/2 \approx 2800$ km.
It is important to stress that the light storage time must be less than the period of the GW (both in the simple Michelson and in the Fabry-Perot version). If not, the consecutive maxima and minima from the same GW will cancel out the change in phase of the light in the arm. Defining the pole frequency f_p as:

$$f_p \equiv \frac{1}{4\pi\tau_s} \tag{2.22}$$

it can be shown [9] that the cavity is optimally sensitive to GWs at frequencies $f \ll f_p$, while for frequencies $f \gg f_p$ the sensitivity degrades linearly with f.
To enhance as much as possible the optical response to a GW signal, the light beam must be resonant inside the long arm Fabry-Perot cavities, that means $k_L L = n\pi$ with $n = 0, \pm 1, \pm 2, \ldots$. Hence, the mirrors of the resonant cavities must be hold in the right position within a precision[4] of $\approx 10^{-10}$ m. This is achieved by a length sensing and control system that "lock" the Fabry-Perot cavities of the two arms at the resonant length and the interferometer on some dark fringe.

2.2.2 Noise sources

For a GW amplitude of $h_0 \sim 10^{-21}$, the displacement of the mirrors is $\Delta L \approx h_0 L$ (see (2.18)) and for $L \sim 4$ km:

$$\Delta L \approx 10^{-18}\,\mathrm{m} \tag{2.23}$$

that is smaller[5] than the size of a nucleus of a factor 10^3.
Several noise sources can affect the detectors' sensitivity at this level. This means that there are different noise sources that can produce a fluctuation in the power detected at the output port disturbing or compromising a possible detection.
Usually, the detectors' sensitivity is described in terms of amplitude spectral density $S_n^{1/2}(f)$ (see Section 2.3) with dimension $\mathrm{Hz}^{-1/2}$.

---

[4] The laser beam has a transverse size of few cm at the mirrors. This means that the laser beam senses the position of the surface of the mirror averaged over a scale of few cm. In this way, the length of the mirror is well defined also at this small scale.

[5] It is important to stress that this is the coherent displacement of all the atoms of a macroscopic body, i.e the mirror. The corresponding phase shift that should be measured is for a Fabry-Perot interferometer with a finesse of 200, $\Delta\Phi \approx 10^{-8}$ rad [9].

Quantum noise Shot noise and radiation pressure are the lowest reachable noise levels; they come from the quantum nature of light and can affect the power detected by a photodiode. The union of these noises is called quantum noise.

Shot noise originates from the fact that the laser light comes in discrete quanta, the photons. This noise can be intuitively explained as the Poisson distribution related with the process of counting the photons at the output port.

Let N_γ be the number of photons that arrives on the photodetector in an observation time T. Then the average power measured at the photodetector during this observation time is:

$$P = \frac{N_\gamma \hbar \omega_L}{T} \tag{2.24}$$

Whenever we count a number of discrete independent events, the set of outcomes follows the Poisson distribution. For large counts N, the Poisson distribution approaches to a Gaussian, with standard deviation equal to $\sqrt{N}$. Therefore, the fluctuation in the number of photons produces a fluctuation in the observed power given by:

$$(\Delta P)_{shot} = \frac{\sqrt{N_\gamma}\hbar\omega_L}{T} = \left(\frac{\hbar\omega_L}{T}P\right)^{1/2} . \tag{2.25}$$

Considering for semplicity a Michelson interferometer, with no Fabry-Perot cavites in the arms and in the absence of GWs, the contribution due to the shot noise is:

$$S_n^{1/2}(f)_{shot} = \sqrt{\frac{\lambda_L}{4\pi L}\frac{2\hbar\omega_L}{P_{in}}} . \tag{2.26}$$

Equation (2.26) indicates that, to reduce the shot noise, the power of the laser should be increased. This is achieved with a power-recycling mirror, i.e a partially transmitting mirror between the laser and the beam splitter that creates a resonance cavity for the light exiting the beam splitter in the direction of the laser. In this way, a new Fabry-Perot cavity is created where the end mirror is the whole interferometer. In addition, fixing the working point at the dark fridge, the light leaving the beam splitter directed to the laser increases.

If a GW signal is present, the effect in the interferometer is the creation of small sidebands (as described in the previous Section); introducing a mirror at the output port - the signal-recycling mirror - and tuning its position to create a Fabry-Perot cavity, the sidebands can resonate in the interferometer.

However, it is not possible to increase the laser power without limit. Indeed, a beam of photons that impinges on a mirror and it is reflected back, exerts a pressure on the mirror itself. If this radiation pressure were constant, it could simply be compensated by the mechanism that holds the mirrors in place. However, since the number of photons arriving on the mirror fluctuates, the radiation pressure fluctuates, too, and generates a stochastic force that shakes the mirrors [9]. If, in order to beat the shot noise, the power increases beyond a certain limiting value, the fluctuations in the radiation pressure will become important and will dominate over the shot noise.

In addition, the shot noise contribution is proportional to $P_{bs}^{-1/2}$ while the radiation pressure to $P_{bs}^{1/2}$. The situation is conceptually similar to the Heisenberg microscope. Using photons to measure the position of an object, the photons impart non-deterministically a recoil to the object, here in the form of fluctuations of the radiation pressure, and this recoil disturbs the measure that we are performing. So, a quantum effect due to the uncertainty principle can be important in the measurement of the position of a macroscopic body like the mirror of an interferometer, which typically weights tens of kg.

The detector sensitivity can be improved beyond the so-called quantum noise limit via the injection of squeezed states of light into the output of the interferometer [54]. Squeezed light is a special state of light where the amplitude uncertainty or the phase uncertainty can be reduced at the price of a degradation of the other. Replacing the vacuum fluctuations at the output port by the continuous injection of squeezed vacuum states of light facilitates a manipulation of the measurement uncertainty.

Free-falling masses and seismic noise So far, I have considered the interferometric mirrors as free falling masses. The mirrors obviously cannot be truly free.

The mirrors can behave as if free in a certain frequency region suspending them to a set of pendulums in cascade.

A single pendulum with resonance frequency F_0, at frequencies $F \gg F_0$ attenuates the strain sensitivity by a factor F_0^2/F^2 , and a multistage filter made by N stages provides an attenuation factor $\sim (F_0^2/F^2)^N$. Therefore one must choose F_0 much smaller than the GW frequency of interest in order to have the mirrors acting as free masses even though they are held in place.

Since the interferometers can work only if the beams are well aligned with each other and the arms length are and remain very closed matched, it is necessary the use of a feedback control system that limits the crucial degrees of freedom in position and angle at the required operational point.

However, the Earth's ground is in continual motion, with amplitudes of order a few microns. In the region $1 \div 10$ Hz, this is mostly due to human activity such as local traffic, trains, etc. as well as to local phenomena such as winds. In addition, the microseismic background can affect a GW interferometer mostly in the form of surface waves that shake the suspension mechanisms and, finally, the mirrors.

These effects influence the strain sensitivity, which can be expressed as [9]:

$$S_n^{1/2}(f)|_{sism} \simeq A \left(\frac{1\,\mathrm{Hz}}{f} \right)^{\nu} \mathrm{m} \cdot \mathrm{Hz}^{-1/2} \tag{2.27}$$

where $\nu \approx 2$ when $f > 1$ Hz and A is of the order of 10^{-7} in a quiet location.
In practice for the actual ground-based detectors, the seismic noise can be reduced below a level interesting for GW detection only at frequencies above 10 Hz due to the resonance frequency of the pendula. This is the main reason why a ground-based interferometer cannot search for GWs below the 10 Hz region [9].
Including the pendulum wire, that has some finite mass, the equation of motion of the chain of pendulum is obviously more complicated showing a harmonic series of resonances (called "violin modes") that cause amplification at each resonance. In typical interferometer designs, the fundamental violin mode comes at a few hundred Hz.
In addition, Newtonian noise - or gravity gradient noise - is an effect which comes from the Newtonian non-stationary gravitational forces acting on a moving body. An example is given by the fluctuation of the gravitational field of the Earth, coupling to the test masses of the interferometer, due to the micro-seismic noise. The fact that gravitational forces can't be shielded ensures that this noise can't be attenuated in case of ground-based detectors.

Thermal noise Thermal noise arises from the random movements of the particles that compose a body in thermodynamical equilibrium with the sorrounding environment. In GWs detectors, thermal noise affects mainly the mirrors and their suspending wires.
The main contributions come from the pendulum thermal noise at frequencies between 3 and 30 Hz.
The intermediate region between 30 and 300 Hz is instead limited by the sum of the contributions coming from the thermal excitation of the suspension wire violin modes and of the mirror resonant mode.
The thermal noise is also reponsable for the Brownian motion of the mirrors. The atoms of a mirror at temperature T have a Brownian motion due to their kinetic energy. which gives rise to mirror thermal noise. Just as with the violin modes, its effect can be computed performing a normal mode decomposition. This is presently the dominant noise between a few tens and a few hundred Hz.
Thermal noise is mitigated by using heavier mirrors and suspending the mirrors with high quality factor wires and/or cooling the mirrors at cryogenic temperatures.

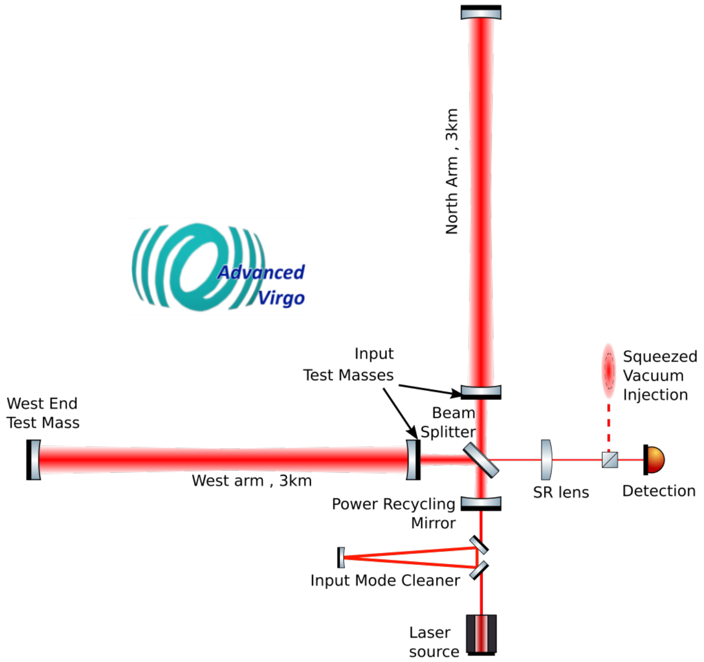

Figure 2.3: Sketch of the Advanced Virgo configuration.

Other noises So far, I have described fundamental noises that come from the intrinsic limits of the detector. There are also different noise sources that can reduce the detector sensitivity:

- *control noises,* introduced in the system or amplified by the control loops used to maintain the correct operating point;
- *enviromental noises,* like electromagnetic fields coupling to the detector output, originated by the natural setting where the detector is constructed. To limit perturbations from outer environment (gas density fluctuations, 'gas damping' effects, acoustic noise...), the optics and the laser beam are under vacuum;
- *technical noises,* coming from the actual implementation of the detector. For example, the laser frequency and power noises fluctuations can be relevant, or if there is not a perfect match between the arms, the so-called frequency noise can appear at the output port (generally, limited by a mode cleaning cavity).

To summarize the general configuration of the actual ground-based interferometer detectors, I will describe the Virgo detector configuration for the last observing run O3 [55]. There are of course some differences with the two LIGO detectors (for example, the signal-recycling mirror not present in Virgo during O3).

The Virgo interferometer is a 3 km-long power-recycled Fabry-Perot Michelson, located at Cascina, Italy (the optical scheme is in Figure 2.3). All the mirrors of the interferometer are suspended to a chain of pendulums for seismic isolation. The last suspension stage is a monolithic silica fiber fused to the mirror on one side and attached to a marionette on the upper side. The input beam is provided by a laser with a wavelength in the near infrared $\lambda = 1064$ nm that travels in ultra-high vacuum tubes. The power at the input of the interferometer during O3 was about 25 W. The beam of the low-noise laser source is filtered geometrically and has its amplitude and beam pointing fluctuations further reduced by a 140 m long triangular cavity, called Input Mode Cleaner.

The finesse of the 3 km long Fabry–Perot cavities in the arms was 450, which means that the effective length travelled by the beams is increased by a factor 290 with respect to the physical arm length. The resulting increase of light power in the arms induced input mirrors deformation and required a thermal compensation system. Since the interferometer is locked close to a dark fringe, the power recycling mirror is used to enhance the power on the beam-splitter mirror. Frequency-independent squeezing technique was installed and used during O3 to reduce the quantum noise limit above a few hundreds Hz.

The readout of the interferometer main output signal is based on homodyne (or DC) detection [56] and the used photodiode signal is proportional to the interferometer differential arm length.

2.2.3 Calibration of GW detectors

As described, the interferometer mirrors must be controlled to hold all crucial degrees of freedom at the required operating point. For this reason, the strain amplitude of the GW detector $x(t)$ must be reconstructed from the dark fringe photodiode measurement but also from the control signals that are applied to maintain the free-falling masses at their nominal position.

The control system of advanced detectors is rather complex with the goal to keep a destructive interference at the interferometer output port (for more details, see [55]). As a consequence, below a few hundred Hz it is necessary to subtract the control signals from the dark fringe signal before reconstructing $x(t)$. Above a few hundred Hz, the suspended mirrors behave as free-falling masses and the length variations induced by a passing GW generate directly variations of the output power of the interferometer. To reconstruct $x(t)$, it is necessary to calibrate the sensing and control loop elements by measuring their transfer functions using the Photon Calibrator technique [57]. This consists in the injection of deterministic excitation signals using radiation pressure in-

duced by auxiliary lasers whose power is known absolutely.
The reconstruction of $x(t)$ is also the opportunity to subtract well identified noise sources, whose contribution is measured by witness channels. Not all sources of noise can be subtracted but detectors' sensitivity can be improved in some frequency range.
Absolute timing calibration is also critical when performing multi-detector analysis for both detection (cross-correlation assumed the arrival time of the GW to be synchronized) and source sky position determination based also on the arrival time of the signal in each detector. The master timing system is controlled by GPS and provide coherent timing information to all detectors elements. The absolute timing precision is of the order of 0.01 ms or less since the typical timing accuracy of the CBC searches is of the order of 0.1 ms.
Using known signals "injected" in the interferometer, also known as calibration lines, it is possible to estimate the uncertainties in the reconstructed strain. The calibration lines consist in excitation signals (sinusoidal or flat in a frequency band) applied to the end test masses. The uncertainties are estimated comparing the reconstructed strain to the known forced motion applied to the end mirrors.
For the Virgo detector during O3, the upper limit on bias and associated uncertainty was 5% in amplitude, 35 mrad in phase and 10 μs in timing in most of the sensitive frequency band [55].

2.3 Strain sensitivity and noise budget

The output of any GW detector is a time series, which describes for instance the oscillation state of a resonant bar, or the phase shift of the light recombined after traveling in the two arms of an interferometer. This output will be a combination of (hopefully) a GW signal and of noise.
To understand how signal and noise combine, it is useful to think of a GW detector as a linear system. The input and output of the detector are scalar quantities, while the GW is described by a tensor h_{ij}. So, in general, the input of the detector will have the form

$$x(t) = h(t) + n(t) \tag{2.28}$$

where

$$h(t) = D^{ij} h_{ij} \tag{2.29}$$

and D^{ij} is a constant tensor which depends on the detector geometry.
For a linear system, the output of the detector in the frequency space is a linear function of the input by the transfer function of the system. $n(t)$ in (2.28) is a fictitious noise

that, if it were injected at the detector input and if there were no other noise inside the detector, would produce at the output the noise that is actually observed [9]. The input signal can be used to compare the performances of different detectors since the detectors' transfer functions can be very different.

The great advantage of referring everything to the input is that $n(t)$ gives a measure of the minimum detectable value of $h(t)$ that, apart from the geometrical factor D_{ij}, depends only on the incoming GW.

To characterize the noise $n(t)$ of the detector, the power spectral density (PSD) $S_n(f)$ is defined as [58]:

$$\langle \tilde{n}^*(f)\tilde{n}(f')\rangle = \delta(f-f')\frac{1}{2}S_n(f) \tag{2.30}$$

where the angle brackets denote an ensemble average over many noise realizations. The ensemble average can be measured considering different segments of duration T, computing the Fourier transform $\tilde{n}(f)$ with resolution $1/T$ for each segment, and then taking the average. Since the GW signal and detector output are both real, it follows that $\tilde{h}(f) = \tilde{h}(-f)$ and $\tilde{n}(f) = \tilde{n}(-f)$; therefore, $S_n(f) = S_n(-f)$. For this reason, $S_n(f)$ is called the one-sided PSD and Fourier integrals over all frequencies can be written as integrals over positive frequencies only.

More rigorously[6], for a time series[7] $x(t)$, the PSD is defined as the Fourier transform of the auto-correlation function $R(\tau)$:

$$\frac{1}{2}S_n(f) = \int_{-\infty}^{+\infty} e^{-i2\pi f\tau}R(\tau)d\tau \tag{2.31}$$

where[8]

$$R(\tau) = \lim_{T\to\infty}\frac{1}{2T}\int_{-T}^{+T} x(t+\tau)x(t)dt\,. \tag{2.32}$$

The physical units of the power spectrum are $[x]^2/Hz$ where $[x]$ is the physical unit of the considered time series.

The square root of the PSD is the amplitude spectral density (ASD) $S_n^{1/2}(f)$ also called spectral strain sensitivity, or spectral amplitude. If the noise increases of a common factor, the ASD scales linearly while the PSD scales with the squared factor.

The noise budget compares the measured detector sensitivity with the incoherent sum of all known noise contributions. Each noise projection depends on the noise level, as

---

[6] In general, $n(t)$ does not satisfy the conditions for a well-defined Fourier transforms; for example, it goes not to 0 for $t \to \pm\infty$.

[7] The time series is considered as an ergodic process. A stochastic process is said to be ergodic if its statistical properties can be deduced from a single, sufficiently long realization of the process.

[8] The auto-correlation function goes to 0 very fast for $\tau \to \pm\infty$. For white noise, since the noise at time t is uncorrelated to the noise at the time $t+\tau$, $R(\tau) = \delta(\tau)$ [9].

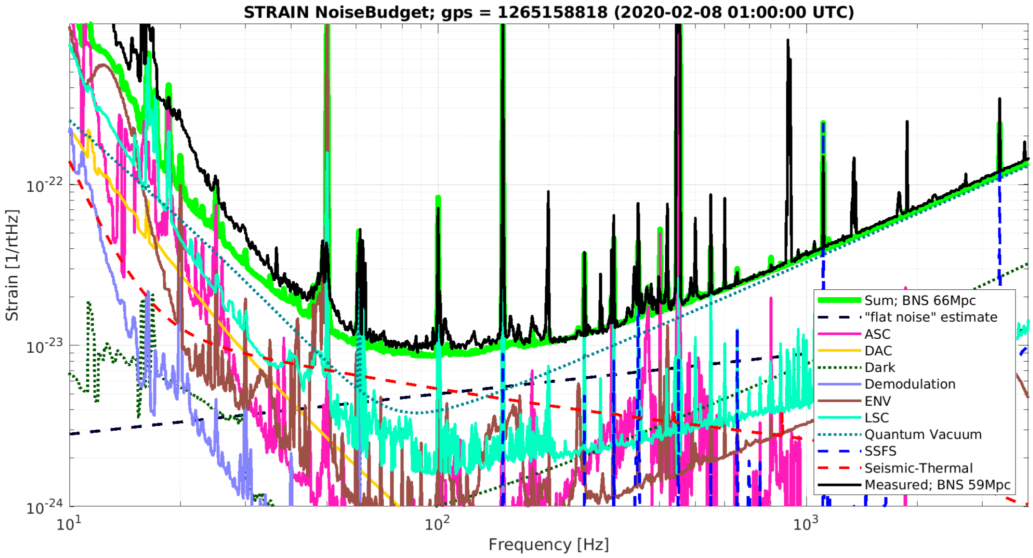

Figure 2.4: Virgo noise budget for the observing run O3 generated at a time of near best sensitivity of the detector (February 8th, 2020). The different noise sources shown are described in the text. The green line represents the sum of these noises and it can be compared to the measured total noise shown in black. *Credit to [59].*

measured by external probes, and of its coupling to the strain channel [59].

The noise budget in Figure 2.4 shows the current understanding of the limiting noise sources for the last observing run O3 of the Virgo detector (for the LIGO's detectors during O3 see [60]). The green solid trace shows the sum of all known contributing noise sources. There is excellent agreement between the modeled and measured noise (black trace) above roughly 100 Hz, while additional noise sources below 100 Hz are not yet understood. More in details, at frequencies above 1 kHz the sensitivity is mostly limited by quantum shot noise. In the most sensitive frequency range, between 80 Hz and 200 Hz, there are significant contributions from three sources: quantum shot noise, mirror coating thermal noise and a "flat noise" of unknown physical origin. At low frequencies between 20 Hz and 50 Hz, the dominant noise sources are quantum radiation pressure noise that is increased by the frequency independent light squeezing and the laser intensity noise. The 30% of the noise remains not understood in that frequency range, so other significant noise sources must be identified.

2.4 The LIGO-Virgo-Kagra Collaboration

The current network of ground-based detectors is composed of the two Advanced LIGO detectors located at Hanford and Livingston in the USA, the Advanced Virgo detector located at Cascina in Italy, the GEO-600 detector located near Hannover in Germany

and the underground KAGRA detector near Kamioka in Japan (see [61] and references therein). A copy of Advanced LIGO detector is currently under construction in India.
The arms of Advanced LIGO are 4 km long while Advanced Virgo and KAGRA have arms of 3 km. GEO-600 arms are 600 m long which makes the detector less sensitive than Advanced LIGO and Advanced Virgo and is mainly used so far to test advanced technology. KAGRA is the first detector located underground and whose Fabry-Perot mirrors are cooled down at 20 K to reduce respectively seismic noise and thermal noise.
From 2010 the LSC (LIGO Scientific Collaboration) and the Virgo Collaboration scientists combine and jointly analyze all data that come from their interferometers. The combined data improved measurements of source locations on the sky and confidence in detected signals. Beginning in 2021, the KAGRA Collaboration, that developed the 3 km-long underground interferometer, is also co-authoring observational results from the second half of the last observing run and onward. Together, these three entities comprise the LIGO-Virgo-KAGRA Collaboration (or LVK Collaboration for short).
Ground-based detectors alternate between phases of observation (observing runs) and periods of commissioning and upgrades to improve the sensitivity of the instruments. Three runs have been performed so far with Advanced Virgo and Advanced LIGO.
The first run O1 operated from September 2015 to January 2016. On the February 11, 2016 the LIGO and Virgo Collaboration announced the observation of the first GW signal, GW150914 (see next Subsection).
In the second run O2, from November 2016 to August 2017, LIGO detectors saw several further GW events. Some of them were also seen by the Virgo Collaboration as the extraordinary event GW170817 that came from the collision of two neutron stars and it was also detected electromagnetically by γ-ray satellites and optical telescopes.
The O3 run started on 1 the April 2019, and finished on 27 March 2020. This last run has produced a large number of detection, a total of 90 combined with the previous runs (see Figure 2.5). These detection allow to estimate the rate of compact binary mergers in the universe, probe the population of compact objects and unveil the distribution of blak hole/neutron star masses [62].

2.4.1 GW detections

The first GW signal detected by ground-based detectors was GW150914 on September 14, 2015 at 09:50:45 UTC. The signal was observed only by LIGO detectors since at that time the Virgo detector was being upgraded. With only two detectors the source position was primarily determined by the relative arrival time and localized to an area of approximately 600 deg^2 (90 % credible region).

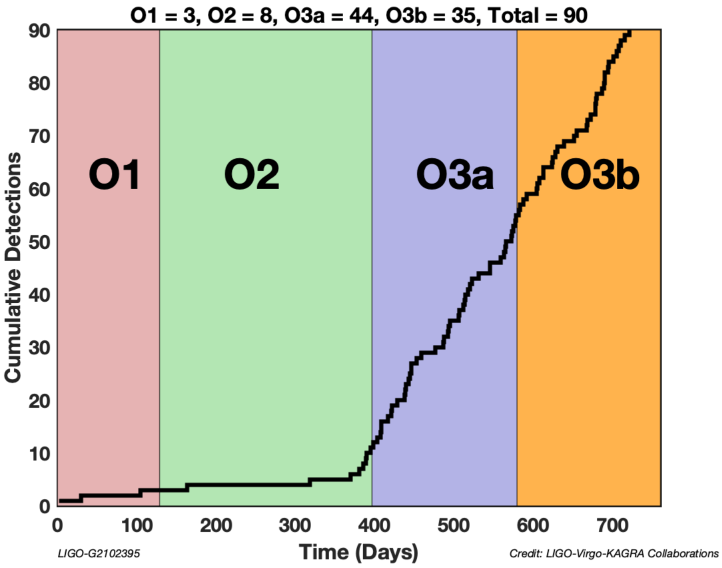

Figure 2.5: Cumulative events detected during the three observing runs with the LIGO and Virgo detectors. The increase in the detected events reflects the improvement of the detectors' sensitivity.

The basic features of GW150914 describe [14] the coalescence of two black holes at a luminosity distance of 410 Mpc. In the source frame, the estimated black hole masses are 36 $\mathrm{M}_{\odot}$ and 29 $\mathrm{M}_{\odot}$, and the final black hole mass is 62 $\mathrm{M}_{\odot}$.

The detected waveform matches the predictions, accurately modeled by post-Newtonian approximation, for the inspiral and the merger of black holes and the ringdown of the resulting single black hole. In 0.2 s the signal swept in frequency from 35 to 250 Hz, reaching a peak GW strain of 1×10^{-21} with a signal-to-noise ratio of 24.

This was the first direct detection of GWs and the first observation of a binary black hole merger. The era of GW astronomy began with this detection.

GW170817 was the first GW signal from a binary neutron star coalescence which was accompanied by the observations across the electromagnetic spectrum [31]. Approximately 1.7 s after the GW detection by the LIGO and Virgo detectors on the August 17, 2017, the Fermi Gamma-ray Burst Monitor detected and triggered on the short γ-ray burst 170817A [63], marking the first confident joint EM–GW observation in history. These detection triggered an observing campaign across the whole electromagnetic spectrum, and a counterpart was detected 11 hours after the initial GW alert in NGC 4993 [64]. Less than two years after the debut of GW astronomy, GW170817 marks the beginning of a new era of discovery, confirming the long-held hypothesis that binary neutron stars mergers are linked to short γ-ray bursts and to kilonova emission. The source has been followed in ultraviolet, optical, infrared and radio waves. A search for high-energy neutrinos was also conducted with no detection.

The multi-messanger detection allow also to set important constrains [32] on the speed of GWs, on modified gravity theories and finally to infer the first measurement of the Hubble constant with GWs.

The multi-messenger astronomy represents the only way to obtain a complete knowledge of the astrophysical sources and their emission engines, providing complementary insight into the physics of the progenitors and their environment[9] [65].

Starting with the O3 observing run, the LVK Collaboration sends prompt Public Alerts for any GW transient event detection with a latency within minutes. These alerts enable the physics and astronomy community to pursue multi-messenger observations of GW sources and maximize the science reach of the GW instruments.

Some of the exceptional events observed during the last observing run O3 are [66]:

- GW190412, the merger of two black holes with asymmetric masses;
- GW190425, the second observed binary neutron star merger (without the detection of the electromagnetic counterpart);
- GW190521, the first detection of an intermediate mass black hole;
- GW190814, a system with a secondary that could be either a black hole or a neutron star;
- GW200105 and GW200115, the first detected neutron star-black hole binary mergers.

2.4.2 Future perspectives

The GW detections by the ground-based interferometric detectors have open a new window on the Universe. The next observing runs of Advanced LIGO and Advanced Virgo are already planned; O4 should start in March 2023 for a duration of 1 year and a sensitivity further improved compared to O3. The designed sensitivity of Advanced LIGO and Advanced Virgo should be reached during O5 by 2025 leading to a detection rate of more than one GW event per day.

The increasing sample of the detected compact binary mergers will provide more information on the populations of black holes and neutron stars with especially better measurement of the black hole spins. More detections of binary neutron star mergers

---

[9] Indeed, GWs and neutrinos carry information from the inner regions of the astrophysical engines, from which photons and charged cosmic rays cannot reach us. Photons can give a precise (arcsecond) localization, to identify the host galaxy and the source environment.

with electromagnetic counterparts will provide new insight on the EOS, on the physics of neutron stars and also a more accurate measurement of the Hubble constant.
Improving the detectors sensitivities, new sources of GW - not related to compact binary mergers - could be detected such as rotating neutron stars, magnetars, core-collapse supernovae or the stochastic GW background.
In the more distant future, third-generation detectors like the proposed Einstein Telescope (ET) [67] or Cosmic Explorer (CE) [68] may reach sensitivities an order of magnitude higher than what is achieved by Advanced LIGO and Advanced Virgo. ET is currently envisioned as an underground infrastructure in Europe housing three interferometers in a triangular configuration, each with 10 km arm lengths. CE retains the 'L'-shape interferometer configuration used in the current interferometers but increases the arm lengths to up to 40 km.

2.5 CW searches

The GW signals detected so far come from the coalescence of compact objects, as black holes or neutron stars. In Section 1.5, I have described the different types of signals and sources that, in principle, could be detected by ground-based detectors.
CW signals emitted by a spinning neutron stars are the main targets of the pipeline developed in this work. As reported in Subsection 1.5.1, CW signals can be fully characterized by the set of parameters:

$$\theta = (\alpha, \delta, \mathbf{f}, h_0, \psi.\iota, \phi) \tag{2.33}$$

where α and δ are the ascension and the declination that fixes the sky position, $\mathbf{f} = (f, \dot{f}, \ddot{f}..)$ are the rotation frequency spin-down parameters, h_0 is the amplitude of the CW signal, ϕ the phase while ψ and ι are the angles related to the wave polarization.
In the case of pulsars, for example, the parameters linked to the source - the extrinsic parameters $(\alpha, \delta, \mathbf{f})$ - are known through radio observation. Sometimes, like in the case of the Vela pulsar, the values of the angles ψ and ι are also known from X-ray observations (see [69]).
As shown in Subsection 1.5.1 for a rigid body rotating around a principal axis of inertia, the CW signal is monochromatic at the source with the GW frequency that is twice (or for different emission mechanisms, proportional to) the rotation frequency of the source.
In Subsection 1.7.2, it is also shown that due to the emission of electromagnetic (and hopefully also gravitational) waves, neutron stars lose energy and hence, the rotation frequency decreases in time.

Intrinsic parameters		Extrinsic parameters	
h_0	Amplitude	α	Right ascension
ψ	Polarization parameter	δ	Declination
η	Polarization parameter	f	Rotation frequency
ϕ	Phase	$\dot{f}, \ddot{f}, ..$	Spin-down parameters

Table 2.1: Table of the intrinsic and extrinsic parameters that define a CW signal.

Given the long-lived and weak nature of CWs, the signal must be integrated over a long time duration to be detected with statistical significance. For example, let us consider a CW signal that needs 1 yr of coherent integration time to be clearly detected in the Fourier spectrum of the data. Since the frequency resolution is $1/yr \approx 10^{-7}$ Hz, to remain in the same frequency bin during that year, the first derivative $\dot{f}$ of the GW frequency would need to satisfy $\dot{f} \cdot 1yr < 1/1yr$, or $\dot{f} < 10^{-15}$ Hz/s and its second derivative $\ddot{f} < 6 \times 10^{-23}$ Hz/s^2 (assuming a Taylor expansion of the rotation spin-down). In general, the measured parameters for known sources are much larger of these values. In order to maintain the benefit of long observation times, it is therefore necessary to remove the effects of the source spin-down from the data. It also necessary to take into account the Earth's orbital motion around the Sun that spreads the CW signal in several frequency bins due to the Doppler effect.

It is clear that according to our knowledge of the source, the search for a CW signal must be different and should also take into account the computational cost of the analysis. Indeed, if the evolution of the rotation parameters is known via electromagnetic observations, it is possible to correct for the time evolution of the expected GW frequency. In addition, if the sky position is accurately known, it is possible to correct for the Doppler modulation via barycenteric correction. If the shape of the signal is known, matched filtering, or coherent methods, can be used.

In general, the more we know about the sources parameters, the more computationally feasible it is to integrate data coherently for longer time periods in order to improve the sensitivity (see Figure 2.6).

As the knowledge about the source parameters decreases, the parameter space to investigate increases, making the use of fully coherent searches impractical [71]. In this case, semi-coherent techniques can be used (see [72] for a detailed review of CWs searches for unknown sources). In semi-coherent methods, the available data are divided in chunks that are first analyzed coherently (e.g., using a matched filter on a

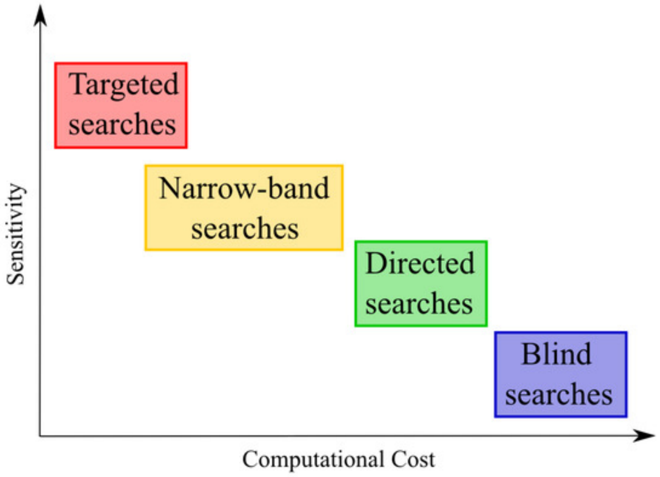

Figure 2.6: Schematic plot of the different types of CW search in terms of sensitivity and computational cost. *Credit to [70].*

template bank) and then combined incoherently, for instance, by summing the detection statistics computed in each chunk to construct a single final detection statistic.

In the next paragraphs, I review the different searches that can be performed according to the assumption on the source.

Targeted search Targeted searches assume to know with high accuracy the extrinsic parameters observing the electromagnetic emission from the source. The targets are known pulsars for which the observations in radio, optical, X-ray and gamma-ray bands provide ephemerides for the sky position, and also accurate measurements of the rotation frequency and the spin-down parameters (e.g. for the Crab and Vela pulsars).

The minimum detectable amplitude for targeted searches, defined as the average amplitude that entails a detection probability of 90% for a false alarm rate of 1%, is [73]:

$$h_{min} \approx 11\sqrt{\frac{S_n(f)}{T_{obs}}} \tag{2.34}$$

where $S_n(f)$ is the one-sided power spectral density of the noise detector and T_{obs} the observation time. The expression for h_{min} is obtained considering the average over different positions, inclinations, and polarization of the source. The numerical factor depends on the specific matched filter implementation.

In Section 2.6, I analyze the required accuracy for the electromagnetic observations and the matched filter technique.

Narrow-band search In targeted searches, the GW frequency is assumed proportional to the rotation frequency. When this assumption is relaxed, “narrow-band” searches investigate small region around the expected GW frequency for the models analyzed in the targeted searches. In this way, narrow-band searches take into account more sophisticated models, e.g., a differential rotation between the rigid crust and superfluid parts of the star. In general, a narrow-band search for a given target is less sensitive than its respective targeted case due to the increased trial factor. For example in [49], it is estimated that the minimum detectable amplitude is $\sim 2 \div 3$ times worse than the sensitivity of a targeted search.

Directed search In directed searches, the star’s position is known, but the rotation parameters are unknown, e.g. a non-pulsating X-ray source at the center of a supernova remnant. With respect to targeted and narrow-band searches, these pipelines are usually less sensitive, but allow to explore a larger number of waveform templates. Directed searches are usually carried out by semi-coherent method and the minimum detectable signal is:

$$h_{min} \approx 30 \div 40 \frac{\sqrt{S_n(f)}}{(T_{obs} T_{coh})^{1/4}} \tag{2.35}$$

where T_{coh} is the time length of each chunk for the semi-coherent method (see for example [74]).

All-sky search All-sky searches are performed if there is no assumptions on the source parameters. These searches are mainly based on hierarchical semi-coherent procedures in which the data is divided in short chunks and combined incoherently.
Considering N segments each with observation time T_{coh}, the minimum detectable signal can be estimated [75] as:

$$h_{min} \approx \frac{A}{N^{1/4}} \sqrt{\frac{S_n(f)}{T_{coh}}} \tag{2.36}$$

where the exact numerical factor A depends on the specific hierarchical method employed and on the chosen parameter space.
It is of great interest to perform all-sky searches since, even though these searches are the least sensitive, the closest observed neutron star (i.e. pulsar) is almost at 100 pc while the population synthesis calculations indicate that in a sphere of radius 100 pc, there should be $10^{3 \div 4}$ neutron stars [16] that could emit "stronger" CW signals since closer (indeed, $h_0 \propto 1/r$).

These searches can produce the so-called "search candidates", potential astrophysical signals that need to be investigated in detail [76]. These candidates undergo a series of post-processing veto steps, e.g. searching for known instrumental lines near the outlier frequency, and then, the most interesting ones are followed up with different techniques in order to clearly establish their significance (see [72]).

If no CW signal detection can be claimed, CW searches can provide upper limits on the signal strain. For a given confidence level, the upper limit curve determines the value of the signal amplitude h_0 above which it is possible to exclude the existence of CW signals for a particular source or frequency. Upper limits are useful to set astrophysical constraints on some strain-related quantities, as in the case of the ellipticity for the targeted searches.

2.6 Targeted search

As described in the previous Section, targeted searches assume to know with high accuracy the source parameters, as the sky position and the rotation parameters. Due to the source spin-down, coherent methods must take into account the time evolution of the rotation frequency of the source. Indeed, assuming the GW phase $\Phi(t)$ locked to the rotation phase, to match the expected signal one needs to track the time evolution of the rotation frequency.

The observed GW frequency changes in time also because of the Doppler effect due to the Earth's rotation motion around its axis and the Earth's orbital motion around the Sun. It can be shown [16] that the frequency shift for the Doppler effect due to the rotation motion is of the second order compared to the orbital one since the orbital velocity $v_{orb}/c \simeq 10^{-4}$ while the rotation velocity $v_{rot}/c \simeq 10^{-6}$.

To first order in v/c, the frequency measured by an observer with a velocity $\vec{v}$ respect to the source is

$$f = f_0 \left(1 + \frac{\vec{\mathbf{v}} \cdot \hat{\mathbf{r}}}{c}\right) \tag{2.37}$$

where $\hat{\mathbf{r}}$ is the unit vector in the direction of the source. Since the term $\vec{\mathbf{v}} \cdot \hat{\mathbf{r}}$ changes in time[10], the shift in frequency in a time T is:

$$\Delta f_{Doppler} = f_0 \frac{(\Delta v)_T}{c} \tag{2.38}$$

---

[10] If the term $\vec{\mathbf{v}} \cdot \hat{\mathbf{r}}$ was constant, there would be only a constant shift in the frequency that would be easily identified in the frequency spectrum.

where $(\Delta v)_T$ is the change of the component of the velocity in the direction of the source during the observing period T.

To correct the Doppler effect, both the detector position and the source sky position must be measured with high accuracy. The detector position, measured with respect to the Solar System Barycenter (SSB), is well known also considering small effects as the oscillations of the Earth around the Earth-Moon barycenter. It follows that the main error comes from the uncertainty on the angular position of the source [16].

For an observation time T, the Earth rotates of an angle $\Delta\theta$ and to correct for the Doppler shift with an accuracy smaller than the experimental resolution, in order of magnitude it is necessary that:

$$\frac{f_0}{c}(\Delta v)_T \Delta\theta < \frac{1}{T} \tag{2.39}$$

Taking[11] $(\Delta v)_T \approx v_{orb}\omega_{orb}T$, to apply the Doppler correction the accuracy of the source location must be with a rough estimate:

$$\Delta\theta < 0.1\,\text{arcsec}\left(\frac{10^7\,\text{s}}{T}\right)^2\left(\frac{1\,\text{kHz}}{f_0}\right) \tag{2.40}$$

This is the requirement to properly correct the Doppler effect and the relative shift in frequency in a CW search. For many pulsars (hence, for the targeted search), this requirement is satisfied since the position is known to this accuracy or better and coherent analysis over large time period can be performed.

In the next Subsection, I describe the matched filtering, a very general data analysis technique that allows to dig out a signal whose shape is known in a larger noise. Matched filtering is widely used in GW data analysis, for example for the detection of CBC signals [77] and also for the targeted search of CW signal in the $\mathcal{F}$-statistic and in the 5-vector method.

In Subsections 2.6.2 and 2.6.3, I briefly review the $\mathcal{F}$-statistic and the Bayesian method: the two independent pipelines that - with the 5-vector method - are used by the LVK Collaboration for the targeted search of CW signals.

2.6.1 Matched filtering

Matched filter methods can be used to recover the signal $h(t)$ whose expected shape is known but buried into the noise $n(t)$, i.e. $|h(t)| \ll |n(t)|$. The detector output $s(t)$ is

---

[11] During a time T, the Earth orbits the Sun of an angle $\Delta\theta \approx \omega_{orb} \cdot T$. If $\Delta\theta \ll 1$, in order of magnitude the change in time of the velocity component along the source direction is $(\Delta v)_T / v_{orb} \sim \Delta\theta$. The approximation $\Delta\theta \ll 1$ is valid if $T \lesssim 4$ months.

modelled as:

$$s(t) = h(t) + n(t) \tag{2.41}$$

Matched filtering is based on the application of a filter $K(t)$ that matches the expected signal $h(t)$ whose shape must be known. The filter $K(t)$ defines the quantity $\hat{s}$:

$$\hat{s} = \int_{-\infty}^{+\infty} s(t)K(t)dt \tag{2.42}$$

Then, $K(t)$ is chosen to maximize the signal-to-noise ratio S/N where S is the mean value of $\hat{s}$ when the signal is present and N is the root mean square value of $\hat{s}$ when the signal is absent [16].
By defining the Fourier transform of a time series $x(t)$ as $\tilde{x}(f)$ and the complex conjugate as $\tilde{x}^*(f)$, it follows that:

$$S = \int_{-\infty}^{\infty} \langle s(t)\rangle K(t)dt = \int_{-\infty}^{\infty} \tilde{h}(f)\tilde{K}^*(f)df \tag{2.43}$$

$$N^2 = \left[\langle \hat{s}^2(t)\rangle - \langle \hat{s}(t)\rangle^2\right]_{h=0} = \int_{-\infty}^{\infty} \frac{1}{2} S_n(f)|\tilde{K}(f)|^2 df \tag{2.44}$$

because of the definition of the one-sided noise spectral density $S_n(f)$ in (2.30) and $\langle \hat{s}(t)\rangle^2_{h=0} = 0$. The signal-to-noise ratio is:

$$\frac{S}{N} = \frac{[\langle \hat{s}\rangle]_{h\neq 0}}{[\langle \hat{s}^2\rangle - \langle \hat{s}\rangle^2]^{1/2}_{h=0}} = \frac{\int_{-\infty}^{\infty} \tilde{h}(f)\tilde{K}^*(f)df}{\left(\int_{-\infty}^{\infty} \frac{1}{2} S_n(f)|\tilde{K}(f)|^2 df\right)^{1/2}} \tag{2.45}$$

Defining the scalar product for two time series $A(t)$ and $B(t)$ as:

$$(A|B) = \mathbf{\mathit{Re}} \int_{-\infty}^{\infty} \frac{\tilde{A}^*(f)\tilde{B}(f)}{(1/2)S_n(f)} df \tag{2.46}$$

the S/N can be written in terms of a time series $u(t)$ whose Fourier transform is $\tilde{u}(f) = \frac{1}{2} S_n(f)|\tilde{K}(f)|^2$ as

$$\frac{S}{N} = \frac{(u|h)}{(u|u)^{1/2}} \tag{2.47}$$

It is clear that to maximize the S/N the two "vectors" must be parallel, which means $\tilde{u}(f)$ proportional to $\tilde{h}(f)$:

$$\tilde{K}(f) \propto \frac{\tilde{h}(f)}{S_n(f)} \tag{2.48}$$

This is the matched filtering theory that allows to dig out a signal whose shape is known from a much larger noise. As described in Section 3.5, the 5-vector method, the data analysis pipeline that is the starting point of the ensemble procedure described in this work, is a matched filter in the frequency domain.

2.6.2 The $\mathcal{F}$-statistic

The $\mathcal{F}$-statistic is a frequentist data analysis pipeline for the CW search, described in [78, 79]. It is based on the maximum likelihood detection which consists of maximizing the likelihood function with respect to the parameters of the signal. The starting point is the natural logarithm of the likelihood function:

$$\ln \Lambda = (x|h) - \frac{1}{2}(h|h) \tag{2.49}$$

where the inner product $(\cdot|\cdot)$ is defined in (2.46), i.e. by a filter matched to the detection noise spectrum. The $\mathcal{F}$-statistic is obtained by maximizing the likelihood function with respect to the four intrinsic parameters (h_0, ψ, ι, ϕ) leaving the dependence on the extrinsic parameters. Since in a targeted search the extrinsic parameters are supposed to be known, a targeted search based on the $\mathcal{F}$-statistic would reduce to the computation of one value for the statistic, that is later compared to the expected noise-only distribution for Gaussian noise in order to assign the significance.
The analysis is based on the rewrite of the expected signal as the linear combination of four terms;

$$h(t) = \sum_{a=1}^{4} \lambda^a h_a(t) \tag{2.50}$$

Each term corresponds to a particular combination of the intrinsic phase evolution and of the sidereal modulation where the four basis waveforms are:

$$h_1(t) = F_+(t)\cos\Phi(t) \qquad h_2(t) = F_\times(t)\cos\Phi(t) \tag{2.51}$$

$$h_3(t) = F_+(t)\sin\Phi(t) \qquad h_4(t) = F_\times(t)\sin\Phi(t) \tag{2.52}$$

where $F_{+/\times}$ are the antenna patterns, that define the response of the detector to the GW signal[12]. Then the $\mathcal{F}$-statistic, defined to be twice the log of the maximized likelihood

---

[12] The functions $F_{+/\times}$ are inferred from the scalar product of the detector tensor D^{ij}, defined for an interferemoter with arms along the x- and y-axis

$$D_{ij} = \frac{1}{2}\left(\hat{x}_i\hat{x}_j - \hat{y}_i\hat{y}_j\right) \tag{2.53}$$

ratio, is just

$$2\mathcal{F} = (x|x) - (x - \sum_{a=1}^{4} \lambda^b h_b(t)|x - \sum_{c=1}^{4} \lambda^c h_a(t)) = \sum_{a,d} (\Gamma^{-1})^{a,d} (x|h_a)(x|h_d) \quad (2.55)$$

where the matrix Γ is defined as $(a, d = 1, 2, 3, 4)$:

$$\Gamma^{a,d} \equiv \left(\frac{\partial h}{\partial \lambda_a} | \frac{\partial h}{\partial \lambda_d} \right) = (h_a|h_d) \quad (2.56)$$

and the best-fit values for the λ_a are:

$$\lambda_a = \sum_b (\Gamma^{-1})^{a,b} (x|h_b) \quad (2.57)$$

If the data are composed purely of Gaussian noise, it is easy to show [78] that the $\mathcal{F}$-statistic satisfies a non-central χ^2 distribution with 4 degrees of freedom and has a non-centrality parameter equal to the squared optimal SNR $\rho^2 \equiv (h|h)$, defined by

$$\rho = \frac{256\pi^4 \epsilon^2 I^2 f^4 \mathcal{K}}{d^2} \frac{T_{obs}}{S_h(f_{gw})} \quad (2.58)$$

for an observation time T_{obs} and a single-sided noise special density $S_h(f)$. The term $\mathcal{K}$ depends on the sky location, orientation of the source and the number of considered detectors.

The $\mathcal{F}$-statistic is optimal in the Neyman-Pearson sense whereby the detection probability is maximized at a fixed false-alarm probability [80].

2.6.3 The Bayesian pipeline

Bayesian statistics provide a complete and straightforward framework to perform a targeted search and to infer the parameters that best describe the signal if present [70].

The Bayesian method is applied after a complex heterodyne method, described in [81], to reduce the amount of data to analyze and to unwind the apparent phase evolution of the source (due to spin-down and Doppler effect). Then, the posterior on the amplitude

---

and the polarization tensors $\hat{\mathbf{e}}_{+/\times}$ in (3.1):

$$F_{+/\times}(\hat{n}) = D_{ij} \cdot \hat{e}^{ij}_{+/\times}(\hat{n}) \quad (2.54)$$

where $\hat{n}$ refers to the sky position.

is

$$p(h_0|\mathbf{x}, I) \propto \int^{\theta} p(\mathbf{x}|h_0, \theta, I)p(h_0|I)p(\theta|I)d\theta \tag{2.59}$$

where $\mathbf{x}$ are the heterodyned data, $\theta = \{\cos\iota, \phi, \psi\}$ while $p(\mathbf{x}|h_0, \theta, I)$ is the likelihood given the signal model and $p(h_0|I)$ the prior on the amplitude. The prior is usually chosen flat between zero and some cut-off or with a Fermi-Dirac-like distribution.

From the posterior, it is possible to infer an estimation for the unknown parameter or in case of no detection, a 95% credible upper limit using the cumulative posterior. The marginalization on the parameters θ is usually performed numerically, e.g. using Markov Chain Monte Carlo [82] in which the parameter space is explored more efficiently and without spending much time in the areas with very low probability densities, or using nested sampling [83].

The marginal likelihood, or Bayesian evidence, $Z_{\mathcal{M}}$ for a particular model $\mathcal{M}$ is

$$Z_{\mathcal{M}} \equiv p(\mathbf{x}|I) = \int^{h_0} \int^{\theta} p(\mathbf{x}|h_0, \theta, I)p(h_0|I)p(\theta|I)d\theta dh_0 \tag{2.60}$$

that can be compared to the evidence that the data consists of only Gaussian noise (null hypothesis) to form the odds $\mathcal{O}$ for the two models [83]

$$\mathcal{O} = \frac{Z_{\mathcal{M}}}{Z_{noise}} \tag{2.61}$$

and to perform model selection.

2.7 Latest results for the targeted search

The latest targeted search for CWs from known pulsars is reported in [84] analyzing a set of 236 pulsars using LIGO and Virgo O3 data combined with O2 data.

The analysis take into account the glitches for some pulsars during the considered runs and also if there are information from electromagnetic observations to restrict the priors on the ι and ψ parameters. The ephemerides come from the observations from the CHIME, Hobart, Jodrell Bank, MeerKAT, Nancay, NICER and UTMOST observatories.

The three independent pipelines used in the search are: the time-domain Bayesian method, the $\mathcal{F}$-statistic method (described in the previous Subsections) and the 5-vector method (see next Chapter). All the pipelines searched for the standard single harmonic GW emission with a frequency at twice the pulsar rotation frequency but only the Bayesian method has been broadly applied to a large number of targets.

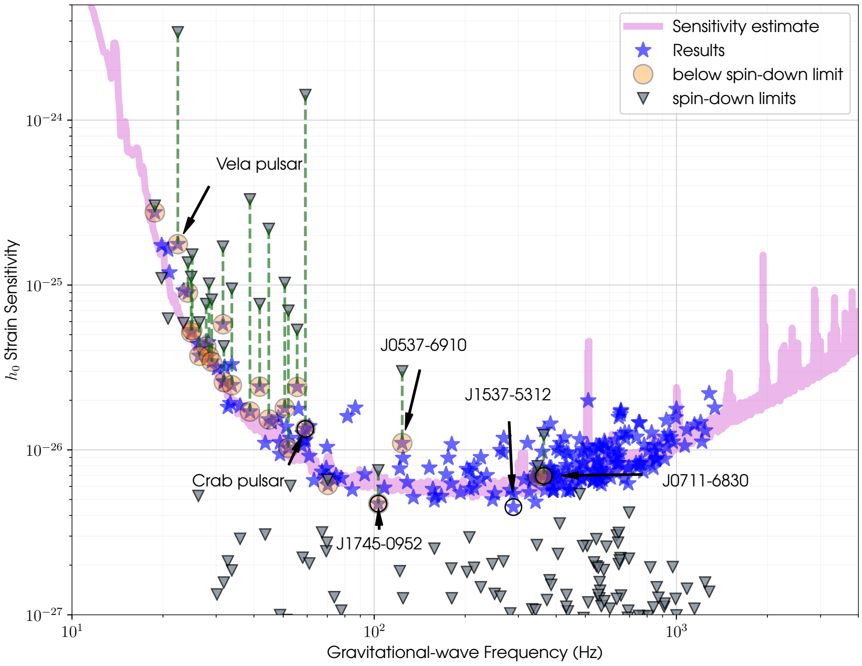

Figure 2.7: Results for the targeted search of the O3 data of the LIGO and Virgo detectors using the Bayesian pipeline and considering a set 236 known pulsars. The blue stars are the 95% credible upper limits on the GW amplitude while the grey triangles are the spin-down limits and the pink line is the minimum detectable amplitude. Upper limits that are below the spin-down limits are circled. *Credit to [84].*

In addition, the Bayesian and the $\mathcal{F}$-statistic pipelines assumed a dual harmonic emission scenario with a GW frequency at once and twice the rotation frequency. To complete the search, the 5-vector method limited the search to the single harmonic scenario but assuming a GW frequency at the star rotation frequency. Furthermore, the $\mathcal{F}$-statistic has been used to test the dipole radiation as predicted by the Brans-Dicke theory [85].

No GW detection has been reported, and upper limits on the amplitudes are given in Figure 2.7 while the upper limits on the ellipticity are shown in Figure 2.8. Figure 2.9 shows the results for the spin-down ratio, i.e., the ratio between the amplitude upper limit and the amplitude corresponding to the theoretical spin-down limit.

The pulsar with the smallest upper limit on h_0 was J1745-0952 with 4.72×10^{-27} while the best limit on the ellipticity is 5.26×10^{-9} for J0711-6830.

Among the 236 pulsars, 90 millisecond pulsars have a spin-down ratio less than 10 while 23 pulsars have strain amplitudes lower than the limits calculated from their electromagnetically measured spin-down rates. 9 of these 23 pulsars beat their spin-down limits for the first time.

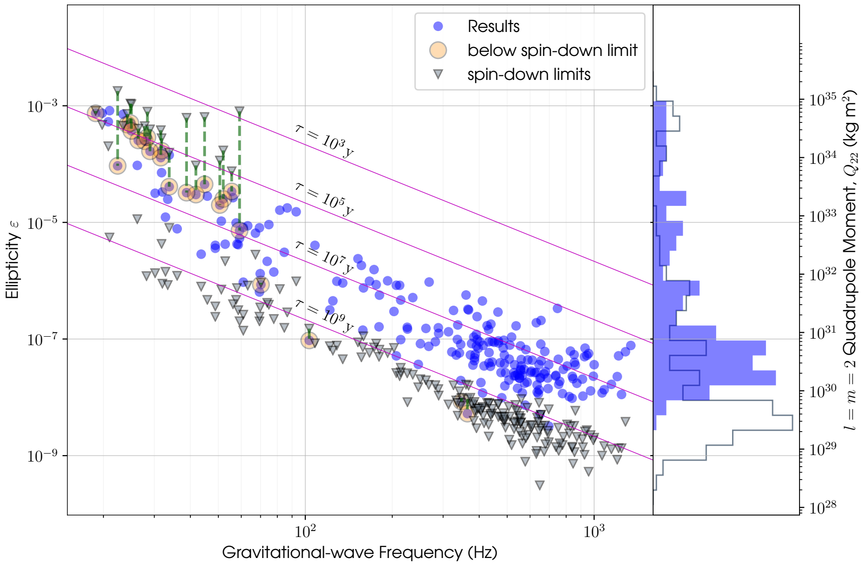

Figure 2.8: Results for the targeted search of the O3 data of the LIGO and Virgo detectors using the Bayesian pipeline and considering a set 236 known pulsars. The blue circles are the 95% credible upper limits on the ellipticity while the grey triangles are the spin-down limits. Upper limits that are below the spin-down limits are circled while the pink lines are contour lines of equal characteristic age τ. To the right of the plot, histograms of both these direct limits and spin-down limits are shown by filled and empty bars respectively. *Credit to [84].*

For the Crab and Vela pulsars, these limits are factors of ~ 100 and ~ 20 lower than their spin-down limits, respectively. A previous search using O1 plus O2 data on 222 pulsars is given in [86]. In that search, the percentage of GW emission contributing to the spin-down luminosity for Crab and Vela pulsars was less than 0.017% and 0.18%, respectively. Compared to the O2+O3 search described above, these numbers decrease as expected to 0.009% for Crab but increased for Vela up to a maximum of 0.27%. This unexpected result is due to the presence of a significant noise line in the LIGO Hanford detector very close to the expected GW frequency for the Vela during O3.

A separate dual harmonic search has been performed on the same dataset (O2+O3) for the energetic young pulsar and frequent glitcher J0537-6910 in [87]. No CW signal has been detected in this search but, for the first time, the spin-down limit for this type of GW emission on this source has been surpassed.

The latest results from the O3 fully coherent narrow-band search can be found in [88].The search looks for CW from 18 pulsars using the 5-vector and $\mathcal{F}$-statistic narrow-band pipelines. For 7 of these pulsars, the upper limits are lower than their spin-down limits. These results overcome the corresponding ones from the previous narrow-band searches, improving the upper limits even if the parameter space investigated in this search is larger.

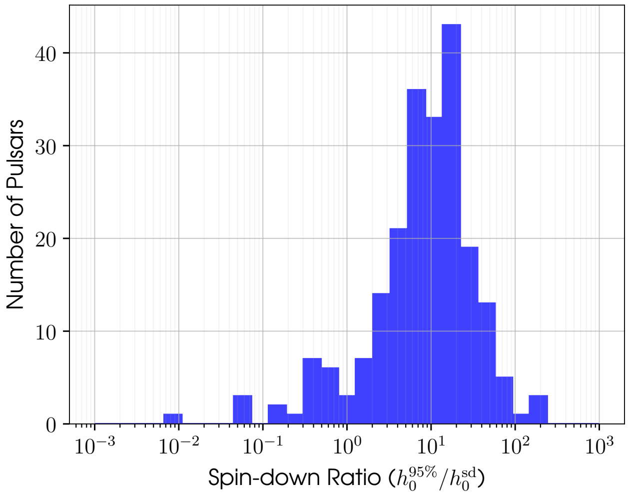

Figure 2.9: Histogram of the spin-down ratios for the upper limits in Figure 2.7. *Credit to [84].*

2.8 Challenges in CW signal detection

As shown for the targeted search in the previous Section but also for the other type of searches, there is no evidence of a CW signal in the LIGO and Virgo data.

Over the next years, current detectors and also the new detector generation (e.g. Einstein Telescope) will improve the detection likelihood increasing the explored range in the Galaxy. At the same time, theoretical uncertainties in what sensitivity is needed for the first CW detection are very large; whether the first detection is imminent or still many years distant remains unclear.

A recent phenomenological population synthesis study [89], based on an exponentially decaying ellipticity with a maximum value $\sim 10^{-5}$ with a supernova rate of once per century concluded that the expected number of detectable, young and isolated neutron stars for Advanced LIGO sensitivity is less than 1 and is almost 25 for Einstein Telescope during 1 year-long observing run.

In the following, I describe the critical issues that could in principle get more difficult the detection of CW signal by a targeted search.

- It is not unlikely that the assumed models are not well representative of the realistic emission scenario for CW. This means that it is also important to improve the pipelines robustness with respect to the model [76]. For example, the emission mechanism described in Subsection 1.5.1, assumes the neutron star as a rigid body rotating around a principal axis of inertia not considering a realistic model for the neutron star structure. For this reason, narrow-band searches consider a possible mismatch between the emitted and the theoretical GW frequency.

- A not correct frequency evolution can be due to a difference between the measured spin-down parameter and the intrinsic parameter due to dynamical effects that entail an excess in the measured spin-down value [90].
- The proper motion of the source can be relevant if not uniform[13]. For example, gravitational fields in globular cluster - where many pulsars are found - can accelerate the source producing a frequency modulation compared to the one induced by the spin-down evolution [16].
- A motion of the source can in principle produce a shift of the sky position during the observation time of the order of the accuracy required for the targeted search (in principle, this can be corrected if the source transverse velocity is known).

---

[13] A uniform motion would produce a constant shift in frequency

Chapter 3

Targeted search using the 5-vector pipeline

As described in the previous Chapters, the targeted search is the most sensitive search for CW signals since the source position and rotation frequency are known and fully coherent methods can be used.

In this Chapter, I describe the 5-vector pipeline used by the LVK Collaboration for different CW searches. The pipeline has been developed in the last years by the Rome Virgo group and is composed by an optimized data framework for the CW search, the Band Sample Data framework, and by the 5-vector method, the data analysis procedure for the single pulsar targeted search. I also describe the contribution to this pipeline due to my research: the Doppler correction implementation for sources in binary system and the characterization of a different multi-detector extension that takes into account the different detectors' noise level.

3.1 The Band-Sample Data framework

At fixed computing cost (especially for "expensive" analysis), a good and quick data management is equivalent to an increase in sensitivity since it is possible to explore with a better sensitivity a broader parameter space. Therefore, the choice of an optimized data management for the selected search is an important point for any analysis.

The Band Sampled Data (BSD) collection is a new data framework - developed by the Rome Virgo group [91] - that consists of band-limited, down-sampled time series, called BSD files. This framework can be described as a database of sub-databases where the BSD file is a complex time series that covers 10 Hz/1 month of the original data (see Figure 3.1). Using the BSD libraries, it is possible to extract frequency sub-bands (less than 10 Hz) or time sub-periods (less than 1 month). As well, it is possible to select

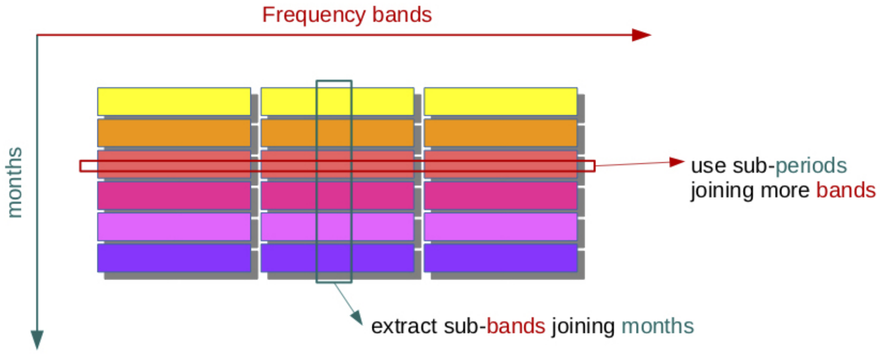

Figure 3.1: Time versus frequency representation of BSD data, where each block represents a 10 Hz and one month of data (one BSD file). Using BSD libraries it is possible to extract frequency sub-bands (less than 10 Hz) or time sub-periods (less than 1 month). As well, it is possible to select larger frequency bands (more than 10 Hz), grouping the 10 Hz pieces, and/or larger-periods, grouping the one month data. *Credit to [91].*

larger frequency bands (more than 10 Hz), grouping the 10 Hz pieces, and/or larger-periods, grouping the one month data.

The starting point for the construction of the BSD collection is a database of overlapped by half in time Fast Fourier Transforms (FFTs), called Short FFTs DataBase (SFDB) [92]. The SFDB is composed of FFTs computed using chunks of calibrated data sampled at 4096 Hz whose duration is linked to the frequency resolution (chosen bigger than the frequency spread due the time Doppler effect).

The step-by-step procedure for the BSD files production is shown in Figure 3.2 and can be summarized in these steps:

- Start with a list of SFDB covering 1 month of data
- For each FFT in the SFDB extract a selected 10 Hz frequency band
- Switch to time domain of the selected frequency band using inverse-FFT (producing complex data sampled at 10 Hz)
- Select the central half of the chunck
- Store in a BSD file which contains 10 Hz sampled data for a 10 Hz frequency band spanning 1 month of data

One of the great advantage in the use of the BSD collection is the possibility to elaborate the files as required and rapidly produce one single instance of the data, ready for the next step of the analysis. This flexibility allows, for example, to create a set of FFTs with a duration (and hence a frequency resolution) optimized for the search. The BSD

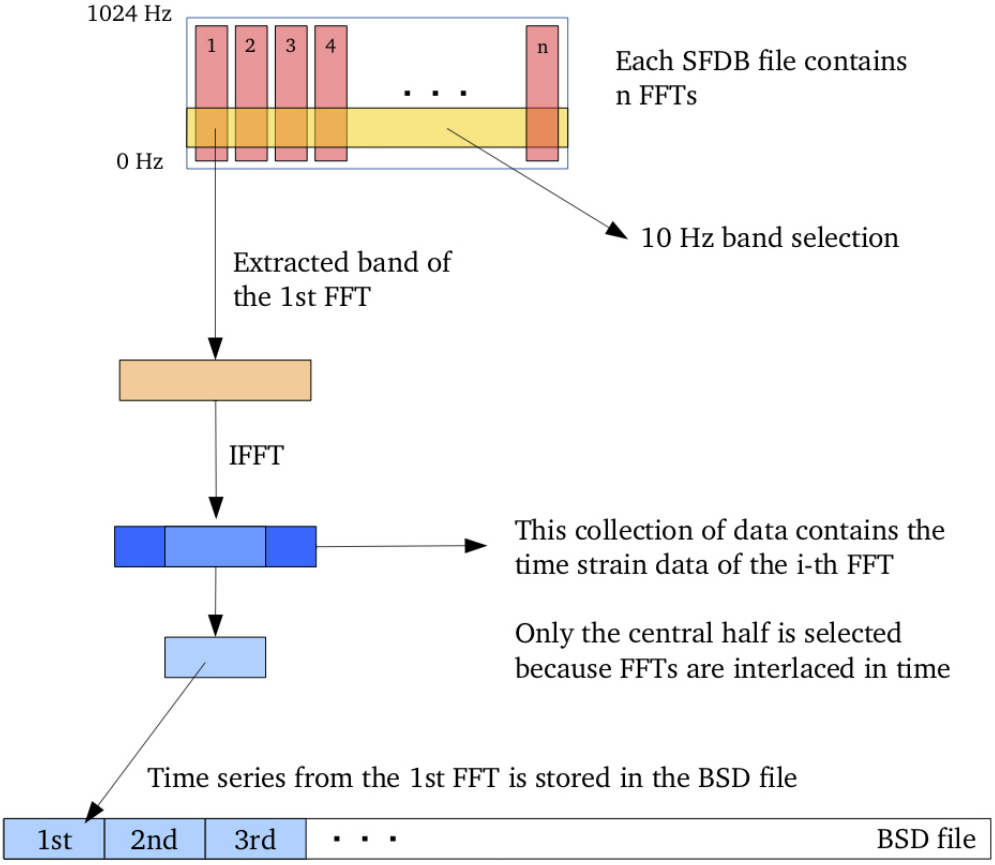

Figure 3.2: Each FFT appears as a (vertical, labeled from 1 to n) box. The horizontal box in yellow indicates the selected 10 Hz. The extraction, and hence the sub-sampling, is done on each FFT and is represented by the flesh-colored box for the first FFT. Only the positive half of each FFT is used and this brings to the construction of a complex time series, which it is called reduced-analytic time series (in figure represented by the blue block). The procedure described above, is repeated for all the required 10 Hz sub-bands. *Credit to [91]*

framework includes also detailed information, stored as a header in every file, which is needed in several steps of the analysis. The information are, for example, the starting time of each dataset and the position and velocity of the detector in a chosen reference frame, in particular the Solar System barycenter (SSB) which is used to remove the Doppler effect in the case of CW searches. Given the set of FFTs, the BSD construction is computationally very cheap and fast. As an example, the total creation time is only a few core-hours for a band of 1024 Hz, four months of data and two detectors. The needed storage capacity is also very small, of the order of 260 GB.

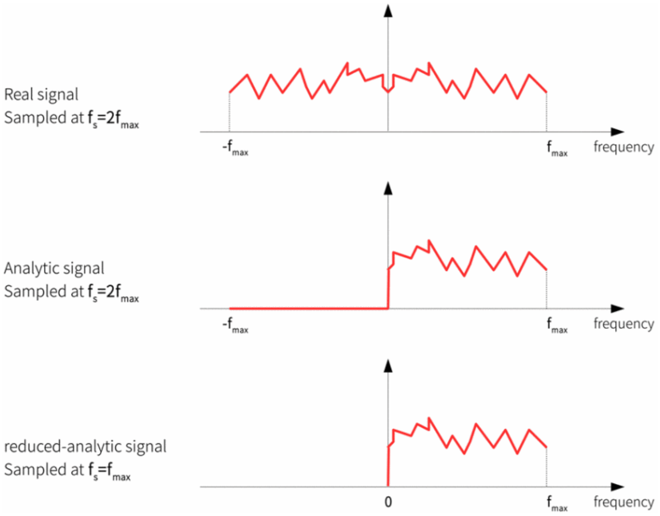

Figure 3.3: Analytic signal compared with the reduced analytic signal used in the BSD file. *Credit to [91].*

3.1.1 The analytical signal

The data stored in the BSD is a complex-valued time series that is a slightly different version of the classical analytic signal, namely a reduced analytic signal with no negative frequency components.

In general, to obtain the analytic signal, first you need to select the 10 Hz frequency band from the SFDB shifting the initial frequency to 0 Hz. Then, each frequency domain chunk has to be zero-padded and inversely Fourier-transformed.

The reduced-analytic signal is instead built discarding the negative zero component sampling at the maximum frequency of the positive band (see Figure 3.3).

From the point of view of signal reconstruction, for a standard analytic signal the sampling frequency is equal to that of the original real valued signal, i.e. at least two times the maximum frequency of the band, as required by the Nyquist theorem. In the BSD data, the sampling frequency is half of the one used for analytic signals. However, there is a perfect equivalence between the analytic signal and the reduced-analytic signal since the latter can be obtained taking only the odd time samples of the former.

Using appropriate normalization factors, it can be shown [91] that the power spectrum of the reduced-analytic signal is equal to the power spectrum of the starting real data with the amplitude of the reduced-analytic signal that is half of the original real data.

The BSD procedure, compared to the construction of the analytic signal, has the advantage of reducing the computing time (half data to be handled) in the data processing, while saving the full information needed to analyze the data or even reconstruct the full time series, if needed.

3.2 The GW strain signal

In Subsection 1.5.1, I have computed the CW signal emitted by a triaxial neutron star rotating around a principal axis of inertia. The perturbation metric $\boldsymbol{h}(t)$ is:

$$\boldsymbol{h}(t) = h_+(t)\hat{\mathbf{e}}_+ + h_\times(t)\hat{\mathbf{e}}_\times \,. \tag{3.1}$$

while the polarization amplitudes h_+ and $h_\times$, can be written as:

$$h_+(t) = h_0\frac{1+\cos^2(i)}{2}\cos[\Phi(t)] \tag{3.2}$$

$$h_x(t) = h_0\cos(i)\sin[\Phi(t)]\,. \tag{3.3}$$

where $\Phi(t) = 2\pi f_{gw}(t - r/c)$ and h_0 is the amplitude defined in (1.62) for a rigid body rotating around a principal axis. The unit vectors $\hat{\mathbf{e}}_+$ and $\hat{\mathbf{e}}_\times$ are defined as:

$$\hat{\mathbf{e}}_+ = \begin{pmatrix} 1 & 0 & 0 \\ 0 & -1 & 0 \\ 0 & 0 & 0 \end{pmatrix} , \qquad \hat{\mathbf{e}}_\times = \begin{pmatrix} 0 & 1 & 0 \\ 1 & 0 & 0 \\ 0 & 0 & 0 \end{pmatrix} \tag{3.4}$$

In the next Subsections, I describe the signal at the output of a ground-based detector and introduce the formalism used by the 5-vector method.

3.2.1 Response of the detector

To evaluate the GW strain at the detector, first I need to write the expression (3.1) in the detector frame:

$$H(t) = \boldsymbol{M}(t)\boldsymbol{h}(t)\boldsymbol{M}(t)^T \tag{3.5}$$

where $\boldsymbol{M}(t)$ is the three-dimensional orthogonal matrix of transformation form the TT frame to the detector's proper reference frame (the apix T indicates the matrix transposition). This rotation matrix can be written as the combination of three rotations:

$$\boldsymbol{M}(t) = M_3 M_2 M_1^T \tag{3.6}$$

where M_1 is the rotation matrix from the wave frame to the celestial sphere coordinate frame, M_2 the rotation matrix from the celestial coordinates to the cardinal coordinates of the Earth and M_3, the rotation matrix from the cardinal coordinates to the detector reference frame (see [93] for the complete expressions).

The response of the interferometric detectors in the long wavelength approximation[1] is well known [93]; it is defined as the difference between the wave induced relative length changes of the two interferometer arms:

$$h(t) = \frac{1}{2}\mathbf{n}_1 \cdot [H(t) \cdot \mathbf{n}_1] - \frac{1}{2}\mathbf{n}_2 \cdot [H(t) \cdot \mathbf{n}_2] \tag{3.7}$$

where $\mathbf{n}_{1/2}$ are the unit vectors parallel to the interferometer arms,

$$\mathbf{n}_1 = (1, 0, 0) \qquad \mathbf{n}_2 = (\cos\xi, \sin\xi, 0) \tag{3.8}$$

with ξ the angle between the arms[2].
It follows that, the GW strain at the detector can be described as:

$$h(t) = h_+ F_+(t;\psi) + h_\times F_\times(t;\psi) \tag{3.9}$$

where the two beam-pattern functions, $F_+(t;\psi)$ and $F_\times(t;\psi)$, are periodic functions of time with period of one sidereal day and given by (see [93] for the detailed computation):

$$F_+(t;\psi) = \sin\xi\,[a(t)\cos(2\psi) + b(t)\sin(2\psi)]\ , \tag{3.10}$$

$$F_\times(t;\psi) = \sin\xi\,[b(t)\cos(2\psi) - a(t)\sin(2\psi)]\ . \tag{3.11}$$

where ψ is the wave polarization angle defined as the angle from $\hat{z} \times \hat{x}$ to the x-axis of the wave frame, measured counterclockwise with respect to $\hat{n}$, where $\hat{z}$ is the direction of the north celestial pole (see Figure 3.4).
The two functions $a(t), b(t)$ depend on the source position in the sky (α and δ) and on the detector position and orientation on the Earth (λ is the latitude and γ is the angle measured counterclockwise from East to the bisector of the interferometers arms) [94]:

$$\begin{aligned} a(t) = &+ \frac{1}{16}\sin 2\gamma(3-\cos 2\lambda)(3-\cos 2\delta)\cos[2(\alpha-\Phi_r-\Omega_\oplus t)] \\ &- \frac{1}{4}\cos 2\gamma\sin\lambda(3-\cos 2\delta)\sin[2(\alpha-\Phi_r-\Omega_\oplus t)] \\ &+ \frac{1}{4}\sin 2\gamma\sin 2\lambda\sin 2\delta\cos(\alpha-\Phi_r-\Omega_\oplus t) \\ &- \frac{1}{2}\cos 2\gamma\cos\lambda\sin 2\delta\sin[\alpha-\Phi_r-\Omega_\oplus t] \\ &+ \frac{3}{4}\sin 2\gamma\cos^2\lambda\cos^2\delta \end{aligned} \tag{3.12}$$

---

[1] In the long wavelength approximation, the reduced wavelength of the GW signal is much larger of the size of the detector.

[2] For the actual interferometric detectors, $\xi = \pi/2$ and $\mathbf{n}_2$ is parallel to the y-axis.

where Φ_r is a deterministic phase which defines the position of the Earth in its diurnal motion at $t = 0$ (the sum $\Phi_r - \Omega_{\oplus} t$ coincides with the local sidereal time of the detector's site), and

$$\begin{aligned} b(t) = &+ \cos 2\gamma \sin\lambda \sin\delta \cos\left[2(\alpha - \Phi_r - \Omega_{\oplus} t)\right] \\ &+ \frac{1}{4}\sin 2\gamma (3 - \cos 2\lambda) \sin\delta \sin\left[2(\alpha - \Phi_r - \Omega_{\oplus} t)\right] \\ &+ \cos 2\gamma \cos\lambda \cos\delta \cos\left(\alpha - \Phi_r - \Omega_{\oplus} t\right) \\ &+ \frac{1}{2}\sin 2\gamma \sin 2\lambda \cos\delta \sin\left(\alpha - \Phi_r - \Omega_{\oplus} t\right) \end{aligned} \tag{3.13}$$

Three-dimensional representations of the absolute value of $F_{+/\times}$ as a function of the sky position are often called *antenna patterns*.

The two beam-pattern functions, $F_+(t;\psi)$ and $F_\times(t;\psi)$, are periodic functions in time. Their time dependency is sinusoidal and cosinusoidal with arguments $\Omega_{\oplus} t$ and $2\Omega_{\oplus} t$, where $\Omega_{\oplus}$ is the sidereal angular frequency of the Earth.

The effect of detector response on a monochromatic signal with angular frequency ω_0 is to introduce an amplitude and phase modulation which determine a split of the signal power into five frequencies $\omega_0, \omega_0 \pm \Omega_{\oplus}, \omega_0 \pm 2\Omega_{\oplus}$. The distribution of power among the five bands depends on the source and detector angular parameters.

3.2.2 The 5-vector formalism

The expression (3.1) can be described in a different way by a polarization ellipse. The polarization ellipse is characterized by the ratio $\eta = a/b$ of its semiminor to its semimajor axis and by the angle that defines the direction of the major axis a with respect to the celestial parallel of the source. This angle is equal to angle ψ introduced previously. The ratio η varies in the range $[-1, 1]$, where $\eta = 0$ for a linearly polarized wave and $\eta = \pm 1$ for a circularly polarized wave ($\eta = 1$ if the circular rotation is counterclockwise). The complex form of (3.1) can be expressed as:

$$\boldsymbol{h}(t) = H_0[H_+ \hat{\mathbf{e}}_+ + H_\times \hat{\mathbf{e}}_\times] e^{i\Phi(t)}\,, \tag{3.14}$$

where

$$H_+ = \frac{\cos(2\psi) - j\eta \sin(2\psi)}{\sqrt{1+\eta^2}} \tag{3.15}$$

$$H_\times = \frac{\sin(2\psi) + j\eta \cos(2\psi)}{\sqrt{1+\eta^2}}\,. \tag{3.16}$$

Introducing the two functions $A_+ = F_+(\psi = 0)$ and $A_\times = F_\times(\psi = 0)$:

$$A_+ = a_0 + a_{1c}\cos(\Omega_\oplus t) + a_{1s}\sin(\Omega_\oplus t) + a_{2c}\cos(2\Omega_\oplus t) + a_{2s}\sin(2\Omega_\oplus t) \tag{3.17}$$

$$A_\times = b_{1c}\cos(\Omega_\oplus t) + b_{1s}\sin(\Omega_\oplus t) + b_{2c}\cos(2\Omega_\oplus t) + b_{2s}\sin(2\Omega_\oplus t) \tag{3.18}$$

where the coefficients depend on source and detector position [95], it is possible to re-write the GW strain at the detector as:

$$h(t) = H_0(H_+A_+ + H_\times A_\times)e^{i\Phi(t)} \tag{3.19}$$

For the computation of the two functions A_+ and $A_\times$, it is important to note that the Earth's sidereal angular frequency $\Omega_\oplus$ is linked to the local sidereal time Θ, the source right ascension α and the detector longitude β by the relation $\Omega_\oplus t = \Theta - \alpha + \beta$.
Since the real part of the complex strain in (3.19) must be equal to the expression in (3.1), it follows that:

$$\eta = -\frac{2\cos(i)}{1+\cos^2(i)} \tag{3.20}$$

$$H_0 = h_0\sqrt{\frac{1+6\cos^2(i)+\cos^4(i)}{4}} \tag{3.21}$$

For $\psi = 0$ the following relations can be found:

$$H_+(\psi = 0) = \frac{h_+}{H_0} \qquad \text{and} \qquad Im(H_\times(\psi = 0)) = -\frac{h_\times}{H_0} \tag{3.22}$$

As shown in equation (3.19), $h(t)$ is the product of two terms: the first, $(A_+H_+ + A_\times H_\times)$, is a "slow" amplitude and phase modulation at the sidereal frequency while the exponential term is a "fast" term, due to the intrinsic source frequency.

3.3 Pre-processing

The phase $\Phi(t)$ in (3.19) shows a time dependence due to different phenomena that modulate in time the received signal frequency. The main physical phenomena to be considered are the spin-down and the Doppler effect due to the Earth motion.
Indeed, the spin-down entails a time model for the phase in the neutron star source frame. Choosing to time the signal phase evolution with respect to the Solar System barycenter (SSB), which is an inertial reference frame, the phase can be expressed as

the Taylor expansion respect to the baricentric time τ

$$\Phi^{src}(\tau) = 2\pi \left[f(\tau - \tau_{ref}) + \frac{1}{2}\dot{f}(\tau - \tau_{ref})^2 + ... \right] \tag{3.23}$$

where τ_{ref} is the reference time and $f, \dot{f}, \ddot{f}, ...$ are the CW frequency ($f = \partial\Phi/\partial\tau$) and the spin-down parameters.

The phase in the detector frame can be computed considering the relation of the wavefront detector arrival time t_{arr} to its source emission time τ [96],

$$\Phi(t_{arr}) = \Phi^{src}(\tau(t_{arr})) \tag{3.24}$$

For the moment, let us consider isolated neutron stars where the relation is:

$$\tau(t_{arr}) = t_{arr} + \Delta_R + \Delta_E + \Delta_S \tag{3.25}$$

where Δ_R is the classic Roemer delay that gives the main contribution while the Einstein delay Δ_E and the Shapiro delay Δ_S are relativistic wave-propagation effects.

The main contribution (up to ≈ 8.5 minutes [97]) is given by the classic Roemer delay:

$$\Delta_R = \frac{\vec{r} \cdot \vec{n}}{c} \tag{3.26}$$

where $\vec{r}$ is the vector identifying the detector position in the SSB and $\vec{n}$ is the unit vector toward the source[3].

The term Δ_E is the Einstein delay which is the sum of two contributions, one due to the gravitational redshift produced by the Sun and the other due to the time dilation produced by Earth's motion. Δ_S is the Shapiro delay due to the curvature of spacetime near the Sun. The Einstein delay is of order of about $2 \cdot 10^{-3}$ s, while the Shapiro delay brings a negligible contribution for CW, unless the source line of sight passes very near the Sun's limb.

3.3.1 The BSD heterodyne correction

As described in the previous Section, the CW signal is modulated mainly by the spin-down and Doppler effect. Different approaches [94, 97] have been proposed to demodulate the strain data in order to enhance the signal-to-noise ratio of the expected CW signal.

---

[3] For the closest pulsars, there is also a parallax timing term in the Roemer delay that takes account of the curvature of the wave fronts emitted from the source [97].

In the BSD approach, detector's data are ready to be corrected without the need to apply filters or to re-sample, since this is already done by construction. This difference is useful in order to have a more general data framework which can be used also for other searches if needed.

In the following, I assume the frequency and spin-down parameters $[f, \dot{f}, \ddot{f}, ..]$ for a given source at the reference time τ_{ref}, to be known. The signal phase shift due to the source spin-down can be written as:

$$\Phi_{sd} = 2\pi \int_{\tau_{ref}}^{t} \left[\dot{f}(t' - \tau_{ref}) + \frac{1}{2}\ddot{f}_0(t' - \tau_{ref})^2 + \dots \right] dt' \,. \tag{3.27}$$

The corresponding phase factor for the Doppler correction is (up to a constant term):

$$\Phi_d = 2\pi \int_{\tau_{ref}}^{t} f_0(t') \frac{\vec{r} \cdot \hat{n}}{c} dt' \approx \frac{2\pi}{c} p_{\hat{n}}(t) f(t) \tag{3.28}$$

where $p_{\hat{n}}(t)$ is the position of the detector in the chosen reference frame, projected along the source sky position $\hat{n}$.

The total signal phase correction can be written as the sum of the spin-down and the Doppler contributions:

$$\Phi_{corr}(t) = \Phi_{sd}(t) + \Phi_d(t) \tag{3.29}$$

Heterodyne de-modulation is then applied by multiplying the data by the exponential factor $e^{-i\Phi_{corr}(t)}$,

$$x(t) = [h(t) + n(t)] e^{-i\Phi_{corr}(t)} \tag{3.30}$$

This technique is useful for correcting pulsar signals for the phase modulation caused by the spin-down/Doppler shift and hence to precisely unwind the apparent phase evolution of the source. Once this correction has been applied, a CW signal would become monochromatic except for the sidereal and residual modulations. These might be present due to inappropriate modeling of the frequency evolution (higher order spin-down terms, source frequency glitches) or to parameter uncertainties like a not perfect estimation of source position parameters.

The amplitude modulation due to the antenna pattern is different for each detector of the network and can be used to build a detection statistic as well as to estimate signal parameters, as shown in Section 3.5.

3.4 Binary system correction

If the source is in a binary system, the relation (3.25) should include the term Δ_{bin} that takes into account the shift in the time of arrival of the signal due to the motion of the source within the binary system.

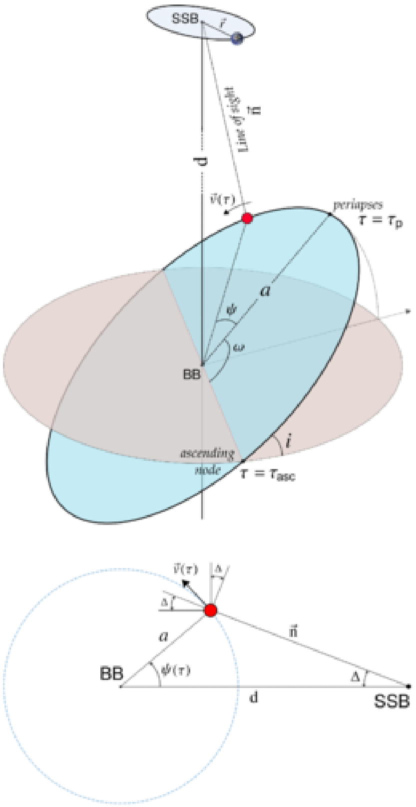

Figure 3.4: *Top-plot* Source in binary orbit to show orbital parameters definition. *Bottom-plot* Projection in two dimension assuming circular orbit. *Credit to* [98].

The term Δ_{bin} is the light-time travel across the orbit (i.e. the Roemer delay for the binary motion) and can be written as:

$$\Delta_{bin} = -\frac{R(\tau)}{c} \tag{3.31}$$

where R is is the radial distance of the CW emitting source from the binary barycenter (BB) with $R > 0$ if the source is further away from us than the BB. Following [99],

$$\frac{R(\tau)}{c} = a_p \left[\sin\omega \left(\cos E - e\right) + \cos\omega \sin(E\sqrt{1-e^2}) \right] \tag{3.32}$$

where $a_p = a \sin \iota / c$ is the projected semi-major axis[4] (with ι the inclination angle and a the semi-major axis) and e the orbital eccentricity. The eccentric anomaly E is defined by the Kepler's equation:

$$\tau - \tau_p = \frac{P}{2\pi} \left(E - e \sin E \right) \tag{3.33}$$

with P the orbital period and τ_p the time of periapse.
Knowing the source sky position allows to rewrite the timing relation (3.25)

$$\tau(t_{SSB}) = t_{SSB} - \frac{R(\tau)}{c} \tag{3.34}$$

that is equivalent to consider the detector in the SSB.
Using a linear phase model approximation, the phase can be approximated as

$$\Phi(t) \approx 2\pi f \left[\Delta t - \frac{R(t)}{c} \right] \tag{3.35}$$

where $\Delta t = t_{SSB} - \tau_{ref}$. It is possible to approximate $E(\tau) \approx E(t)$ since the change in E during R/c is negligible and to consider

$$t - t_p \approx \frac{P}{2\pi} \left(E - e \sin E \right) \tag{3.36}$$

It follows that:

$$\Phi(t) \approx 2\pi f \left[\Delta t - a_p \left(\sin\omega \left(\cos E - e \right) + \cos\omega \sin(E\sqrt{1 - e^2}) \right) \right] \tag{3.37}$$

that is the phase model for eccentric orbit.
In the case of low eccentric orbit ($e \to 0$), the phase model can be simplified. This is not a strong assumption since the 75% of the pulsars in binary system in the ATNF catalogue has $e < 0.01$. Considering $E(t) = E_0(t) + eE_1(t) + ...$ and the Kepler's equation, the Roemer delay to leading order in e is:

$$\frac{R(t)}{c} = a_p \left[\sin\psi(t) + \frac{k}{2} \sin 2\psi(t) - \frac{\beta}{2} \cos 2\psi(t) - \frac{3}{2}\beta \right] \tag{3.38}$$

with

$$k = e \cos\omega \tag{3.39}$$

---

[4] Note that most of the astronomical observations provide the projected semi-major axis and not the semi-major axis since they are only sensitive to the projection of the binary orbit in the absence of polarization information.

$$\beta = e \sin \omega \tag{3.40}$$

and the mean orbital phase

$$\psi(t) = \Omega(t - t_{asc}) \tag{3.41}$$

measured from the time of ascending nodes t_{asc}. For small eccentricity and mean orbital angular velocity $\Omega = \frac{2\pi}{P}$, t_{asc} is:

$$t_{asc} = t_p - \frac{\omega}{\Omega} \tag{3.42}$$

For the linear phase model and for the small-eccentricity limit, it follows that:

$$\Phi(t) \approx 2\pi f \left[\Delta t - a_p \left(\sin \psi(t) + \frac{k}{2} \sin 2\psi(t) - \frac{\beta}{2} \cos 2\psi(t) - \frac{3}{2}\beta \right) \right] \tag{3.43}$$

Starting from this phase model, I use the heterodyne method to remove the signal modulation due to the orbital motion of the source and to apply the 5-vector pipeline also to binary systems.

3.5 The 5-vector method

The data analysis method chosen in this work for the single pulsar analysis is the 5-vec method, a matched filter in the Fourier frequency domain [95]. Assuming that the detectors strain data $x(t)$ can be written as the sum of the noise $n(t)$ with the expected signal $h(t)$,

$$x(t) = h(t) + n(t) \tag{3.44}$$

and assuming stationary and Gaussian noise $n(t)$, the barycentric and spin-down corrections are applied on $x(t)$ as described in Subsection 3.3.1. As a consequence, the signal is now monochromatic apart from an amplitude and phase sidereal modulation and is given by [49]:

$$h(t) = H_0(H_+ A_+ + H_\times A_\times) e^{i(\omega_0 t + \gamma)} \tag{3.45}$$

that is, the product of a fast periodic term, with frequency $f_0 = \omega_0 / 2\pi$ and absolute phase γ, and a slow term given by a linear combination of sines and cosines with argument $\Omega_\oplus$ and $2\Omega_\oplus$. Then, the signal is completely described by its Fourier components at the 5 angular frequencies $\omega_0, \omega_0 \pm \Omega_\oplus, \omega_0 \pm 2\Omega_\oplus$. This set of 5 complex numbers constitutes the signal 5-vector. Given a generic time series $g(t)$, the corresponding 5-vector is:

$$\mathbf{G} = \int_T g(t) e^{-i(\omega_0 t - \mathbf{k}\Omega_\oplus t)} dt \tag{3.46}$$

where $\mathbf{k} = [0, \pm 1, \pm 2]$ and T is the observation time. In the following, I will indicate with $\mathbf{X}$ the data 5-vector and with $\mathbf{A}_+, \mathbf{A}_\times$ the template 5-vectors, obtained by applying the definition (3.46) to equations (3.17) and (3.18). These two last quantities depend only on known parameters and on the signal templates.

Introducing the generator 5-vectors $\mathbf{V}$,

$$\mathbf{V} = e^{-i\mathbf{k}\Omega_\oplus t} = \mathbf{W} e^{j\mathbf{k}(\alpha - \beta)} \tag{3.47}$$

where[5] $\mathbf{W} = e^{j\mathbf{k}\Theta}$, it is easy to show that:

$$h(t) = H_0 \mathbf{A} \cdot \mathbf{W} e^{i(\omega_0 t + \gamma)} \tag{3.48}$$

where $\mathbf{A}$ is:

$$\mathbf{A} = H_+ \mathbf{A}^+ + H_\times \mathbf{A}^\times \,. \tag{3.49}$$

$\mathbf{A}$ is a combination of the $+$ and $\times$ template 5-vectors with components that depend on a combination of the coefficient introduced in (3.17) and (3.18) weighted with exponential of $\alpha - \beta$ [95].

The data 5-vector is:

$$\begin{aligned} \mathbf{X} &= \int_T x(t) \mathbf{V} e^{-i\omega_0 t} dt = \int_T (h(t) + n(t)) \mathbf{V} e^{-i\omega_0 t} dt \\ &= H_0 e^{i\gamma} \mathbf{S} + \mathbf{N} \,. \end{aligned} \tag{3.50}$$

where $\mathbf{N}$ is the noise 5-vector,

$$\mathbf{N} = \int_T n(t) e^{-i(\omega_0 t - \mathbf{k}\Omega_\oplus t)} dt \,, \tag{3.51}$$

and $\mathbf{S}$ is the "empirical" computation of the signal 5-vector $\mathbf{A}$:

$$\mathbf{S} = \int_T s(t) e^{-i(\omega_0 t - \mathbf{k}\Omega_\oplus t)} dt \tag{3.52}$$

for

$$s(t) = \frac{h(t)}{h_0 e^{i\gamma}} \tag{3.53}$$

---

[5] The second equation holds for the relation $\Omega_\oplus t = \Theta - \alpha + \beta$ where Θ is the local sidereal time, α is source right ascension and β the detector longitude.

The construction of the signal 5-vec $\mathbf{S}$ is “empirical” and this is a very important point of the method. The detection of the signal is based on the construction of a matched filter to the signal $+$ and $\times$ components: if these components were obtained using the definition in (3.49), the matching condition would not take into account the presence of holes in the data and the effect of all the operations done on the data, such as cleaning. Then, in practice it is necessary to simulate in time domain the signal $s_+(t)$ and $s_\times(t)$ components, which depend only on the source and detector position and approximate the quantities A_+ and $A_\times$. By operating on them with all the procedures used for the data, it is possible to compute the corresponding empirical 5-vec $\mathbf{S}_+, \mathbf{S}_\times$ by using the definition (3.46).

3.5.1 Parameters estimation

For the estimation of the unknown parameters (amplitude and polarization parameters), it is important to consider two different cases.
In the first case, the two polarization parameters η and ψ are known[6] ("2 degrees of freedom" case), therefore the shape of the signal is also known and the matched filter theory can be used. To estimate the amplitude and the phase of the signal, h_0 and γ, the matched filter transfer function[7] is $\frac{\mathbf{A}^*}{|\mathbf{A}|^2}$. The filter output is the estimation of the signal complex amplitude[8]:

$$\hat{h}_0 = \frac{\mathbf{X} \cdot \mathbf{A}}{|\mathbf{A}|^2} \,. \tag{3.54}$$

In the second case ("4 degrees of freedom" case), the polarization parameters are unknown and it is possible to estimate only the two quantities:

$$\hat{H}_+ = \frac{\mathbf{X} \cdot \mathbf{A}^+}{|\mathbf{A}^+|^2} \qquad \text{and} \qquad \hat{H}_\times = \frac{\mathbf{X} \cdot \mathbf{A}^\times}{|\mathbf{A}^\times|^2} \,. \tag{3.55}$$

$\hat{H}_+$ and $\hat{H}_\times$ are complex numbers that can be interpreted as two matched filter between the data and the signal templates $\mathbf{A}^{+/\times}$, used in order to maximize the signal-to-noise ratio.
Assuming the noise is Gaussian with mean value zero, the two matched filters are estimators [49] of the signal plus and cross amplitudes $H_0 e^{i\gamma} H_+$, $H_0 e^{i\gamma} H_\times$.

---

[6] For example, estimations of η (or i) and ψ can be provided by X-ray observations [94] because these observations provide accurate determination of the orientation of spin axis of the selected pulsar. On the other hand, the physics of pulsar is complex, and a model leading to the above estimations could have several uncertainties.

[7] The superscript $*$ in $\mathbf{A}^*$ refers to the complex conjugation of the complex vector $\mathbf{A}$.

[8] It is important to underline that in all the equations starting from this section with $\mathbf{A}$, I will always refer to its empirical realization $\mathbf{S}$.

The estimator of the signal amplitude is given by:

$$\hat{H}_0 = \sqrt{|\hat{H}_+|^2 + |\hat{H}_\times|^2}\,. \tag{3.56}$$

Introducing the quantities A,B and C

$$H_+ H'_\times = A + iB \qquad \text{and} \qquad |\hat{H}_+|^2 - |\hat{H}_\times|^2 = C \tag{3.57}$$

it is simply to infer the estimations of η and of ψ,

$$\hat{\eta} = \frac{-1 + \sqrt{1 - 4B^2}}{2B}\,, \tag{3.58}$$

$$\cos(4\hat{\psi}) = \frac{C}{4A^2 + C^2}\,, \tag{3.59}$$

$$\sin(4\hat{\psi}) = \frac{2A}{4A^2 + C^2}\,. \tag{3.60}$$

3.5.2 5-vector detection statistic

In [95], the detection statistic S for the 5-vector method is defined as:

$$S = |\mathbf{A}^+|^4 |\hat{H}_+|^2 + |\mathbf{A}^\times|^4 |\hat{H}_\times|^2, \tag{3.61}$$

in order to check the statistical significance of a candidate by making a comparison between its value and its expected distribution in the case of noise.

In the hypothesis of Gaussian noise with zero mean, variance σ^2 and no signal, the two complex estimators have also Gaussian distribution with mean zero and variance:

$$\sigma^2_{+/\times} = \frac{\sigma_x^2}{|\mathbf{A}^{+/\times}|^2} \tag{3.62}$$

with $\sigma_x^2 = \sigma^2 \cdot T$ and T, the observation time. σ_x^2 is the variance of each component of the noise 5-vector, following a Gaussian distribution with zero mean. This means that the real and the imaginary part of (3.55) are independent normally distributed random variables with mean zero and variance $\sigma^2_{+/\times}/2$ [49].

In general, the central-χ^2 distribution can be seen as the distribution that models the sum of squares of several independent and identically distributed Gaussian random variables with the same mean and variance. For this reason, if a complex random variable Y has a Gaussian distribution, that is:

$$\mathit{Re}(Y) \sim N(x;0,\sigma^2) \quad \text{and} \quad \mathit{Im}(Y) \sim N(x;0,\sigma^2)\,, \tag{3.63}$$

the random variable $R = |Y|^2 = |\mathit{Re}(Y)|^2 + |\mathit{Im}(Y)|^2$ has a central-χ square distribution with 2 degrees of freedom:

$$R \sim \frac{1}{2\sigma^2} e^{-\frac{x}{2\sigma^2}}\,. \tag{3.64}$$

The distribution in (3.64) is an exponential distribution,

$$R \sim \exp(x;\theta) = \frac{1}{\theta} e^{-\frac{x}{\theta}} \tag{3.65}$$

with mean $\theta = 2\sigma^2 = \sigma^2_{+/\times}$. Therefore, the statistic S is the weighted combination of two random variables $S^+ = |\hat{H}_+|^2$, $S^\times = |\hat{H}_\times|^2$ with exponential distribution. Since

$$R \sim \exp(x;\theta) \quad \Longrightarrow \quad aR \sim \frac{1}{|a|}\exp(\frac{x}{a};\theta)\,, \tag{3.66}$$

and

$$S = aS^+ + bS^\times\,, \tag{3.67}$$

the distribution of S is the convolution of two exponentials with different means.
It follows that the distribution of S in the case of Gaussian noise with zero mean, variance σ^2 and no signal, is:

$$S \sim f(S) = \frac{e^{-\frac{S}{\sigma_x^2|\mathbf{A}^\times|^2}} - e^{-\frac{S}{\sigma_x^2|\mathbf{A}^+|^2}}}{\sigma_x^2(|\mathbf{A}^\times|^2 - |\mathbf{A}^+|^2)} \tag{3.68}$$

if $a = |\mathbf{A}^+|^4$ and $b = |\mathbf{A}^\times|^4$.
The situation is quite different if a signal of amplitude H_0 is present into the data.
In this case, the real and the imaginary part of (3.55), have still Gaussian distribution but with different mean values. Therefore the random variable $R = |Y|^2 = |\mathit{Re}(Y)|^2 + |\mathit{Im}(Y)|^2$, where

$$\mathit{Re}(Y) \sim N(x;\mu_1,\sigma^2) \quad \text{and} \quad \mathit{Im}(Y) \sim N(x;\mu_2,\sigma^2)\,, \tag{3.69}$$

has a noncentral-χ^2 distribution with 2 degrees of freedom (apart from the factor k):

$$g(x;H_0) = \frac{k}{2} e^{-\frac{kx+\beta}{2}} I_0(\sqrt{k\beta x}) \tag{3.70}$$

where I_0 is the modified Bessel function of the first kind of zero order, and

$$x = |\hat{H}_{+/\times}|^2 \equiv S^{+/\times} \quad , \quad k = 2\frac{|\mathbf{A}^{+/\times}|^2}{\sigma_x^2} \quad , \quad \beta = 2\frac{H_0^2|e^{j\Phi_0}H_{+/\times}\mathbf{A}^{+/\times}|^2}{\sigma_x^2} . \tag{3.71}$$

The distribution of S is now the more complicated convolution of the function $g(y_+)$ and $g(y_\times)$ where $y_+ = |\mathbf{A}^+|^4|\hat{H}_+|^2$ and $y_\times = |\mathbf{A}^\times|^4|\hat{H}_\times|^2$ that can be resolved by numerical integration for given signal parameters [49].

3.5.3 Multidetector extension

Let us consider a network of n detectors and for the j-th detector, let us compute the corresponding signal $\mathbf{X_j}$ and template 5-vectors $\mathbf{A_j}^{+/\times}$.
In [100], the 5n-vectors are defined as:

$$\mathbf{X} = [\mathbf{X_1}, ..., \mathbf{X_n}] \tag{3.72}$$

$$\mathbf{A}^+ = [\mathbf{A_1^+}, ..., \mathbf{A_n^+}], \tag{3.73}$$

$$\mathbf{A}^\times = [\mathbf{A_1^\times}, ..., \mathbf{A_n^\times}] \tag{3.74}$$

combining the data 5-vectors $\mathbf{X_j}$ and the template 5-vectors $\mathbf{A_j^{+/x}}$ (with $j = 1, .., n$) for the considered pulsar in the j-th detector. For instance, in a multidetector search using the two LIGO detectors, the data 10-vector are composed by the first five components equal to the LLO 5-vector components and the last five equal to the LHO 5-vector components.
Using the 5n-vectors, the multi-detector single pulsar statistic S is:

$$S = |\mathbf{A}^+|^4|\hat{H}_+|^2 + |\mathbf{A}^\times|^4|\hat{H}_\times|^2 \tag{3.75}$$

where (the same for $\hat{H}_\times$)

$$\begin{aligned} \hat{H}_+ = \frac{\mathbf{X}\cdot\mathbf{A}^+}{|\mathbf{A}^+|^2} = \frac{\sum_{j=1}^{n}\mathbf{X}_j\cdot(\mathbf{A}_j^+)^*}{\sum_{k=1}^{n}\mathbf{A}_k^+\cdot(\mathbf{A}_k^+)^*} = \\ = \frac{1}{|\mathbf{A}^+|^2}\left(|\mathbf{A}_1^+|^2\cdot\hat{H}_{+,1} + ... + |\mathbf{A}_n^+|^2\cdot\hat{H}_{+,n}\right) \end{aligned} \tag{3.76}$$

In the two estimators $\hat{H}_{+/\times}$, each data 5-vector "interacts" only with the corresponding template.

In the hypothesis of Gaussian noise with zero mean and variance σ_j^2 in the j-th detector, the corresponding components of the data 5-vector are also distributed according to a complex Gaussian distribution with mean value zero and variance $\sigma_j^2 \cdot T_j$. Therefore, the two complex estimators $\hat{H}_{+/\times}$ have also Gaussian distributions,

$$\hat{H}_{+/\times} \sim Gauss\left(x;\, 0, \sigma_{+/\times}^2\right) \tag{3.77}$$

with

$$\sigma_{+/\times}^2 = \sum_{j=1}^{n} \frac{\sigma_j^2 \cdot T_j \cdot |\mathbf{A}_j^{+/\times}|^2}{|\mathbf{A}^{+/\times}|^4} \tag{3.78}$$

Since $|\hat{H}_{+/\times}|^2 = \mathit{Re}[\hat{H}_{+/\times}]^2 + \mathit{Im}[\hat{H}_{+/\times}]^2$, it follows that:

$$|\hat{H}_{+/\times}|^2 \sim Exp(x; \sigma_{+/\times}^2) = \frac{1}{\sigma_{+/\times}^2} e^{-\frac{x}{\sigma_{+/\times}^2}} \tag{3.79}$$

It is possible to compute the noise S distribution considering the weighted linear combination in (3.75).

If a CW signal is present into the analyzed data, the distributions of the two complex estimators $\hat{H}_{+/\times}$ are:

$$\hat{H}_{+/\times} \sim Gauss\left(x\,;\; H_0 \cdot e^{j\gamma} \cdot H_{+/\times}\,,\; \sigma_{+/\times}^2\right) \tag{3.80}$$

where $H_{+/\times}$ are the polarization functions, H_0 is the amplitude and γ the phase.
$|\hat{H}_{+/\times}|^2$ have a non central-χ^2 distribution (apart from the factor $k_{+/\times}$):

$$|\hat{H}_{+/\times}|^2 \sim \frac{k_{+/\times}}{2} e^{-\frac{k_{+/\times}x + \lambda_{+/\times}}{2}} I_0(\sqrt{k_{+/\times}\lambda_{+/\times}x}) \tag{3.81}$$

where I_0 is the modified Bessel function of the first kind, and

$$k_{+/\times} = \frac{2}{\sigma_{+/\times}^2} \qquad \lambda_{+/\times} = k_{+/\times} \cdot |H_{+/\times}|^2 \cdot H_0^2\,. \tag{3.82}$$

Compared to the single detector case, the distributions are the same. The difference is the expression for the variances $\sigma_{+/\times}^2$.
As an example, let us consider a network of n detectors with the same observation time t and co-located $|\mathbf{A}_k^{+/\times}|^2 = |\mathbf{A}_1^{+/\times}|^2\,, \forall\, k$. The variances $\sigma_{+/\times}^2$ in this case are:

$$\sigma_{+/\times}^2 = \frac{t}{|\mathbf{A}_1^{+/\times}|^2} \frac{\sum_{j=1}^{n} \sigma_j^2}{n} \tag{3.83}$$

This is equal to the case of one detector with variance equal to the arithmetic mean of the variances of the n detectors.

Compared to the most sensitive detector (i.e. the detector with smallest σ^2), not necessarily a multidetector analysis outperforms the most sensitive detector.

In Section 3.6, I describe a different way to construct the 5n-vector weighting the 5-vectors according to the detector noise and observation time.

3.5.4 5n-vector for multiple sources detection

The 5n-vectors generalize the 5-vector procedure to a network of n detectors. The definition in (3.72) combines together the 5-vectors computed from each detector.

Fixing a set of n pulsars, I can also consider the 5n-vector as the combination of the 5-vectors of different pulsars in the same detectors. In this case, I consider the 5n-vector as a matched filter at the $5n$ frequencies where the combined signal is expected.

The noise distributions of $\hat{H}_{+/\times}$ are the same since there is just a re-definition of n, that in this case, is the number of pulsars.

For the signal distributions, I need to consider that each pulsar can emit with different amplitudes. The signal distributions of $\hat{H}_{+/\times}$ are:

$$\hat{H}_{+/\times} \sim Gauss\left(x\,;\,\sum_{i=1}^{n}\left(\frac{|\mathbf{A}^{+,i}|^2}{|\mathbf{A}^{+}|^2}H_{0,i}\cdot e^{j\gamma_i}\cdot H_{+/\times,i}\right)\,,\,\sigma^2_{+/\times}\right) \tag{3.84}$$

In the case of single pulsar in n detectors, this expression is the same of (3.80) since the amplitude and the polarization functions do not depend on the index i.

In [49], the λ_+ (the same for $\lambda_\times$) parameter is defined as:

$$\lambda_+ = \left(E\left[\frac{Re\{H_+\}}{\sigma_+/\sqrt{2}}\right]\right)^2 + \left(E\left[\frac{Im\{H_+\}}{\sigma_+/\sqrt{2}}\right]\right)^2 \tag{3.85}$$

that, considering equation (3.84), implies

$$\frac{\lambda_+}{k_+} = \left[\sum_{i=1}^{n}\left(\frac{|\mathbf{A}^{+,i}|^2}{|\mathbf{A}^{+}|^2}H_{0,i}\cdot Re\{e^{j\gamma_i}H_{+,i}\}\right)\right]^2 + \left[\sum_{i=1}^{n}\left(\frac{|\mathbf{A}^{+,i}|^2}{|\mathbf{A}^{+}|^2}H_{0,i}\cdot Im\{e^{j\gamma_i}H_{+,i}\}\right)\right]^2 \tag{3.86}$$

For $n = 1$ or in the case of single pulsar in n detectors, the expressions of $\lambda_{+/\times}$ are the same found in the previous Subsection.

It is clear that for a large pulsars set where few signals are expected near the detection threshold, this procedure is not efficient and robust since the matched filter is computed simultaneously at the expected $5n$ frequencies.

3.5.5 Upper limit computation

If the data are consistent with the noise hypothesis, it is possible to set upper limit on the pulsar amplitude. In the description of the upper limit computation, I follow the mixed frequentist/Bayesian procedure in [86].

Using the Bayes theorem, the posterior distribution on the amplitude H_0, given the measured value $\overline{S}$ of the detection statistic, is:

$$P(H_0|\overline{S}) = \frac{L(\overline{S}|H_0)\Pi(H_0)}{\int L(\overline{S}|H_0')\Pi(H_0')dH_0'} \tag{3.87}$$

where $L(\overline{S}|H_0)$ is the likelihood, $\Pi(H_0)$ the prior on the amplitude and $\int L(\overline{S}|H_0')\Pi(H_0')dH_0'$ is the evidence.

The 95% credible upper limit on the amplitude is the value $H_0^{95\%}$ that entails a cumulative distribution probability of 0.95, i.e. $P(H_0 > H_0^{95\%}|\overline{S}) = 0.95$.

The upper limit computation is a mixed Bayesian/frequentist procedure since the likelihood is estimated considering the signal distribution of the statistic S at the measured value $\overline{S}$ for the signal amplitude H_0.

The signal distribution for the amplitude H_0 can be inferred considering the linearity of the 5-vector:

$$\mathbf{X} = \mathbf{X}^{n(t)} + \mathbf{X}^{h(t)} \tag{3.88}$$

where $\mathbf{X}^{n(t)}$ is the data 5-vector when there is only noise $x(t) = n(t)$ and $\mathbf{X}^{h(t)}$ is the data 5-vector computed for the expected signal $x(t) = h(t)$. It follows that:

$$\hat{H}_{+/\times} = \hat{H}^{n(t)}_{+/\times} + \hat{H}^{h(t)}_{+/\times} \tag{3.89}$$

since the two estimators are linear due to the scalar product with respect to the sidereal templates. The term $\hat{H}^{h(t)}_{+/\times}$ can be written as:

$$\hat{H}^{h(t)}_{+/\times} = H_0 \cdot \hat{H}^{h(t)/H_0}_{+/\times} \tag{3.90}$$

where $\hat{H}^{h(t)/H_0}_{+/\times}$ is the estimator computed for $H_0 = 1$. This allows to reduce the computational cost since the estimators can be computed just once and then, re-scaled using a scalar amplitude without performing the spin-down and Doppler correction each time.

To fix the signal distribution, one need also to fix the two polarization parameters η and ψ. Assuming uniform priors for ψ and for $\cos\iota$, it is possible to marginalize over

these two parameters taking random values in the corresponding range for each noise 5-vector, i.e. for each realization of $\hat{H}^{h(t)}_{+/\times}$.
Starting from a set of possible signal amplitudes from a prior distribution $\Pi(H_0)$, I reconstruct the signal distribution for S for each amplitude value, hence the likelihood $L(\bar{S}|H_0)$.
The posterior in (3.87) can be used to set an upper limit on the amplitude H_0 of the complex definition of the expected signal defined in (1.62).
To compare the obtained upper limit with the result of the Bayesian pipeline (or the $\mathcal{F}$-statistic), the upper limits on H_0 is converted to the upper limits on h_0. The relation between the two definitions is (see Section 3.2):

$$h_0 = \frac{2}{\sqrt{1 + 6\cos^2(\iota) + \cos^4(\iota)}} \cdot H_0 \tag{3.91}$$

The upper limit on h_0 can be inferred considering the mean value of the conversion factor due to the marginalization over the parameter $\cos(\iota)$. In this way, it follows that $h_0^{95\%} \approx 1.37 H_0^{95\%}$.

3.6 Weighted multidetector extension

In this Section, I propose a different way to consider a multidetector extension that takes into account the different sensitivities of the detectors. Indeed, the 5n-vector in (3.72) combines together the 5-vectors from each detector. Since the noise level in the detectors can be very different, the 5n-vector can reduce the signal to noise ratio compared to the 5-vector of the most sensitive detector.
The weighted data 5n-vector is:

$$\mathbf{X} = [c_1\mathbf{X}_1, ..., c_n\mathbf{X}_n] \tag{3.92}$$

where the weights c_j are defined as:

$$c_j = \frac{\sqrt{n}}{\sqrt{\sum_{i=1}^{n}\left(\frac{T_i}{S_i}\right)}}\sqrt{\frac{T_j}{S_j}} = \sqrt{\mathcal{H}} \cdot \sqrt{\frac{T_j}{S_j}} \tag{3.93}$$

S_j and T_j are the PSD (that is $\propto \sigma_j^2$) and the observation time in the j-th detector while $\mathcal{H}$ is the harmonic mean of the time-weighted power spectral densities.

The matched filters are (the same for $\hat{H}_\times$):

$$\begin{aligned}\hat{H}_+ = \frac{\mathbf{X}\cdot\mathbf{A}^+}{|\mathbf{A}^+|^2} = \frac{\sum\limits_{j=1}^{n} c_j\mathbf{X}_j\cdot(\mathbf{A}_j^+)^*}{\sum\limits_{k=1}^{n}\mathbf{A}_k^+\cdot(\mathbf{A}_k^+)^*} = \\ = \frac{1}{|\mathbf{A}^+|^2}\left(c_1|\mathbf{A}_1^+|^2\hat{H}_{+,1} + ... + c_n|\mathbf{A}_n^+|^2\hat{H}_{+,n}\right)\end{aligned} \tag{3.94}$$

In the hypothesis of Gaussian noise for the j-th detector with variance σ_j^2, the two complex estimators $\hat{H}_{+/\times}$ have also Gaussian distributions,

$$\hat{H}_{+/\times} \sim Gauss\left(x;\,0,\sigma^2_{+/\times}\right) \tag{3.95}$$

with

$$\sigma^2_{+/\times} = \sum_{j=1}^{n}\frac{(c_j\sigma_j)^2\cdot T_j\cdot|\mathbf{A}_j^{+/\times}|^2}{|\mathbf{A}^{+/\times}|^4} \tag{3.96}$$

Using the c_j, I re-define the noise variance in each detector:

$$(c_j\sigma_j)^2 \propto c_j^2\cdot S_j = \frac{n\cdot T_j}{\sum\limits_{i=1}^{n}\left(\frac{T_i}{S_i}\right)} \tag{3.97}$$

If the observation time was the same ($\forall\, j,\; T_j = t$), this corresponds to "equalize" the noise in each detector. In this case, it follows that:

$$\begin{aligned}\sigma^2_{+/\times} = \sum_{j=1}^{n}\frac{(c_j\sigma_j)^2\cdot T_j\cdot|\mathbf{A}_j^{+/\times}|^2}{|\mathbf{A}^{+/\times}|^4} = \sum_{j=1}^{n}\frac{n\cdot t\cdot|\mathbf{A}_j^{+/\times}|^2}{\sum\limits_{i=1}^{n}\left(\frac{1}{\sigma_i^2}\right)|\mathbf{A}^{+/\times}|^4} = \\ = \frac{n\cdot t}{\sum\limits_{i=1}^{n}\left(\frac{1}{\sigma_i^2}\right)|\mathbf{A}^{+/\times}|^2} = \frac{n\cdot t}{\sum\limits_{i=1}^{n}\left(\frac{1}{\sigma_i^2}\right)\sum\limits_{k=1}^{n}|\mathbf{A}_k^{+/\times}|^2}\end{aligned} \tag{3.98}$$

Let us consider the toy case of n co-located detectors where $|\mathbf{A}_k^{+/\times}|^2 = |\mathbf{A}_1^{+/\times}|^2, \forall\, k$; the variances are

$$\sigma^2_{+/\times} = \frac{t}{\sum\limits_{i=1}^{n}\left(\frac{1}{\sigma_i^2}\right)|\mathbf{A}_1^{+/\times}|^2} \tag{3.99}$$

This is equal to the case of one detector with observation time t and variance V^2:

$$V^2 = \frac{1}{\sum_{i=1}^{n}\left(\frac{1}{\sigma_i^2}\right)} = \frac{\mathcal{H}}{n} \tag{3.100}$$

where $\mathcal{H}$ is the harmonic mean of the variances. Since there is the condition:

$$min\{\sigma_1^2, ..., \sigma_n^2\} \leq \mathcal{H} \leq n \cdot min\{\sigma_1^2, ..., \sigma_n^2\} \tag{3.101}$$

this means that:

$$\frac{min\{\sigma_1^2, ..., \sigma_n^2\}}{n} \leq \frac{\mathcal{H}}{n} \leq min\{\sigma_1^2, ..., \sigma_n^2\} \tag{3.102}$$

It follows that for n co-located detectors with the same observation time, I always have an improvement in the detection sensitivity using the coefficients c_j, differently of what I have found in (3.83) for the classic definition of the 5n-vector.
For example, let us consider the case of two co-located detectors $n = 2$ (equal to consider different datasets of the same detector), with $\sigma_2^2 = C \cdot \sigma_1^2$ and $C > 1$:

$$\sigma_{+/\times}^2 = \frac{C \cdot \sigma_1^2 \cdot t}{(C+1) \cdot |\mathbf{A}_1^{+/\times}|^2} \tag{3.103}$$

The minimum detectable signal is h_{min}:

$$h_{min} \propto \sqrt{\frac{C}{C+1}\frac{\sigma_1^2}{t}} \tag{3.104}$$

It is clear that in the general case (different detectors' locations and observation times), the multi-detector analysis not necessarily outperforms the most sensitive detectors.
It is important to briefly describe the signal distribution for $|\hat{H}_{+/\times}|^2$. If a CW signal is present into the analyzed data, the distributions of the two complex estimators $\hat{H}_{+/\times}$ are:

$$\hat{H}_{+/\times} \sim Gauss\left(x\,;\, H_0 \cdot e^{j\gamma} \cdot H_{+/\times} \cdot M_{+/\times}\,,\, \sigma_{+/\times}^2\right) \tag{3.105}$$

where $H_{+/\times}$ are the polarization functions, H_0 is the amplitude, γ the phase and

$$M_{+/\times} = \sum_{j=1}^{n} \frac{c_j \cdot |\mathbf{A}_j^{+/\times}|^2}{|\mathbf{A}^{+/\times}|^2} \tag{3.106}$$

is a known factor for the targeted search.
$|\hat{H}_{+/\times}|^2$ have a non central-χ^2 distribution (apart from the factor $k_{+/\times}$):

$$|\hat{H}_{+/\times}|^2 \sim \frac{k_{+/\times}}{2} e^{-\frac{k_{+/\times}x+\lambda_{+/\times}}{2}} I_0(\sqrt{k_{+/\times}\lambda_{+/\times}x}) \tag{3.107}$$

where I_0 is the modified Bessel function of the first kind, and

$$k_{+/\times} = \frac{2}{\sigma^2_{+/\times}} \qquad \lambda_{+/\times} = k_{+/\times} \cdot |H_{+/\times}|^2 \cdot H_0^2 \cdot M_{+/\times} \,. \tag{3.108}$$

Respect to the classic definition of the 5n-vector, the distributions do not change. There is just a re-definition of the variances for the detectors noise. This means that using the coefficients c_j, it is changed how $\lambda_{+/\times}$ depends on the detectors' sensitivity.

Chapter 4

The 5n-vector ensemble method

As described in Section 2.7, targeted searches for the detection of CW signals from known pulsars found no evidence of signals using the data from the last observing runs of the LIGO and Virgo detectors. This thesis tries to improve the detection probability for the targeted search using a statistical ensemble method. The idea is to statistically combine the effects of several sources - i.e. an ensemble of pulsars - that are individually undetectable but near the detection threshold.

In this Chapter, I describe first the ensemble procedures developed so far in the GW community. Then, I focus on the ensemble procedure designed in this thesis to improve the detection probability, and based on the definition of a new ensemble statistic and on a rank truncation procedure. In addition, I describe the statistical properties of the new statistic and the procedure to set upper limits on global parameters.

4.1 Ensemble procedures

In the hypothesis of weak signals that can not be individually detectable, different methods have been proposed that look at a signal from an ensemble, i.e. a set, of pulsars. An ensemble signal is defined as the superposition of signals from different individually undetectable sources.

The methods proposed to detect an ensemble signal can be gathered in two main groups. In the first group, the expected signals are combined together and the methods look at a stochastic GW signal. I will refer to this group as "Stochastic procedures".

In the second group, there are the methods that statistically combine the information from individual sources, inferred using CW analysis described in Section 2.7. In general, these methods are multiple tests that consider a set of statistical inferences simultaneously. I will refer to this group as "Multiple test procedures".

4.1.1 Stochastic procedures

In CW analysis, the first method to detect CW signals from an ensemble of pulsars was proposed by Giazotto et al. in [101]. In this paper, the authors proposed a "quadratic detection" measuring the square of the gravitational signal and detecting the sidereal modulation which results from the detector position and from the anisotropy of the neutron stars distribution. This technique is very similar to the radioastronomy observation technique that consists in scanning the sky around the source, and in measuring the differences of the total signal on/off of the source.

As well explained in [101], "the problem of detection of the gravitational wave emission from an ensemble is very close to the search for a gravitational cosmological background". Indeed, the superposition of weak signals from individually undetectable pulsars can form an astrophysical stochastic gravitational-wave background (SGWB) which could be observed by current detectors [102]. The observation of a SGWB from neutron stars can be used to constrain population ensemble properties, e.g. the number N_{band} of neutron stars in a certain analysis frequency band and the average ellipticity ϵ_{av} of the considered population.

Recent results in [103] constrain the average ellipticity of Galactic neutron stars to $\epsilon_{av} < 1.8 \times 10^{-8}$ with $N_{band} = 1.6 \times 10^{7}$ performing a cross-correlation to search for a common signal in multiple datasets simultaneously. In a different search [104], the authors found $\epsilon_{av} < 1.1 \times 10^{-7}$ with $N_{band} = 8.8 \times 10^{4}$ for the Galactic millisecond pulsar performing a stochastic targeted search for an anisotropic SGWB knowing a priori its angular distribution along with the spectral properties.

Stochastic procedures could provide insights into the ensemble properties for the entire set of neutron stars in the Galaxy and not merely for the set of known pulsars. On the contrary, stochastic searches are less sensitive compared to the CW targeted search where the known source properties allow to correct for the spin-down and the Doppler effect increasing the detection probability for a CW signal.

As explained in [103], "Because SGWB and CW searches attempt to answer different physical questions, they can work in synergy. Using the methods of the former, it would be possible to perform rapid, blind all-sky searches for neutron star signals and transmit the coordinates of possible outliers as inputs of the latter, for a more refined and sensitive search".

4.1.2 Multiple test procedures

The problem of combining independent tests has been discussed and described in different works (see for example [105]). In this Section, I briefly review the most used methods for multiple testing.

Let us consider N independent experiments that try to detect an effect linked to a certain parameter θ_i for the i-th experiment.

The null hypothesis $H_i : \theta_i = 0$ is tested against the alternative $K_i : \theta_i > 0$ for the i-th experiment, according to a test statistic S_i. The p-value P_i for the i-th experiment is defined as:

$$P_i = P(S_i \geq s_i | H_i) \tag{4.1}$$

where s_i is the observed value for S_i. If S_i has a continuous distribution, P_i is a uniform random variable in the interval $[0, 1]$ under the H_i hypothesis. "Smalls" values of P_i lead to rejection of H_i; that is, the statistic S_i would indicate rejection at the significance level α if $s_i \geq s_\alpha$ where $s_\alpha : P(S_i > s_\alpha | H_i) = \alpha$.

A multiple test considers the combined null hypothesis H:

$$H = H_1 \cap ... \cap H_N : \theta_1 = ... = \theta_N = 0 \tag{4.2}$$

versus the combined alternative hypothesis K,

$$K = K_1 \cup ... \cup K_N : \text{at least one } \theta_i > 0 \tag{4.3}$$

Multiple test combine the data from the N experiments into a single detection statistic to test N against K efficiently.

Traditional multiple tests use the single p-values P_i to test either each hypothesis separately, as in the Bonferroni-like procedures [106], or all hypotheses simultaneously as in the case of the non parametric procedures [107] (as for the Fisher test [108]).

The Bonferroni-like procedures are based on individual hypothesis tests but do not consider combined evidence. The Bonferroni criterion compares the minimum p-value with a threshold adjusted to achieve a desired significance level and to control the Family-Wise Error Rate (FWER). The FWER is the probability of making at least one Type I Error ("false alarm" error) [109]. It is known [110] that these procedures increase the probability of producing false negatives reducing statistical power.

Non parametric procedures are test statistics that consider the combination of $P_1, ..., P_N$. In these procedures, the P_i are assumed independent and uniform random variables under the null hypothesis regardless the form of the statistics S_i.

In 1925 [108], Fisher was the first to suggest a method of combining the p-values considering the statistic $F = -2\sum_{i=1}^{N} \log P_i$ that under the null hypothesis follows a χ^2

distribution:

$$F = -2\sum_{i=1}^{N} \log P_i \sim \chi^2(x; 2N) \tag{4.4}$$

since $-2\log P_i \sim \chi^2(x; 2)$. The significance of the test is established considering the p-value for the statistic F.

Based on this statistic, different methods have been proposed considering, for example, a weighted combination of the p-values, a truncation method [111], and also a rank truncation method [112].

Commonly used statistics for combining p-values that can be found in literature are the Pearson statistic $P = -\sum_{i=1}^{N} \log(1 - P_i)$ or the Stouffer statistic $S = \sum_{i=1}^{N} \Phi^{-1}(P_i)$ where Φ is the standard normal cumulative distribution function. Each of this definition is monotonic in the p-values, and therefore optimal in some setting [113]. Indeed, it has been shown [105] that the multiple optimal test is different according to the analyzed problem.

As said in [107], "Combining p-values is usually required in one of two situations: (1) when either the values of the actual statistics that need to be combined or the forms of their distributions are unknown or (2) this information is available but the distributions are such that there is no known or reasonably convenient method available for constructing a single overall test".

For the targeted search of CWs, the distribution of S_i under the null hypothesis is, in general, well-known and an overall test can be constructed starting from the S_i. In addition, since I expect few signals near the detection threshold, these traditional tests could be ineffective and have substantial power loss [114].

4.1.3 CW multiple test procedures

In the CW analysis, the N experiments considered in the previous Section are the N individual searches for the set of pulsars considered in a targeted search for a given dataset. The null hypothesis corresponds to the noise hypothesis while the parameter θ_i for the i-th pulsar is the amplitude of the CW signal.

Ensemble procedures can improve the detection probability combining individually undetectable sources that are hopefully near the detection threshold. In this Subsection, I describe two different procedures proposed in the last years for the detection of CWs from an ensemble of known pulsars.

In [79], the authors describes a multiple test which combines the detection statistics of single pulsar rather than the measured p-values. The original idea was proposed by Cutler and Shutz in [80] and based on the detection of the single source: they defined an overall $\mathcal{F}$-statistic as the linear combination of the $\mathcal{F}_i$ statistics for each pulsar (defined in Subsection 2.6.2),

$$\mathcal{F} = \sum_{i=1}^{N} \mathcal{F}_i \tag{4.5}$$

for an ensemble of N pulsars. This procedure takes into account also weak sources, reducing the SNR of the combined statistic.

The authors in [79] define an ensemble statistic as the weighted linear combination of $\mathcal{F}_i$ statistics, optimizing the definition in [80]. They evaluated the prior distribution of the GW "strength" from each source into the ensemble and by applying the general theory of hypothesis testing, they obtained a Neyman-Pearson criterion for detecting GWs from an ensemble of pulsars. This leads to an optimal detection statistic, which in idealized situations (i.e., when prior knowledge of the signal and model for the noise are an accurate representation of reality) provides the highest detection probability with a given false-alarm probability.

The authors found that the most efficient combination entails weights a_i proportional to the expected value of the optimal SNR of each source:

$$a_i \propto \frac{f_i^4 \mathcal{K}_i}{d_i^2 \, S_n(2f_i)} \tag{4.6}$$

where f_i is the rotation frequency, d_i the distance and $\mathcal{K}_i$ is an averaged geometrical factor describing the GW polarization and orientation of the i-th pulsar.

A hierarchical Bayesian method for combining GW observations from an ensemble of known pulsars is described in [115] for two purposes: to create a detection statistic for identifying a signal from the ensemble, and to estimate the parameters of the distribution of the pulsars ellipticities. Incorporating assumed common distribution as a common prior on the ellipticity of stars, with an unknown hyperparameter, a more efficient detection statistic can be produced than combining the data for the ensemble of pulsars in a nonhierarchical way.

The authors performed a pilot search using real data for 92 pulsars from the LIGO S6 science run, with the assumption of the same two ellipticity distributions: an exponential and a half-Gaussian. They found no evidence of a signal from the ensemble, but set upper limits on the two distributions hyperparameter. These upper limits are almost 2 orders of magnitude less constraining than those that can be produced using the electromagnetically derived pulsar spin-down limits.

In the next Section, I consider an ensemble procedure similar to [79] defining a new ensemble statistic as the simple linear combination of the statistics defined by the 5-vector method.

4.2 Simplest definition of the ensemble statistic

The simplest way to define an ensemble statistic for a set of N pulsars is the linear combination of the statistics of single pulsar S_i:

$$t = \sum_{i=1}^{N} a_i S_i \tag{4.7}$$

This multiple test procedure based on the definition of a new ensemble statistic is similar to the procedure introduced in [79]. The coefficients a_i are in general unknown and should be chosen trying to maximize the detection probability.
In this Section, I describe different choices for the coefficients of the statistic t and show the corresponding detection probabilities in a specific case. I also describe the issues related to the statistic t in the case of large ensemble and few expected signals.

Theoretical choice Let us consider a random variable $Y = \sum_{i=1}^{N} a_i X_i$, that is the linear combination of N random variables X_i with unknown coefficients a_i.
Let us suppose that in the case of signal the X_i distribution is a non central-χ^2 distributions with K degrees of freedom and non-centrality parameter Λ_i (with no signal $\Lambda_i = 0$). The critical ratio CR is defined as:

$$\text{CR} = \frac{(\mu_{sig} - \mu_n)^2}{\Theta_n^2} \tag{4.8}$$

where μ_{sig} is the mean of the signal distribution of Y, while μ_n and Θ_n^2 are respectively the mean and variance of Y when there is noise only.
According to the X_i distribution, the CR is:

$$\text{CR} = \frac{(\sum_{j=1}^{N} a_j \Lambda_j)^2}{2K \sum_{k=1}^{N} a_k^2} \tag{4.9}$$

Indeed, for a generic non central-χ^2 distribution with J degrees of freedom and non-centrality parameter L, the mean value μ is:

$$\mu = J + L \tag{4.10}$$

while the variance Θ^2 is:

$$\Theta^2 = 2(J + 2L) \tag{4.11}$$

Maximizing the CR for the coefficients a_i,:

$$\begin{aligned}\frac{\partial(\mathrm{CR})}{\partial a_i} &= 2\left(\sum_{j=1}^{N} a_j\Lambda_j\right)\Lambda_i \cdot 2K\sum_{k=1}^{N} a_k^2 - \left(\sum_{t=1}^{N} a_t\Lambda_t\right)^2 \cdot 4Ka_i = 0 \\ &= 4K\left(\sum_{j=1}^{N} a_j\Lambda_j\right)\left(\Lambda_i\sum_{k=1}^{N} a_k^2 - a_i\sum_{t=1}^{N} a_t\Lambda_t\right) = 0\end{aligned} \tag{4.12}$$

It follows that there is a hyperplane where the function CR$(a_1, .., a_{N_s})$ has the maximum value:

$$a_i = \frac{\lambda_i \sum_{k=1,k\neq i}^{N} a_k^2}{\sum_{t=1,t\neq i}^{N} a_t\Lambda_t} \tag{4.13}$$

A simple choice for the coefficients $\bar{a}_i$ that maximizes the CR is:

$$\bar{a}_i = \Lambda_i\,. \tag{4.14}$$

For example, the $\mathcal{F}$-statistic has 4-D χ^2 distribution with non centrality parameter equal to the squared optimal signal to noise ratio ρ^2 in the case of signal [93]. Linearly combining the $\mathcal{F}$-statistic values from different pulsars, the coefficients that maximize the CR are $\bar{a}_i = \rho_i^2$, in agreement with [79].
If the statistic S_i is defined using the 5-vector method (Subsection 3.5.2), the statistic t can be rewritten as:

$$t = \sum_{i=1}^{N} a_i S_i = \sum_{i=1}^{N}(b_{+,i}S_{+,i} + b_{\times,i}S_{\times,i}) \tag{4.15}$$

where $S_{+/\times,i}$ are the squared modulus of the two matched filters for the i-th pulsar. $S_{+/\times,i}$ have 2-D χ^2 distributions (apart from the factor $k_{+/\times,i}$, see Equations (3.79) and (3.70)). Therefore, the coefficients that maximize the CR are:

$$\bar{b}_{+/\times,i} = \lambda_{+/\times,i} \cdot k_{+/\times,i} = \frac{|H_{+/\times,i}|^2|\mathbf{A}_i^{+/\times}|^4 H_{0,i}^2}{\sigma_i^4 \cdot T_{obs}^2} \tag{4.16}$$

These results are in agreement with [116], since the coefficients that maximize the CR for the single pulsar ($N = 1$) statistic S are $b_{+/\times} = |H_{+/\times}|^2|\mathbf{A}^{+/\times}|^4$.
If S is defined using the 5n-vector method (Subsection 3.5.3), the coefficients of t that maximize the CR are:

$$\bar{b}_{+/\times,i} = \lambda_{+/\times,i} \cdot k_{+/\times,i} = \frac{|H_{+/\times,i}|^2|\mathbf{A}_i^{+/\times}|^8 H_{0,i}^2}{(\sum_{j=1}^{n} \sigma_j^2 \cdot T_j \cdot |\mathbf{A}_{j,i}^{+/\times}|^2)^2} \tag{4.17}$$

where $|\mathbf{A}_i^{+/\times}|^2 = \sum_{j=1}^{n} |\mathbf{A}_{j,i}^{+/\times}|^2$ and T_j is the observation time in the j-th detector. As sanity check, if $n = 1$ the expression in (4.17) is equal to (4.16).
The coefficients in (4.17) depend on the polarization functions $H_{+/\times,i}$ and on the amplitude $H_{0,i}$ that are unknown in a real analysis.
The ensemble statistic with coefficients in (4.17) represents the theoretical limit that one can approach with an appropriate choice for the coefficients.

With 5-vectors In the preliminary study in [116], I proposed a joint ensemble statistic using 5-vectors and combining multi-detector statistics for single pulsar, defined as the noise-weighted sum of the detection statistics in each detector:

$$t = \sum_{i=1}^{N} \left(\sum_{j=1}^{n} \frac{1}{\sigma_j^2 \cdot T_j} \cdot S_{i,j} \right) \tag{4.18}$$

where i is the index of the pulsar and j, the index of the detector. $S_{i,j}$ is the "classic" detection statistic defined in (3.61) for the i-th pulsar in the j-th detector.

With 5n-vectors In [117], I proposed a different ensemble statistic, based on the 5n-vectors and on (4.15), considering the coefficients:

$$b_{+/\times,i} = \frac{|\mathbf{A}_i^{+/\times}|^4}{\sum_{j=1}^{n} \sigma_j^2 \cdot T_j \cdot |\mathbf{A}_{j,i}^{+/\times}|^2} \tag{4.19}$$

As described in the next Section, the coefficients in (4.19) normalize the single pulsar statistic with respect to the detectors' sensitivity and observation time. In this way, the noise distribution of this normalized single pulsar statistic is the same for each pulsar, while the signal distribution also has an analytic expression in contrast to [100, 116].

Detection probabilities comparison To test the different definitions of the t statistic, I considered a set of 100 fake pulsars. For each fake pulsar, I fixed randomly the sky position. I chose a uniform distribution for the polarization parameters, an exponential distribution for the GW frequency between 20 Hz and 120 Hz and a uniform distribution for the first derivative of the GW frequency. I ranked these signals by decreasing values of α, defined as the ratio between the injected amplitude H and the minimum detectable amplitude h_{min}:

$$H = \alpha \cdot h_{min} \approx \alpha \cdot 11 \sqrt{\frac{S(f_{gw})}{T_{obs}}} \tag{4.20}$$

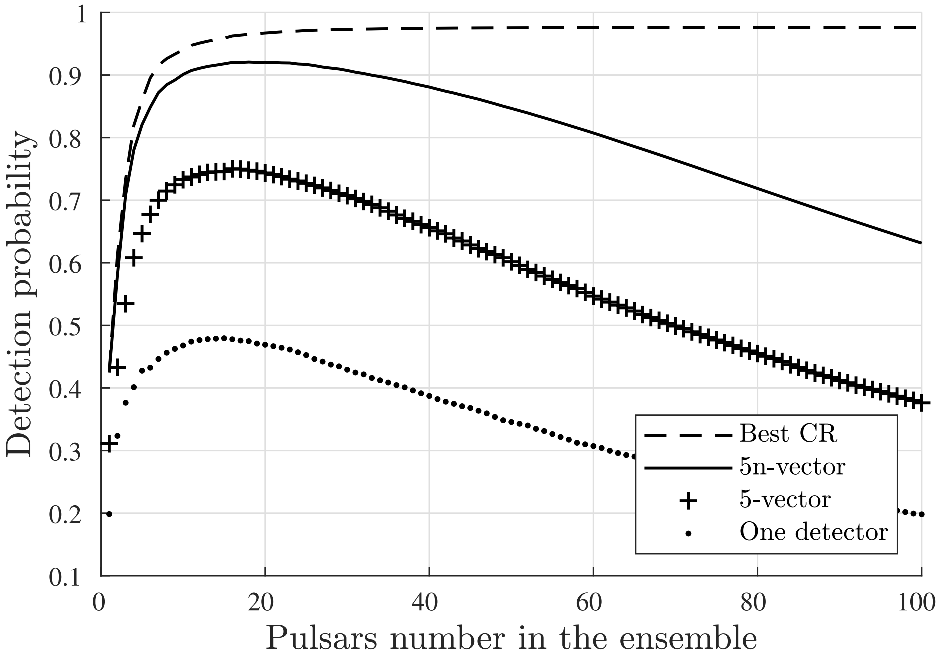

Figure 4.1: Detection probability for a fixed false alarm probability of 1% increasing the number of simulated pulsars in the ensemble and considering Gaussian noise in two detectors equal to LLO in O3a run. The injected signals are ranked by decreasing values of α (see Equation (4.20)). The dashed line is obtained considering the t definition with coefficients in (4.17), the continuous line with coefficients in (4.19), the '+' and '$\cdot$' line with the t definition using 5-vectors as in [116]. The '$\cdot$' line is obtained considering only one detector.

where $S(f_{gw})$ is the one-sided power spectral density at the expected signal frequency f_{gw}, and T_{obs} the observation time.

In Figure 4.1, I considered two ideal detectors with sensitivity and observation time equal to LLO design case for O3a run. As α prior distribution with $0.01 < \alpha < 0.6$, I chose an exponential distribution with mean value equal to 0.09.

The continuous line, obtained with coefficients in (4.19), approaches the t definition with coefficients in (4.17) and outperforms the t definition in [116]. In Figure 4.1, the detection probability increases twofold compared to single detector case and is 20% better compared to [116].

For each definition (except for the dashed line where the coefficients are amplitude-weighted), the detection probability increases with an increasing number of signals in the ensemble up to a maximum and then starts to decrease. This is linked to the prior exponential distribution that fixes the signals' “strength"; by adding smaller and smaller signals, they do not contribute to the ensemble signal but, rather, to the noise.

Problems In Figure 4.1, I ranked the pulsars in the ensemble for decreasing values of α. This allows to optimize the detection probability for each of the explored definitions since I added pulsars to the t statistic according to the "strength" of the signal. The factor α fixes the strength of the signal since it fixes the amplitude.

In a real analysis, the amplitude of the expected signal is clearly unknown. Since α is unknown, the realistic procedure is to consider the entire ensemble, i.e. the last point in Figure 4.1 for each definition. From Figure 4.1 but also theoretically, this can not be an optimal procedure since for large ensembles and for the actual detectors' sensitivity, I will expect few signals near the detection threshold.

For example, let us consider the set of 236 known pulsars used for the O3 targeted search of the LVK Collaboration [84]. Of the analyzed pulsars, only 23 pulsars have an upper limit on the amplitude that is lower than the spin-down limit. The spin-down limit is computed in the strong assumption that the pulsar radiates its rotation energy entirely in GWs (see Subsection 1.7.2).

Figure 4.1 shows that if I want to optimize the detection probability for an ensemble where there are few "strong"[1] signals, I need to define a criteria to rank pulsars and also to define an ensemble statistic as a function of the number of pulsars.

4.3 The normalized 5n-vectors

In this Section, I describe the main features of the single pulsar statistic S with the coefficients defined in (4.19):

$$\begin{aligned} S &= b_+ S_+ + b_\times S_\times = b_+ \cdot |\hat{H}_+|^2 + b_\times \cdot |\hat{H}_\times|^2 \\ &= \frac{|\mathbf{A}^+|^4}{\sum_{j=1}^{n} \sigma_j^2 \cdot T_j \cdot |\mathbf{A}_j^+|^2} |\hat{H}_+|^2 + \frac{|\mathbf{A}^\times|^4}{\sum_{k=1}^{n} \sigma_k^2 \cdot T_k \cdot |\mathbf{A}_k^\times|^2} |\hat{H}_\times|^2 \end{aligned} \tag{4.21}$$

where n is the number of considered detectors and $|\hat{H}_{+/\times}|^2$ are defined in (3.76) for the 5n-vector method. The definition in (4.21) is still valid if one detector (i.e. $n = 1$) is considered.

As shown in the previous Section, this choice of the coefficients increases the detection probability of the ensemble statistic t compared to the definitions in [116] and approaches the results of the theoretical choice in the case analyzed in Figure 4.1.

---

[1] In this contest, "strong" means near the detection threshold and individually undetectable.

The coefficients in (4.19) are equal to the inverse of the variance in (3.95):

$$b_{+/\times} = \frac{|\mathbf{A}^{+/\times}|^4}{\sum_{j=1}^{n} \sigma_j^2 \cdot T_j \cdot |\mathbf{A}_j^{+/\times}|^2} \equiv \frac{1}{\sigma_{+/\times}^2} \tag{4.22}$$

In the case of Gaussian noise and considering (3.79), the distribution of $b_{+/\times} \cdot S_{+/\times}$ is:

$$b_{+/\times} \cdot S_{+/\times} \equiv b_{+/\times} \cdot |\hat{H}_{+/\times}|^2 \sim Exp(x;1) = e^{-x} \tag{4.23}$$

The normalized statistic S is the sum of two exponential random variables with mean values equal to one. It follows that:

$$S \sim Erlang(x;2,1) = x \cdot e^{-x} \tag{4.24}$$

that is the Erlang distribution with the scale and shape parameters, equal to 2 and 1, respectively. A random variable $\mathbf{X}$ has an Erlang distribution with shape parameter α and scale parameter β if the probability distribution function is:

$$\mathbf{X} \sim Erlang(x;\alpha,\beta) = \frac{x^{(k-1)} e^{-x/\beta}}{\beta^k (k-1)!} \tag{4.25}$$

If a signal is present into the data, $b_{+/\times} \cdot S_{+/\times}$ distribution is proportional to non central-χ^2 distribution:

$$\begin{aligned} b_{+/\times} \cdot S_{+/\times} &\sim 2 \cdot \chi^2(2x;2,\lambda_{+/\times}) = \\ &= e^{-x+\frac{\lambda_{+/\times}}{2}} I_0(\sqrt{\lambda_{+/\times} 2x}) \end{aligned} \tag{4.26}$$

Therefore, the S signal distribution is the sum of two non central-χ^2 random variables that is again non central-χ^2 distributed with four degrees of freedom and non centrality parameter λ:

$$\begin{aligned} \lambda = \lambda_+ + \lambda_\times &= H_0^2 \left(k_+ \cdot |H_+|^2 + k_\times \cdot |H_\times|^2 \right) \\ &= 2 \cdot H_0^2 \left(\frac{|\mathbf{A}^+|^4 \cdot |H_+|^2}{\sum_{j=1}^{n} \sigma_j^2 \cdot T_j \cdot |\mathbf{A}_j^+|^2} + \frac{|\mathbf{A}^\times|^4 \cdot |H_\times|^2}{\sum_{k=1}^{n} \sigma_k^2 \cdot T_k \cdot |\mathbf{A}_k^\times|^2} \right) \end{aligned} \tag{4.27}$$

This is a significant result since for the normalized S statistic, the signal distribution is analytical respect to the classical definition (see Subsection 3.5.2). Analytical signal distributions can be easily and effectively used to test theoretically the sensitivity of the proposed method without considering real data.

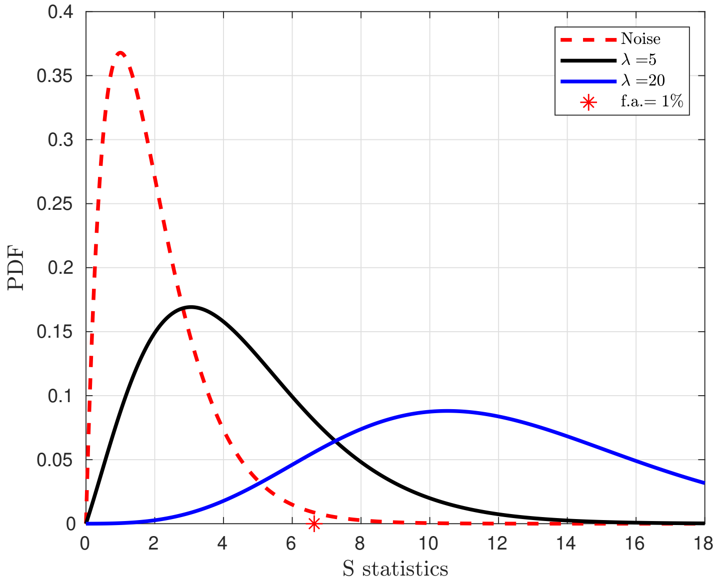

Figure 4.2: Theoretical distributions for the normalized S statistic. The red dashed line is the noise distribution (the Gamma(2,1)) while the continuous lines are two signal distributions for different λ values. The red star is the value of the detection statistic $\hat{S}$ that entails a false alarm probability of 1%, i.e. $P(S > \hat{S}|\textit{noise}) = 0.01$.

The signal distribution for the normalized S statistic is fixed by λ. According to (4.27), λ depends on the squared amplitude but also on the polarization parameters in the functions $H_{+/\times}$ and on the orientation of the j-th detector respect to the source in the $\mathbf{A}_j^{+/\times}$. In a theoretical test (see Section 5.2), I can choose different values of λ to consider different signals, without fixing amplitude, polarization parameters, sky position of the source and sensitivities of the considered detectors.

Figure 4.2 shows the noise and signal distributions for two different values of λ while Figure 4.3 shows the detection probability at the 1% false alarm probability as a function of λ.

The value of λ fixes the signal distribution and hence, the detection probability that is $P(S > \hat{S}|\text{signal})$ where $\hat{S}$ is the value that entails a false alarm of 1% (red star in Figure 4.2). For single pulsar analysis, the value of λ that entails a detection probability of 95% is almost 25.

In Section 5.2, I will describe a theoretical sensitivity test for the proposed ensemble method using the theoretical distributions for the normalized S statistic described in this Section.

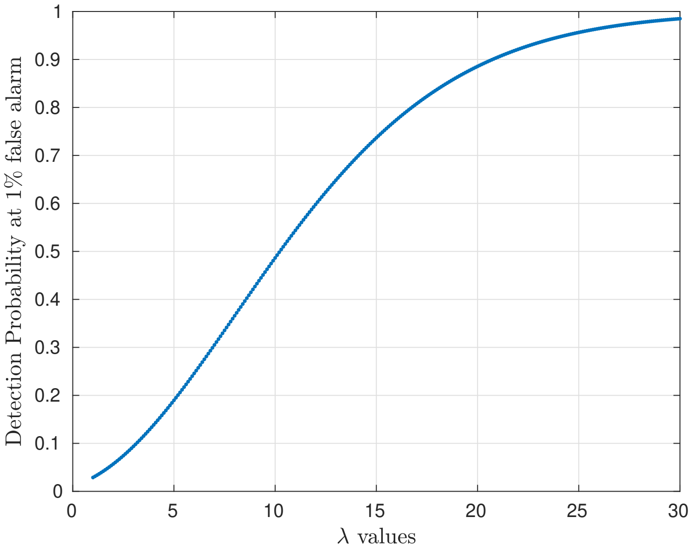

Figure 4.3: Detection probability at 1% false alarm probability for the normalized S statistic as a function of λ that fixes the signal distribution.

4.4 The rank truncation method

As shown in Figure 4.1, in order to improve the detection probability for the ensemble method, I need to rank pulsars trying to estimate each signal 'strength'. Indeed, in a real analysis the α parameter that ranks the sources in Figure 4.1 is unknown.

In [116], I used the single pulsar p-value as a statistical parameter to rank the sources in the ensemble. Nevertheless, by increasing the number of pulsars, a series of non-significant results may together suggest significance. This is the well-known look-elsewhere effect.

For a set of 100 pulsars, that means 100 measurements or points in the parameter space, I expect on average 1 p-value from single pulsar analysis below a fixed 1% threshold in the hypothesis of noise (see Figure 4.4). Hence, by considering an ensemble statistic with the simple sum of the statistics from these low p-values pulsars, I would obtain a significant result also in the noise hypothesis.

The definition of the new ensemble statistic must consider the number of trials, or rather the number of pulsars in the ensemble.

In general, the single pulsar p-value can be a statistical criteria to rank pulsars since to the smallest p-values could correspond to signals. If the noise distributions are the same (as for the normalized S statistic), ranking pulsars for increasing p-values is equal to

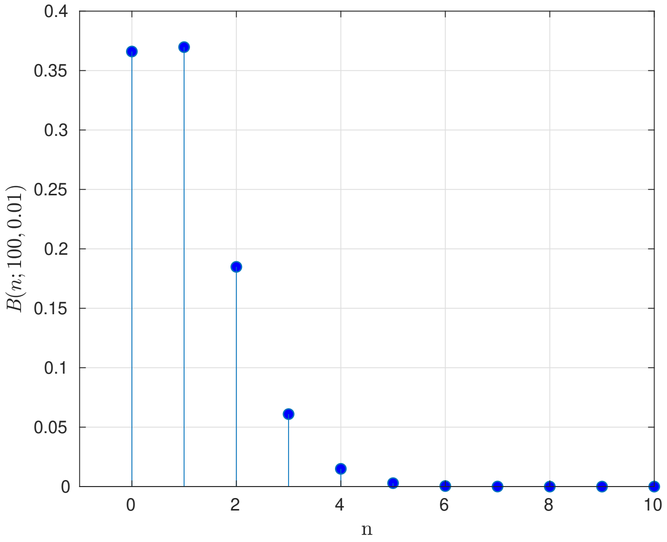

Figure 4.4: Binomial distribution $B(n;N,p)$ with $N = 100$ and $p = 0.01$. $B(n;N,p)$ is the probability to obtain n single pulsar p-values below the fixed threshold p analyzing a set of N pulsars. The mean value of this Binomial distribution is $Np = 1$.

rank pulsars for decreasing values of the single pulsar statistic:

$$\overline{S}_{(1)} < \overline{S}_{(2)} < ... < \overline{S}_{(N)} \tag{4.28}$$

By considering $\overline{S}_{(i)}$ as order statistic (see Appendix B), I can control the look-elsewhere effect since the $S_{(i)}$ distribution depends on N, the number of measured statistics (i.e the number of analyzed pulsars).

In [117], I proposed the partial sum $T(k)$ of the order statistics,

$$T(k) = \sum_{i=N-k+1}^{N} S_{(i)} \tag{4.29}$$

as the ensemble detection statistic for the rank truncation method. Indeed, the $T(k)$ distributions depend on N for each k; in this way, I combine pulsars with the smallest p-values that are assumed near the detection threshold controlling the look-elsewhere effect.

If I knew that among the N pulsars there is at most one signal, the optimal procedure to control the look-elsewhere effect would be the Šidák correction, as used in CWs narrow-band analysis [49, 88].

4.5 The statistic T(k)

In this Section, I characterize the $T(k)$ statistics trying to reconstruct the noise distributions for each value of k. Indeed, the aim is to construct a p-value of ensemble as a function of k using the $T(k)$ statistics.
The proposed ensemble statistic $T(k)$,

$$T(k) = \sum_{i=N-k+1}^{N} S_{(i)} \tag{4.30}$$

is defined as the partial sum of the order statistics for the normalized S statistic.
For $k = N$, the $T(N)$ statistic coincides with the t statistic. In this case, considering the entire set of pulsars, the order is no more important and $T(N)$ is the simple sum of the N normalized statistics. Since in the noise hypothesis $S \sim Erlang(x; 2, 1)$, the statistic $T(N)$ follows the Erlang distribution:

$$T(N) \sim Erlang(x; 2 \cdot N, 1) \tag{4.31}$$

that is a Gamma distribution with integer shape and scale parameters. For $k = 1$, $T(1)$ is the largest order statistic of an $Erlang(2, 1)$ random variable since $T(1) = \overline{S}_{(N)}$. From order statistic theory (see Appendix B), the distribution $f_N(x)$ of the largest order statistic is

$$f_N(x) = \frac{dF_N(x)}{dx} = N \cdot [F(x)]^{(N-1)} \cdot f(x) \tag{4.32}$$

where $F(x)$ and $f(x)$ are the cumulative distribution function (cdf) and the probability distribution function (pdf) of the starting statistic. Since in the noise hypothesis $S \sim Erlang(x; 2, 1)$,

$$T(1) \sim N \cdot [1 - xe^{-x}]^{(N-1)} \cdot xe^{-x} \tag{4.33}$$

see Figure 4.5. $k = 1$ and $k = N$ are special cases where the distributions of the $T(k)$ statistic are analytical.
In the general case $1 < k < N$, the convolution of order statistics has no simple expression. The complexity of the analytic form of $T(k)$ is due to the dependency introduced by ordering the p-values (i.e. the statistics values): when the $(k+1)$-th p-value, that is a random variable, happens to be relatively small, the k smallest p-values have to squeeze into a relatively tiny interval from zero to that value.
In [118], the authors analyzed the distribution of the sum of the largest order statistics from Gamma random variables with n degrees of freedom (rate parameter equal to 1). If n is integer, the pdf and cdf are given by a finite sum of Gamma densities (see Equation

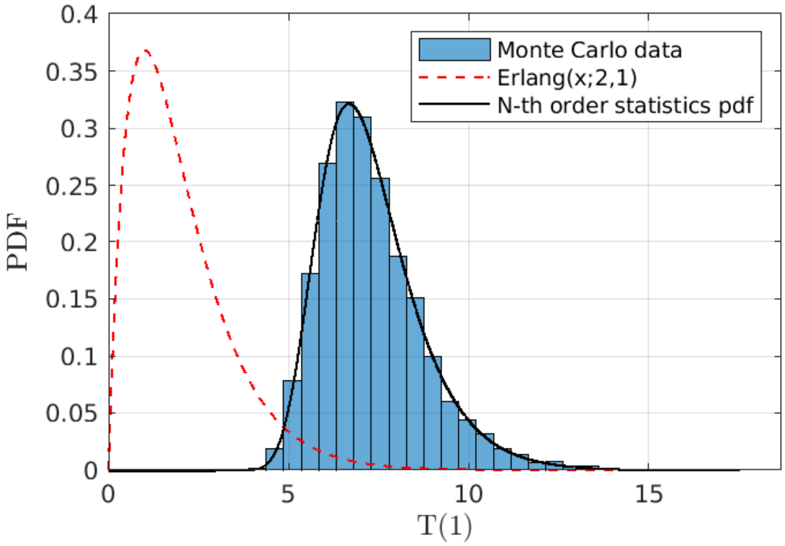

Figure 4.5: Noise distribution (blue histogram) for $T(1)$ and inferred using the Monte Carlo algorithm described in Subsection 4.5.1. The dashed line is the single pulsar noise distribution using the normalized statistic. The continuous line is the theoretical probability distribution function for the largest order statistic for $N = 100$ defined in (4.33).

(2.6) in [118]). However, this expression is quite complicated.

In the next Subsection, I use a Monte Carlo algorithm to recover the $T(k)$ noise distributions as a function of k.

4.5.1 Noise distribution

To describe the Monte Carlo algorithm, first I consider the case of Gaussian noise with zero mean value (i.e. $S \sim Erlang(x; 2, 1)$).

To infer the $T(k)$ noise distribution for an ensemble of N pulsars, I propose the following procedure.

1. Generate an $Erlang(x; 2, 1)$ distribution with 200 000 points to simulate the noise distribution of single pulsar.
2. Select randomly N points to simulate an ensemble detection.
3. Rank for decreasing values these N points (that is for increasing p-values).
4. Repeat steps $1 - 3$, M times (e.g. $M = 10\,000$).

The variable $T(k)$ is the sum of the k largest points selected each times. In this way, I can reconstruct the distribution of $T(k)$ for each value of k with M (that is a tunable parameter) points.

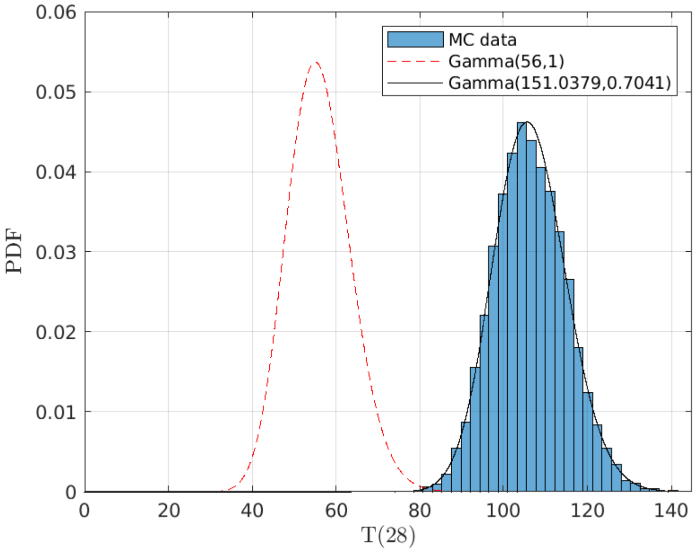

Figure 4.6: Noise distribution (blue histogram) for $T(28)$ inferred using the Monte Carlo algorithm described in Subsection 4.5.1. The dashed line is the distribution of the simple sum of 28 Erlang random variables. The continuous line is the fitted Gamma distribution to the histogram.

The described procedure can be generalized to real data starting the Monte Carlo algorithm from the N different experimental distributions for the S statistic. Empirically, I have found that a Gamma function can fit the distribution to a good approximation for all values of k, see Figure 4.6.

As shown in Figure 4.7, the distribution of $T(N)$ coincides with the distribution of t, since the shape parameter approaches $2N = 200$ and the scale parameter tends towards 1, as expected. The fitting parameters in Figure 4.7 depend only on N, the number of considered pulsars and clearly on the assumption of Gaussian noise for the detectors' data.

4.5.2 P-value of ensemble

Reconstructing the $T(k)$ noise distributions for each k, I can compute the p-value of ensemble as a function of k. In Section 5.2, I will show the improvement in the detection probability respect to the single pulsar analysis.

Fixing a set of N sources, I compute the N p-values from the single pulsar analysis and then, defining the $T(k)$ statistic, a p-value of ensemble as a function of k. It is important to stress that k is the number of order statistics rather than the number of pulsars with the k smallest p-values.

For example, let us consider an ensemble of 100 pulsars and suppose that for $k = 10$, the

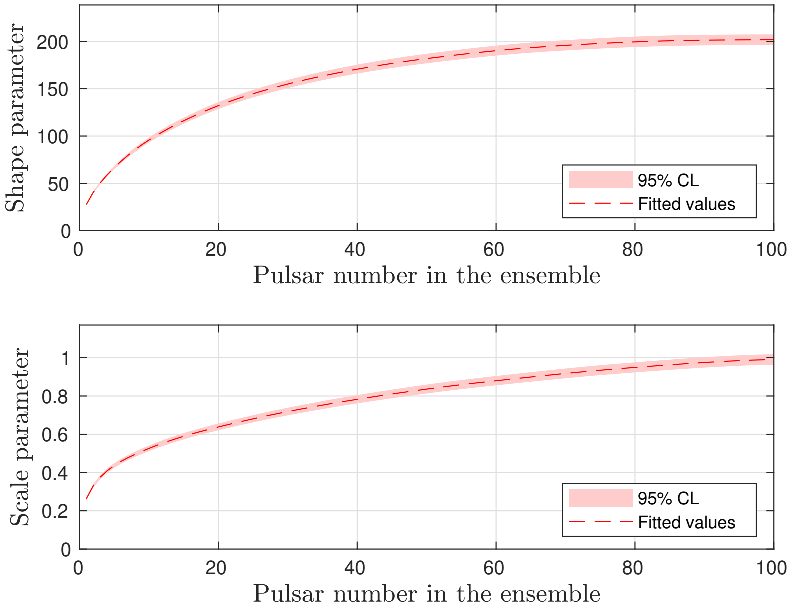

Figure 4.7: Shape and scale parameters as a function of k, inferred from the fit to the $T(k)$ noise distributions from the Monte Carlo algorithm using a Gamma distribution. The coloured region shows the 95% confidence interval for the fitted parameter.

p-value of ensemble for the $T(10)$ statistic is well below a fixed false alarm threshold, e.g. 1%:

$$P\left(T(10) > \overline{T}(10)|\text{noise}\right) \ll 1\% \tag{4.34}$$

where $\overline{T}(10)$ is the detected value of $T(10)$ according to the single pulsar analysis.
Can I infer the detection of a CW signal from each of the 10 pulsars with the smallest p-values? Following [119], I suggest that the answer to this question is no. Indeed, the p-value is computed from the noise distribution of $T(10)$, that is the sum of the 10 largest order statistics. This means that the $T(10)$ distribution is computed from the N different distributions from each pulsar.
It follows that, even though I have defined a p-value of ensemble as a function of k, the statistical inference concerns the entire set of considered pulsars. The claim of a rank truncation method is the same of the Fisher's combination test that there are some effects among all the N tests, regardless that a certain $k < N$ led to a rejection.
Assuming that H_i is the null hypothesis for the i-th pulsar, the p-values for the $T(k)$ statistics test the overall hypothesis that each H_i is true.

4.5.3 Signal distribution

In the hypothesis of Gaussian noise, the signal distribution for the normalized single pulsar statistic is a non-central χ^2 distribution with four degrees of freedom and non-centrality parameter λ, defined in (4.27), that fixes the "strength" of the signal.
First, let us consider $k = N$. In this case, the order is no important since I am considering the entire set of pulsars. $T(N)$ can be defined as the sum of N non-central χ^2 distributions. It follows that:

$$T(N) \sim \chi^2(x; 4N, \Lambda) \tag{4.35}$$

The non-centrality parameter Λ for $T(N)$ is the sum of the non-centrality parameters λ_i from the i-th pulsar:

$$\Lambda = \sum_{i=1}^{N} \lambda_i = \sum_{i=1}^{N} 2 \cdot H_{0,i}^2 \left(\frac{|\mathbf{A}_i^+|^4 \cdot |H_{+,i}|^2}{\sum_{j=1}^{n} \sigma_j^2 \cdot T_j \cdot |\mathbf{A}_{j,i}^+|^2} + \frac{|\mathbf{A}_i^\times|^4 \cdot |H_{\times,i}|^2}{\sum_{k=1}^{n} \sigma_k^2 \cdot T_k \cdot |\mathbf{A}_{k,i}^\times|^2} \right) \tag{4.36}$$

Λ fixes the $T(N)$ distribution univocally and depends on the weighted sum of the squared amplitudes.
For a generic value of k, I have to consider the convolution of the k largest order statistics for non-central χ^2 random variables.
To reconstruct the $T(k)$ signal distributions for each k, I propose a Monte Carlo algorithm similar to the procedure described for the noise distribution:

1. Fix the value of λ for each pulsar.
2. Generate N non-central χ^2 distributions with $200\,000$ points with the appropriate λ to simulate individual signal distributions.
3. Select randomly N points, one from each distribution to simulate an ensemble detection.
4. Rank for decreasing values these N points (that is for increasing p-values).
5. Repeat steps $2 - 5$, M times (e.g. $M = 10\,000$).

Reconstructing the $T(k)$ signal distributions is important to compute the detection probability for the ensemble procedure as a function of k, as described in Section 5.2.
The procedure can be generalized to real data starting the Monte Carlo algorithm from the N different experimental signal distributions for the S statistic.

4.6 Upper limit of ensemble

In the single pulsar analysis, if the p-value is consistent with the noise hypothesis, it is possible to set the upper limit on the amplitude using a mixed frequentist-Bayesian approach, as described in Subsection 3.5.5.

For the classical definition of the statistic S, the signal distribution is not analytical. Marginalizing on the polarization parameters and using the linearity of the 5-vectors, it is possible to reconstruct the signal distribution for different values of the amplitude.

The posterior distribution on the amplitude H_0, given the measured value $\bar{S}$ of the detection statistic, is:

$$P(H_0|\bar{S}) = \frac{L(\bar{S}|H_0)\pi(H_0)}{\int L(\bar{S}|H_0')\pi(H_0')dH_0'} \tag{4.37}$$

where $L(\bar{S}|H_0)$ is the likelihood (the value of the signal distribution at $\bar{S}$), $\pi(H_0)$ the prior on the amplitude and $\int L(\bar{S}|H_0')\pi(H_0')dH_0'$ the evidence.

Introducing the normalized S statistic, the signal distribution is analytical and fixed by the non-centrality parameter λ.

Marginalizing over the polarization parameters, λ is $\propto H_0^2$ (the other parameters are known for targeted search). Since $H_0 > 0$, the signal distribution is fixed by H_0 validating the procedure in Subsection 3.5.5.

Assuming Gaussian noise, an upper limit can be also set on the λ parameter without marginalizing over the polarization parameters, just replacing H_0 with λ in (3.87).

The ensemble analysis, using the $T(k)$ statistic, computes a p-value of ensemble for each value of k. This Section explores the possibility to set upper limit using the ensemble statistic in the case of no detection.

The upper limit must be set on population parameters since from a multiple test, I can not infer statistical information about the single pulsar parameters. This is clear considering Gaussian noise and the Λ parameter that is the sum of the non-centrality parameters λ_i of single pulsar. Indeed, different combinations of λ_i could entail the same value of Λ, i.e. different weighted combinations of the squared amplitudes could have the same value. For this reason and also because the $T(k)$ signal distributions are not analytical, the entire set of pulsars and the $T(N)$ statistic should be considered.

In the next Subsections, I describe two different approaches; first, considering the upper limit on a population parameter that fixes the $T(N)$ distribution, then two independent hierarchical procedures to constrain the value of an hyper-parameter for the assumed common distribution for the amplitudes (or for the ellipticities).

4.6.1 Λ parameter

The ensemble parameter that fixes the $T(N)$ signal distribution is Λ defined in (4.36).
I can use a Bayesian framework and the measured value $\overline{T}(N)$ to set the upper limit on the Λ parameter:

$$P(\Lambda|\overline{T}(N)) = \frac{L(\overline{T}(N)|\Lambda)\Pi(\Lambda)}{\int L(\overline{T}(N)|\Lambda')\Pi(\Lambda')d\Lambda'} \tag{4.38}$$

where $L(\overline{T}(N)|H_0)$ is the likelihood (the value of the signal distribution at $\overline{T}(N)$), $\Pi(H_0)$ the prior on the amplitude and $\int L(\overline{T}(N)|H_0')\pi(\Lambda')d\Lambda'$ the evidence. From the measured value of the ensemble statistic, I can estimate the value $\Lambda^{95\%}$ that entails a detection probability of 95%, $P(\Lambda > \Lambda^{95\%}|\overline{T}(N)) = 0.95$.
The definition of Λ can be written as:

$$\Lambda = \sum_{i=1}^{N} H_{0,i}^2 \cdot f_i(\eta, \psi). \tag{4.39}$$

where the terms f_i are:

$$f_i(\psi, \eta) = 2 \cdot \left(\frac{|\mathbf{A}_i^+|^4 \cdot |H_{+,i}|^2}{\sum_{j=1}^{n} \sigma_j^2 \cdot T_j \cdot |\mathbf{A}_{j,i}^+|^2} + \frac{|\mathbf{A}_i^\times|^4 \cdot |H_{\times,i}|^2}{\sum_{k=1}^{n} \sigma_k^2 \cdot T_k \cdot |\mathbf{A}_{k,i}^\times|^2} \right) \tag{4.40}$$

The coefficients $f_i(\psi, \eta)$ depend on the polarization parameters ψ and η in the polarization functions $|H_{+/\times,i}|^2$. Assuming a uniform distribution for $\cos(\iota)$ and ψ, I can consider an averaged value $\overline{f_i}$ for each $f_i(\psi, \eta)$. It follows that:

$$\Lambda \approx \sum_{i=1}^{N} H_{0,i}^2 \cdot \overline{f_i} \tag{4.41}$$

From the relation in (4.41), $\Lambda^{95\%}$ can be used to constrain, for example, the sum of the weighted squared amplitudes.
It is also possible to return information about global parameters depending on some assumptions for the single pulsars amplitudes.

- Assuming an equal amplitude $\overline{h}$ for each pulsar in the ensemble,

$$\Lambda \approx \overline{h}^2 \cdot \sum_{i=1}^{N} \overline{f_i} \tag{4.42}$$

I can constrain the value $\overline{h}$ using $\Lambda^{95\%}$:

$$\overline{h} \approx \sqrt{\frac{\Lambda^{95\%}}{\sum_{i=1}^{N} \overline{f_i}}} \tag{4.43}$$

- Assuming that each amplitude is a multiple of the single pulsar upper limit with a common factor δ:

  $$\Lambda \approx \delta^2 \cdot \sum_{i=1}^{N} (\mu_{H_0,i})^2 \overline{f_i} \tag{4.44}$$

  where $\mu_{H_0,i}$ is the upper limit on the amplitude for the i-th pulsar. It follows that:

  $$\delta \approx \sqrt{\frac{\Lambda^{95\%}}{\sum_{i=1}^{N} (\mu_{H_0,i})^2 \overline{f_i}}} \tag{4.45}$$

- Since $\Lambda = \sum_{i=1}^{N} \lambda_i$ where $\lambda_i = H_{0,i}^2 \cdot \overline{f_i}$ is the parameter that fixes the signal distribution for the i-th pulsar, I can also consider an averaged $\overline{\lambda}$:

  $$\overline{\lambda} = \frac{\sum_{i=1}^{N} \lambda_i}{N} \tag{4.46}$$

  and constrains the amplitudes using $\Lambda^{95\%}$:

  $$\overline{H}_{0,i} = \sqrt{\frac{\Lambda^{95\%}}{N \cdot \overline{f_i}}} \tag{4.47}$$

- Assuming that only the j-th pulsar emits CWs. In this case, $\Lambda = \lambda_j$ and

  $$\overline{H}_{0,j}^{(1)} = \sqrt{\frac{\Lambda^{95\%}}{\overline{f_j}}} = \sqrt{N} \cdot \overline{H}_{0,j} \tag{4.48}$$

The described procedure works in case of Gaussian noise where the $T(N)$ signal distribution is analytical. In the case of real data, the $T(N)$ distribution inferred from the Monte Carlo procedure can be different. For a large ensemble of pulsars and using a multidetector analysis, I expect that the Gaussian noise could be a reasonable approximation.

4.6.2 Hierarchical Bayesian method

Hierarchical Bayesian inference (see Appendix C) allows to study population properties of the analyzed ensemble of pulsars [120].
Assuming a common distribution for the amplitudes (or the ellipticities) of the pulsars in the ensemble, it is possible to set upper limits on the hyperparameter that fixes the assumed common distribution.
Let us consider an ensemble of N pulsars and a common distribution fixed by the hyperparameter μ_α for the set of amplitudes H_i where $i = 1, .., N$.
Let $\overline{T}(N)$ be the measured value of the ensemble statistic according to the analyzed data. I can constrain the value of the hyperparameter μ_α considering the posterior pdf inferred from a Bayesian procedure:

$$P(\mu_\alpha|\overline{T}(N)) \propto L(\overline{T}(N)|\mu_\alpha)\Pi(\mu_\alpha) \tag{4.49}$$

$\Pi(\mu_\alpha)$ is the prior distribution on the hyperparameter while the likelihood $L(\overline{T}(N)|\mu_\alpha)$ can be defined as the value of the signal distribution for $T(N)$ at the value $\overline{T}(N)$ if the common distribution of the amplitudes is fixed by the hyperparameter μ_α. The $T(N)$ signal distribution and hence, the likelihood, is fixed by Λ:

$$L(\overline{T}(N)|\mu_\alpha) = \int L(\overline{T}(N)|\Lambda)\Pi(\Lambda|\mu_\alpha)d\Lambda \tag{4.50}$$

From the definition in (4.36), deducing the analytical prior on Λ for an assumed exponential distribution of the amplitudes with hyperparameter μ_α is not straightforward.
For the Central Limit Theorem, it is possible to approximate this prior with a Gaussian distribution with appropriate mean and variance that depend on μ_α. Indeed, if $H_i \sim Exp(x; \mu_\alpha)$, Λ is the sum of N squared exponential random variables and for $N \gg 1$ the prior can be approximated with a Gaussian distribution where the mean is the weighted sum (with coefficients $\bar{f}_i$) of the mean values for the squared exponential random variables. I will describe an example in Section 5.3.
Differently, I can also consider:

$$L(\overline{T}(N)|\mu_\alpha) = \int L(\overline{T}(N)|H_1, .., H_N)\Pi(H_1, .., H_N|\mu_\alpha)dH_1..dH_N \tag{4.51}$$

where since the H_i are independent:

$$\Pi(H_1, .., H_N|\mu_\alpha) = \prod_{i=1}^{N} \Pi(H_i|\mu_\alpha) \tag{4.52}$$

The order in the parameters $H_1, .., H_N$ in $L(\overline{T}(N)|H_1, .., H_N)$ is important because to fix the signal distribution you need to consider the value H_1 for the first pulsar, H_2 for the second and so on. Indeed, Λ is the weighted sum of the squared amplitudes with weights that depend on the sky position and on the detectors sensitivity at the expected GW frequency for each pulsar. It follows that:

$$P(\mu_\alpha|\overline{T}(N)) \propto \left[\int L(\overline{T}(N)|H_1, .., H_N) \left(\prod_{i=1}^{N} \Pi(H_i|\mu_\alpha) \right) dH_1..dH_N \right] \Pi(\mu_\alpha) \quad (4.53)$$

In this case, since N could be large (order of hundreds) the posterior in (4.53) involves a large number of integrals and to explore a large prior volume all at once.
To solve this problem, I can consider a classic hierarchical procedure where the integral is broken into individual integrals for each event. This corresponds to consider:

$$L(\overline{T}(N)|H_1, .., H_N) \approx \prod_{i=1}^{N} L(\overline{S}_i|H_i) \quad (4.54)$$

where $\overline{S}_i$ is the measured value of the statistic S_i for the i-th pulsar and $\overline{T}(N) = \sum_{i=1}^{N} \overline{S}_i$.
The posterior is:

$$P(\mu_\alpha|\overline{S}_1, .., \overline{S}_N) \propto \left(\prod_{i=1}^{N} \int L(\overline{S}_i|H_i)\Pi(H_i|\mu_\alpha)dH_i \right) \Pi(\mu_\alpha) \quad (4.55)$$

It is difficult to evaluate the approximation in (4.54). The $T(N)$ signal distribution is the convolution of the S_i signal distributions since $T(N) = \sum S_i$ that can be very different from the simple product.
The posterior in (4.55) is independent from the ensemble procedure that I have described in this Chapter and is similar to what is proposed in [115]. It does not depend on the Gaussian noise hypothesis and it can be used to constrain the hyperparameter μ_α using the likelihood $L(\overline{S}_i|H_i)$ computed for the i-th pulsar analysis.

Chapter 5

Method validation

In Chapter 3, I have described the 5-vector method pipeline for the single pulsar targeted search while in Chapter 4, I have introduced the $T(k)$ statistics and the rank truncation method to optimize the detection probability for an ensemble of known pulsars.

In this Chapter, I describe the sensitivity tests that I performed for the single pulsar analysis and for the proposed ensemble procedure using the $T(k)$ statistics to validate the proposed pipeline.

In Section 5.1, first I describe how to reconstruct the noise distribution for the statistic S for the single pulsar targeted search. Then, considering the hardware injections in the O3 data for the LIGO detectors, I test the single pulsar analysis procedure estimating the intrinsic parameters also using a mixed frequentist-Bayesian method (as for the upper limit computation).

In Section 5.2, I show the improvement in the detection probability for an ensemble of pulsars with the $T(k)$ statistics using theoretical tests and also hardware/software injections in the O3 dataset of the LIGO detectors.

In Section 5.3, I test the upper limit procedures described in Section 4.6 on the global parameter Λ and on the hyper-parameter of the assumed common distribution for the amplitudes/ellepticities.

5.1 Tests of the single pulsar analysis

The normalized detection statistic S, introduced in this thesis and defined in Equation (4.21), entails a common theoretical noise distribution - $Gamma(x; 2, 1)$ - for any pulsar. From the normalized detection statistic, I can introduce the ensemble statistics $T(k)$ and compute the ensemble p-value.

In this Section, first I describe the "off-source frequencies" method to reconstruct the experimental noise distribution for the S statistic. Then, I report different tests of the

5-vector pipeline based on the detection of hardware injections. I also provide an independent estimation of the amplitude using the posterior pdf, used for the upper limit computation.

5.1.1 Experimental noise distribution

In general, detectors data can show departure from Gaussianity and the theoretical noise distribution for the detection statistic can not be used for the p-value or upper limit computation. Indeed, the theoretical distribution is inferred in the hypothesis of stationary and Gaussian noise for the detectors' data.

Using the BSD files and the related libraries, it is possible to select and organize the data in small frequency band around the expected GW frequency in order to reduce the amount of data to analyze and hence, the computational cost of the analysis. Below ≈ 80 Hz, large disturbances (or vetted lines) can influence the data in the selected frequency band; when the Gaussian hypothesis does not hold, it is important to reconstruct the distribution of the detection statistic from the data itself.

The experimental noise distribution for the detection statistic can be built from the data itself considering a range of off-source frequencies near but different from the one where the signal is supposed to be [49]. For each of the selected off-source frequencies, that means for each of the selected bins in the frequency domain, I compute the value of the S statistic using the 5-vectors. In this way, I reconstruct the experimental noise distribution for the statistic.

The general procedure to reconstruct the experimental distribution can be summarised in the following steps:

- From the BSD files, extract a sub-band around the expected GW frequency
- Bands with known lines are excluded (not considering the corresponding bins)
- Bands with unidentified lines are excluded (± 0.01 Hz)
- Consider a band around the expected GW frequency and select randomly a set of off-source frequencies
- For each off-source frequency, compute the value of the detection statistic

The procedure can be slightly different if small datasets are considered. For example, if I analyzed the entire O3 dataset, the frequency resolution would be $\approx 10^{-8}$ Hz and there would be enough points (i.e. off-source frequencies) to accurately reconstruct the noise distribution considering frequency band of ≈ 0.1 Hz.

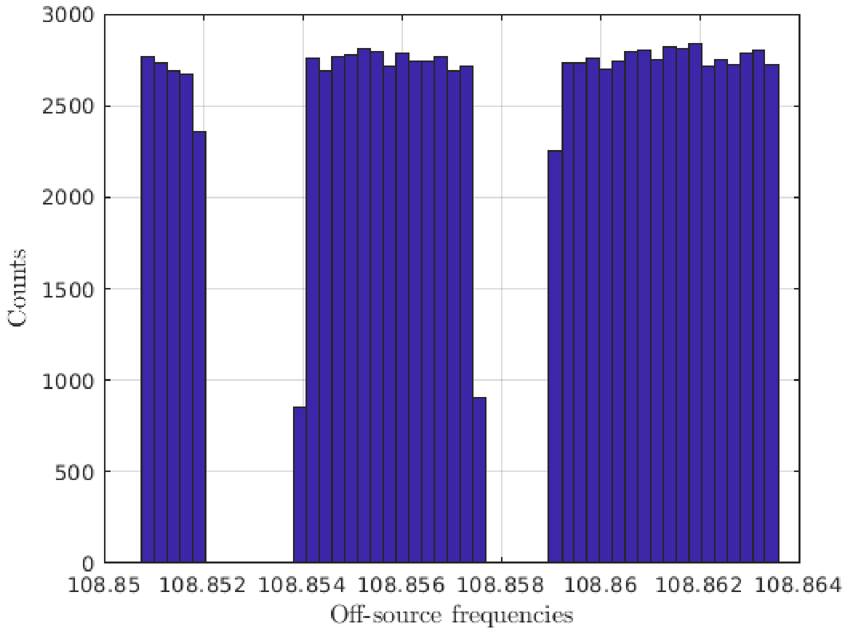

Figure 5.1: Test of the veto procedure introduced in this thesis. For the BSD frequency band [108.7838; 108.9189] Hz (in the case of the hardware injection P03, see Subsection 5.1.2), I add to the file with the known lines provided by the LVK Collaboration, two fake frequency bands to veto: [108.8520; 108.8540] Hz and [108.8575; 108.8590] Hz. The Figure shows the histogram of the off-source frequencies used to reconstruct the S noise distribution and selected by the veto procedure.

On the contrary, analyzing one day-long datasets I could fix 1 Hz-wide frequency band to have at least 86400 points to reconstruct the distribution.

The veto method for the known and unidentified lines has been introduced in this thesis. A MATLab function performs the veto, reading the file provided by the LVK Collaboration of the frequency bands with vetted lines and excluding these bands from the selected off-source frequencies.

A test for the veto procedure is described in Figure 5.1, where fake bands to veto have been added in the file provided by the LVK to test the MATLab function. Figure 5.1 shows the histogram of the chosen off-source frequencies to reconstruct the experimental noise distribution.

5.1.2 Hardware injections

Hardware injections are simulated signals added to the detectors data physically displacing the detectors' test masses [121]. Differential displacement of the test masses mimics the detectors' response to a GW signal. Continuous hardware injections can be

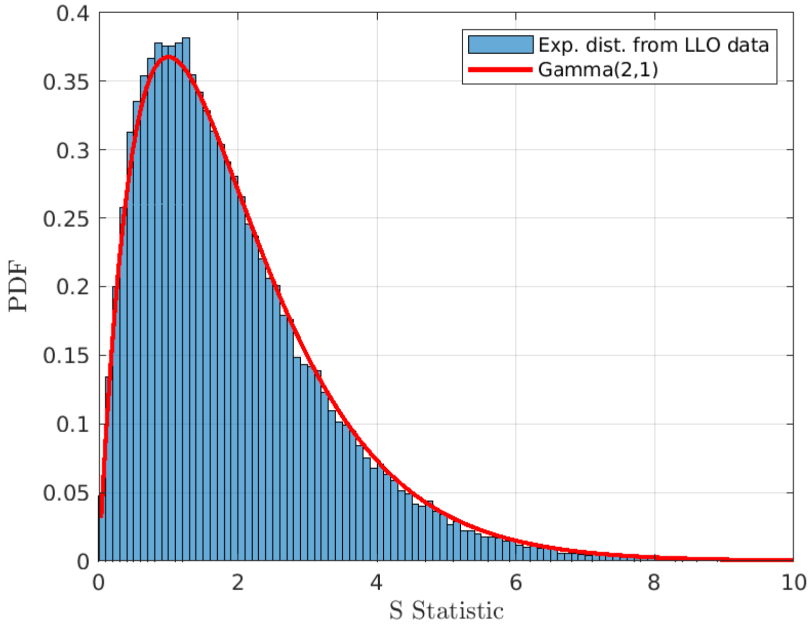

Figure 5.2: Experimental noise distribution (blue histogram) for the normalized single pulsar statistic for the P03 inferred from a set of off-source frequency around the expected GW frequency. The red line is the theoretical noise distribution - $Gamma(x; 2, 1)$ - for stationary Gaussian noise.

used to test CW analysis methods.

During the O3 run, 17 hardware injections that simulate different CW signals from spinning neutron stars were added in the two LIGO detectors. The list of injected pulsar parameters can be found in [122]. For Virgo, no CW injections were performed during O3 (there were some injections during O3b but the signal was removed a posteriori in the strain data).

In this Section, I consider two different hardware injections to test the 5-vector pipeline. I report the results for the injected pulsar P03 (SNR(1 yr) $\approx$ 30) that simulates an isolated spinning neutron stars with $f_{gw} \simeq 108.8$ Hz and for P16 (SNR(1 yr) $\approx$ 68), a neutron star in binary system with $f_{gw} \simeq 234.5$ Hz.

I use the normalized detection statistic defined in (4.21) that entails the $Gamma(x; 2, 1)$ as noise distribution in the hypothesis of stationary Gaussian noise.

As shown in Figure 5.2 for PO3 and LLO O3 data, the experimental S noise distribution is in good agreement with the $Gamma(x; 2, 1)$ distribution, showing that in the selected frequency band (0.2 Hz wide), the noise is Gaussian distributed.

Figures 5.3 and 5.4 show the amplitude spectral density in the frequency band around the expected GW frequency for P03 (the same for P16 in Figure 5.5 and 5.6) and for each detector after the Doppler and spin-down corrections using the BSD heterodyne

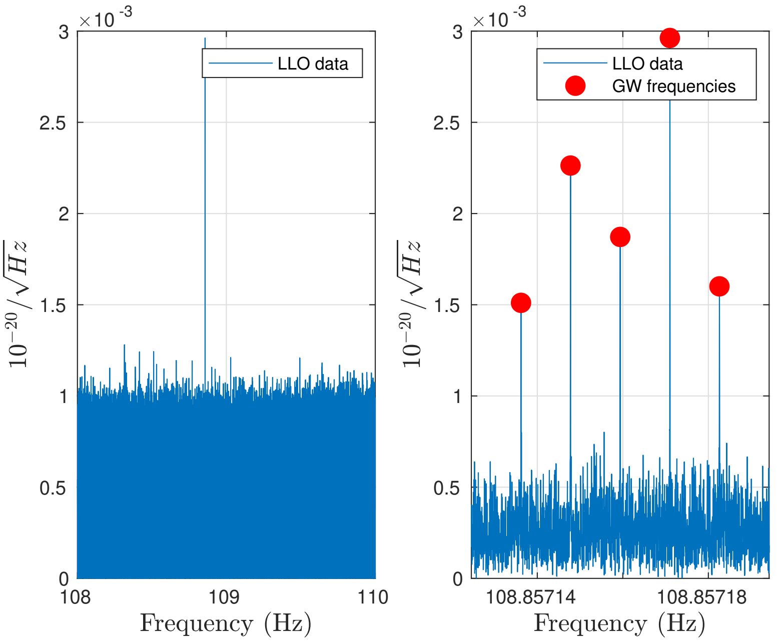

Figure 5.3: Amplitude spectral density for P03 and LLO data after the corrections for Doppler and spin-down effect. The right plot is the zoom around the GW frequency; the red dots show the expected 5 frequencies due to the Earth sidereal motion. Central peak frequency is the expected GW frequency.

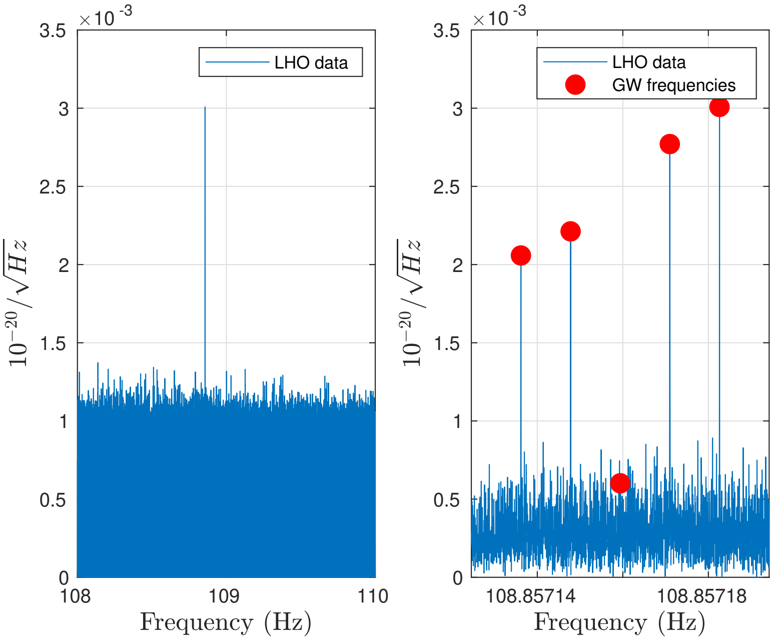

Figure 5.4: Amplitude spectral density for P03 and LHO data after the corrections for Doppler and spin-down effect. The right plot is the zoom around the GW frequency; the red dots show the expected 5 frequencies due to the Earth sidereal motion. Central peak frequency is the expected GW frequency.

Hardware Injection	Detector	ϵ_{H_0}	ϵ_{η}	ϵ_{ψ}
P03	LLO	0.93	0.54%	1.49%
	LHO	0.95	1.27%	0.39%
P16	LLO	0.91	0.66%	-
	LHO	0.93	0.90%	-

Table 5.1: Table of the parameters mismatch for the hardware injections P03 and P16 analyzing O3 data from the two LIGO detectors.

method. The red dots are the theoretical expected 5 frequency peaks for the GW signal due to the sidereal modulation. The different "heights" of corresponding peaks in the two detectors depend on the antenna pattern, i.e. on the signal 5-vector templates $\mathbf{A}^{+/\times}$. It is important to note that the formalism used to construct the hardware injections' signal is independent from the 5-vector method.

In Table 5.1, there are the results obtained for the two hardware injections considering the O3 datasets of the two LIGO detectors. The estimation of the intrinsic parameters (see Subsection 3.5.1) is not influenced by the choice of the detection statistic since it depends only on the estimators $\hat{H}_{+/\times}$.

The parameter mismatch definition depends on the considered parameter:

- ϵ_{H_0} is the ratio between the estimated $\hat{H}_0$ and injected amplitude H_0,

$$\epsilon_{H_0} = \frac{\hat{H}_0}{H_0} \tag{5.1}$$

- ϵ_{η} is the normalized relative errors, defined as:

$$\epsilon_{\eta} = \left| \frac{\eta - \hat{\eta}}{(\eta_{max} - \eta_{min})} \right| = \left| \frac{\eta - \hat{\eta}}{2} \right| , \tag{5.2}$$

  that is normalized in such a way that the maximum relative error between two values is 1 (in fact $\eta_{max} = +1$ and $\eta_{min} = -1$)

- the normalized relative error ϵ_{ψ} will be:

$$\epsilon_{\psi} = \left| \frac{\psi - \hat{\psi}}{(\psi_{max} - \psi_{min})} \right| = \left| \frac{\psi - \hat{\psi}}{\pi} \right| . \tag{5.3}$$

  since $\psi_{max} = \pi/2$ and $\psi_{min} = -\pi/2$.

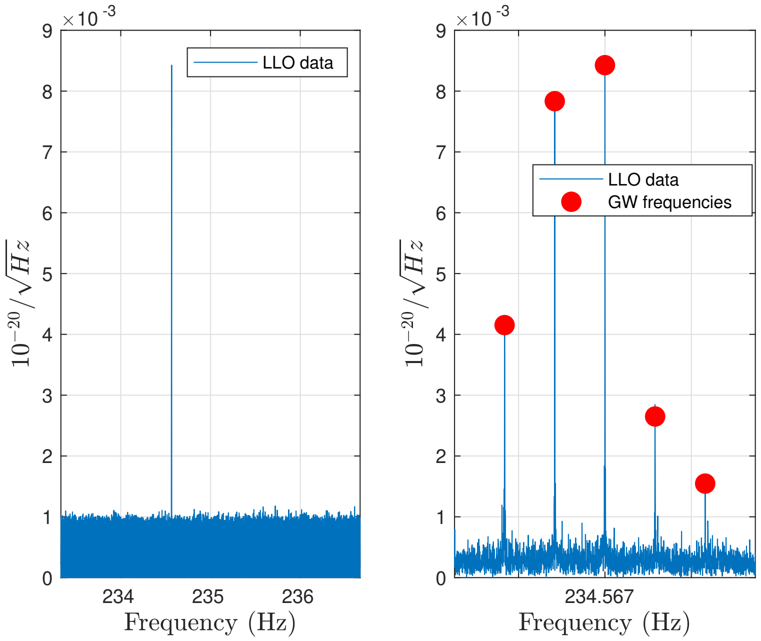

Figure 5.5: Amplitude spectral density for P16 and LLO data after the corrections for Doppler and spin-down effect. The right plot is the zoom around the GW frequency; the red dots show the expected 5 frequencies due to the Earth sidereal motion. Central peak frequency is the expected GW frequency.

The small discrepancies (below 10%) in Table 5.1 for the amplitude fall within the uncertainties of the actuation system used for the injections. For P16, the ψ parameter is not well defined, since $\eta \approx 1$ and the signal is circularly polarized.

5.1.3 Posterior pdf

In Subsection 3.5.5, I have described the hybrid Bayesian procedure for the computation of the upper limit on the amplitude using the 5-vector method.
The posterior, defined in Equation (3.87), is

$$P(H_0|\overline{S}) = \frac{L(\overline{S}|H_0)\Pi(H_0)}{\int L(\overline{S}|H_0')\Pi(H_0')dH_0'} \tag{5.4}$$

where $\overline{S}$ is the measured value of the detection statistic.
I can use the posterior $P(H_0|\overline{S})$ to compute an independent estimation of the amplitude as in [121]. Indeed, since for the hardware injection the SNR is high considering the entire O3 dataset, I expect that the posterior should be peaked near the injected value. This is also an indirect test for the upper limit computation since an accurate reconstruction of the posterior entails an accurate computation of the upper limit.

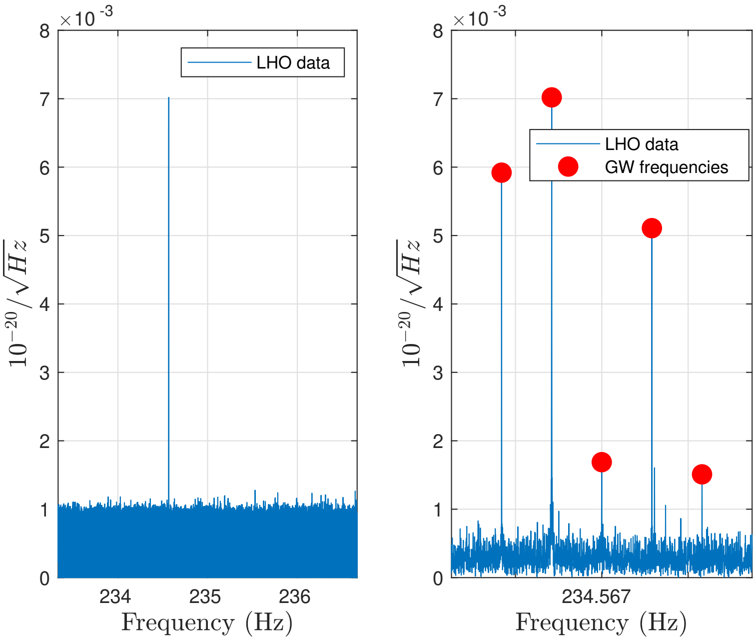

Figure 5.6: Amplitude spectral density for P16 and LHO data after the corrections for Doppler and spin-down effect. The right plot is the zoom around the GW frequency; the red dots show the expected 5 frequencies due to the Earth sidereal motion. Central peak frequency is the expected GW frequency.

Figures 5.7 and 5.8 show the posterior pdf for the amplitude for P03 and P16 considering each LIGO detector and also the multi-detector case using the 5n-vectors. The posterior is obtained marginalizing over the parameters ψ and $\cos\iota$ using uniform priors, and considering a set of amplitudes in the range between 0 and a multiple of the minimum detectable amplitude in the selected frequency band.

For each value of the amplitude, using the Bayes theorem in (5.4) with uniform prior, I reconstruct the posterior $P(H_0|\overline{S})$. The likelihood $L(\overline{S}|H_0)$ is the signal distribution for the statistic S fixed by the amplitude H_0 and evaluated at the measured value of the statistic $\overline{S}$.

The median value of each posterior - that can be considered as an estimator of the injected amplitude - is in good agreement with the independent results in Table 5.1 inferred from the classic procedure for the amplitude estimation of the 5-vector method. Table 5.2 shows the parameter ϵ_{H_0}, that is the ratio between the median value of each posterior and the injected value for the considered hardware injection, and the 95% credible interval inferred from the posteriors. There is a small discrepancy for the amplitude that fall within the uncertainties of the actuation system used for the injections. The ϵ_{H_0} values mirror the distance between the median value of the posterior and the injected value (dashed line).

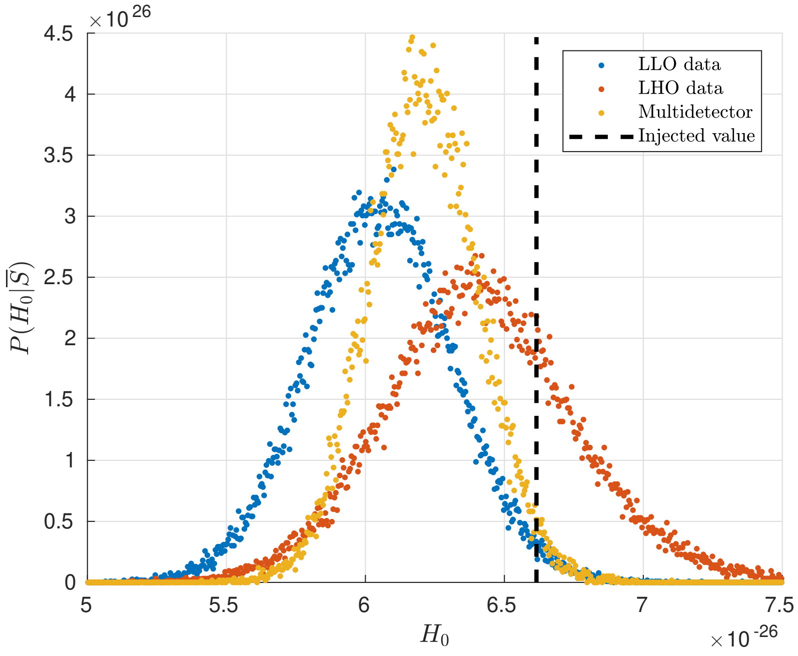

Figure 5.7: Posterior distribution for P03 as a function of fixed values of the amplitude for each detector (blue dots for LLO, red dots for LHO) and for the multi-detector case (yellow dots). The dashed line is the injected value.

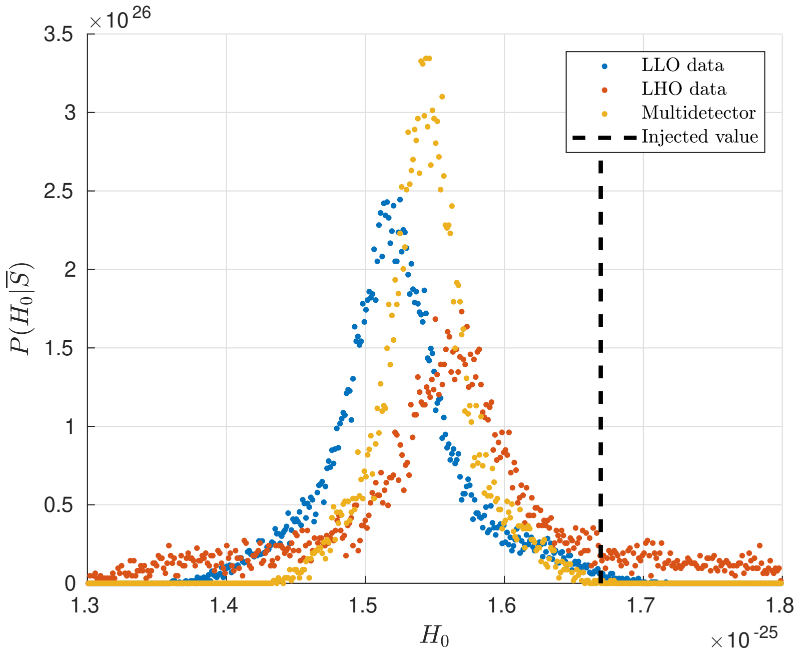

Figure 5.8: Posterior distribution for P16 as a function of fixed values of the amplitude for each detector (blue dots for LLO, red dots for LHO) and for the multi-detector case (yellow dots). The dashed line is the injected value.

Hardware Injection	Detector	ϵ_{H_0}	95% Credible interval
P03	LLO	0.91	$(5.5 \times 10^{-26}, 6.6 \times 10^{-26})$
	LHO	0.97	$(5.7 \times 10^{-26}, 7.1 \times 10^{-26})$
	Joint	0.94	$(5.8 \times 10^{-26}, 6.6 \times 10^{-26})$
P16	LLO	0.91	$(1.4 \times 10^{-25}, 1.6 \times 10^{-25})$
	LHO	0.94	$(1.4 \times 10^{-25}, 1.9 \times 10^{-25})$
	Joint	0.92	$(1.5 \times 10^{-25}, 1.6 \times 10^{-25})$

Table 5.2: Table of the amplitude estimation using the posteriors for the hardware injections P03 and P16 inferred from O3 data and considering the two LIGO detectors for single and multi detectors analysis. In this case, ϵ_{H_0} is the ratio between the median of the posteriors in Figures 5.7 and 5.8, and the H_0 injected value (6.64×10^{-26} for P03 and 1.66×10^{-25} for P16).

The posteriors in Figures 5.7 and 5.8 show also that the injected value is near the edge of the credible interval for some posteriors. This could be due to the high SNR that entails narrow distributions.

The accuracy of the parameters estimation can be improved noticing that the 5 frequencies where the signal is expected could have sidebands. These sidebands spread the signal in more bins respect to the expected peaks reducing the accuracy of the detection. The sidebands are not due to the Doppler or spin-down corrections but are linked to the presence of gap into the data[1]. The estimation of the amplitude, and in general of the CW parameters, can improve making a folding of the data and templates over the sidereal day before computing the 5-vectors.

5.2 Tests of the ensemble procedure

In Chapter 4, I have described a rank truncation method for the CW targeted search for an ensemble of N known pulsars. The proposed method ranks the pulsars in the ensemble according to the p-values P_i (with $i = 1, ..., N$) computed using the normalized statistic S_i distribution and the measured value $\overline{S}_i$: $P_i = P(S_i \geq \overline{S}_i | noise)$.

Ranking the pulsars in the ensemble for increasing P_i, I have introduced the ensemble statistic $T(k)$ as the partial sum of the first k order statistics (statistic S_i with the k-th

---

[1] For example, the sideband can be observed very clearly also in the spectrum of the template functions where no noise is present and no correction is performed. Indeed, the signal templates are computed considering the same gap of the data (see Section 3.46). By removing the gaps, the sidebands in the $A_{+/\times}$ spectrum disappear.

smallest P_i) and defined a p-value of ensemble $P(k)$ as a function of k:

$$P(k) = P(T(k) \geq \overline{T}(k)|noise) \tag{5.5}$$

with

$$\overline{T}(k) = \sum_{i=N-k+1}^{N} \overline{S}_{(i)} \tag{5.6}$$

and $\overline{S}_{(i)}$ is the i-th smallest measured value for the detection statistic for a certain pulsar in the ensemble. For example, for an ensemble of N pulsars with $P_j \leq P_i \; \forall i$ and $P_k \geq P_i \; \forall i$, the smallest and the largest order statistics are $\overline{S}_{(1)} \equiv \overline{S}_k$ and $\overline{S}_{(N)} \equiv \overline{S}_j$, respectively.

In this Section, I describe the sensitivity tests for the ensemble procedure described in Section 4.5. First, I consider a theoretical test to verify that using the statistic $T(k)$, I can optimize the detection probability for a set of pulsars. Then, I generalize the Monte Carlo procedure that reconstructs the $T(k)$ distributions, and the results of the theoretical test, considering software and hardware injections in the last observing run for the LIGO and Virgo detectors.

5.2.1 Theoretical test

For the theoretical test of the $T(k)$ detection probability for the ensemble procedure, I consider the theoretical distributions for the single pulsar statistic both in the case of noise and in the case of signal. Indeed, using the normalized S_i statistic (introduced in (4.21)) for the analysis of the i-th pulsar, the noise distribution is the Gamma[2] distribution - $S_i \sim Gamma(x; 2, 1)$ - while the signal distribution is also analytical - non central-χ^2 distribution $S_i \sim 2\chi(2x; 4, \lambda_i)$ - and fixed by the parameter λ_i defined in (4.27).

Starting from the theoretical noise and signal distributions for S_i, I need only to fix the number N of pulsars in the ensemble and the strength of the signals, that is the λ_i parameter for the i-th pulsar. Indeed, I do not need to consider real data to reconstruct the S distributions in the case of noise and especially in the case of signals. Choosing the λ_i parameter corresponds to fix the extrinsic parameters (and so, the detectors sensitivity) but also the amplitude and the polarization parameters. This allows to reduce the computational cost of the test since I do not need to reconstruct the distribution and to inject signals into real data.

---

[2] The Erlang distribution, described in Section 4.3, is the Gamma distribution with integer shape and scale parameters.

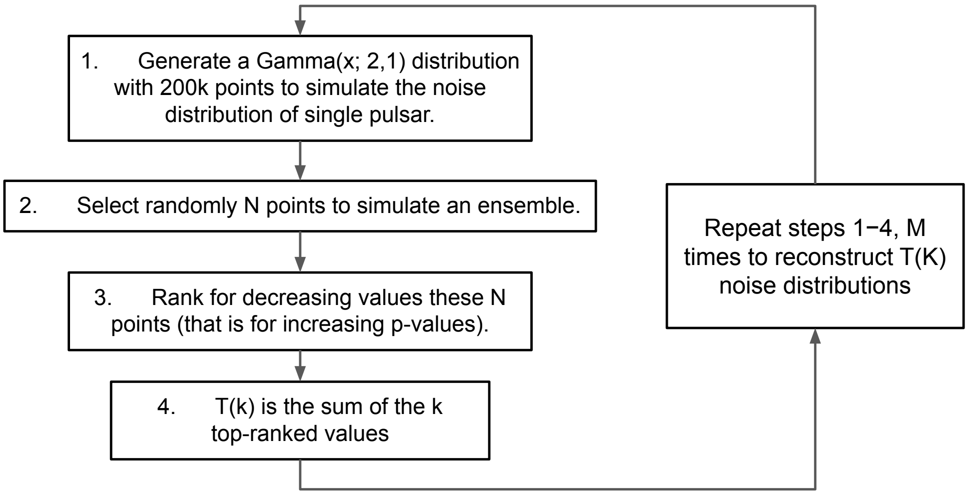

Figure 5.9: Workflow of the Matlab function *MCnoise()* that for a fixed N reconstructs the theoretical $T(k)$ noise distribution for each k using the Monte Carlo procedure described in Subsection 4.5.1.

I can reconstruct the $T(k)$ noise and signal distributions for each k following the Monte Carlo procedure described in Subsections 4.5.1 and 4.5.3. In Figure 5.9 and in Figure 5.10, there are the workflows of the two MATLab functions that reconstruct the $T(k)$ noise and signal distributions.

The theoretical test aims to show the improvement of the detection probability using the statistic $T(k)$ compared to the detection probability of single pulsar. I want also to test that the proposed rank truncation method can optimize the detection probability for the targeted search if there are few signals in the ensemble.

To fix the signal “strength", I consider two different distributions for the λ_i parameters. Specifically, I consider an exponential distribution with different mean values $\overline{\Lambda}$ and a flat distribution with only 10 signals present, fixing the corresponding λ_i value to a given P_d. P_d is the detection probability for single pulsar at a fixed false alarm probability of 1%:

$$P_d = P(S \geq S^{1\%}|signal) \tag{5.7}$$

where

$$S^{1\%} : P(S \geq S^{1\%}|noise) = 0.01 \tag{5.8}$$

Figure 5.11 (the same for Figure 5.12) shows in the left plot, the detection probability for the statistics $T(k)$ at the 1% false alarm probability compared with P_d for each pulsar

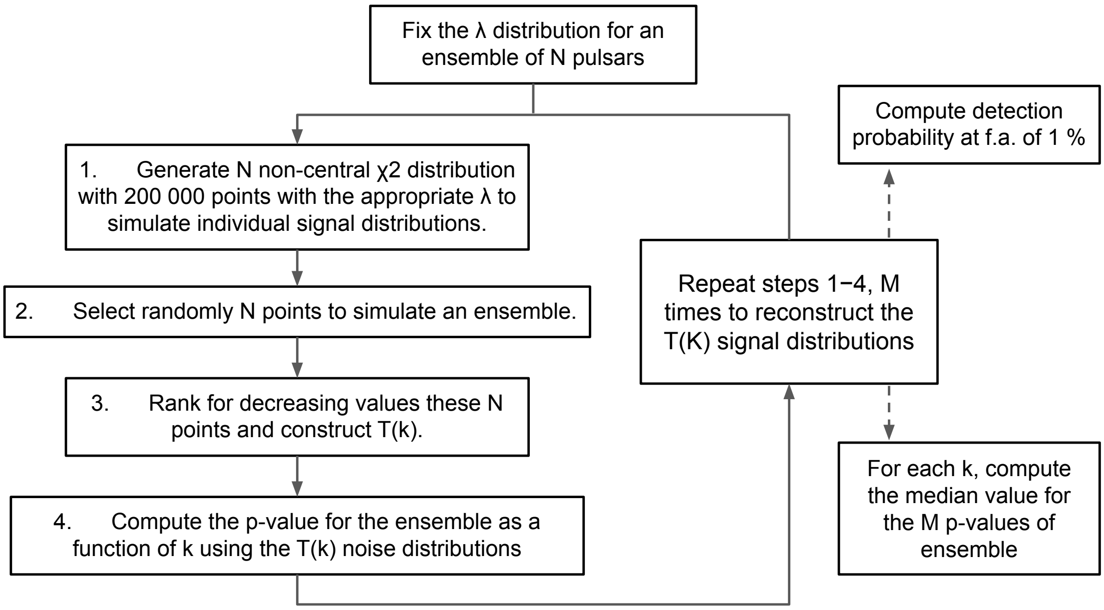

Figure 5.10: Workflow of the Matlab function *MCsig()* that fixing the strength for each pulsar (that is the λ parameter) reconstructs the theoretical $T(k)$ signal distribution for each k using the Monte Carlo procedure described in Subsection 4.5.3.

while the right plot shows the median values of the $P(k)$ signal distributions for the statistics $T(k)$ as a function of k. The $P(k)$ signal distributions are inferred from the Monte Carlo procedure shown in Figure 5.10 using the $T(k)$ noise distributions. The set of median p-values is an indication of the sensitivity of the method since you have 50% of probability to obtain a set of p-values below the considered curve.

By increasing the mean value $\overline{\Lambda}$, the median of the p-value decreases (right plot in Figure 5.11) as expected since the detection probability for the $T(k)$ increases (left plot in Figure 5.11). The "stars" in the left plot indicates the P_d for each pulsar according to the fixed λ_i value, and allow to easily compare the detection probability of the ensemble with the detection probability of each pulsar.

Figure 5.12 shows that using $T(k)$, I improve the detection probability even if there are few signals in the ensemble. Indeed, Figure 5.12 clearly shows the importance of the proposed rank truncation method. Considering only the simple sum of the statistics for the entire pulsars set (i.e. $T(100)$ in Figure 5.12), I would obtain the last point in the left/right plot. For example, for 10 signals each with $P_d = 25\%$ (red line/red stars), $T(N)$ entails a detection probability of $\approx 40\%$ and a median p-value of $\approx 2\%$. Ranking pulsars for decreasing p-values and defining the statistics $T(k)$, I optimize the detection probability since for $k \approx 10$, the detection probability curve has a maximum at $\approx 55\%$ while the minimum of the median p-value is below the 1% threshold. The larger is the

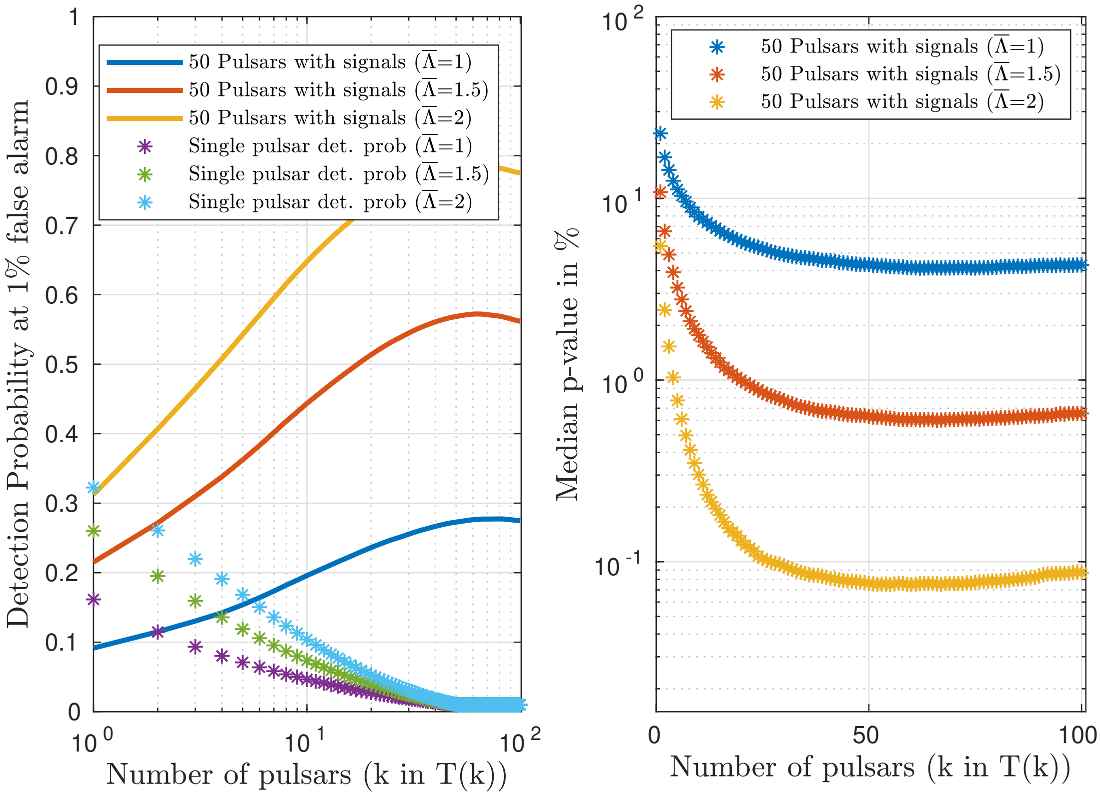

Figure 5.11: *Left plot*: detection probability at 1% false alarm probability for the $T(k)$ statistics as a function of k for $N = 100$ and choosing the λ_i parameter from exponential distributions with different mean values $\overline{\Lambda}$. The stars show the detection probability of single pulsar for each value of λ_i from each exponential distribution. In this way, it is possible to compare the detection probability of ensemble with the largest detection probability for single pulsar analysis. *Right plot*: Median p-value for the distribution of the p-value inferred from the Monte Carlo procedure using the noise distribution parameter for the statistic $T(k)$ as a function of k.

difference between the maximum $T(k)$ detection probability and the $T(N)$ detection probability, the more efficient is the rank truncation method.

5.2.2 Dependence on N

It is clear that fixing the number of signals and P_d for each signal, you can improve the detection probability decreasing N. Similarly, if the number and the strength of the signals are fixed, the detection probability for the statistics $T(k)$ decreases increasing N. This is shown in Figure 5.13 and in Figure 5.14, where the λ distributions are the same analyzed in Figure 5.11 and 5.12 but the number of pulsars is $N = 500$.

Increasing the number of pulsars with $\lambda = 0$ decreases the performance of the proposed rank truncation method. Indeed, the $T(k)$ noise/signal distributions depends on N for

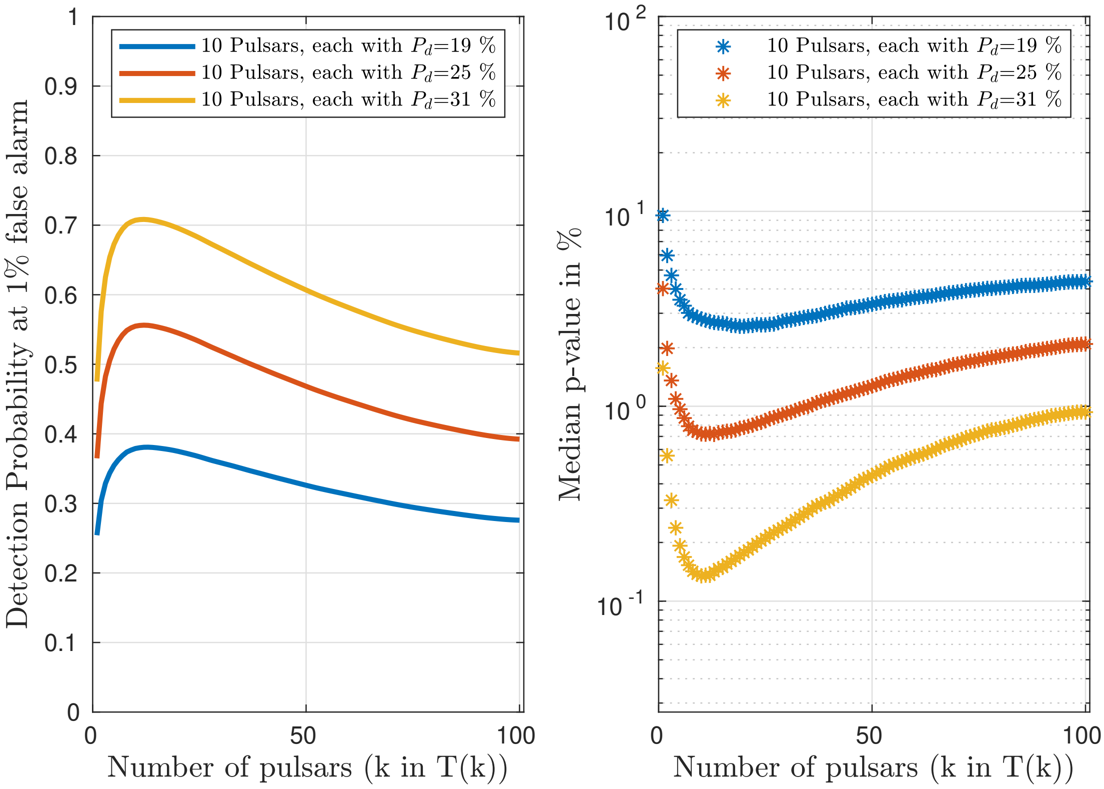

Figure 5.12: *Left plot*: detection probability at 1% false alarm probability for the $T(k)$ statistics as a function of k for $N = 100$ and choosing the λ_i different from 0 only for 10 pulsars. The value of λ_i is fixed from the detection probability of single pulsar (for example, the red line is obtained considering 10 pulsars, each with detection probability of 25%). *Right plot*: Median p-value for the distribution of the p-value inferred from the Monte Carlo procedure using the noise distribution parameter for the statistic $T(k)$ as a function of k.

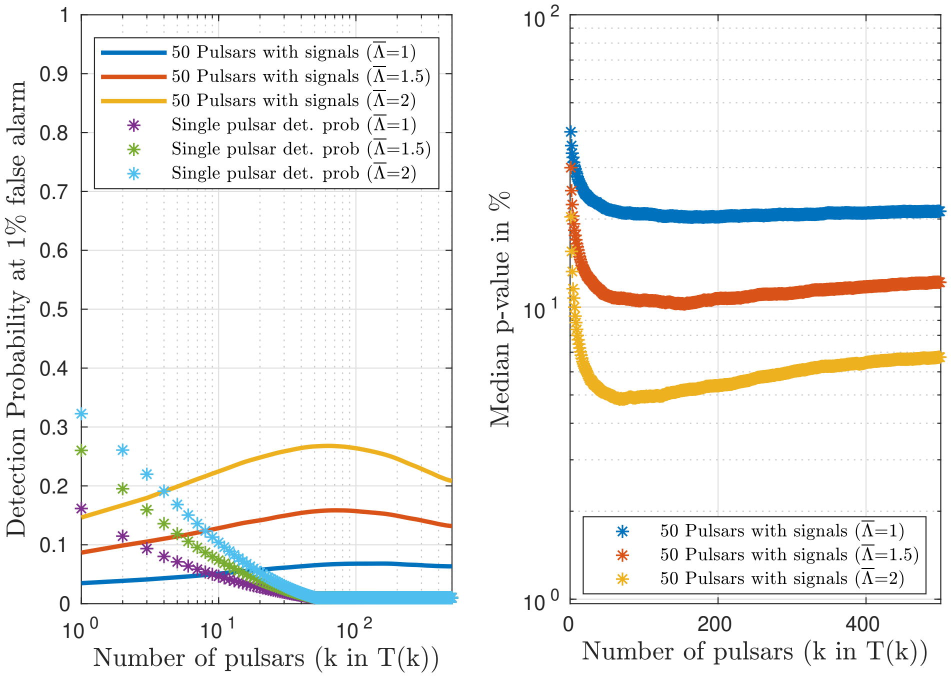

Figure 5.13: Same case of Figure 5.11 but considering an ensemble of 500 pulsars to show the dependence of the detection probability of ensemble on the number of pulsar N.

each k.

These tests show the dependencies on N for the ensemble procedure for a fixed number of signals. In a real analysis, however, I cannot optimize N. For example, I can fix a criterion to select the most promising sources. If this criterion is based on the data, I will necessarily introduce an “order" in the set of pulsars. This is, for example, the case of the coherence, an independent parameter that measures the resemblance between the shape of the expected signal and the data [95].

The coherence is not strictly related to the value of the measured statistic but it can happen that the highest values for the coherence correspond to the smallest p-values, also in the hypothesis of no signal. In general, any statistical parameter computed from the data is in some way related to the p-value since it is linked to the measured value of the statistic.

A reasonable choice is to fix N according to physical observations. For example, I can fix N considering only the "high target" pulsars that have upper limit on the strain amplitude below the spin-down limit or considering the set of millisecond pulsars.

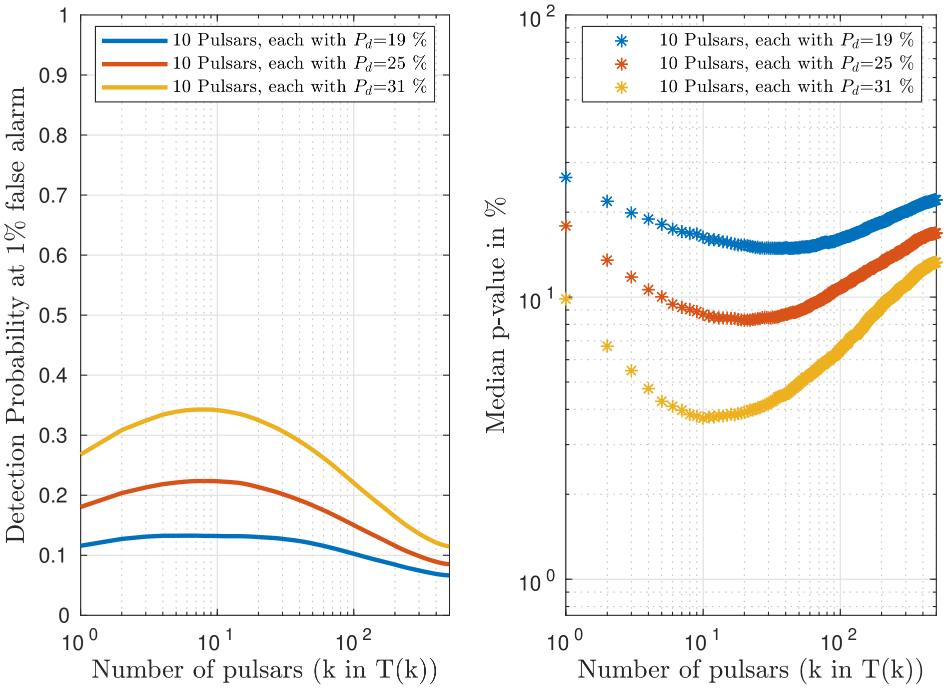

Figure 5.14: Same case of Figure 5.12 but considering an ensemble of 500 pulsars to show the dependence of the detection probability using the statistics $T(k)$ on the number of pulsar N.

5.2.3 Monte Carlo generalization for real data

Detectors noise in real data does not necessarily follow a stationary Gaussian distribution. As described in Subsection 5.1.1, to reconstruct the S noise distribution, I select a set of off-source frequencies in a small frequency band around the expected GW frequency. Similarly, I need to reconstruct the experimental distributions for the $T(k)$ statistics in order to apply the ensemble procedure to real data.

For an ensemble of N pulsars, I can reconstruct the experimental noise distributions for the $T(k)$ statistics starting from the N experimental noise distribution for the single pulsar statistic. To generalize the Monte Carlo algorithm described in Subsection 4.5.1, I replace the Gamma distribution in step one of Figure 5.9 with the N different experimental noise distributions inferred from the data. For each k, I fit the experimental $T(k)$ noise distributions using a Gamma distribution. If the detector noise followed a Gaussian distribution in the fixed frequency band for each pulsar, I would expect the fitted shape and scale parameters for $T(N)$ close to $2N$ and 1, respectively.

From the $T(k)$ experimental noise distributions, I can compute the p-value of ensemble $P(k)$ considering the Gamma distribution with the fitted shape and scale parameters.

5.2.4 Tests with hardware injections

To test the ensemble procedure considering real data and the experimental Monte Carlo procedure, I can first use the hardware injections that are present in the strain data.
Considering the entire O3 dataset, the hardware injections can be easily detected due to their high signal to noise ratio SNR (see Subsection 5.1.2). To test the ensemble procedure, I need to consider signals that can not be individually detectable and hopefully, near the detection threshold. To reduce the SNR for hardware injections, I have to reduce the observation time in order to increase the minimum detectable signal that is proportional to $\propto 1/\sqrt{T_{obs}}$ (see Equation (2.34)).
Using the BSD framework (Section 3.1), I can fix the smallest[3] datasets (1 day long) to have hardware injections that can not be detected with high significance for 1 Hz-wide frequency band. Then, I can consider an ensemble of different days and perform, for each day, a targeted search for the fixed hardware injection. Using the obtained results, I construct the statistics $T(k)$ and compute the ensemble p-value as a function of k.
In this test, I fix the hardware injection (P03 in [121]) and consider an ensemble with $N = 20$ of consecutive 1-day long datasets starting from 15/08/2019 of the LIGO Livingston detector.
Figure 5.15 shows a *summary plot* for the analysis of ensemble; the top-left plot shows the scale and shape parameters of the Gamma distribution fitted to the experimental S_i noise distributions (where i is the index of the day), the top-right plots show the results of the fits using a Gamma distribution for the $T(k)$ noise distributions for each k while the bottom plot compares the ordered P_i (red dots) with the p-value of ensemble $P(k)$ (blue line). This is a *summary plot* because it is possible to check the results of the fit to the experimental distributions for the single pulsar statistics (hence the noise in the frequency band selected for each pulsar), to the $T(k)$ noise distributions for each k, and to compare the ensemble p-value with the single pulsar p-values.
For this test, where I have fixed the hardware injection considering different datasets (20 consecutive days), the top-left plot shows how the noise in the detector evolves in time and how much different is from the Gaussian assumption. The parameters of the Gamma distribution from the fit to the experimental noise distribution can be very different from the expected values for Gaussian noise depending on the considered day. The time evolution of the noise from one day to the next modifies also the SNR of the hardware injection.
As shown in Figure 5.15, the p-values for each day are consistent with the noise hypothesis while the p-value of ensemble is well below the 1% threshold showing clear

---

[3] "Smallest" according to the 5-vector method that is based on the sidereal modulation of the expected CW signal.

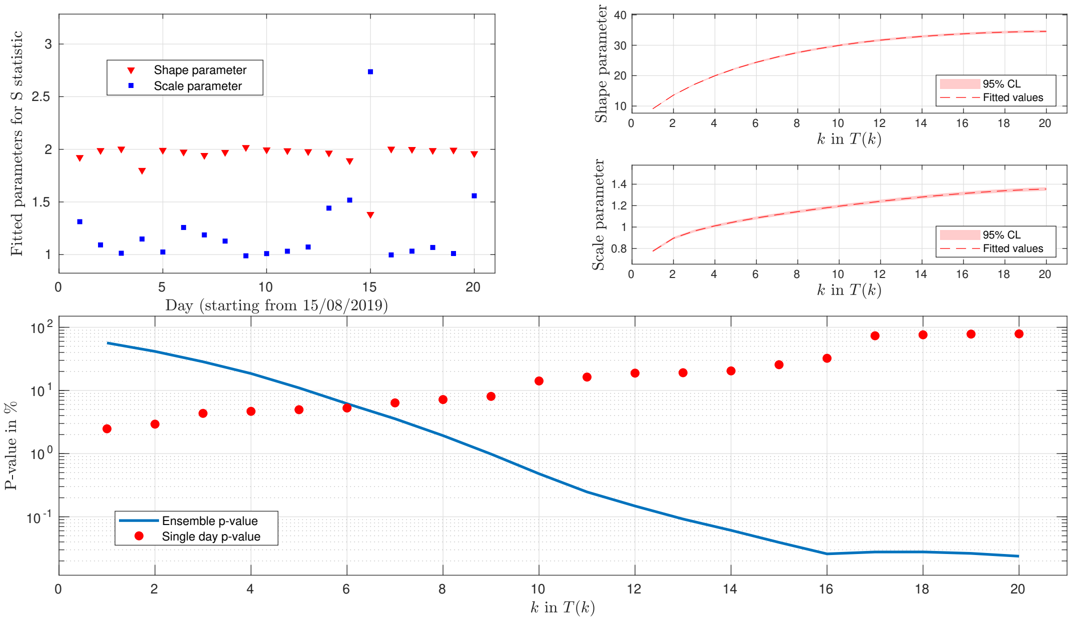

Figure 5.15: *Top-left plot* Fitted shape (red triangle) and scale parameters (blue square) using a Gamma distribution to the experimental S_i noise distribution for the i-th pulsar, inferred using a range of off-source frequencies. *Top-right plots* Fitted shape and scale parameters (dashed lines) with 95% confidence level (coloured area) for the $T(k)$ noise distributions for each k inferred from the Monte Carlo procedure. *Bottom plot* P-value of ensemble (blue line) $P(k)$ defined in (5.5) compared with the single pulsar p-value, ranked for increasing values.

evidence for a signal from the ensemble. Increasing the number of considered days the p-value of ensemble decreases. In this case, since the ensemble has only signals, the best choice for the ensemble statistic is the simple sum of the statistics, i.e. $T(N)$.

5.2.5 Tests with software injections

In order to have more and different signals to test the pipeline, software injections can be added to the detectors data series with the expected spin-down and Doppler modulations. The fake signal must be injected at the beginning of the analysis, i.e. before the heterodyne corrections and all the analysis procedure must be followed in order to compute the detection statistic corresponding to a software injection.

For the software injections, it is necessary to pick the parameters for the expected CW signal. First, I fix $N = 100$, that is an ensemble of 100 pulsars. For each simulated pulsar, I fix randomly the sky position, a uniform distribution for the parameters ψ and $\cos\iota$, a uniform distribution for the GW frequency between 100 Hz and 110 Hz and a uniform distribution for the first derivative of the GW frequency.

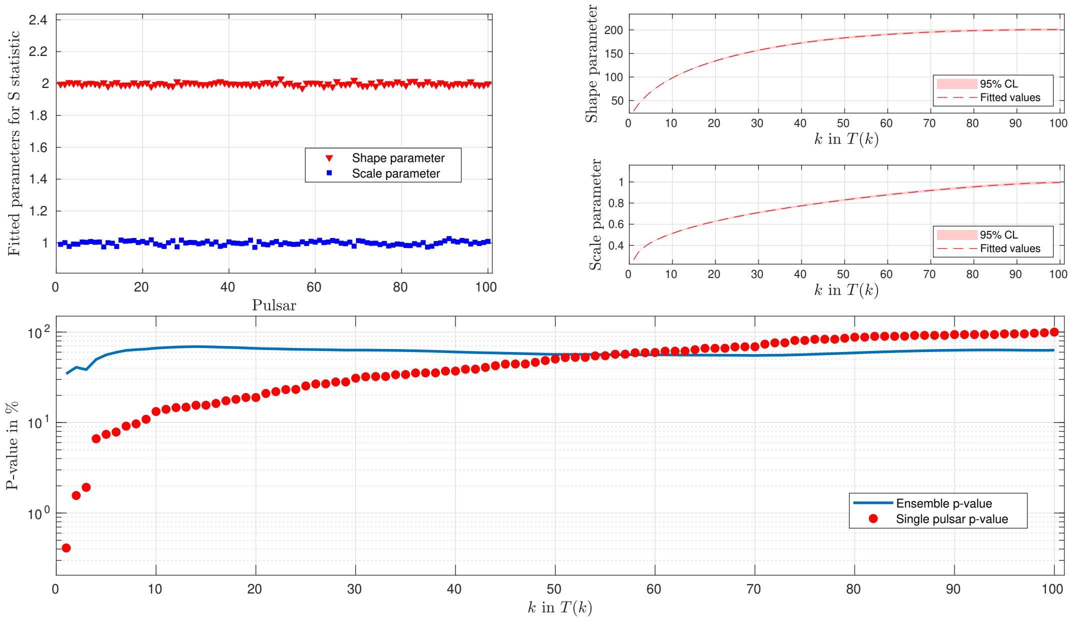

Figure 5.16: Ensemble of 100 simulated pulsars with only noise ($\alpha = 0$ for each pulsar). *Top-left plot* Fitted shape (red triangle) and scale parameters (blue square) using a Gamma distribution to the experimental S_i noise distribution for the i-th pulsar, inferred using a range of off-source frequencies. *Top-right plots* Fitted shape and scale parameters (dashed lines) with 95% confidence level (coloured area) for the $T(k)$ noise distributions for each k inferred from the Monte Carlo procedure. *Bottom plot* P-value of ensemble (blue line) $P(k)$ defined in (5.5) compared with the single pulsar p-value, ranked for increasing values.

I fix the sensitivity and the observation time considering O3 design sensitivity and O3 run duration (almost 11 months) for the LIGO Livingston detector. The injected amplitude H is chosen as a fraction α of the minimum detectable amplitude for the targeted search h_{min} (see (2.34))

$$H = \alpha \cdot h_{min} \approx \alpha \cdot 11\sqrt{\frac{S(f_{gw})}{T_{obs}}} \tag{5.9}$$

where $S(f_{gw})$ is the one-sided power spectral density at the expected GW frequency and T_{obs} is the detector observation time.

Figure 5.16 is the summary plot for the simulated ensemble with no injected signals ($\alpha = 0$ for each simulated pulsar). I do not consider any signals to check the performance of the procedure in case of noise.

The fitted shape and scale parameters are almost 2 and 1 respectively (top-left plot) since the pulsars' f_{gw} are in a frequency band where the LLO O3 data are almost stationary and Gaussian. This is shown also in the top-right plots since for $k = N$, $T(N)$ is the

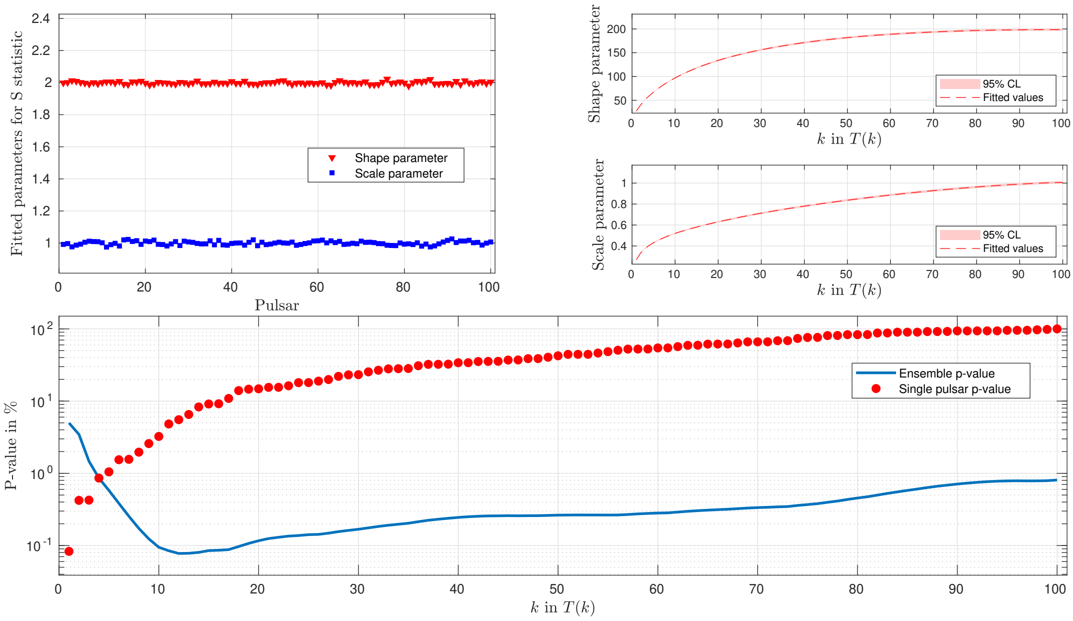

Figure 5.17: Ensemble of 100 simulated pulsars with only 10 signals, each with single test detection probability of $\sim 25\%$. *Top-left plot* Fitted shape (red triangle) and scale parameters (blue square) using a Gamma distribution to the experimental S_i noise distribution for the i-th pulsar, inferred using a range of off-source frequencies. *Top-right plots* Fitted shape and scale parameters (dashed lines) with 95% confidence level (coloured area) for the $T(k)$ noise distributions for each k inferred from the Monte Carlo procedure. *Bottom plot* P-value of ensemble (blue line) $P(k)$ defined in (5.5) compared with the single pulsar p-value, ranked for increasing values.

simple sum of N Gamma random variables and $T(N) \sim Gamma(x; 2N, 1)$.

The ensemble p-value $P(k)$ are full consistent with noise as expected. The single pulsar p-values P_i are also consistent with noise with one pulsar with a p-value below the 1%, as expected for an ensemble of $N = 100$ pulsars.

In Figure 5.17, I consider only 10 pulsars, out of 100, with $\alpha \neq 0$. The α value for each signal is 0.5, that corresponds to a detection probability for the single pulsar analysis of about 25%. The detection probability of single pulsar is almost equal since the detectors sensitivities are similar (for each pulsar, 100 Hz $< f_{gw} <$ 110 Hz)

The single pulsar p-values show no clear evidence of a signal, with the exception of four pulsars with P_i between 0.01% and 1%. The ensemble p-value has a minimum at $k \approx 10$ with $P(10) \approx 0.01\%$ with the expected shape as showed in Figure 5.12. The V-shape justifies the proposed rank truncation method to optimize the detection probability if few signals are present into the analyzed ensemble.

The ensemble p-value shows no strong evidence of a signal from the considered ensemble but it returns some hints and strong motivation for a follow-up at least for the pulsars with the smallest p-values.

5.3 Ensemble upper limits tests

To test the upper limit procedures described in Section 4.6, I use the same set of 100 simulated pulsars described in the previous Section, with different distributions for the set of injected amplitudes. I fix the 100 injected amplitudes taking the factor α_i for the i-th pulsar from a chosen distribution. I describe in this Section three different cases for the α distribution: exponential distribution, uniform distribution (see Figure 5.18) and the noise case ($\alpha_i = 0\,\forall i$).

The upper limits procedures constrain the global parameter Λ and the hyper-parameter of the common distribution assumed for the amplitudes. Figures 5.19, 5.20 and 5.21 show the results for the three analyzed cases: for each figure, the left-plot shows the posterior and the upper limit on Λ while the right-plot shows the posteriors and the upper limits on the hyper-parameter using the hierarchical procedures described in Section 4.6.

5.3.1 Λ parameter

The Λ parameter, defined in (4.36), fixes the theoretical signal distribution for the $T(N)$ statistic. For the Bayes theorem, the posterior on Λ is (see Section 4.6):

$$P(\Lambda|\overline{T}(N)) = \frac{L(\overline{T}(N)|\Lambda)\Pi(\Lambda)}{\int L(\overline{T}(N)|\Lambda')\Pi(\Lambda')d\Lambda'} \tag{5.10}$$

where $\overline{T}(N)$ is the measured value of the ensemble statistic, $\Pi(\Lambda)$ is the prior and $L(\overline{T}(N)|\Lambda)$ is the likelihood. The likelihood can be estimated form the theoretical $T(N)$ signal distribution evaluated at the value $\overline{T}(N)$ for different Λ.

The upper limit $\Lambda^{95\%}$ on the Λ parameter is defined as:

$$\Lambda^{95\%} : \int_0^{\Lambda^{95\%}} P(\Lambda|\overline{T}(N))d\Lambda = 0.95 \tag{5.11}$$

I choose a uniform prior for the Λ parameter since it is difficult to guess a priori the distribution for Λ, that is the linear combination of the squared amplitudes. The lowest value for the uniform prior can be set considering the "no-signals" case, i.e. $\Lambda = 0$, while the largest values can be set considering an ideal case where for each pulsar $\lambda_i \approx 5$ (and hence $P_d \approx 20\%$) that entails $\Lambda \approx 500$.

The results in the left-plot of Figures 5.19 and 5.20 show that the the injected values are in the 95% credible interval for the estimated hyper-parameter. The discrepancies between the peaks of the posterior and the injected value can be due to the selected priors; choosing a common distribution for the α factors entails also a distribution for the Λ parameter, different from the uniform prior chosen in these tests. Indeed, Λ is defined as the weighted sum of squared amplitudes, and so in this case of the α factors. For large values of N and if the α factors follow a common distribution, the Λ prior can be approximated by a Gaussian distribution (as it will be described in the next Subsection). A uniform prior for Λ is more general and does not entail any assumptions of the common distribution for α, as in the case of hierarchical procedures.

For the noise case with no signals - Figure 5.21 - the posterior is consistent with $\Lambda = 0$ as expected. The upper limit $\Lambda^{95\%}$ is $\Lambda^{95\%} \simeq 60$.

5.3.2 Hierarchical procedures

In Section 4.6, I have introduced two independent hierarchical procedures to constrain the hyper-parameter of the common distribution for the amplitudes.

Since the α_i factors for the injected amplitudes follow a common distribution, the hierarchical procedures must constrain the hyper-parameter μ_α of this common distribution. The two hierarchical procedures consider the parameter Λ, setting the upper limit $\mu^{(\Lambda)}$, or the single pulsar likelihoods to infer the upper limit $\mu^{(S)}$.

From Equation (4.49), the upper limit $\mu^{(\Lambda)}$ is:

$$\mu^{(\Lambda)} \; : \; \int_0^{\mu^{(\Lambda)}} P(\mu_\alpha|\overline{T}(N))d\mu_\alpha = 0.95 \tag{5.12}$$

with

$$P(\mu_\alpha|\overline{T}(N)) \propto \left(\int L(\overline{T}(N)|\Lambda)\Pi(\Lambda|\mu_\alpha)d\Lambda \right) \Pi(\mu_\alpha) \tag{5.13}$$

Choosing a uniform prior for the hyper-parameter μ_α, the prior $\Pi(\Lambda|\mu_\alpha)$ must be evaluated. This conditional probability depends on the distribution of the factors α_i.

Since I expect few signals near the detection threshold, it is reasonable to consider an exponential distribution for α with mean value μ_α. For large ensemble $N \gg 1$, $\Pi(\Lambda|\mu_\alpha)$ can be approximated with a Gaussian distribution for the Central Limit Theorem.

The mean and variance of the Gaussian distribution depends on the chosen prior and on the value of μ_α since Λ is the weighted sum of the squared α_i factors. Choosing an exponential prior[4] for α_i, the mean/variance value of the Gaussian distribution that approximates $\Pi(\Lambda|\mu_\alpha)$ is the weighted sum of the mean/variance values for the squared exponential random variables.

From Equation 4.55, the upper limit $\mu^{(S)}$ is

$$\mu^{(S)} \ : \ \int_0^{\mu^{(S)}} P(\mu_\alpha|\overline{S}_1, .., \overline{S}_N) d\mu_\alpha = 0.95 \tag{5.17}$$

where

$$P(\mu_\alpha|\overline{S}_1, .., \overline{S}_N) \propto \left(\prod_{i=1}^{N} \int L(\overline{S}_i|H_i) \Pi(H_i|\mu_\alpha) dH_i \right) \Pi(\mu_\alpha) \tag{5.18}$$

If an exponential distribution for α_i is assumed, the prior $\Pi(H_i|\mu_\alpha)$ can be chosen exponential since $H_i = \alpha_i \cdot h_{min}$. The term $L(\overline{S}_i|H_i)$ is the likelihood for the i-th pulsar. Using the results for the upper limit of the single pulsar analysis, it is straightforward to evaluate the posterior $P(\mu_\alpha|\overline{S}_1, .., \overline{S}_N)$.

In other words, I consider three different injected distributions for α (exponential, uniform and the noise case) while for the hierarchical procedures, the prior for the α distribution is chosen exponential. It is possible to evaluate different priors changing accordingly $\Pi(H_i|\mu_\alpha)$, and the mean and the variance of the Gaussian distribution that approximates $\Pi(\Lambda|\mu_\alpha)$.

The right-plot in Figures 5.19, 5.20, 5.21 show the posteriors for the two hierarchical procedures: $P(\mu_\alpha|T(N)$ (blue dots) and $P(\mu_\alpha|\overline{S}_1, .., \overline{S}_N)$ (yellow dots). The results (for example, the upper limit) are consistent for the two independent procedures.

The case of Figure 5.19 is instructive since the priors - $\Pi(\Lambda|\mu_\alpha)$ and $\Pi(H_i|\mu_\alpha)$ - mirror the injected α distribution and the peak of the hyperparameter posteriors are close to the injected value as expected.

In Figure 5.20, the prior is based on a wrong assumption since the injected α distribu-

---

[4] If X is an exponential random variable with pdf $f(x)$ and mean value μ, the squared exponential random variable X^2 has pdf $f_{X^2}(x)$,

$$f_{X^2}(x) = f\left(\sqrt{x}\right) \frac{d\sqrt{x}}{dx} = \frac{1}{2} \frac{e^{-\frac{\sqrt{x}}{\sqrt{x}\mu}}}{\mu} \tag{5.14}$$

and the mean value μ_{X^2} is

$$\mu_{X^2} = \int_0^\infty x \cdot f(x) = 2\mu^2 \tag{5.15}$$

Similar argument can be used for the variance $\sigma^2_{X^2}$:

$$\sigma^2_{X^2} = \int_0^\infty \left(x - 2\mu^2\right)^2 \cdot f(x) = 20\mu^4 \tag{5.16}$$

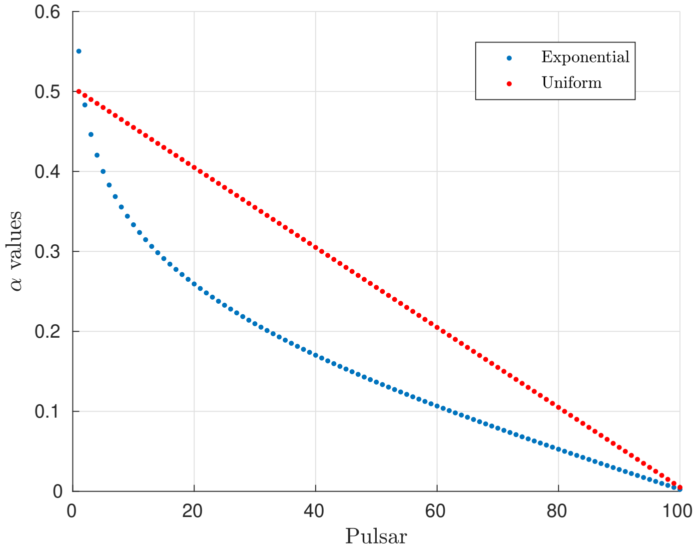

Figure 5.18: Set of α_i values (with $1 < i < 100$ that indicates the pulsar in the ensemble of the 100 simulated pulsars) used to reconstruct the two distributions for the α factor defined in (4.20): exponential distribution with mean value 0.15 (blue dots) and uniform distribution with $0 < \alpha < 0.55$ (red dots).

tion is uniform. The injected value is still in the confidence interval of the posteriors but in this case, the signals are "stronger" with twenty pulsars with $0.4 < \alpha < 0.5$ as shown in Figure 5.18. This can be seen also in the left-plot of Figure 5.20 where the posterior $P(\overline{T}(N)|\Lambda)$ peaks almost at 200 while in Figure 5.19, the peak is at almost 100.
For the noise case in Figure 5.21, the posteriors and the upper limits $\mu^{(\Lambda)}$ and $\mu^{(S)}$ are consistent.

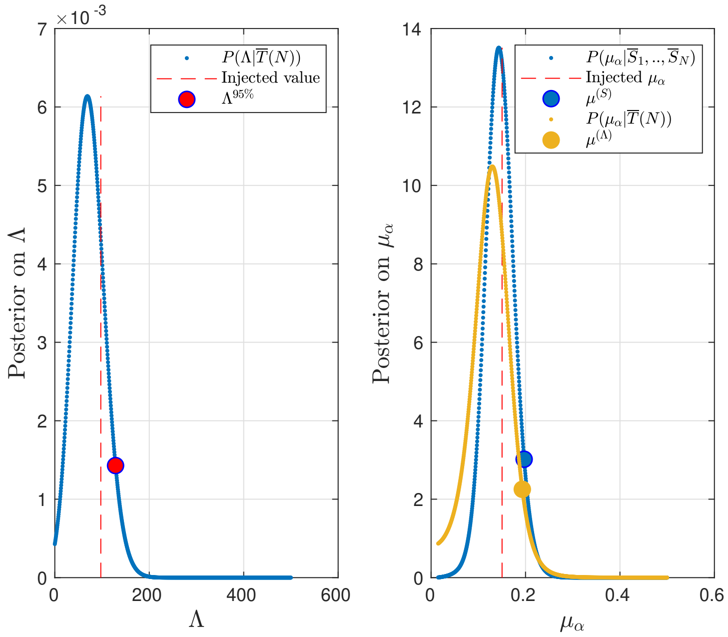

Figure 5.19: Ensemble of 100 simulated pulsars with exponential distribution with mean value 0.15 for the α factors. *Left plot* Posterior distribution (blue curve) and upper limit (red point) on the Λ parameter assuming a uniform prior. The dashed line is the injected value of Λ .*Right plot* Posterior distribution and upper limit on the hyper-parameter μ_α for the two independent hierarchical procedures using Λ (yellow curve) or the single pulsar likelihoods (blue curve).

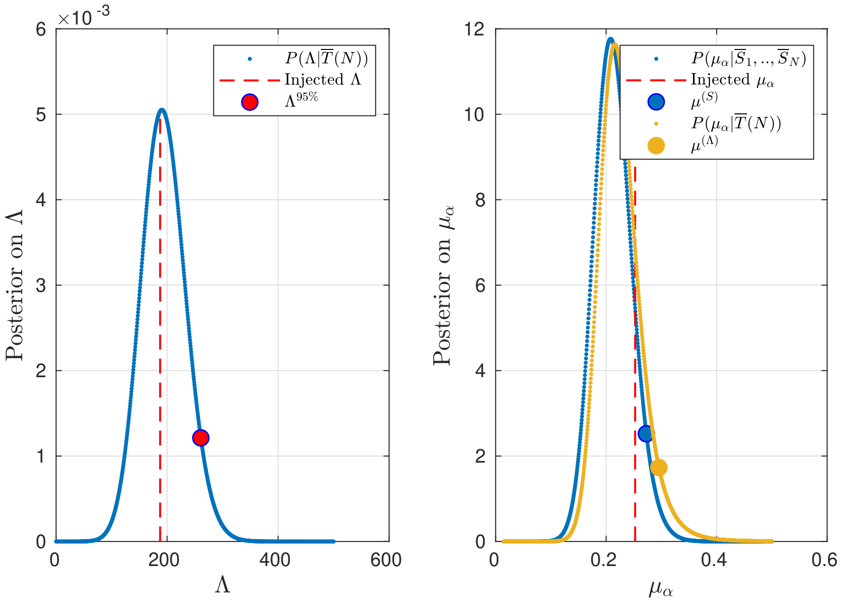

Figure 5.20: Ensemble of 100 simulated pulsars with uniform distribution between $0.005 < \alpha < 0.5$. *Left plot* Posterior distribution (blue curve) and upper limit (red point) on the Λ parameter assuming a uniform prior. The dashed line is the injected value of Λ .*Right plot* Posterior distribution and upper limit on the hyper-parameter μ_α for the two independent hierarchical procedures using Λ (yellow curve) or the single pulsar likelihoods (blue curve).

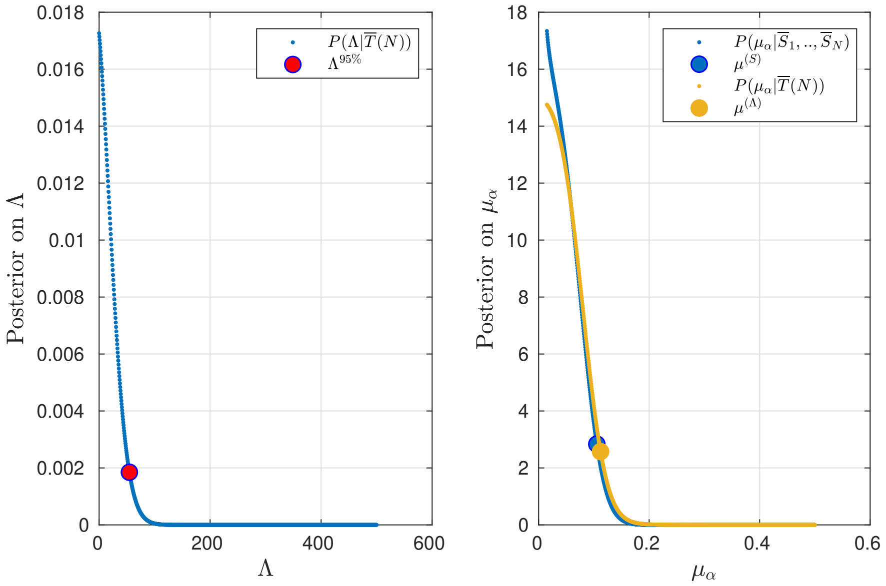

Figure 5.21: Ensemble of 100 simulated pulsars with $\alpha = 0$ for each pulsar. *Left plot* Posterior distribution (blue curve) and upper limit (red point) on the Λ parameter assuming a uniform prior. The dashed line is the injected value of Λ .*Right plot* Posterior distribution and upper limit on the hyper-parameter μ_α for the two independent hierarchical procedures using Λ (yellow curve) or the single pulsar likelihoods (blue curve).

Chapter 6

Results using O3 data

In this Chapter, I show the results of the application of the 5n-vector ensemble method to the set of known pulsars in Table 6.1 using O3 data from the LIGO and Virgo detectors. The set of pulsars almost coincide with the one in [84].
As described in Chapter 4, the 5n-vector ensemble method is based on the analysis of single pulsars; indeed, combining the normalized statistics of single pulsar, I construct the statistics $T(k)$ to improve the detection probability for a signal of ensemble.
In the first part of this Chapter, I describe the O3 dataset and the set of pulsars based on the LVK targeted search in [84]. Then, I present the first results of the targeted search - also for binary systems - using the 5n-vector method.
In the second part, I show the results of the ensemble procedure considering three different set of pulsars. Since there is no evidence of a CW signal from the ensemble, I set the 95% confidence upper limit on the global parameter Λ and using two independent hierarchical Bayesian frameworks, the upper limit on the hyperparameter of an assumed exponential distribution for the ellipticities.

6.1 Data set

As described in Section 2.5, targeted searches assume to know with high accuracy the source parameters, namely the sky position and the rotation parameters. Therefore, targeted searches have a strong multi-messenger approach since electromagnetic observations can constrain the source extrinsic parameters. These electromagnetic observations have been made in radio and X-ray wavelengths.
In this Section, I describe the data set used for the analysis and composed by the GW data set, that is the data from the LIGO and Virgo detectors, and the electromagnetic data set from the different telescopes that provide the pulsar parameters.

6.1.1 GW data

The O3 observing run started the 2019 April 1 (MJD: 58574.625) and ended the 2020 March 27 (MJD: 58935.708) for both the LIGO and Virgo detectors. O3 consisted of two sections, separated by a one month-long commissioning break. O3a ran from 2019 April 1, 15:00 UTC until 2019 October 1, 15:00 UTC. O3b ran from 2019 November 1, 15:00 UTC, to 2020 March 27, 17:00 UTC.

The duty cycles for this run were 76%, 71%, and 76% for LLO, LHO, and Virgo, respectively. The O3 data set is publicly available via the Gravitational Wave Open Science Center[1].

For O3, the maximum 1 σ amplitude uncertainties for the frequency band 10-2000 Hz were in the range [-5,+7]% and [-5.5,+5.5]% for LHO and LLO, respectively, and for Virgo the maximum uncertainty was 5%. These ranges are the maximum upper and lower bound over the full frequency range and over different measurement epochs over the run, so at specific frequencies/times the uncertainty can be far smaller. The data used underwent cleaning processes, specifically the removal of narrowband spectral artifacts corresponding to calibration line frequencies and power line frequencies. A discussion on the consequences of performing a search using LIGO data with the narrowband cleaning can be found in Appendix A of [84].

6.1.2 EM data

The set of analyzed pulsars in Table 6.1 corresponds almost with the set analyzed in [84].

The observatories which have contributed to the data set are: the Canadian Hydrogen Intensity Mapping Experiment (CHIME), the Mount Pleasant Observatory 26 m telescope, the 42 ft telescope and Lovell telescope at Jodrell Bank, the MeerKAT project, the Nancay Decimetric Radio Telescope, the Neutron Star Interior Composition Explorer (NICER) and the Molonglo Observatory Synthesis Telescope (as part of the UTMOST pulsar timing programme). The ephemerides have been created using pulse time-of-arrival observations that mainly overlapped with O3 observing period.

To estimate the theoretical spin-down limit or the upper limit for the fiducial ellipticity for a certain source, the pulsars' distances are needed. For many pulsars, the distance can be found in the ATNF Pulsar Catalog [123]. These are distances mostly based on the observed dispersion measure and calculated using the Galactic electron density distribution model of [124], although others are based on parallax measurements, or inferred from associations with other objects or flux measurements. The distances used for each

---

[1] https://www.gw-openscience.org/O3/index/

pulsar are given in Table 6.1. Distance errors are primarily based on uncertainties in the Galactic free electron distribution, which can lead to distance errors on the order of a factor of two. Nearby pulsars, for which parallax measurements are possible, will generally have smaller distance uncertainties.

The spin-down limits require also the value for the first period derivative of the pulsar. The observed spin-down does not necessarily reflect the intrinsic spin-down of the pulsar, as it can be contaminated by the relative motion of the pulsar with respect to the observer. This is particularly revalent for millisecond pulsars, which have intrinsically small spin-downs that can be strongly affected, particularly if they are in the core of a globular cluster where significant intracluster accelerations can occur, or if they have a large transverse velocity with respect to the Solar System. The spin-down can also be contaminated by the differential motion of the Solar System and pulsar due to their orbits around the Galaxy. For the non-globular-cluster pulsars, if their proper motions and distances are well enough measured, these effects can be corrected for to give the intrinsic period derivative.

I select the pulsars whose rotation frequency is greater than 10 Hz to match the sensitivity band of the GW detectors. This leads to primarily targeting millisecond pulsars and fast spinning young pulsars. There are 165 millisecond pulsars with frequencies above about 100 Hz.

In this analysis, I have not considered the pulsars that glitched during O3. In general, for the pulsars which experienced glitching, each inter-glitch period is analyzed independently and then the resulting statistics are summed. For the single pulsar analysis, this procedure entails a decrease of the search sensitivity. For simplicity, I decide to not consider glitching pulsars in this analysis.

6.2 Single pulsars analysis

In this Section, I describe the results of the analysis of single pulsar using the 5n-vector method. I use the normalized single pulsar statistic S defined in 4.21 using the weighted multidetector extension of the 5-vector, described in Section 3.6. The results described here are obtained using O3 data from the two LIGO and Virgo detectors.

For each pulsar, I consider a small frequency band - at least 0.1 Hz wide - around the expected GW frequency that is assumed exactly two times the rotation frequency of the source (single harmonic search). The frequency band extracted from the BSD files is chosen considering the spin-down of the source and in case of binary systems, considering also the Doppler effect due to the orbital motion.

Using the heterodyne correction described in Subsection 3.3.1, I remove the spin-down

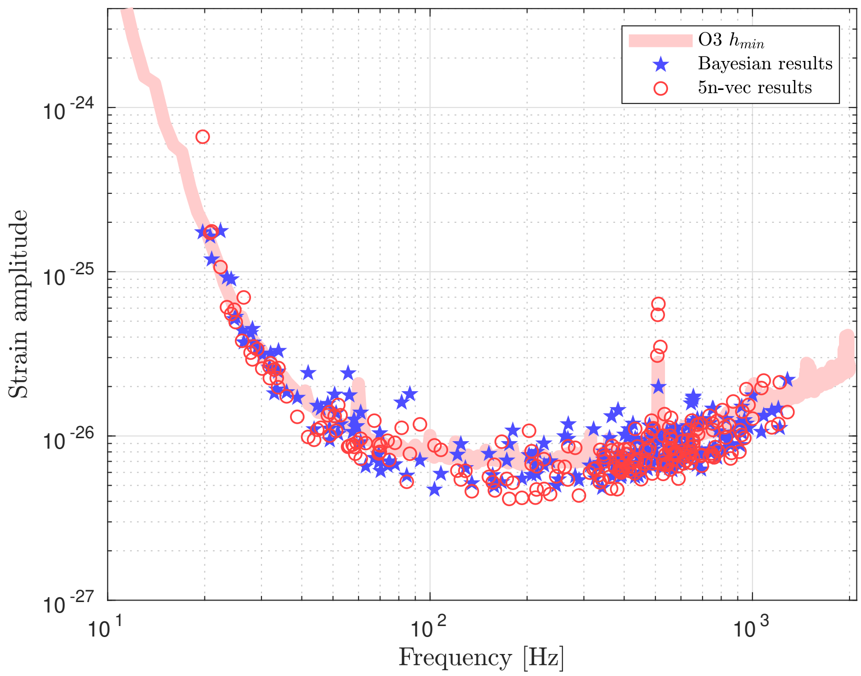

Figure 6.1: Strain amplitude as a function of the frequency for O3 data of the LIGO and Virgo detectors. Blue stars are the upper limits inferred using the Bayesian method for the 223 analyzed pulsars as in [84] while the red circles are the upper limits for the 5n-vec method. The continuous pink line is the h_{min}, the minimum detectable amplitude for the O3 run considering a multidetector analysis.

and the Doppler frequency modulation for the expected GW signal. For the first time for the 5n-vectors, I implement the Doppler correction for binary systems described in Section 3.4. Using the BSD framework, the computational cost of the analysis is reduced to a few CPU-minutes per source per detector.

The experimental noise distribution is inferred considering a range of off-source frequencies as described in Subsection 5.1.1. The measured value of the statistics is compared with the noise distribution computing the p-value.

In agreement with [84], there is no evidence of a CW signal from any pulsar in O3 data. Using the procedure in Subsection 3.5.5, I set 95% credible upper limit on the amplitude h_0 for each pulsar[2].

As shown in Figure 6.1, the upper limits from the 5n-vector method (red circles) are in agreement with the results of the Bayesian method (blue stars as in [84]). The comparison is also shown in Figure 6.2 with the histogram of the normalized difference D_n

---

[2] The 5n-vector method uses a description of the GW signal based on the concept of polarization ellipse. The relation of the amplitude parameter H_0 used by the 5n-vector method with both the standard strain amplitude h_0 is described in Subsection 3.5.5

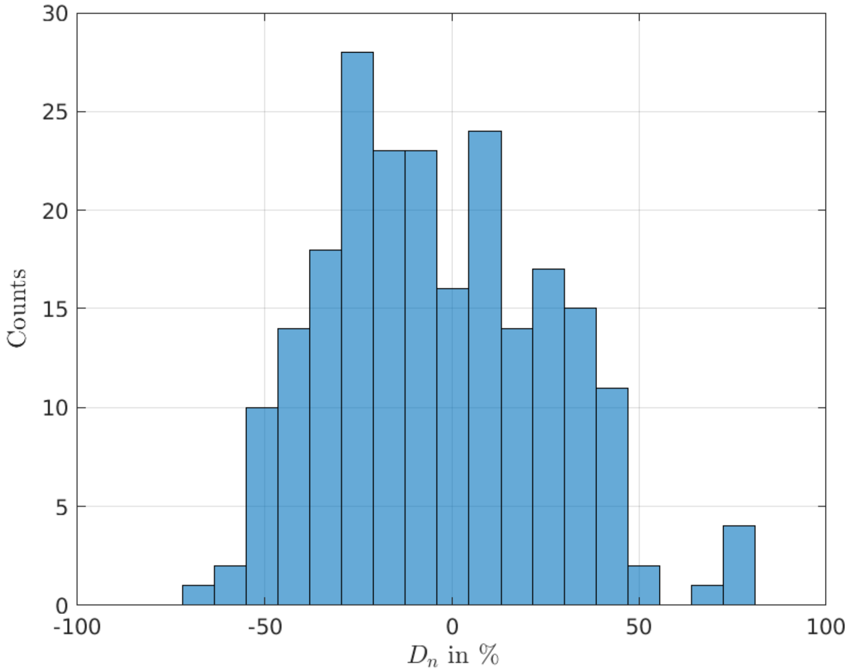

Figure 6.2: Histograms of the normalized difference D_n of the upper limits defined in (6.1) to compare the 5n-vector method and the Bayesian method results.

defined as:

$$D_n = \frac{X - Y}{max(X,Y)} \tag{6.1}$$

where X is the upper limit from the 5n-vectors for a certain pulsar and Y is the corresponding upper limit from the Bayesian method. Figure 6.2 shows that the distribution is peaked almost at zero with a preference for negative values of D_n. This means that the 5n-vector method provides upper limits that are slightly smaller than the corresponding Bayesian upper limits.

Figure 6.3 shows the so-called spin-down ratio, that is the ratio between the upper limit on the amplitude from the 5n-vector method and the theoretical spin-down limit.

In Figure 6.4, there is the comparison between the upper limits on the ellipticity from the 5n-vector method (red circles) and the Bayesian method (blue stars). The much lower limits on ϵ inferred for the millisecond pulsars easily follow from the frequency scaling in the ellipticity definition (from Equation 1.62).

These results rely on the pulsar distance, frequency derivative and principal moment of inertia, which all have associated uncertainties. As in [84], these uncertainties are not taken into account in this analysis, since I use the best-fit values listed in Table 6.1 and a fiducial moment of inertia of 10^{38} kg m^2 , which is the standard fiducial number used

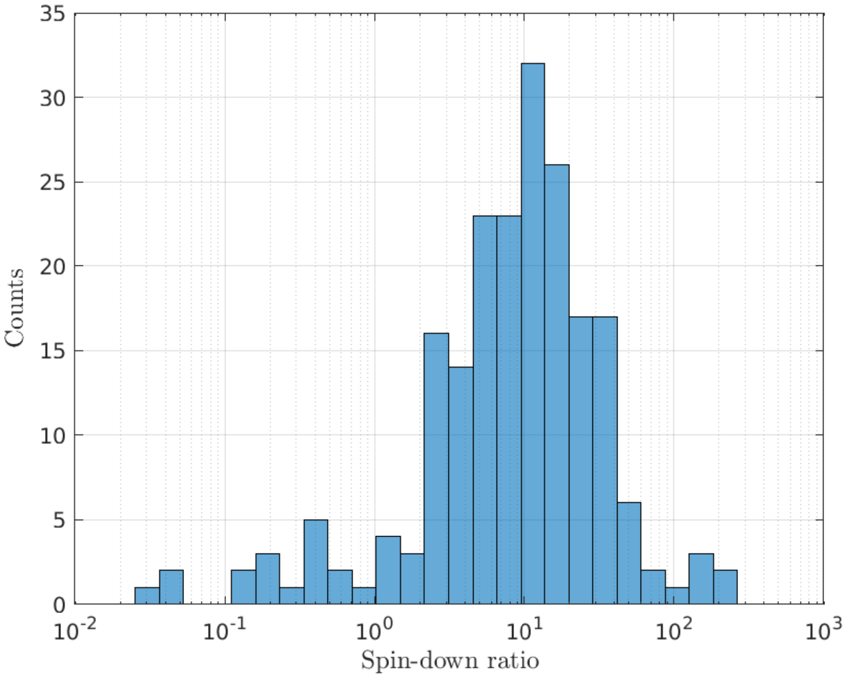

Figure 6.3: Histograms of the spin-down ratio for the analyzed pulsars - for which calculating a spin-down rate was possible - obtained by using the 5n-vector method.

in the literature.

From the 5n-vector results, 17 pulsars have upper limits below the corresponding spin-down limit (*high-value* pulsars), with 102 pulsars within a factor of 10 of their spin-down limit. For the Bayesian analysis, the high value pulsars are 23 (82 pulsars within a factor of 10). The missing high-value pulsars for the 5n-vector method are the 3 glitching pulsars (Crab, J0908-4913, J1105-6107) and the three pulsars J1745-0952, J1756-2251, J1925+1720 that have spin-down ratio for the 5n-vector of 1.16, 1.33 and 1.17 respectively.

In the following, as *high-value* pulsars I consider the pulsars with the spin-down ratio $\lesssim 1$; in this way, apart form the glitching pulsars, the high-value pulsars set correspond to the one in [84].

6.3 Ensemble analysis

In this Section, I show the results of the ensemble analysis proposed in this thesis based on O3 data and the set of 223 pulsars analyzed in Section 6.2.

I choose three different ensemble from the set in Table 6.1: the entire set for the three detectors, the millisecond pulsars ($f_{gw} > 100$ Hz) set for the LIGO detectors and the

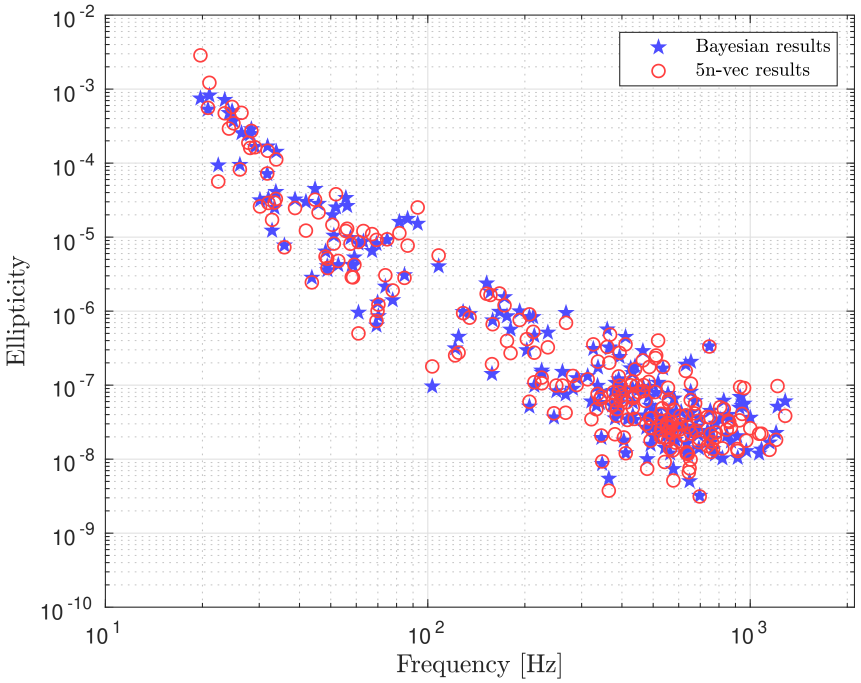

Figure 6.4: Upper limits on the ellipticity for the set of analyzed pulsars from the 5n-vector method (red dots) and from the Bayesian method (blue stars).

high-value pulsars set ($h_0^{95\%}/h_{sd} \lesssim 1$) for the LIGO detectors. This corresponds to fix $N = 223$ for the first set, $N = 165$ for the millisecond pulsars set and $N = 20$ for the high-value pulsars set.

After analyzing each pulsar singularly, I reconstruct the statistics $T(k)$ and compute a p-value of ensemble as a function of k. The results are shown in the form of summary plot; the top-left plot shows the fitted shape and scale parameters of a Gamma distribution for the experimental noise distribution for the statistic S as a function of the pulsar frequency, the top-right plots show the fitted shape and scale parameters to the $T(k)$ noise distributions as a function of k while the bottom-plot compares the ordered single pulsar p-values with the ensemble p-values from the $T(k)$ statistics.

Since there is no evidence of signal form the ensemble, I set 95% credible upper limit on the global parameter Λ and on the hyperparameter μ_ϵ that is the mean value of the assumed exponential distribution for the ellipticities.

6.3.1 All pulsars, all detectors

The summary plot for the entire set of analyzed pulsars is shown in Figure 6.5. For this analysis, I consider the two LIGO and Virgo detectors.

I use a criterion based on noise to select the detectors that are used for the multi-detector analysis of single pulsar. Since the normalized statistic S in the hypothesis of Gaussian noise is distributed according to a $Gamma(x; 2, 1)$, from the fitted parameters to the experimental noise S distribution (top-left plot in Figure 6.5) I can easily check the Gaussianity in the selected frequency band for each pulsar. For the multi-detector analysis, I consider the detectors that have fitted shape and scale parameters respectively in the range $[1.6, 2.4]$ and $[0.8, 1.2]$ (that is a maximum difference of 20% from the theoretical values). This procedure allows to exclude the detectors with large noise disturbances that can influence the Monte Carlo procedure for the $T(k)$ noise distributions.
From the bottom-plot of Figure 6.5, there is no evidence of a signal form the ensemble. Three pulsars have single pulsar p-value (red dots) slightly below 1% as expected for a set of 223 pulsars. The p-value computed for the statistics $T(k)$ are consistent with the noise hypothesis.

6.3.2 Millisecond pulsars, LIGO detectors

The summary plot for the millisecond pulsars is shown in Figure 6.6. For this analysis, I consider only the two LIGO detectors with the same noise criteria introduced in the previous Subsection. In this case, I do not consider the Virgo detector that has a higher noise level. As shown in Section 3.6, a multidetector analysis does not necessarily entail a better sensitivity compared to the most sensitive detectors considered in the analysis.
As shown in the bottom plot in Figure 6.6, there are four pulsars - J2055+3829, J0824+0028, J1551-0658, J1751-2857 - below the 1% threshold. There is no evidence for any of these pulsars; the combination of the two LIGO detectors entails lower p-values respect to the three detectors case.
For example considering the pulsar J2055+3829, the p-values for the single detector-single pulsar analysis are 0.12, 0.01, 0.76 for LLO, LHO and Virgo respectively. The multidetector analysis considering all the three detectors entails a p-value of 0.009 while considering only the two LIGO detectors, the p-value is 0.0015.
The ensemble p-value has a minimum of almost 2% for $k = 4$ with no evidence of signal from the ensemble. The strong decrease for the first values of k is due to the presence of the four pulsars with relatively small p-values below the 1%. For a set of 165 pulsars, the expected number of p-values below 1% should be almost 2.

6.3.3 High-value pulsars, LIGO detectors

The summary plot for the high-value pulsars, that is the set of analyzed pulsars with spin-down ratio $\lesssim 1$, is shown in Figure 6.7. For this analysis, I consider only the two

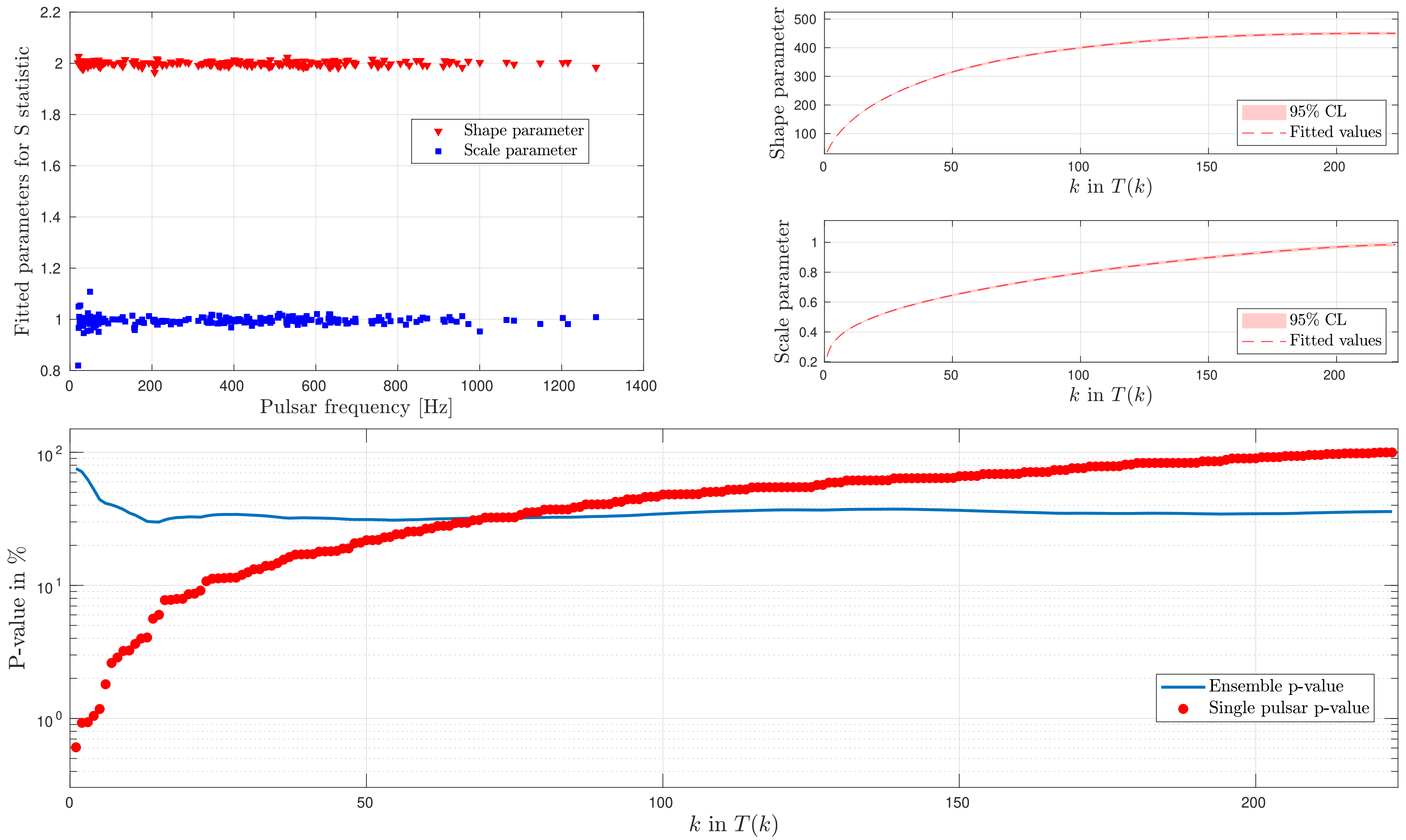

Figure 6.5: Summary plot of the ensemble composed by the 223 pulsars in Table 6.1 considering O3 data and the three detectors (two LIGO and Virgo). *Top-left plot* Fitted shape (red triangle) and scale parameters (blue square) using a Gamma distribution to the experimental noise distribution for each pulsar as a function of the frequency for the considered pulsar. *Top-right plots* Fitted shape and scale parameters (dashed lines) with 95% confidence level (coloured area) for the $T(k)$ noise distributions for each k inferred from the Monte Carlo procedure. *Bottom plot* P-value of ensemble (blue line) compared with the single pulsar p-value (red dots), ranked for increasing values.

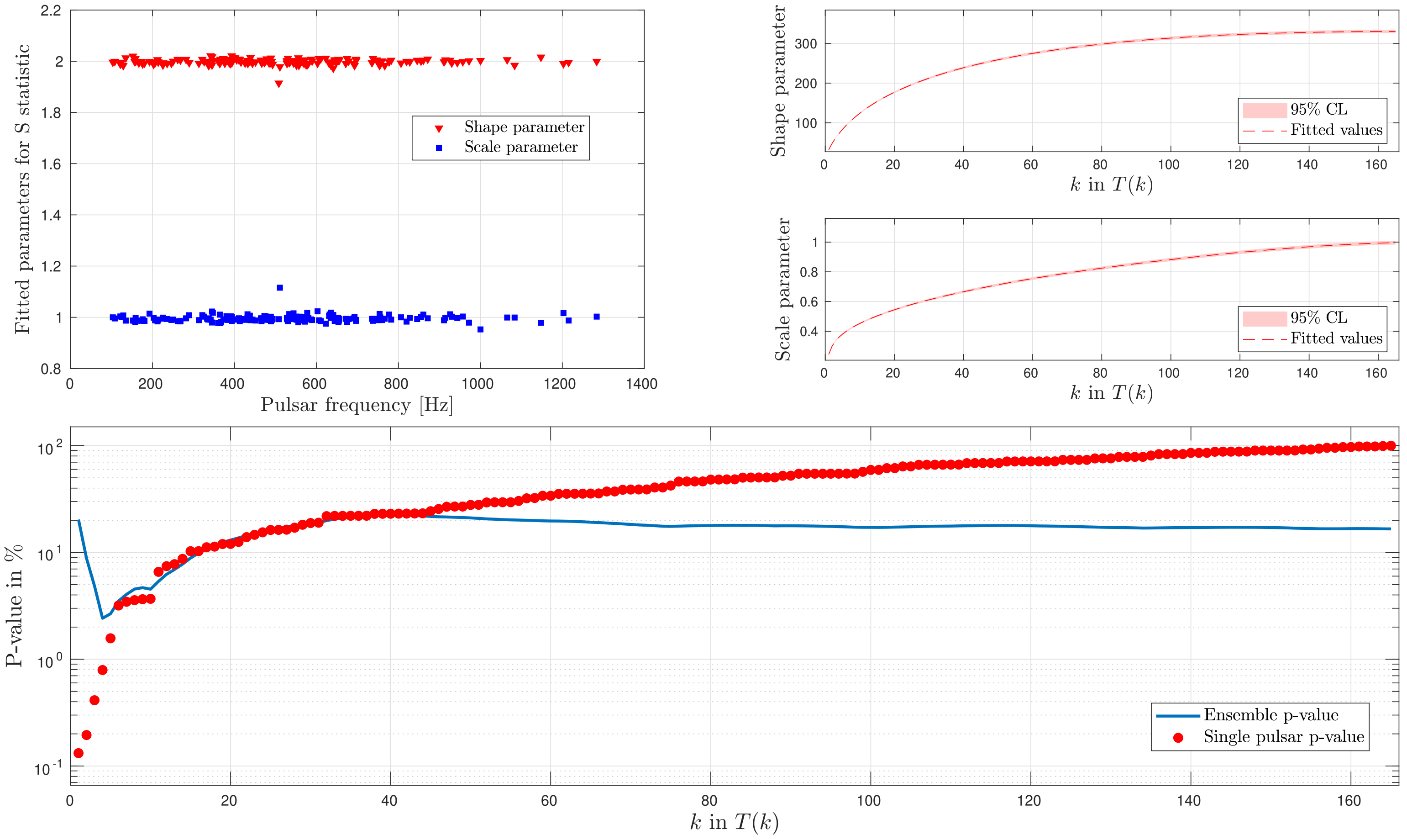

Figure 6.6: Summary plot of the ensemble composed by the millisecond pulsars in Table 6.1 considering O3 data and the two LIGO detectors. *Top-left plot* Fitted shape (red triangle) and scale parameters (blue square) using a Gamma distribution to the experimental noise distribution for each pulsar as a function of the frequency for the considered pulsar. *Top-right plots* Fitted shape and scale parameters (dashed lines) with 95% confidence level (coloured area) for the $T(k)$ noise distributions for each k inferred from the Monte Carlo procedure. *Bottom plot* P-value of ensemble (blue line) compared with the single pulsar p-value (red dots), ranked for increasing values.

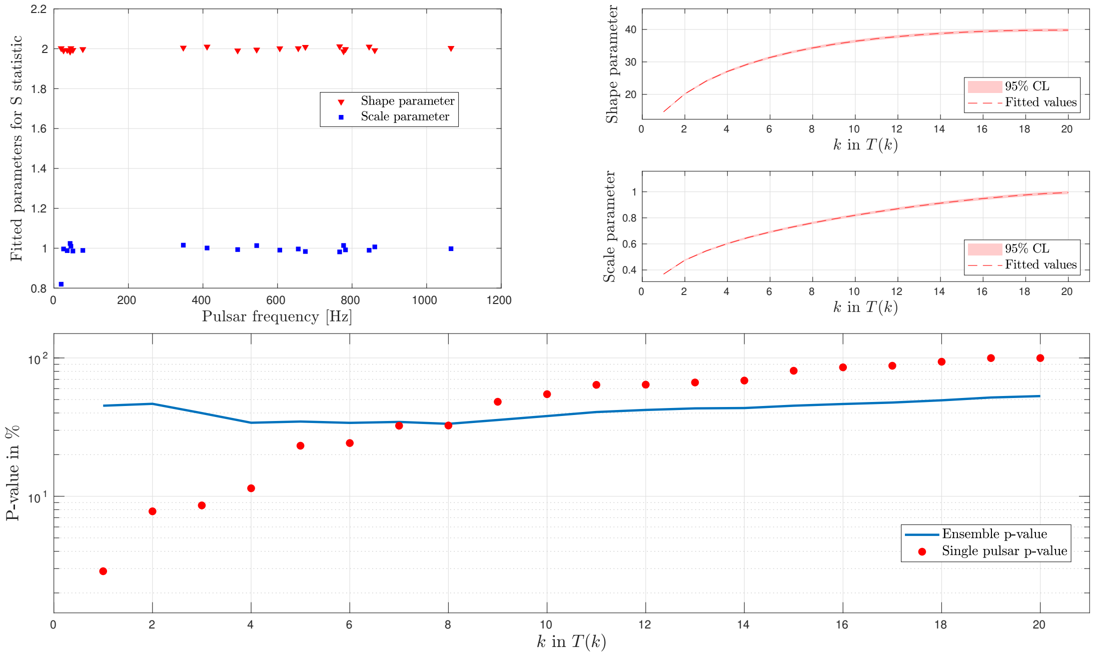

Figure 6.7: Summary plot of the ensemble composed by the high-value pulsars with spin-down ratio $\lesssim 1$ (see Figure 6.3) considering O3 data and the two LIGO detectors. *Top-left plot* Fitted shape (red triangle) and scale parameters (blue square) using a Gamma distribution to the experimental noise distribution for each pulsar as a function of the frequency for the considered pulsar. *Top-right plots* Fitted shape and scale parameters (dashed lines) with 95% confidence level (coloured area) for the $T(k)$ noise distributions for each k inferred from the Monte Carlo procedure. *Bottom plot* P-value of ensemble (blue line) compared with the single pulsar p-value (red dots), ranked for increasing values.

LIGO detectors with the same noise criteria introduced in the previous Subsection.
The high-value pulsars for O3 data are 20 (as in [84] excluding the glitching pulsars) . As showed by the the blue line in the bottom plot of Figure 6.7, the p-value of ensemble is full consistent with the noise hypothesis.

6.3.4 Upper limits

The procedures to set upper limits with the ensemble procedure are described in Section 4.6 and validated in Section 5.3.
The validation tests reported in Section 5.3 consider a set of 100 simulated pulsars with GW frequency between 100 Hz and 110 Hz. The injected amplitudes H are fixed by the factor α since $H = \alpha \cdot h_{min}$. Assuming a common distribution (exponential in Figure 5.19 and uniform in Figure 5.20) for the α factors, the two independent hierarchical procedures, described in Subsection 4.6.2, show the posterior distribution of the mean

of the assumed exponential distribution for α.

For the single pulsar analysis, I set the 95% credible upper limits on the amplitude and - assuming a fiducial moment of inertia value and the distance without uncertainties - the 95% credible upper limits on the ellipticity. Indeed, in a real analysis the physical parameters to constrain are the amplitude and the ellipticity linked to the CW strength and to the neutron star EOS.

For the upper limit computation, I consider the entire set of known pulsars in Table 6.1 and the O3 dataset for the LIGO and Virgo detectors.

Using the statistic $T(N)$, that is the simple sum of the statistics for the pulsars in the analyzed ensemble, I set 95% credible upper limit on the parameter Λ that fixes the $T(N)$ signal distribution. Λ, defined in Equation (4.36), is the weighted sum of the squared amplitudes. The upper limit is fixed with a mixed Bayesian-frequentist procedure similar to the procedure for the single pulsar case. The prior on Λ is chosen uniform while the likelihood is the value of the $T(N)$ signal distribution evaluated at the measured value $\overline{T}(N)$. The posterior $P(\Lambda|\overline{T}(N))$, shown in the left plot of Figure 6.4, is compatible with 0 as expected for the noise case. The 95% credible upper limit is:

$$\Lambda^{95\%} = 96.4 \tag{6.2}$$

It is not possible to infer information for the single pulsar from the upper limit $\Lambda^{95\%}$ since Λ is a global parameter for the ensemble. $\Lambda^{95\%}$ can be used to show the improvement in the method sensitivity analyzing future runs or, as described in Subsection 4.6.1, it can be used to constrain different global parameters of the ensemble based on some assumptions for the single pulsars amplitudes.

For example, by assuming that each pulsar in the ensemble have the same amplitude $\overline{h}$, from the upper limit $\Lambda^{95\%}$ it follows that $\overline{h} = 2 \times 10^{-27}$; while by assuming that each amplitude is a multiple of the single pulsar upper limit with a common factor δ, from the upper limit $\Lambda^{95\%}$ it follows that $\delta = 0.07$.

For the hierarchical procedures, considering the analysis in [115] and the stochastic searches in [103, 104], I assume a common exponential distribution for the ellipticities with the hyperprior $\Pi(\mu_\epsilon)$ that is log-uniform between 10^{-10} and 10^{-7}. The posteriors $P(\mu_\epsilon|\overline{T}(N))$ and $P(\mu_\epsilon|\overline{S}_1, .., \overline{S}_N)$ are shown in the right plot of Figure 6.4.

The upper limit on μ_ϵ is

$$\mu_\epsilon^{(\Lambda)} = 2.7 \times 10^{-9} \tag{6.3}$$

for the hierarchical procedure using the Λ parameter, and

$$\mu_\epsilon^{(S)} = 1.8 \times 10^{-9} \tag{6.4}$$

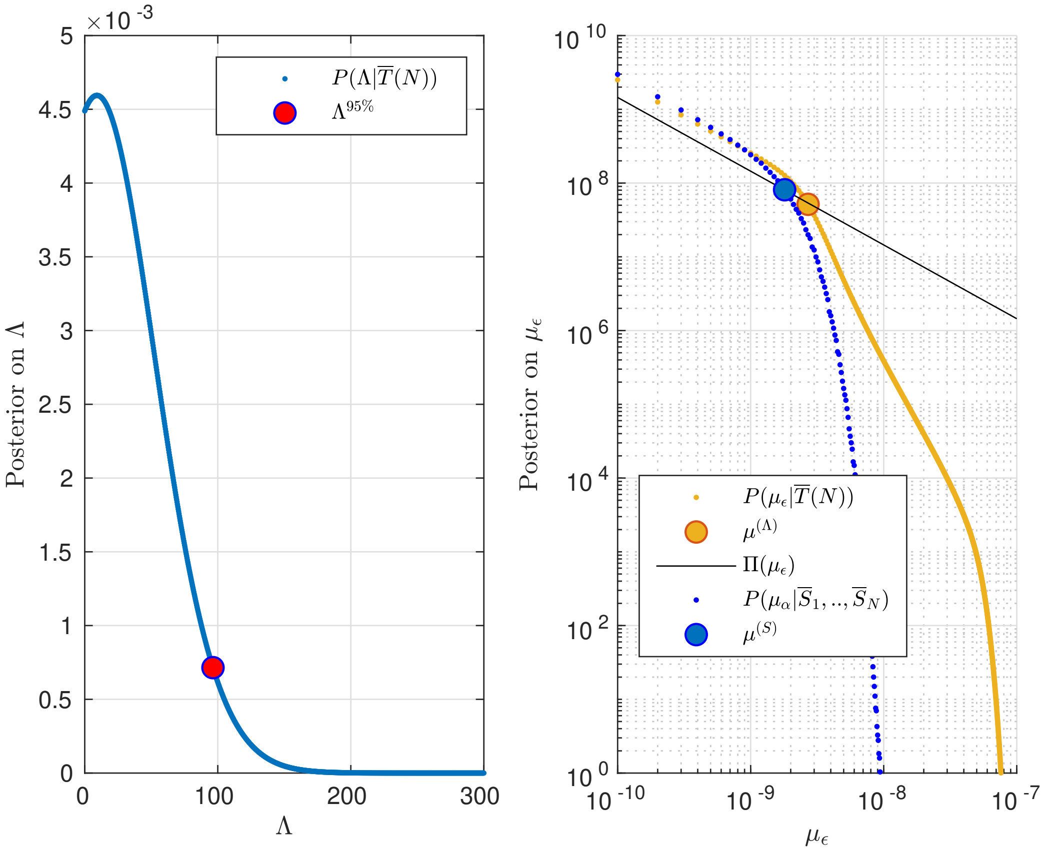

Figure 6.8: Upper limits inferred from the ensemble procedure considering the set of 223 pulsars in Table 6.1 and considering the O3 data for the LIGO and Virgo detectors. *Left plot:* posterior distribution for the global parameter Λ (defined in Equation 4.36). The red point indicates the 95% credible upper limit for Λ. *Right plot:* posterior distribution for the two independent hierarchical procedures described in Subsection 4.6.2 to set the upper limits on the mean μ_ϵ of the assumed exponential distribution. The continuous line is the log-uniform hyperprior on μ_ϵ. The blue and yellow points indicate the 95% credible upper limit for μ_ϵ.

for the hierarchical procedure using the single pulsar results.

The results and also the posteriors can be directly compared with Figure 8 in [115] where the authors analyzed 92 pulsars using data from the LIGO S6 science run. The 90% upper limit on the mean of the assumed exponential distribution is 3.8×10^{-8} in [115].

The upper limit set in this thesis is more than one order of magnitude below this value. It should be noted that the ensemble analyzed here is larger than the ensemble in [115], and in addition, the combined O3 data for the LIGO and Virgo detectors are largely more sensitive than the LIGO S6 science run data.

The upper limits in [103, 104] on average ellipticity for the neutron star population are $\mathcal{O}(10^{-8})$ from cross-correlation-based searches of a stochastic gravitational wave background. It is not straightforward to compare these limits with the one obtained in this thesis since targeted searches are focused on known pulsars that represent only a small subset of the entire set of neutron stars in our Galaxy. Indeed, the results in [103, 104] depend on the estimated number of neutron stars that emit CWs in the analyzed frequency band.

6.3.5 Comments

As shown in Figures 6.5, 6.6 and 6.7 there is no evidence of CW signal from the three different ensemble considered in this thesis. In the following, I report some comments and assumptions on the 5n-vector analysis that should be taken into account.

- The results described in the previous Subsections consider a single harmonic emission whit the GW frequency that is exactly twice the rotation frequency of the source. So far, the dual harmonic search (GW frequency at both once and twice the rotation frequency) is not implemented for the 5n-vector method.
- For the first time using the 5n-vector method, I show the results for the analysis of pulsars in binary systems. The heterodyne correction for binary systems is described in Section 3.4.
- Using the multidetector procedure in Section 3.6, the results are in agreement with [84]. However, it is still not clear when a multidetector analysis outperforms the most sensitive detector analysis. A criteria depending on the source sky position and on the detectors' sensitivities and observation times should be studied in the next future to choose when and which detectors should be used in a multidetector analysis.
- Glitching pulsars, as the Crab, are not considered in the single pulsar analysis and therefore, also in the ensemble analysis. The general procedure for glitching pulsar is to analyze each inter-glitch period independently and then to sum the resulting statistics. In future searches, glitching pulsars can be included in the ensemble procedure considering the resulting statistic for the single pulsar analysis or considering each inter-glitch period as an independent pulsar.
- The upper limits on the ellipticity for the single pulsar analysis and also on the hyperparameter for the exponential distribution do not consider the uncertainties on the distance. As in [115], the distance should be included as a variable assuming, for example, a Gaussian prior with a mean given by each pulsar's best fit distance, and a standard deviation of 20% of that value, and a hard cutoff at zero.

- The hierarchical procedures assume that all the analyzed pulsar ellipticities are drawn from a common distribution that can be too simplistic to describe the true ϵ distribution. For example, the population of young pulsars and old recycled millisecond pulsars have undergone different evolution that could mean that the distribution of ellipticities for these two populations may be quite different. Therefore, a bimodal distribution or two independent exponential distributions with different means could be more appropriate.

- The upper limits procedures from the ensemble statistic $T(N)$ use the theoretical signal distribution to evaluate the likelihood. Theoretical distribution can be used in the hypothesis of Gaussian noise in the analyzed frequency band for each pulsar. This can be controlled looking at the fitted Gamma parameters for the $T(N)$ statistic in the top-right plot of Figures 6.5, 6.6 and 6.7.

6.4 Application and future prospects

In this Section, I describe the possible application and the future prospects for the proposed ensemble procedure. The next observing runs for the LIGO and Virgo detectors and especially the next generation of GW detectors will improve the sensitivity and hopefully bring us closer to detect CWs from pulsars for the first time. In addition, the ensemble procedure can improve the detection probability for targeted searches.

The rank truncation method developed in this thesis can be easily generalized to different pipelines, e.g. to the $\mathcal{F}$-statistic, and also to different search methods, e.g. to the semi-coherent searches.

In Subsection 6.4.3, I describe also a possible application of the ensemble method to the comb identification for the noise detector characterization.

6.4.1 O4 run and 3G detectors

LIGO, Virgo, and KAGRA are closely coordinating to start the O4 Observing run together. The start for the O4 run is programmed for March 2023 and it will last one full year with a one-month break for maintenance in the middle. LIGO projects a sensitivity goal of 160-190 Mpc for the binary neutron stars range. Virgo projects a target sensitivity of 80-115 Mpc. KAGRA is expected to start observing alongside Virgo and LIGO, and then at some point, step away for commissioning and return to observing with a greater sensitivity toward the end of O4.

In the more distant future, third-generation (3G) detectors like the proposed Cosmic

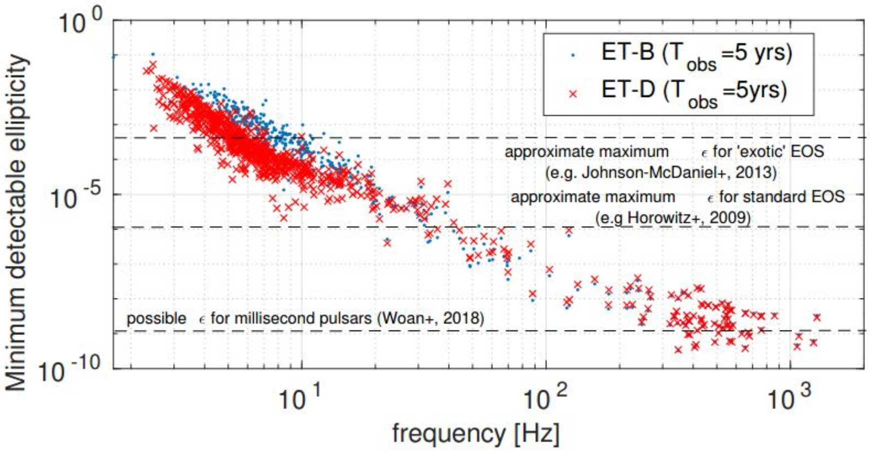

Figure 6.9: Minimum ellipticity detectable by ET at 90% confidence level in a targeted search, assuming an observation time 5 yr. Dashed line are theoretical limit for the ellipticity assuming different equation of state. Two detector sensitivity curves, ET-B and ET-D, are taken into account (details in [125]).

Explorer or Einstein Telescope may reach sensitivities one order of magnitude higher than what is achieved by Advanced LIGO and Advanced Virgo. Figure 6.9 shows the minimum detectable ellipticity (at 90% confidence level) for currently known pulsars potentially emitting in the detector band, assuming two proposed ET configurations and a full coherent matched filter analysis over an observation time of 5 years. The minimum detectable value of the ellipticity for each pulsar is inferred from the minimum detectable amplitude for targeted search considering the design sensitivity (Equation (2.34)). ET will be sensitive to ellipticities of the order of few times 10^{-10} for the nearest millisecond pulsars, and of $10^{-6} - 10^{-7}$ for young pulsars.

Follow-up

The 5n-vector method and the ensemble procedure described in this thesis use a frequentist approach: the significance of a certain candidate, characterised by a value of the detection statistic, is established through the p-value, that is the probability to obtain a larger value for the statistic in the hypothesis of noise only.
Given an observed data sample, claiming the discovery of a new signal requires determining that the sample is sufficiently inconsistent with the hypothesis that only background is present in the data. The test statistic $T(k)$ can be used to measure the inconsistency of the observation in the hypothesis of the presence of background only, typically assumed as a null hypothesis. The p-value has, by construction, a uniform distribution

between 0 and 1 for the background-only hypothesis H_0 and tends to have small values in the presence of the signal (hypothesis H_1). A researcher will often "reject the null hypothesis" when the p-value turns out to be less than a predetermined threshold (called significance level), often 0.01.

If this p-value is very small, usually less than or equal to the significance level, it suggests that the observed data is inconsistent with the assumption that the null hypothesis is true, and thus that hypothesis must be rejected. The p-value refers only to the null hypothesis and does not make reference to or allow conclusions about any other hypotheses, such as the alternative hypothesis.

As reported in [126], "It should be emphasized that in an actual scientific context, rejecting the background-only hypothesis in a statistical sense is only part of discovering a new phenomenon. One's degree of belief that a new process is present will depend in general on other factors as well, such as the plausibility of the new signal hypothesis and the degree to which it can describe the data". In this work, a small p-value can be used to recognize interesting ensemble of pulsars as starting point for the detection.

The question is: what happens if a p-value of ensemble is below a fixed significance threshold?

A targeted search presents perhaps the most challenging case for confirmation, since the search is already based on a matched filter and hence there is little or no additional SNR to be gained in follow-up. Moreover, the SNR value is unlikely to be high, given the previously unsuccessful searches. This scenario implies that taking further data may be necessary, to gain confidence. It is clear that to claim a detection, the signal should be seen in different pipelines; the Bayesian approach for both the single pulsar and the ensemble searches is an important alternative pipeline to be considered.

It is also clear that the results for the ensemble search are based on the analysis of single pulsar. A p-value of ensemble that is below the fixed threshold for a certain value of k can be an alert for the k pulsars in the analyzed subset. To follow-up these candidates, the self consistency of the signal should be analyzed. For example, the maximum SNR for combined interferometers should generally be higher than the maximum SNR of any single interferometer. Then, a CW signal from a non-glitching neutron star should have the SNR that grows with the square root of the observation time.

It would also be desirable to infer the noise distribution not from the detectors noise (e.g. using off-source frequencies) but considering a large number of randomly chosen points in the sky to better assess confidence (sky-shifting technique [127]). This would be an independent way to check the significance of a particular candidate.

6.4.2 Extension to different search methods

The rank truncation method described in Section 4.4 can be easily generalized to different pipelines for the targeted search and/or also to different CW searches. Indeed, the rank truncation method is a general multiple testing procedure that improves the detection probability for a signal from the ensemble when few signals are present near the detection threshold. Ranking pulsars for increasing p-values and then, defining the statistics $T(k)$ as the partial sum of order statistics do not imply any assumptions on the used statistic S for the analysis of single pulsar.

In Subsection 5.2.4, I have showed a different application of the ensemble procedure fixing the hardware injection to analyze. Then, considering consecutive days where the signal was injected but below the detection threshold, I performed an ensemble procedure to improve the detection probability. It follows that a different use of the ensemble procedure could be in directed searches where semi-coherent methods are used.

$\mathcal{F}$-statistic

Let us suppose that the S_i statistic used for the targeted search of the i-th pulsar is defined by the $\mathcal{F}$-statistic method.

As described in Subsection 2.6.2, the $\mathcal{F}$-statistic uses a frequentist approach; the p-value computed from the measured value of the statistic quantifies the consistence of the data with the noise hypothesis. In the case of Gaussian noise, the $\mathcal{F}$-statistic follows a non-central χ^2 distribution with 4 degrees of freedom and has a non-centrality parameter equal to the squared optimal SNR ρ^2.

The main difference with the 5n-vector method is the normalized noise distribution for the statistic. Indeed in the case of no signal, the $\mathcal{F}$-statistic follows a χ^2 distribution with 4 degrees of freedom.

In this thesis, I introduce a normalized definition of the statistic S in Equation (4.21) since the rank truncation method can only be applied if the considered statistic for the single pulsar analysis has the same noise distribution for each pulsar. With a different noise distribution, ranking for increasing p-values does not necessarily correspond to rank for decreasing values of the detection statistics and order statistics can not be used.

The application of a rank truncation method to the $\mathcal{F}$-statistic is straightforward; the Monte Carlo procedure to reconstruct the $T(k)$ noise/signal distributions is the same described in Figures 5.9 and 5.10. The only difference is the starting noise/signal distributions for each pulsar.

In [78], the authors define an ensemble statistic as the weighted sum of the $\mathcal{F}$-statistics with coefficients a_i that depend on the average optimal SNR:

$$a_i \propto \frac{f_i^4 \mathcal{K}_i}{d_i^2\, S_n(2f_i)} \tag{6.5}$$

where f_i is the rotation frequency, d_i the distance and $\mathcal{K}_i$ is an averaged geometrical factor describing the GW polarization and orientation of the i-th pulsar. Discussing the obtained results, the authors try to answer to the questions: "Will collecting more pulsars return higher P_{DE} values than an individual detection? How many sources should be combined to obtain the maximum P_{DE} at given P_{FA}?" (P_{DE} is the detection probability while P_{FA} is the false alarm probability). These questions are essential for an ensemble procedure; to answer to these, I introduce the rank truncation method to optimize the detection probability when there are few signals in the ensemble.

A detailed study that compares the performance of the rank truncation method with the definition in [78] is needed. It is important to stress that by fixing N - the number of pulsars in the ensemble - the procedure in [78] entails the computation of a "single" ensemble statistic that should be compared with $T(N)$.

Narrow band and semi-coherent searches

Narrow-band searches allow a mismatch between the GW frequency and the rotation frequency of the source. The frequency/spin-down plane is divided into frequency sub-bands (typically 10^{-4} Hz wide). For each point of the grid, the detection statistic and the corresponding p-value is computed. To take into account the number of trials, the computed p-values must be adjusted using, for example, the Šidák correction. The outliers are identified among the candidates using a threshold nominally corresponding to 1%.

A simple extension of the ensemble method is to consider the maximum value of the detection statistics from the frequency/spin-down grid for each pulsar and then, to perform the ensemble search as described in this thesis. Narrow band searches, as described in Section 2.5, have lower sensitivity due to the trial factors. A more detailed analysis on how the ensemble procedure is influenced by the narrowband sensitivities, is needed.

Ensemble procedures can be also extended to semi-coherent searches. The general idea for semi-coherent searches (common to different pipelines) can be sketched as:

- divide the full dataset in several “short” segments;
- compute the statistic S_i over each segment;
- take the sum of the statistic S_i.

In other words, a semi-coherent search is an ensemble procedure where the neutron star is fixed, and the information of consequent short segments are combined together.
Neglecting the details of the particular pipeline, a rank truncation method can be useful to increase the detection probability. Indeed, the short segments are of the order of sidereal days; detectors noise can change considerably during the observing run and from one day to the next. This means that the sensitivity of the coherent search over the short segments (and hence the SNR) changes in time and depends on the considered time segments. The same signal could be near the detection threshold for a particular segment but deeply buried into noise in a different one. Applying the ensemble procedure - as in the case of the test with hardware injection in Subsection 5.2.4 - will optimize the semi-coherent search if there are few segments where the signal is near the detection threshold.

6.4.3 Comb identification

In the Paragraph 3 of Section D in [128], it is described a method to detect "Sub-threshold combs in coherence data". Combs are frequency lines in the coherence between GW noise detectors that occur in a distinct pattern with even spacing in frequency between each tooth (each single line) of the comb. Tooth frequencies are given by $f_n = f_0 + n \cdot \delta_f$, where f_0 is the offset (from 0 Hz) of the comb, δ_f is the spacing, and n is an integer. These combs are associated with linear or non-linear coupling of non-sinusoidal sources or with non-linear coupling of sinusoidal sources.
"Sub-threshold comb" means that there is no obvious single frequency that exceeds the typical levels of noise, but there is a set of frequencies with a specific spacing that, when summed together, gives something larger than expected if the same number of bins were chosen in random way and summed.
The “comb-finder” in [128] is a tool which sums the power over many possible tooth spacing and offset and checks whether that sum is larger than expected. To calculate the significance of the combined power, a cross correlation estimator is used for each of the tooth frequency and then, "the optimal way to combine these statistics is using a weighted sum" [128]. For a comb with N teeth:

$$\hat{Y}^N_{comb} = \frac{\sum_i^N \hat{Y}_i \hat{\sigma}_{Y_i}^{-2}}{\sum_i^N \hat{\sigma}_{Y_i}^{-2}} \tag{6.6}$$

and the variance

$$\hat{\sigma}^N_{comb} = \left[\sum_i^N \hat{\sigma}_{Y_i}^{-2} \right]^{-1/2} \tag{6.7}$$

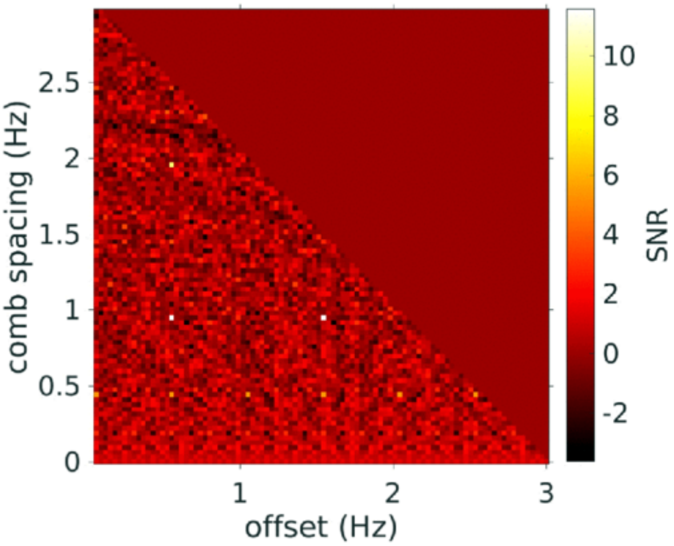

Figure 6.10: Output of the comb-finder where the pixels colour indicate $S_{m,n}$ the strength of the SNR. The loudest pixels indicate a coherent 1 Hz comb with 0.5 Hz offset identified during O1. *Credit to [128].*

where $\hat{Y}_i$ is the cross-correlation estimator and $\hat{\sigma}_{Y_i}$ the associated standard deviation and the subscript i indicates the discrete frequency bin f_i so that, for example, $\hat{Y}_i = \hat{Y}(f_i)$. Then, the SNR can be evaluated as a function of the offset number of bins m and spacing n that determine which frequency bins contribute to the comb in question. For a search over a given frequency band $\Delta f = f_{max} - f_{min}$, with a frequency resolution of δ_f, the number of teeth in a comb with bin spacing n will be given by $N = 1 + floor(\Delta f / n)$. The combined SNR statistic $S_{m,n}$ is:

$$S_{m,n} = \frac{\hat{Y}^{(m,n)}_{comb}}{\hat{\sigma}^{(n,m)}_{comb}} = \frac{\sum_i^N \hat{Y}_{m+i\cdot n} \hat{\sigma}^{-2}_{Y_{m+i\cdot n}}}{\left[\sum_i^N \hat{\sigma}^{-2}_{Y_{m+i\cdot n}}\right]^{1/2}} \tag{6.8}$$

An example from O1 data is shown in Figure 6.10.
This is an interesting application of an ensemble procedure. The comb has in general consequent peaks and the SNR $S_{m,n}$ is a sort of partial sum where you do not need to order because you know that if there is a comb the power will decrease with i. The comb finder in [128] depends on the chosen frequency band (e.g. in Figure 6.10 it is 3 Hz wide). The use of a rank truncation method could allow to increase the frequency window and to simplify the search for the offset, that is the first frequency of the comb.

Table 6.1: Table of the parameters (name, GW frequency in Hz, distance in kpc, spin-down limit) and the results inferred using the 5n-vector method (upper limit on the amplitude, upper limit on the ellipticity, p-value) for the 223 analyzed pulsars. More details about the references for the ephemerides and distance estimation can be found in [84].

Pulsar name (J2000)	f_{gw} (Hz)	Distance (kpc)	h_{sd}	$h_0^{95\%}$	$\epsilon^{95\%}$	P-value
J0023+0923	655.7	1.1	$1.3 \cdot 10^{-27}$	$9.1 \cdot 10^{-27}$	$2.2 \cdot 10^{-8}$	0.5
J0030+0451	411.1	0.3	$3.6 \cdot 10^{-27}$	$6.5 \cdot 10^{-27}$	$1.2 \cdot 10^{-8}$	0.71
J0034-0534	1065.4	1.4	$8.9 \cdot 10^{-28}$	$2.0 \cdot 10^{-26}$	$2.2 \cdot 10^{-8}$	0.046
J0101-6422	777.3	1.0	$9.7 \cdot 10^{-28}$	$1.2 \cdot 10^{-26}$	$1.9 \cdot 10^{-8}$	0.11
J0102+4839	674.7	2.3	$6.8 \cdot 10^{-28}$	$1.2 \cdot 10^{-26}$	$5.6 \cdot 10^{-8}$	0.092
J0117+5914	19.7	1.8	$1.1 \cdot 10^{-25}$	$6.6 \cdot 10^{-25}$	$2.9 \cdot 10^{-3}$	0.66
J0125-2327	544.2	0.9	$2.0 \cdot 10^{-27}$	$6.7 \cdot 10^{-27}$	$2.0 \cdot 10^{-8}$	0.82
J0154+1833	845.8	1.6	$3.4 \cdot 10^{-28}$	$1.2 \cdot 10^{-26}$	$2.5 \cdot 10^{-8}$	0.38
J0218+4232	860.9	3.1	$1.5 \cdot 10^{-27}$	$7.9 \cdot 10^{-27}$	$3.2 \cdot 10^{-8}$	1
J0340+4130	606.2	1.6	$7.2 \cdot 10^{-28}$	$9.3 \cdot 10^{-27}$	$3.8 \cdot 10^{-8}$	0.3
J0348+0432	51.1	2.1	$9.3 \cdot 10^{-28}$	$1.1 \cdot 10^{-26}$	$8.2 \cdot 10^{-6}$	0.58
J0406+3039	766.7	-	-	$8.6 \cdot 10^{-27}$	-	0.73
J0407+1607	77.8	1.3	$1.1 \cdot 10^{-27}$	$9.1 \cdot 10^{-27}$	$1.9 \cdot 10^{-6}$	0.22
J0437-4715	347.4	0.2	$8.0 \cdot 10^{-27}$	$7.4 \cdot 10^{-27}$	$9.3 \cdot 10^{-9}$	0.23
J0453+1559	43.7	0.5	$3.1 \cdot 10^{-27}$	$9.5 \cdot 10^{-27}$	$2.4 \cdot 10^{-6}$	1
J0509+0856	493.1	0.8	$9.6 \cdot 10^{-28}$	$1.1 \cdot 10^{-26}$	$3.6 \cdot 10^{-8}$	0.085
J0509+3801	26.1	1.6	$5.3 \cdot 10^{-27}$	$3.8 \cdot 10^{-26}$	$8.2 \cdot 10^{-5}$	0.78
J0557+1550	782.4	1.8	$7.5 \cdot 10^{-28}$	$8.1 \cdot 10^{-27}$	$2.3 \cdot 10^{-8}$	0.92
J0557-2948	45.8	4.3	$2.4 \cdot 10^{-28}$	$1.1 \cdot 10^{-26}$	$2.2 \cdot 10^{-5}$	0.66
J0609+2130	35.9	0.6	$2.9 \cdot 10^{-27}$	$1.7 \cdot 10^{-26}$	$7.3 \cdot 10^{-6}$	0.73
J0610-2100	518.0	3.3	$1.3 \cdot 10^{-28}$	$3.5 \cdot 10^{-26}$	$4.0 \cdot 10^{-7}$	0.4
J0613-0200	653.2	0.6	$2.2 \cdot 10^{-27}$	$7.4 \cdot 10^{-27}$	$9.9 \cdot 10^{-9}$	0.88
J0614-3329	635.2	0.6	$3.0 \cdot 10^{-27}$	$8.0 \cdot 10^{-27}$	$1.2 \cdot 10^{-8}$	0.58
J0621+1002	69.3	0.4	$2.4 \cdot 10^{-27}$	$8.9 \cdot 10^{-27}$	$7.4 \cdot 10^{-7}$	0.33
J0636-3044	506.9	0.7	$2.6 \cdot 10^{-27}$	$3.1 \cdot 10^{-26}$	$8.1 \cdot 10^{-8}$	0.71
J0636+5129	697.1	0.2	$4.2 \cdot 10^{-27}$	$7.7 \cdot 10^{-27}$	$3.1 \cdot 10^{-9}$	0.73
J0645+5158	225.9	1.2	$3.7 \cdot 10^{-28}$	$4.8 \cdot 10^{-27}$	$1.1 \cdot 10^{-7}$	0.85
J0709+0458	58.1	1.2	$2.2 \cdot 10^{-27}$	$8.6 \cdot 10^{-27}$	$2.9 \cdot 10^{-6}$	0.85
J0711-6830	364.2	0.1	$1.2 \cdot 10^{-26}$	$4.8 \cdot 10^{-27}$	$3.8 \cdot 10^{-9}$	0.92
J0721-2038	128.7	2.7	$5.1 \cdot 10^{-28}$	$6.1 \cdot 10^{-27}$	$9.4 \cdot 10^{-7}$	0.55
J0732+2314	489.0	1.1	$8.5 \cdot 10^{-28}$	$5.9 \cdot 10^{-27}$	$2.7 \cdot 10^{-8}$	0.98

Pulsar name (J2000)	f_{gw} (Hz)	Distance (kpc)	h_{sd}	$h_0^{95\%}$	$\epsilon^{95\%}$	P-value
J0740+6620	693.1	1.1	$1.1 \cdot 10^{-27}$	$7.6 \cdot 10^{-27}$	$1.7 \cdot 10^{-8}$	0.68
J0751+1807	574.9	0.6	$1.9 \cdot 10^{-27}$	$7.7 \cdot 10^{-27}$	$1.3 \cdot 10^{-8}$	0.77
J0824+0028	202.8	1.7	$1.8 \cdot 10^{-27}$	$1.1 \cdot 10^{-26}$	$4.2 \cdot 10^{-7}$	0.01
J0835-4510	22.4	0.3	$3.4 \cdot 10^{-24}$	$1.1 \cdot 10^{-25}$	$5.6 \cdot 10^{-5}$	0.26
J0921-5202	206.6	0.4	$2.9 \cdot 10^{-27}$	$6.7 \cdot 10^{-27}$	$6.0 \cdot 10^{-8}$	0.26
J0931-1902	431.2	3.7	$1.8 \cdot 10^{-28}$	$5.9 \cdot 10^{-27}$	$1.1 \cdot 10^{-7}$	0.82
J0955-6150	1000.3	2.2	$9.9 \cdot 10^{-28}$	$1.3 \cdot 10^{-26}$	$2.6 \cdot 10^{-8}$	0.5
J1012-4235	644.9	0.4	$3.1 \cdot 10^{-27}$	$7.9 \cdot 10^{-27}$	$6.6 \cdot 10^{-9}$	0.62
J1012+5307	380.5	0.7	$1.6 \cdot 10^{-27}$	$4.7 \cdot 10^{-27}$	$2.2 \cdot 10^{-8}$	0.97
J1017-7156	855.2	3.5	$2.5 \cdot 10^{-28}$	$7.3 \cdot 10^{-27}$	$3.3 \cdot 10^{-8}$	0.98
J1022+1001	121.6	0.6	$1.8 \cdot 10^{-27}$	$6.2 \cdot 10^{-27}$	$2.5 \cdot 10^{-7}$	0.64
J1024-0719	387.4	1.2	-	$6.3 \cdot 10^{-27}$	$4.8 \cdot 10^{-8}$	0.7
J1035-6720	696.4	1.5	$2.2 \cdot 10^{-27}$	$6.6 \cdot 10^{-27}$	$1.9 \cdot 10^{-8}$	0.92
J1036-8317	586.7	0.9	$2.6 \cdot 10^{-27}$	$6.5 \cdot 10^{-27}$	$1.7 \cdot 10^{-8}$	0.76
J1038+0032	69.3	6.0	$2.1 \cdot 10^{-28}$	$7.8 \cdot 10^{-27}$	$9.2 \cdot 10^{-6}$	0.55
J1045-4509	267.6	0.6	$2.1 \cdot 10^{-27}$	$5.4 \cdot 10^{-27}$	$4.2 \cdot 10^{-8}$	0.7
J1101-6101	31.8	7.0	$4.2 \cdot 10^{-26}$	$2.3 \cdot 10^{-26}$	$1.5 \cdot 10^{-4}$	0.61
J1101-6424	391.4	2.2	$2.2 \cdot 10^{-28}$	$6.0 \cdot 10^{-27}$	$8.0 \cdot 10^{-8}$	0.6
J1103-5403	589.5	1.7	$5.0 \cdot 10^{-28}$	$5.5 \cdot 10^{-27}$	$2.5 \cdot 10^{-8}$	1
J1125-5825	644.7	1.7	$2.0 \cdot 10^{-27}$	$6.9 \cdot 10^{-27}$	$2.7 \cdot 10^{-8}$	0.81
J1125-6014	760.3	1.4	$7.1 \cdot 10^{-28}$	$7.4 \cdot 10^{-27}$	$1.7 \cdot 10^{-8}$	0.85
J1125+7819	476.0	0.9	-	$8.1 \cdot 10^{-27}$	$3.0 \cdot 10^{-8}$	0.3
J1142+0119	394.1	2.2	-	$7.4 \cdot 10^{-27}$	$9.8 \cdot 10^{-8}$	0.42
J1207-5050	413.0	1.3	$6.9 \cdot 10^{-28}$	$8.3 \cdot 10^{-27}$	$5.9 \cdot 10^{-8}$	0.18
J1216-6410	565.1	1.1	$5.0 \cdot 10^{-28}$	$8.3 \cdot 10^{-27}$	$2.7 \cdot 10^{-8}$	0.35
J1231-1411	542.9	0.4	$2.9 \cdot 10^{-27}$	$6.8 \cdot 10^{-27}$	$9.2 \cdot 10^{-9}$	0.84
J1300+1240	321.6	0.6	-	$6.3 \cdot 10^{-27}$	$3.5 \cdot 10^{-8}$	0.58
J1302-3258	530.4	1.4	$7.4 \cdot 10^{-28}$	$6.7 \cdot 10^{-27}$	$3.2 \cdot 10^{-8}$	0.76
J1302-6350	41.9	2.3	$7.7 \cdot 10^{-26}$	$9.9 \cdot 10^{-27}$	$1.2 \cdot 10^{-5}$	0.97
J1312+0051	473.0	1.5	$7.6 \cdot 10^{-28}$	$9.9 \cdot 10^{-27}$	$6.1 \cdot 10^{-8}$	0.2
J1327-0755	746.8	25.0	-	$7.8 \cdot 10^{-27}$	$3.3 \cdot 10^{-7}$	0.91
J1327+3423	48.2	-	-	$1.3 \cdot 10^{-26}$	-	0.5
J1337-6423	212.2	5.9	$1.9 \cdot 10^{-28}$	$4.2 \cdot 10^{-27}$	$5.3 \cdot 10^{-7}$	0.97
J1400-1431	648.5	0.3	$5.1 \cdot 10^{-28}$	$1.2 \cdot 10^{-26}$	$7.5 \cdot 10^{-9}$	0.094
J1411+2551	32.0	1.1	$8.5 \cdot 10^{-28}$	$2.8 \cdot 10^{-26}$	$2.9 \cdot 10^{-5}$	0.33

Pulsar name (J2000)	f_{gw} (Hz)	Distance (kpc)	h_{sd}	$h_0^{95\%}$	$\epsilon^{95\%}$	P-value
J1412+7922	33.8	2.0	$9.5 \cdot 10^{-26}$	$2.0{\cdot}10^{-26}$	$3.3 \cdot 10^{-5}$	0.48
J1420-5625	58.6	1.3	$8.5 \cdot 10^{-28}$	$7.8{\cdot}10^{-27}$	$2.9 \cdot 10^{-6}$	0.91
J1421-4409	313.2	2.1	$3.8 \cdot 10^{-28}$	$6.0{\cdot}10^{-27}$	$1.2 \cdot 10^{-7}$	0.58
J1431-5740	486.6	3.5	$2.8 \cdot 10^{-28}$	$1.2{\cdot}10^{-26}$	$1.8 \cdot 10^{-7}$	0.01
J1435-6100	214.0	2.8	$4.6 \cdot 10^{-28}$	$4.7{\cdot}10^{-27}$	$2.7 \cdot 10^{-7}$	0.83
J1439-5501	69.8	0.7	$2.7 \cdot 10^{-27}$	$8.0{\cdot}10^{-27}$	$1.0 \cdot 10^{-6}$	0.29
J1446-4701	911.3	1.5	$1.1 \cdot 10^{-27}$	$8.0{\cdot}10^{-27}$	$1.4 \cdot 10^{-8}$	0.97
J1453+1902	345.3	1.3	$8.0 \cdot 10^{-28}$	$7.0{\cdot}10^{-27}$	$7.1 \cdot 10^{-8}$	0.44
J1455-3330	250.4	1.0	$1.3 \cdot 10^{-27}$	$6.5{\cdot}10^{-27}$	$9.9 \cdot 10^{-8}$	0.46
J1502-6752	74.8	7.7	$3.0 \cdot 10^{-28}$	$7.1{\cdot}10^{-27}$	$9.3 \cdot 10^{-6}$	0.48
J1513-2550	943.8	4.0	$6.5 \cdot 10^{-28}$	$9.7{\cdot}10^{-27}$	$4.1 \cdot 10^{-8}$	0.83
J1514-4946	557.2	0.9	$1.6 \cdot 10^{-27}$	$8.4{\cdot}10^{-27}$	$2.3 \cdot 10^{-8}$	0.48
J1518+0204A	360.1	8.0	$2.8 \cdot 10^{-28}$	$5.6{\cdot}10^{-27}$	$3.3 \cdot 10^{-7}$	1
J1518+4904	48.9	1.0	$6.3 \cdot 10^{-28}$	$1.0{\cdot}10^{-26}$	$3.8 \cdot 10^{-6}$	0.93
J1525-5545	176.1	3.1	$8.7 \cdot 10^{-28}$	$4.1{\cdot}10^{-27}$	$4.0 \cdot 10^{-7}$	1
J1528-3146	32.9	0.8	$2.1 \cdot 10^{-27}$	$2.5{\cdot}10^{-26}$	$1.7 \cdot 10^{-5}$	0.41
J1529-3828	235.7	4.3	$3.4 \cdot 10^{-28}$	$4.4{\cdot}10^{-27}$	$3.2 \cdot 10^{-7}$	0.97
J1537+1155	52.8	1.1	$6.0 \cdot 10^{-27}$	$1.3{\cdot}10^{-26}$	$4.8 \cdot 10^{-6}$	0.17
J1543-5149	972.3	1.1	$1.9 \cdot 10^{-27}$	$1.5{\cdot}10^{-26}$	$1.8 \cdot 10^{-8}$	0.089
J1544+4937	926.2	3.0	$3.1 \cdot 10^{-28}$	$1.0{\cdot}10^{-26}$	$3.3 \cdot 10^{-8}$	0.59
J1545-4550	559.4	2.2	$1.4 \cdot 10^{-27}$	$9.6{\cdot}10^{-27}$	$6.4 \cdot 10^{-8}$	0.31
J1547-5709	466.1	2.7	$3.9 \cdot 10^{-28}$	$7.1{\cdot}10^{-27}$	$8.3 \cdot 10^{-8}$	0.48
J1551-0658	281.9	1.3	$1.0 \cdot 10^{-27}$	$8.5{\cdot}10^{-27}$	$1.3 \cdot 10^{-7}$	0.16
J1600-3053	555.9	3.0	$4.0 \cdot 10^{-28}$	$1.0{\cdot}10^{-26}$	$9.2 \cdot 10^{-8}$	0.23
J1603-7202	134.8	3.4	$2.5 \cdot 10^{-28}$	$4.6{\cdot}10^{-27}$	$8.2 \cdot 10^{-7}$	0.91
J1614-2230	634.8	0.7	$1.2 \cdot 10^{-27}$	$7.5{\cdot}10^{-27}$	$1.2 \cdot 10^{-8}$	0.77
J1618-3921	166.8	5.5	$3.1 \cdot 10^{-28}$	$9.2{\cdot}10^{-27}$	$1.7 \cdot 10^{-6}$	0.038
J1618-4624	337.2	3.0	$1.9 \cdot 10^{-28}$	$8.2{\cdot}10^{-27}$	$2.1 \cdot 10^{-7}$	0.13
J1622-6617	84.7	4.0	$2.9 \cdot 10^{-28}$	$5.3{\cdot}10^{-27}$	$2.8 \cdot 10^{-6}$	0.9
J1623-2631	180.6	1.8	$1.3 \cdot 10^{-27}$	$5.2{\cdot}10^{-27}$	$2.7 \cdot 10^{-7}$	0.88
J1628-3205	622.7	1.2	-	$7.1 \cdot 10^{-27}$	$2.1 \cdot 10^{-8}$	0.81
J1629-6902	333.3	1.0	$1.1 \cdot 10^{-27}$	$5.8{\cdot}10^{-27}$	$4.7 \cdot 10^{-8}$	0.83
J1630+3734	602.8	1.2	$1.1 \cdot 10^{-27}$	$8.1{\cdot}10^{-27}$	$2.5 \cdot 10^{-8}$	0.49
J1640+2224	632.2	1.5	$3.4 \cdot 10^{-28}$	$1.1{\cdot}10^{-26}$	$3.9 \cdot 10^{-8}$	0.17
J1641+3627A	192.7	7.1	$3.2 \cdot 10^{-28}$	$4.2{\cdot}10^{-27}$	$7.6 \cdot 10^{-7}$	1

Pulsar name (J2000)	f_{gw} (Hz)	Distance (kpc)	h_{sd}	$h_0^{95\%}$	$\epsilon^{95\%}$	P-value
J1643-1224	432.7	1.2	$1.3 \cdot 10^{-27}$	$1.1 \cdot 10^{-26}$	$6.7 \cdot 10^{-8}$	0.042
J1652-4838	528.4	-	-	$5.9 \cdot 10^{-27}$	-	0.91
J1653-2054	484.4	2.6	$5.0 \cdot 10^{-28}$	$1.0 \cdot 10^{-26}$	$1.1 \cdot 10^{-7}$	0.13
J1658-5324	819.9	0.9	$1.9 \cdot 10^{-27}$	$1.1 \cdot 10^{-26}$	$1.4 \cdot 10^{-8}$	0.27
J1705-1903	806.4	2.4	$9.8 \cdot 10^{-28}$	$1.4 \cdot 10^{-26}$	$5.0 \cdot 10^{-8}$	0.091
J1708-3506	443.9	3.3	$3.4 \cdot 10^{-28}$	$6.2 \cdot 10^{-27}$	$9.9 \cdot 10^{-8}$	0.76
J1709+2313	431.9	2.2	$1.9 \cdot 10^{-28}$	$6.4 \cdot 10^{-27}$	$7.1 \cdot 10^{-8}$	0.68
J1713+0747	437.6	1.0	$1.1 \cdot 10^{-27}$	$7.1 \cdot 10^{-27}$	$3.5 \cdot 10^{-8}$	0.57
J1719-1438	345.4	0.3	$2.6 \cdot 10^{-27}$	$7.7 \cdot 10^{-27}$	$2.1 \cdot 10^{-8}$	0.3
J1721-2457	572.0	1.4	-	$7.9 \cdot 10^{-27}$	$3.1 \cdot 10^{-8}$	0.6
J1727-2946	73.8	1.9	$1.3 \cdot 10^{-27}$	$9.4 \cdot 10^{-27}$	$3.1 \cdot 10^{-6}$	0.2
J1729-2117	30.2	1.0	$1.3 \cdot 10^{-27}$	$2.6 \cdot 10^{-26}$	$2.6 \cdot 10^{-5}$	0.85
J1730-2304	246.2	0.5	$2.0 \cdot 10^{-27}$	$5.7 \cdot 10^{-27}$	$4.2 \cdot 10^{-8}$	0.66
J1732-5049	376.5	1.9	$6.2 \cdot 10^{-28}$	$6.4 \cdot 10^{-27}$	$8.0 \cdot 10^{-8}$	0.52
J1737-0811	479.0	0.2	$5.4 \cdot 10^{-27}$	$8.6 \cdot 10^{-27}$	$7.4 \cdot 10^{-9}$	0.43
J1738+0333	341.9	1.5	$1.1 \cdot 10^{-27}$	$5.4 \cdot 10^{-27}$	$6.4 \cdot 10^{-8}$	0.9
J1741+1351	533.7	1.1	$2.1 \cdot 10^{-27}$	$1.4 \cdot 10^{-26}$	$4.9 \cdot 10^{-8}$	0.011
J1744-1134	490.9	0.4	$2.6 \cdot 10^{-27}$	$1.1 \cdot 10^{-26}$	$1.8 \cdot 10^{-8}$	0.099
J1745-0952	103.2	0.2	$7.5 \cdot 10^{-27}$	$8.8 \cdot 10^{-27}$	$1.8 \cdot 10^{-7}$	0.15
J1745+1017	754.1	1.2	$6.0 \cdot 10^{-28}$	$1.1 \cdot 10^{-26}$	$2.2 \cdot 10^{-8}$	0.35
J1747-4036	1215.4	7.2	$2.9 \cdot 10^{-28}$	$2.1 \cdot 10^{-26}$	$9.7 \cdot 10^{-8}$	0.035
J1748-2446A	173.0	6.9	$3.3 \cdot 10^{-28}$	$5.5 \cdot 10^{-27}$	$1.2 \cdot 10^{-6}$	0.72
J1748-3009	206.5	5.0	-	$8.1 \cdot 10^{-27}$	$9.0 \cdot 10^{-7}$	0.13
J1750-2536	57.6	3.2	$5.1 \cdot 10^{-28}$	$8.9 \cdot 10^{-27}$	$8.1 \cdot 10^{-6}$	0.72
J1751-2857	510.9	1.1	$1.2 \cdot 10^{-27}$	$6.4 \cdot 10^{-26}$	$2.5 \cdot 10^{-7}$	0.089
J1753-1914	31.8	2.9	$1.6 \cdot 10^{-27}$	$2.6 \cdot 10^{-26}$	$7.2 \cdot 10^{-5}$	0.54
J1753-2240	21.0	3.2	$8.0 \cdot 10^{-28}$	$1.8 \cdot 10^{-25}$	$1.2 \cdot 10^{-3}$	0.33
J1755-3716	156.4	8.2	$1.5 \cdot 10^{-28}$	$5.2 \cdot 10^{-27}$	$1.7 \cdot 10^{-6}$	0.77
J1756-2251	70.3	0.7	$6.6 \cdot 10^{-27}$	$8.8 \cdot 10^{-27}$	$1.2 \cdot 10^{-6}$	0.43
J1757-1854	93.0	19.6	$4.6 \cdot 10^{-28}$	$1.2 \cdot 10^{-26}$	$2.5 \cdot 10^{-5}$	0.016
J1757-5322	225.5	0.9	$1.5 \cdot 10^{-27}$	$7.2 \cdot 10^{-27}$	$1.3 \cdot 10^{-7}$	0.18
J1801-1417	551.7	1.1	$7.4 \cdot 10^{-28}$	$9.0 \cdot 10^{-27}$	$3.1 \cdot 10^{-8}$	0.4
J1801-3210	268.3	6.1	-	$8.7 \cdot 10^{-27}$	$7.0 \cdot 10^{-7}$	0.089
J1802-2124	158.1	0.8	$2.5 \cdot 10^{-27}$	$6.7 \cdot 10^{-27}$	$1.9 \cdot 10^{-7}$	0.41
J1804-0735	86.6	7.8	$2.9 \cdot 10^{-28}$	$7.8 \cdot 10^{-27}$	$7.7 \cdot 10^{-6}$	0.39

Pulsar name (J2000)	f_{gw} (Hz)	Distance (kpc)	h_{sd}	$h_0^{95\%}$	$\epsilon^{95\%}$	P-value
J1804-2717	214.1	0.8	$1.9 \cdot 10^{-27}$	$6.5{\cdot}10^{-27}$	$1.1 \cdot 10^{-7}$	0.39
J1807-2459A	653.7	3.0	$7.6 \cdot 10^{-28}$	$9.5{\cdot}10^{-27}$	$6.3 \cdot 10^{-8}$	0.39
J1809-1917	24.2	3.3	$1.4 \cdot 10^{-25}$	$5.5{\cdot}10^{-26}$	$2.9 \cdot 10^{-4}$	0.88
J1810+1744	1202.8	2.4	$5.5 \cdot 10^{-28}$	$1.2{\cdot}10^{-26}$	$1.8 \cdot 10^{-8}$	0.84
J1810-2005	60.9	3.5	$2.9 \cdot 10^{-28}$	$9.6{\cdot}10^{-27}$	$8.6 \cdot 10^{-6}$	0.48
J1811-2405	751.7	1.8	$9.9 \cdot 10^{-28}$	$1.2{\cdot}10^{-26}$	$3.7 \cdot 10^{-8}$	0.2
J1813-1749	44.7	6.2	$2.2 \cdot 10^{-25}$	$1.1{\cdot}10^{-26}$	$3.2 \cdot 10^{-5}$	0.83
J1813-2621	451.5	3.2	-	$5.5 \cdot 10^{-27}$	$8.0 \cdot 10^{-8}$	0.97
J1821+0155	59.2	1.7	$4.3 \cdot 10^{-28}$	$9.1{\cdot}10^{-27}$	$4.2 \cdot 10^{-6}$	0.91
J1823-3021A	367.6	7.9	$2.9 \cdot 10^{-28}$	$8.7{\cdot}10^{-27}$	$4.8 \cdot 10^{-7}$	0.14
J1824-2452A	654.8	5.5	$4.1 \cdot 10^{-28}$	$8.6{\cdot}10^{-27}$	$1.0 \cdot 10^{-7}$	0.56
J1825-0319	439.2	3.9	$2.6 \cdot 10^{-28}$	$8.6{\cdot}10^{-27}$	$1.6 \cdot 10^{-7}$	0.27
J1826-2415	425.9	2.7	$5.7 \cdot 10^{-28}$	$7.0{\cdot}10^{-27}$	$10.0 \cdot 10^{-8}$	0.52
J1828-1101	27.8	4.8	$7.7 \cdot 10^{-26}$	$3.2{\cdot}10^{-26}$	$1.9 \cdot 10^{-4}$	0.92
J1829+2456	48.8	0.9	$10.0 \cdot 10^{-28}$	$1.4{\cdot}10^{-26}$	$5.1 \cdot 10^{-6}$	0.6
J1832-0836	735.5	1.6	-	$1.3 \cdot 10^{-26}$	$3.7 \cdot 10^{-8}$	0.1
J1833-0827	23.4	4.5	$5.9 \cdot 10^{-26}$	$6.1{\cdot}10^{-26}$	$4.7 \cdot 10^{-4}$	0.9
J1835-0114	390.9	3.5	$2.7 \cdot 10^{-28}$	$6.1{\cdot}10^{-27}$	$1.3 \cdot 10^{-7}$	0.77
J1838-0655	28.4	6.6	$1.0 \cdot 10^{-25}$	$3.5{\cdot}10^{-26}$	$2.7 \cdot 10^{-4}$	0.67
J1840-0643	56.2	5.0	$2.6 \cdot 10^{-28}$	$8.7{\cdot}10^{-27}$	$1.3 \cdot 10^{-5}$	0.8
J1841+0130	67.2	4.2	$3.2 \cdot 10^{-27}$	$1.2{\cdot}10^{-26}$	$1.1 \cdot 10^{-5}$	0.042
J1843-1113	1083.6	1.3	$1.4 \cdot 10^{-27}$	$2.2{\cdot}10^{-26}$	$2.2 \cdot 10^{-8}$	0.019
J1843-1448	365.5	3.5	-	$8.2 \cdot 10^{-27}$	$2.0 \cdot 10^{-7}$	0.23
J1849-0001	51.9	7.0	$7.0 \cdot 10^{-26}$	$1.5{\cdot}10^{-26}$	$3.8 \cdot 10^{-5}$	0.081
J1853+1303	488.8	1.3	$8.9 \cdot 10^{-28}$	$6.8{\cdot}10^{-27}$	$3.6 \cdot 10^{-8}$	0.8
J1856+0245	24.7	6.3	$1.1 \cdot 10^{-25}$	$5.9{\cdot}10^{-26}$	$5.7 \cdot 10^{-4}$	0.64
J1857+0943	373.0	1.2	$1.2 \cdot 10^{-27}$	$6.6{\cdot}10^{-27}$	$5.3 \cdot 10^{-8}$	0.64
J1902-5105	1147.8	1.6	$1.1 \cdot 10^{-27}$	$1.1{\cdot}10^{-26}$	$1.3 \cdot 10^{-8}$	0.78
J1903+0327	930.3	6.1	$3.9 \cdot 10^{-28}$	$1.4{\cdot}10^{-26}$	$9.4 \cdot 10^{-8}$	0.23
J1903-7051	555.9	0.9	$1.3 \cdot 10^{-27}$	$6.2{\cdot}10^{-27}$	$1.8 \cdot 10^{-8}$	0.9
J1904+0412	28.1	4.6	$2.2 \cdot 10^{-28}$	$2.9{\cdot}10^{-26}$	$1.6 \cdot 10^{-4}$	0.97
J1905+0400	528.5	1.1	$8.0 \cdot 10^{-28}$	$7.0{\cdot}10^{-27}$	$2.5 \cdot 10^{-8}$	0.76
J1909-3744	678.6	1.1	$6.6 \cdot 10^{-28}$	$1.0{\cdot}10^{-26}$	$2.4 \cdot 10^{-8}$	0.26
J1910+1256	401.3	1.5	$7.2 \cdot 10^{-28}$	$8.3{\cdot}10^{-27}$	$7.3 \cdot 10^{-8}$	0.27
J1911-1114	551.6	1.1	$1.3 \cdot 10^{-27}$	$8.2{\cdot}10^{-27}$	$2.7 \cdot 10^{-8}$	0.56

Pulsar name (J2000)	f_{gw} (Hz)	Distance (kpc)	h_{sd}	$h_0^{95\%}$	$\epsilon^{95\%}$	P-value
J1911+1347	432.3	1.4	$1.1 \cdot 10^{-27}$	$7.1{\cdot}10^{-27}$	$4.9 \cdot 10^{-8}$	0.52
J1913+1011	55.7	4.6	$5.3 \cdot 10^{-26}$	$8.6{\cdot}10^{-27}$	$1.2 \cdot 10^{-5}$	0.82
J1914+0659	108.0	8.5	$1.2 \cdot 10^{-28}$	$8.2{\cdot}10^{-27}$	$5.7 \cdot 10^{-6}$	0.22
J1915+1606	33.9	5.2	$1.9 \cdot 10^{-27}$	$2.6{\cdot}10^{-26}$	$1.1 \cdot 10^{-4}$	0.24
J1918-0642	261.6	1.1	$1.3 \cdot 10^{-27}$	$6.5{\cdot}10^{-27}$	$9.9 \cdot 10^{-8}$	0.49
J1923+2515	528.0	1.2	$9.1 \cdot 10^{-28}$	$1.0{\cdot}10^{-26}$	$4.1 \cdot 10^{-8}$	0.15
J1925+1720	26.4	5.1	$5.9 \cdot 10^{-26}$	$7.0{\cdot}10^{-26}$	$4.8 \cdot 10^{-4}$	0.035
J1928+1746	29.1	4.3	$8.2 \cdot 10^{-26}$	$3.4{\cdot}10^{-26}$	$1.6 \cdot 10^{-4}$	0.54
J1933-6211	564.4	0.7	$1.1 \cdot 10^{-27}$	$7.2{\cdot}10^{-27}$	$1.4 \cdot 10^{-8}$	0.6
J1935+2025	25.0	4.6	$1.5 \cdot 10^{-25}$	$4.9{\cdot}10^{-26}$	$3.4 \cdot 10^{-4}$	0.66
J1939+2134	1283.9	4.8	$1.4 \cdot 10^{-27}$	$1.4{\cdot}10^{-26}$	$3.8 \cdot 10^{-8}$	0.65
J1943+2210	393.4	6.8	$1.6 \cdot 10^{-28}$	$6.6{\cdot}10^{-27}$	$2.7 \cdot 10^{-7}$	0.55
J1944+0907	385.7	1.2	$7.4 \cdot 10^{-28}$	$6.1{\cdot}10^{-27}$	$4.7 \cdot 10^{-8}$	0.76
J1946+3417	630.9	6.9	$6.5 \cdot 10^{-29}$	$9.4{\cdot}10^{-27}$	$1.6 \cdot 10^{-7}$	0.32
J1946-5403	737.8	1.1	$7.0 \cdot 10^{-28}$	$7.5{\cdot}10^{-27}$	$1.5 \cdot 10^{-8}$	0.81
J1949+3106	152.2	7.5	$2.9 \cdot 10^{-28}$	$5.6{\cdot}10^{-27}$	$1.7 \cdot 10^{-6}$	0.72
J1950+2414	464.6	7.3	$2.4 \cdot 10^{-28}$	$6.8{\cdot}10^{-27}$	$2.2 \cdot 10^{-7}$	0.69
J1952+3252	50.6	3.0	$1.0 \cdot 10^{-25}$	$1.3{\cdot}10^{-26}$	$1.5 \cdot 10^{-5}$	0.21
J1955+2527	410.4	8.2	$1.5 \cdot 10^{-28}$	$7.7{\cdot}10^{-27}$	$3.6 \cdot 10^{-7}$	0.34
J1955+2908	326.1	6.3	$2.9 \cdot 10^{-28}$	$6.3{\cdot}10^{-27}$	$3.6 \cdot 10^{-7}$	0.54
J2007+2722	81.6	7.1	$7.1 \cdot 10^{-28}$	$1.1{\cdot}10^{-26}$	$1.1 \cdot 10^{-5}$	0.032
J2010-1323	382.9	1.2	$5.3 \cdot 10^{-28}$	$8.3{\cdot}10^{-27}$	$6.2 \cdot 10^{-8}$	0.23
J2017+0603	690.6	1.4	$9.6 \cdot 10^{-28}$	$1.2{\cdot}10^{-26}$	$3.3 \cdot 10^{-8}$	0.16
J2019+2425	508.3	1.2	$4.4 \cdot 10^{-28}$	$5.5{\cdot}10^{-26}$	$2.3 \cdot 10^{-7}$	0.044
J2022+2534	755.9	-	-	$7.6 \cdot 10^{-27}$	-	0.91
J2033+1734	336.2	1.7	$5.5 \cdot 10^{-28}$	$5.2{\cdot}10^{-27}$	$7.6 \cdot 10^{-8}$	0.92
J2039-3616	610.7	1.7	$7.6 \cdot 10^{-28}$	$6.8{\cdot}10^{-27}$	$2.9 \cdot 10^{-8}$	0.84
J2043+2740	20.8	1.5	$6.3 \cdot 10^{-26}$	$1.7{\cdot}10^{-25}$	$5.6 \cdot 10^{-4}$	0.31
J2045+3633	63.1	5.6	$6.2 \cdot 10^{-28}$	$9.0{\cdot}10^{-27}$	$1.2 \cdot 10^{-5}$	0.35
J2047+1053	466.6	2.8	$6.4 \cdot 10^{-28}$	$8.2{\cdot}10^{-27}$	$10.0 \cdot 10^{-8}$	0.39
J2053+4650	158.9	3.8	$7.8 \cdot 10^{-28}$	$4.7{\cdot}10^{-27}$	$6.7 \cdot 10^{-7}$	0.91
J2055+3829	957.3	4.6	$1.1 \cdot 10^{-28}$	$1.9{\cdot}10^{-26}$	$9.1 \cdot 10^{-8}$	0.0091
J2124-3358	405.6	0.4	$2.3 \cdot 10^{-27}$	$7.8{\cdot}10^{-27}$	$2.0 \cdot 10^{-8}$	0.32
J2129-5721	536.7	7.0	$2.6 \cdot 10^{-28}$	$7.7{\cdot}10^{-27}$	$1.8 \cdot 10^{-7}$	0.42
J2144-5237	396.7	1.7	$6.5 \cdot 10^{-28}$	$6.2{\cdot}10^{-27}$	$6.2 \cdot 10^{-8}$	0.59

Pulsar name (J2000)	f_{gw} (Hz)	Distance (kpc)	h_{sd}	$h_0^{95\%}$	$\epsilon^{95\%}$	P-value
J2145-0750	124.6	0.8	$1.3 \cdot 10^{-27}$	$5.4 \cdot 10^{-27}$	$2.7 \cdot 10^{-7}$	0.85
J2150-0326	569.7	-	-	$7.8 \cdot 10^{-27}$	-	0.71
J2205+6012	828.0	3.5	$6.5 \cdot 10^{-28}$	$9.8 \cdot 10^{-27}$	$4.8 \cdot 10^{-8}$	0.53
J2214+3000	641.2	0.6	$2.7 \cdot 10^{-27}$	$8.5 \cdot 10^{-27}$	$1.2 \cdot 10^{-8}$	0.51
J2222-0137	60.9	0.3	$2.0 \cdot 10^{-27}$	$7.3 \cdot 10^{-27}$	$5.0 \cdot 10^{-7}$	0.91
J2229+2643	671.6	1.8	$3.1 \cdot 10^{-28}$	$1.1 \cdot 10^{-26}$	$4.2 \cdot 10^{-8}$	0.2
J2229+6114	38.7	3.0	$3.3 \cdot 10^{-25}$	$1.3 \cdot 10^{-26}$	$2.5 \cdot 10^{-5}$	0.76
J2234+0611	559.2	1.5	$8.2 \cdot 10^{-28}$	$1.3 \cdot 10^{-26}$	$5.9 \cdot 10^{-8}$	0.08
J2234+0944	551.4	0.8	$1.9 \cdot 10^{-27}$	$1.1 \cdot 10^{-26}$	$2.8 \cdot 10^{-8}$	0.11
J2235+1506	33.5	1.5	$6.5 \cdot 10^{-28}$	$2.3 \cdot 10^{-26}$	$2.9 \cdot 10^{-5}$	0.53
J2236-5527	289.5	2.0	$4.6 \cdot 10^{-28}$	$4.3 \cdot 10^{-27}$	$1.0 \cdot 10^{-7}$	0.97
J2241-5236	914.6	1.1	$1.2 \cdot 10^{-27}$	$1.1 \cdot 10^{-26}$	$1.3 \cdot 10^{-8}$	0.44
J2256-1024	871.6	1.3	$1.3 \cdot 10^{-27}$	$1.6 \cdot 10^{-26}$	$2.7 \cdot 10^{-8}$	0.057
J2302+4442	385.2	0.9	$1.5 \cdot 10^{-27}$	$7.0 \cdot 10^{-27}$	$3.8 \cdot 10^{-8}$	0.39
J2317+1439	580.5	2.2	$3.3 \cdot 10^{-28}$	$7.7 \cdot 10^{-27}$	$4.7 \cdot 10^{-8}$	0.67
J2322+2057	415.9	1.0	$6.5 \cdot 10^{-28}$	$6.1 \cdot 10^{-27}$	$3.4 \cdot 10^{-8}$	0.8
J2322-2650	577.5	0.2	$1.2 \cdot 10^{-27}$	$7.9 \cdot 10^{-27}$	$5.2 \cdot 10^{-9}$	0.56

Conclusion

This PhD thesis tries to improve the detection efficiency for continuous gravitational wave (CW) signals combining information from weak sources, such as known pulsars, that could not be individually identified. “Known” indicates objects like the Crab or Vela pulsar, whose position, frequency and frequency evolution are known with high accuracy. This search, that is a targeted search, assumes that the gravitational frequency, emitted by non-axisymmetric neutron star rotating around one of its principal axes of inertia, would be proportional to the rotation frequency of the star. In the simplest model of a rigid body rotating around a principal axis of inertia, the gravitational wave frequency is exactly twice the rotation frequency of the source.

The 5n-vector method, developed by the Rome Virgo group, is one of the three pipelines used in the LIGO and Virgo Collaborations for the detection of a CW signal. In Chapter 3, I review the 5-vector pipeline describing the improvement due to my research: the implementation of the heterodyne correction for pulsars in binary systems, and the optimization of the multidetector extension weighting the considered detectors according to the sensitivity and observation time. For the first time, the 5-vector method can be applied to binary systems for the targeted search and compared with the Bayesian results. The single harmonic search (i.e. gravitational wave frequency exactly twice the rotation frequency of the source), described in Chapter 6, on the 223 known pulsars in Table 6.1 using O3 data shows very good agreement with the Bayesian results in [84]. There is no evidence of a CW signal from the analyzed pulsars and hence, upper limits on the amplitude and on the ellipticity can be set. The pulsar with the smallest upper limit on the strain amplitude is J1745-0952 with 4.72×10^{-27} while the best limit on the ellipticity is 5.26×10^{-9} for J0711-6830.

The single pulsar analysis can be seen as an hypothesis test where the null hypothesis of pure noise is tested against the alternative hypothesis of the presence of a CW signal in the data. To improve the detection probability, I propose a multiple test for the targeted search of CWs from an ensemble of known pulsars, combining multi-detector single pulsar statistics defined through the 5n-vector method. In order to maximize the detection probability when few signals are expected near the detection threshold, I propose a rank-truncation method to select the most promising sources within the ensemble, based on the p-values for single pulsar detection. To rank pulsars according to the p-values, I define a normalized statistic of single pulsar for the 5n-vector method that entails the same noise distribution for each pulsar. The normalized statistic implies also analytical signal distribution that can be easily and effectively used in theoretical test without considering real data.

The ensemble statistics $T(k)$ for the rank truncation method is defined as the partial sum of the k largest order statistics to control the look-elsewhere effect. The convolution of order statistics has in general no simple expression; to reconstruct the $T(k)$ noise and signal distributions for each k, I use a Monte Carlo procedure that can be easily generalized to real data. Reconstructing the $T(k)$ noise distributions for each k, I can compute the p-value of ensemble as a function of k, that is a p-value for the overall hypothesis of the presence of CWs from the ensemble.

To validate the proposed ensemble method, several tests have been described in Chapter 5 using both the theoretical distributions and also real data considering hardware and software injections. The obtained results show a significant improvement in the detection efficiency and a dependence mainly on the power of the combined individual tests and not on the form of the underlying data.

In case of no detection, I propose different procedures to set upper limits using the ensemble procedure and the statistic $T(N)$, i.e. the statistic for the entire ensemble. Using a mixed frequentist-Bayesian procedure, I can constrain the value of the global parameter Λ that fixes the $T(N)$ signal distribution. Assuming a common exponential distribution for the ellipticities, I propose two independent hierarchical procedures to set upper limit on the mean μ_ϵ of the exponential.

Chapter 6 shows the application of the ensemble procedure to the set of 223 pulsars in Table 6.1 considering O3 data. Three different ensemble are analyzed: the full set for the LIGO and Virgo detectors, the millisecond pulsar set for the two LIGO detectors and the high value pulsars set for the two LIGO detectors. The results are shown in the "summary plot" in Figures 6.5, 6.6 and 6.7: the top-left plot shows the scale and shape parameters of the Gamma distribution fitted to the experimental noise distributions for the statistic of single pulsar, the top-right plots show the results of the fits using a Gamma distribution for the $T(k)$ noise distributions for each k while the bottom plot compare the ordered single pulsar p-values (red dots) with the p-value of ensemble (blue line).

There is no evidence of a CW signal from the ensemble; the p-values as a function of k are well above the assumed 1% threshold.

The upper limits procedures are applied to the entire set of pulsars considering the LIGO and Virgo detectors and O3 data. The posterior on the Λ parameter and on μ_ϵ are shown in Figure 6.4. The upper limit set on Λ is $\Lambda^{95\%} = 96.4$ while the upper limit on μ_ϵ is 2.7×10^{-9} for the hierarchical procedure using the Λ parameter and 1.8×10^{-9} for the hierarchical procedure using the single pulsar results. These results are more than one order of magnitude below the upper limit in [115] where the authors considered a classic hierarchical Bayesian procedure on an ensemble of 92 pulsars and data from the LIGO V6 science run.

The 5n-vector ensemble method improves the detection probability for the targeted search of CWs from known pulsars. Application of this procedure on the next observing runs will improve the possibility to detect a CW signal from rotating neutron stars for the first time.

Appendix A

Brief history of GW detectors

As discussed in the introduction of Chapter 2, Pirani's paper - *"On the physical significance of the Riemann tensor"* published in 1956 - can be considered as the starting point and the inspiration for the entire GW detection program.

Actually, this paper was mostly ignored at the time since the community was focused on whether GWs could transmit energy. The question was linked to the complicated definition of "energy" in GR. Energy is conserved if the system is invariant under time, but in GR, "time" is part of the coordinate system, and normally it depends on the position. Therefore, globally, energy is not conserved. However, any curved space–time can be considered to be locally flat and, locally, energy is conserved. This matter was settled by a thought experiment[1] proposed by Richard Feynman during the first "GR" conference at Chapel Hill in 1957. Feynman focused on whether GW could do work or not, and convinced most of the audience that GWs transmit energy.

At the Chapel Hill conference [50], Joseph Weber, an engineer at the University of Maryland, became fascinated by discussions about GWs and decided to design a device that could detect them. In the 1960s, Weber pioneered the effort to build detectors for GWs, using large cylinders of aluminum [129]. Basically, Weber proposed the detection by measuring vibrations induced in a mechanical system; he designed and built a large metal cylinder as a sort of "antenna" to observe the resonant vibrations eventually produced by a transit of a GW pulse. His "antenna" was a big aluminum cylinder about 66 cm in diameter and 153 cm in length, weighing 3 tons. The cylinder was hanging by a steel wire from a support built to isolate vibrations of its environment. In addition, the instrument was placed inside a vacuum chamber and a belt of piezoelectric crystals were placed around the cylinder to convert mechanical vibrations into electrical impulses. Weber built two detectors; in this way, if a detected signal was not recorded simultaneously in both detectors, the signal should be discarded because spurious. In

---

[1] For the description of the Feynman thought experiment, see [50].

two papers at the end of 1960s, Waber claimed the detection of GWs. Several next experiments, based on "resonant bars", did not confirm Weber's results [50].
Despite his failure, Weber is considered a pioneer in experimental gravitation and greatly motivated the research in the field of GWs' detection.
In 1962 Michael Gertsenshtein and Vladislav Pustovoit in Moscow, and independently several years later Weber and Rainer Weiss in America, proposed the use of laser interferometry to monitor the relative motion of freely hanging mirrors for the detection of GWs. In 1967, Weiss demonstrated a laser interferometer with sensitivity limited only by photon shot noise, and in 1972 he completed the invention of the interferometric GW detector by identifying all the fundamental noise sources that such a detector must face, and how to deal with each of them.
In 1980, the American National Science Foundation funded the study of a large interferometer led by MIT (Paul Linsay, Peter Saulson, Rainer Weiss), and the following year, Caltech constructed a 40-meter prototype (Ronald Drever and Stan Whitcomb); this was the born of the “Laser Interferometer Gravitational-Wave Observatory” (LIGO) project. After several failures, in 1994, Barry Barish was appointed laboratory director, and the NSF made clear that LIGO had one last chance for support. Barish's team created a new project plan proposing to build LIGO as an evolutionary detector, where detection of GWs with initial LIGO would be possible, and with advanced-LIGO would be probable. The project established the construction of two detectors in Hanford (Washington) in late 1994 and in Livingston (Louisiana) in 1995.
The Weiss proposal fell handily also to the German group of the Max Planck Institute as they were in the process of designing a novel Weber antenna cooled to temperatures near absolute zero to reduce thermal noise. However, following LIGO, they decided to try the interferometric method with the project GEO600, a Michelson interferometer with two 600 meter long arms built in the lowlands near Hannover and started in 1995.
In the 1996, thanks to the effort of Alain Brillet and Adalberto Giazotto [50], the French CNRS and the Italian INFN started the construction of a new detector, Virgo, in Cascina near Pisa.
From 2007 the LSC (LIGO Scientific Collaboration) and Virgo scientists combine and jointly analyze all data that come from their interferometers. The combined data improved measurements of source locations on the sky and confidence in detected waves.
After 2010, LIGO went off-line for several years for a major upgrade, installing the new Advanced LIGO detectors in the LIGO Observatory infrastructures. Initial Virgo was upgraded to Advanced Virgo, which began operating in 2017. The two LIGO detectors operated from 2009 onwards, during LIGO science run 6 (S6, Jul 2009 to Oct 2010) and LIGO observing runs O1 (Sep 2015 to Jan 2016) and O2 (Nov 2016 to Aug 2017).

The Virgo detector operated from 2007 onwards, with an overlap with the LIGO science runs S5 and S6, and the LIGO observing run O2.

The first run O1 operated at a sensitivity roughly 3 times greater than initial LIGO and on 11 February 2016, LIGO and Virgo Collaborations announced the observation of the first GW signal, GW150914.

In the second run O2, LIGO detectors saw several further GW events. Several of them were also seen by the Virgo Collaboration. The most important event is GW170817 that came from the collision of two neutron stars and was also detected electromagnetically by γ-ray satellites and optical telescopes.

The third run O3 began on 1 April 2019. Further observing runs will be interleaved with commissioning efforts to further improve the sensitivity.

Appendix B

Order statistics

Let $X_1, X_2, .., X_N$ be a set of independent and identically distributed random variables. Let $F(x)$ and $f(x)$ be the cumulative distribution function (cdf) and the probability distribution function (pdf), respectively.
Consider a single realization/measurement for each of these N random variables:

$$x_1,\ x_2, \cdots,\ x_N \tag{B.1}$$

and order these measurements for increasing values.
The k-th order statistic $X_{(k)}$ is defined as the k-th smallest value of the obtained sample [130],

$$X_{(1)} < X_{(2)} < ... < X_{(k)} < ... < X_{(N)} \tag{B.2}$$

$X_{(k)}$ takes the value of x_k if x_k is the k-th value when the realizations are ranked in ascending order.
It is straightforward to infer the cdf $F_N(x)$ for $X_{(N)}$:

$$\begin{aligned} F_N(x) &= P(X_{(N)} < x) = P(X_1 < x \cup ... \cup X_N < x) \\ &= P(X_1 < x) \cup ... \cup P(X_N < x) = [F(x)]^N \end{aligned} \tag{B.3}$$

It follows that the pdf $f_N(x)$ is:

$$f_N(x) = \frac{dF_N(x)}{dx} = N \cdot [F(x)]^{(N-1)} \cdot f(x) \tag{B.4}$$

With similar considerations we can infer the cdf for $X_{(1)}$,

$$\begin{aligned} F_1(x) &= P(X_{(1)} < x) = 1 - P(X_{(1)} > x) = \\ &= 1 - [P(X_1 > x) \cup ... \cup P(X_N > x)] = \\ &= 1 - [1 - F(x)]^N \end{aligned} \tag{B.5}$$

and the pdf,

$$f_1(x) = \frac{dF_1(x)}{dx} = N \cdot [1 - F(x)]^{(N-1)} \cdot f(x) \tag{B.6}$$

The smallest and largest order statistic cdf/pdf are special cases of the k-th order statistic cdf/pdf:

$$F_k(x) = P(X_{(k)} < x) = \sum_{i=k}^{N} \binom{N}{i} [F(x)]^i [F(x)]^{N-i} \tag{B.7}$$

$$f_k(x) = \frac{N!}{(k-1)!(N-K)!} [F(x)]^{k-1} [1 - F(x)]^{N-k} f(x) \tag{B.8}$$

Interesting functions of order statistics are the range $R(X_1, \cdots, X_N) = X_{(1)} - X_{(N)}$, known as a good estimator of the variance, and the sample median $M(X_1, \cdots, X_N)$,

$$M(X_1, \cdots, X_N) = \begin{cases} X_{(k)}, & \text{when N is odd and } k = \dfrac{N+1}{2} \\ \dfrac{X_{(k)} + X_{(k+1)}}{2}, & \text{when N is even and } k = \dfrac{N}{2} \end{cases} \tag{B.9}$$

widely used as a smoother of a time series.

An interesting application of order statistics is the "German tank problem" that has a historical context in World War II [131].

The Germans inscribed their tanks with sequential serial numbers $1, 2, \ldots, m$ when they were manufactured. The total number of tanks m that the Germans had, however, was unknown to the Allied forces. The Allies captured an assumed random sample of n tanks from the German forces without replacement and observed their serial numbers, $x_1, x_2, \ldots, x_n$. The German tank problem is to estimate the total number of tanks m from the observed serial numbers. The statistical estimates of m can be inferred from order statistic theory.

The "tank capturing" can be seen as a stochastic process governed by a uniform random selection, without replacement, from the set of integers from 1 to n. The order statistic $X_{(i)}$ with $i = 1, \cdots, n$ has pdf

$$P\left[X_{(i)} = x\right] = \frac{\binom{x-1}{i-1}\binom{m-x}{n-i}}{\binom{m}{n}}, \quad x \in \{i, i+1, \ldots, m-n+i\} \tag{B.10}$$

where $X_{(i)} = x$ means that $i-1$ sample values are less than x and $n-i$ are greater than x, and $\binom{m}{n}$ is the total number of unordered samples.

Unbiased estimators of the total number m based on order statistics is U_i:

$$U_i = \frac{n+1}{i} X_{(i)} - 1 \qquad \text{for} \qquad i = 1, \cdots, n \tag{B.11}$$

since the expected value of the order statistic

$$E\left[X_{(i)}\right] = i\frac{m+1}{n+1} \tag{B.12}$$

and $E\left[U_i\right] = m$. It is clear that the estimators improve as i increases, i.e. U_n is the best estimator of the total number of tanks. This statistical estimate turned out to be much more accurate than the intelligence estimates.

Appendix C

Bayesian inference and the hierarchical method

Bayesian inference is based on the Bayes theorem and on the idea that the probability associated with a hypothesis is a measure of degree of belief (subjective probability). For statistical inference, where experimental data check the consistency of a certain theory, the Bayes theorem can be written as

$$P(\text{theory}|\text{data}) \propto P(\text{data}|\text{theory})P(\text{theory}) \tag{C.1}$$

$P(\text{theory})$ represents the prior probability that the theory is true, and the likelihood $P(\text{data}|\text{theory})$ is the probability, under the assumption of the theory, to observe the data which were actually obtained. The posterior probability that the theory is correct after seeing the result of the experiment is then given by $P(\text{theory}|\text{data})$.

While the frequentist approach is based on frequencies of events, the Bayesian formalism is based on our knowledge of events. The Bayes theorem updates the initial guess - the prior - that means the information obtained from the data is used to turn the prior belief into a posterior belief.

Considering, for example, the case of a binary black hole coalescence whose signal is defined by a set of 15 parameters indicated with $\vec{\theta} = (\theta_1, \cdots, \theta_{15})$. The posterior distribution $p(\vec{\theta}|d)$ is the probability density function for the parameters given the strain data d. According to Bayes theorem, the posterior distribution is:

$$p(\vec{\theta}|d) = \frac{L(d|\vec{\theta})\Pi(\vec{\theta})}{Z} \tag{C.2}$$

$L(d|\vec{\theta})$ is the likelihood function of the data given the parameters, $\Pi(\vec{\theta})$ is the prior distribution, and Z is a normalization factor called the “evidence”. By writing down the

likelihood, it is implicitly introduced a noise model that for GW astronomy, is typically a Gaussian-noise model. The ratio of the evidence for two different models (for example, signal model against noise model) is called the Bayes factor.
To look at the posterior distribution for just one parameter, it is possible to marginalize over the other parameters called "nuisance parameters" to obtain a marginalized posterior:

$$p(\theta_i|d) = \int \prod_{k\neq i} d\theta_k \, p(\vec{\theta}|d) \tag{C.3}$$

Hierarchical Bayesian inference is a formalism to study the population properties from many individual measurements [120]. Considering CW analysis, it is possible to assume that the ellipticities of the set of N analyzed pulsars follow a common distribution fixed by the parameter Λ (in this case, $\vec{\theta} = (\epsilon_1, \cdots, \epsilon_N)$ is the set of ellipticities). Hierarchical methods try to constrain Λ, called the hyper-parameter, considering the Bayes theorem:

$$p(\Lambda, \vec{\theta}|d) \propto L(d|\Lambda, \vec{\theta})\Pi(\Lambda, \vec{\theta}) \tag{C.4}$$

Marginalizing over the nuisance parameters,

$$p(\Lambda|d) \propto \int d\vec{\theta} \, L(d|\Lambda, \vec{\theta})\Pi(\Lambda, \vec{\theta}) \tag{C.5}$$

it is obtained the posterior for the hyper-parameter. Using the basic property of conditional probability, the prior can be written as:

$$\Pi(\Lambda, \vec{\theta}) = \Pi(\vec{\theta}|\Lambda)\Pi(\Lambda) \tag{C.6}$$

where $\Pi(\Lambda)$ is the hyper-prior. It follows that:

$$p(\Lambda|d) = \frac{L(d|\Lambda)\Pi(\Lambda)}{Z_\Lambda} \tag{C.7}$$

with the hyper-evidence

$$Z_\Lambda = \int d\Lambda \, L(d|\Lambda)\Pi(\Lambda) \tag{C.8}$$

In the case of N independent event, the likelihood is

$$L(d|\Lambda) = \int d\vec{\theta} \, L(d|\Lambda, \vec{\theta})\Pi(\vec{\theta}|\Lambda) \equiv \prod_{i=1}^{N} \int d\theta_i \, L(d|\theta_i)\Pi(\theta_i|\Lambda) \tag{C.9}$$

and it is possible to break the integral into individual integrals for each event to reduce the dimensionality and hence, the computational cost.

Bibliography

[1] Steven Weinberg. *The Physics and Astrophysics of Neutron Stars*. Ed. by John Wiley and Sons. John Wiley and Sons, 1972.

[2] A. Einstein. "Die Grundlage der allgemeinen Relativitätstheorie". In: *Annalen der Physik* 354.7 (1916), pp. 769–822.

[3] Charles W. Misner, Kip S. Thorne, and John Archibald Wheeler. *Gravitation*. Princeton University Press, 1973.

[4] Bernard Schutz. *A first course in General Relativity*. Cambridge University Press, 2012.

[5] R. Arnowitt, S. Deser, and C. Misner. *Gravitation: An Introduction to current research*. J. Wiley and Sons, 1962.

[6] Vincenzo Barone. *Relatività. Principi ed applicazioni.* Bollati e Boringhieri, 2004.

[7] Éanna É Flanagan and Scott A Hughes. "The basics of gravitational wave theory". In: *New Journal of Physics* 7 (2005), pp. 204–204.

[8] Hans Westman and Sebastiano Sonego. "Coordinates, observables and symmetry in relativity". In: *Annals Phys.* 324 (2009), pp. 1585–1611.

[9] Michele Maggiore. *Gravitational waves - Volume1: theory and experiment*. Oxford University Press, 2007.

[10] M. Bailes et al. "Gravitational-wave physics and astronomy in the 2020s and 2030s". In: *Nature Reviews Physics* 3.5 (2021), pp. 344–366.

[11] Kip S. Thorne and Carolee J. Winstein. "Human gravity-gradient noise in interferometric gravitational-wave detectors". In: *Phys. Rev. D* 60 (8 1999), p. 082001.

[12] Alessandra Buonanno and Thibault Damour. "Transition from inspiral to plunge in binary black hole coalescences". In: *Phys. Rev. D* 62 (6 2000), p. 064015.

[13] S. Carroll, S.M. Carroll, and Addison-Wesley. *Spacetime and Geometry: An Introduction to General Relativity*. Addison Wesley, 2004.

[14] The LIGO and Virgo Collaboration. "Observation of Gravitational Waves from a Binary Black Hole Merger". In: *Phys. Rev. Lett.* 116 (6 2016), p. 061102.

[15] E Müller. “Gravitational radiation from core-collapse supernovae”. In: *Classical and Quantum Gravity* 14.6 (1997), pp. 1455–1460.

[16] Michele Maggiore. *Gravitational Waves. Vol. 2: Astrophysics and Cosmology*. Oxford University Press, 2018.

[17] D. I. Jones. “Gravitational wave emission from rotating superfluid neutron stars”. In: *Monthly Notices of the Royal Astronomical Society* 402.4 (2010), pp. 2503–2519.

[18] D. I. Jones. *Learning from the Frequency Content of Continuous Gravitational Wave Signals*. 2021.

[19] Asimina Arvanitaki and Sergei Dubovsky. “Exploring the string axiverse with precision black hole physics”. In: *Phys. Rev. D* 83 (4 2011), p. 044026.

[20] Gianfranco Bertone and Dan Hooper. “History of dark matter”. In: *Rev. Mod. Phys.* 90 (4 2018), p. 045002.

[21] W. Baade and F. Zwicky. “On Super-Novae”. In: *Proceedings of the National Academy of Sciences* 20.5 (1934), pp. 254–259.

[22] A. et al. Hewish. “Observation of a Rapidly Pulsating Radio Source”. In: *Nature* 217 (1968), pp. 709–713.

[23] T. Gold. “Rotating Neutron Stars and the Nature of Pulsars”. In: *Nature* 221 (1969), pp. 25–27.

[24] R. A. Hulse and J. H. Taylor. “Discovery of a pulsar in a binary system.” In: *The Astrophysical Journal Letters* 195 (1975), pp. L51–L53.

[25] Pablo Cerda-Duran and Nancy Elias-Rosa. “Neutron Stars Formation and Core Collapse Supernovae”. In: *The Physics and Astrophysics of Neutron Stars*. Ed. by Luciano Rezzolla et al. Cham: Springer International Publishing, 2018, pp. 1–56.

[26] M. E. Caplan and C. J. Horowitz. “Colloquium: Astromaterial science and nuclear pasta”. In: *Rev. Mod. Phys.* 89 (4 2017), p. 041002.

[27] Paolo Esposito, Nanda Rea, and Gian Luca Israel. “Magnetars: a short review and some sparse considerations”. In: *Timing Neutron Stars: Pulsations, Oscillations and Explosions* (2021), pp. 97–142.

[28] Zdunik, J. L., Fortin, M., and Haensel, P. “Neutron star properties and the equation of state for the core”. In: *A&A* 599 (2017), A119.

[29] Nättilä, J. et al. “Neutron star mass and radius measurements from atmospheric model fits to X-ray burst cooling tail spectra”. In: *A&A* 608 (2017), A31.

[30] J-B Wei et al. “Neutron star universal relations with microscopic equations of state”. In: *Journal of Physics G: Nuclear and Particle Physics* 46.3 (2019), p. 034001.

[31] The LIGO and Virgo Collaboration. “GW170817: Observation of Gravitational Waves from a Binary Neutron Star Inspiral”. In: *Phys. Rev. Lett.* 119 (16 2017), p. 161101.

[32] B. P. Abbott et al. “Gravitational Waves and Gamma-Rays from a Binary Neutron Star Merger: GW170817 and GRB 170817A”. In: *The Astrophysical Journal* 848.2 (2017), p. L13.

[33] S. Bernuzzi A. Perego D. Radice. “AT 2017gfo: An Anisotropic and Three-component Kilonova Counterpart of GW170817”. In: *The Astrophysical Journal* 850.2 (2017), p. L37.

[34] The LIGO and the Virgo Collaboration. “GW170817: Measurements of Neutron Star Radii and Equation of State”. In: *Phys. Rev. Lett.* 121 (16 2018), p. 161101.

[35] S. B. Popov et al. “The Neutron Star Census”. In: *The Astrophysical Journal* 530.2 (2000), pp. 896–903.

[36] Antony Hewish. “Pulsar astronomy”. In: *The Observatory* 126.1194 (2006), p. 381.

[37] Kostas Glampedakis and Leonardo Gualtieri. “Gravitational Waves from Single Neutron Stars: An Advanced Detector Era Survey”. In: *The Physics and Astrophysics of Neutron Stars*. Ed. by Luciano Rezzolla et al. Cham: Springer International Publishing, 2018.

[38] D I Jones. “Gravitational waves from rotating strained neutron stars”. In: *Classical and Quantum Gravity* 19.7 (2002), pp. 1255–1265.

[39] Brynmor Haskell and Kai Schwenzer. “Isolated Neutron Stars”. In: *Handbook of Gravitational Wave Astronomy*. Ed. by Cosimo Bambi, Stavros Katsanevas, and Konstantinos D. Kokkotas. Singapore: Springer Singapore, 2020, pp. 1–28.

[40] S. Chandrasekhar and E. Fermi. “Problems of Gravitational Stability in the Presence of a Magnetic Field.” In: *The Astrophysical Journal* 118 (1953), p. 116.

[41] J. Frieben and L. Rezzolla. “Equilibrium models of relativistic stars with a toroidal magnetic field”. In: *Monthly Notices of the Royal Astronomical Society* 427.4 (2012), pp. 3406–3426.

[42] Michael Kramer and Ben Stappers. *Pulsar Science with the SKA*. 2015.

[43] D. R. Lorimer and M. Kramer. *Handbook of Pulsar Astronomy*. Vol. 4. 2004.

[44] Brynmor Haskell and Andrew Melatos. “Models of pulsar glitches”. In: *International Journal of Modern Physics D* 24.3, 1530008 (2015), p. 1530008.

[45] A. G. Lyne et al. “45 years of rotation of the Crab pulsar”. In: *Monthly Notices of the Royal Astronomical Society* 446.1 (2014), pp. 857–864.

[46] Simon Johnston and A. Karastergiou. “Pulsar braking and the $P\breve{}\dot{P}$ diagram”. In: *Monthly Notices of the Royal Astronomical Society* 467.3 (2017), pp. 3493–3499.

[47] J.J. Condon and S.M. Ransom. *Essential Radio Astronomy*. Princeton Series in Modern Observational Astronomy. Princeton University Press, 2016.

[48] Konstantinos D. Kokkotas. “Gravitational Wave Astronomy”. In: *Reviews in Modern Astronomy*. John Wiley and Sons, Ltd, 2008, pp. 140–166.

[49] P. Astone et al. “Method for narrow-band search of continuous gravitational wave signals”. In: *Phys. Rev. D* 89 (6 2014), p. 062008.

[50] Jorge Cervantes-Cota, Salvador Galindo-Uribarri, and George Smoot. “A Brief History of Gravitational Waves”. In: *Universe* 2.3 (2016), p. 22.

[51] Peter R. Saulson. “Gravitational wave detection: Principles and practice”. In: *Comptes Rendus Physique* 14.4 (2013). Gravitational waves / Ondes gravitationnelles, pp. 288–305.

[52] Éanna É Flanagan and Scott A Hughes. “The basics of gravitational wave theory”. In: *New Journal of Physics* 7 (2005), pp. 204–204.

[53] Charlotte Bond et al. “Interferometer techniques for gravitational-wave detection”. In: *Living reviews in relativity* 19.1 (2016), p. 3.

[54] Moritz Mehmet and Henning Vahlbruch. “The Squeezed Light Source for the Advanced Virgo Detector in the Observation Run O3”. In: *Galaxies* 8.4 (2020).

[55] F Acernese and (The Virgo Collaboration). “Calibration of advanced Virgo and reconstruction of the detector strain h(t) during the observing run O3”. In: *Classical and Quantum Gravity* 39.4 (2022), p. 045006.

[56] F Acernese and (the Virgo Collaboration). “Advanced Virgo: a second-generation interferometric gravitational wave detector”. In: *Classical and Quantum Gravity* 32.2 (2014), p. 024001.

[57] D Estevez et al. “The Advanced Virgo photon calibrators”. In: *Classical and Quantum Gravity* 38.7 (2021), p. 075007.

[58] C J Moore, R H Cole, and C P L Berry. “Gravitational-wave sensitivity curves”. In: *Classical and Quantum Gravity* 32.1 (2014), p. 015014.

[59] Virgo. “Virgo Detector Characterization and Data Quality during the O3 run”. In: (2022).

[60] A. et al. Buikema. “Sensitivity and performance of the Advanced LIGO detectors in the third observing run”. In: *Phys. Rev. D* 102 (6 2020), p. 062003.

[61] M. Bailes, B.K. Berger, and P.R. et al. Brady. “Gravitational-wave physics and astronomy in the 2020s and 2030s”. In: *Nature Review Physics* 3 (2021), pp. 344–366.

[62] The LIGO Scientific Collaboration, The Virgo Collaboration, and The KAGRA Collaboration. *The population of merging compact binaries inferred using gravitational waves through GWTC-3*. 2021.

[63] A. Goldstein et al. “An Ordinary Short Gamma-Ray Burst with Extraordinary Implications:Fermi-GBM Detection of GRB 170817A”. In: *The Astrophysical Journal* 848.2 (2017), p. L14.

[64] B. P. Abbott et al. “Multi-messenger Observations of a Binary Neutron Star Merger”. In: *The Astrophysical Journal* 848.2 (2017), p. L12.

[65] Marica Branchesi. "Multi-messenger astronomy: gravitational waves, neutrinos, photons, and cosmic rays". In: *Journal of Physics: Conference Series* 718 (2016), p. 022004.

[66] The LIGO Scientific Collaboration and the Virgo Collaboration and the KAGRA Collaboration. "GWTC-3: Compact Binary Coalescences Observed by LIGO and Virgo During the Second Part of the Third Observing Run". In: *arXiv e-prints*, arXiv:2111.03606 (2021), arXiv:2111.03606.

[67] Punturo M. et al. "The Einstein Telescope: a third-generation gravitational wave observatory". In: *Classical and Quantum Gravity* 27.19, 194002 (2010), p. 194002.

[68] B P Abbott et al. "Exploring the sensitivity of next generation gravitational wave detectors". In: *Classical and Quantum Gravity* 34.4 (2017), p. 044001.

[69] C.-Y. Ng and Roger W. Romani. "Fitting Pulsar Wind Tori. II. Error Analysis and Applications". In: *The Astrophysical Journal* 673.1 (2008), pp. 411–417.

[70] Magdalena Sieniawska and Michał Bejger. "Continuous Gravitational Waves from Neutron Stars: Current Status and Prospects". In: *Universe* 5.11 (2019).

[71] Patrick R. Brady et al. "Searching for periodic sources with LIGO". In: *Phys. Rev. D* 57 (4 1998), pp. 2101–2116.

[72] Rodrigo Tenorio, David Keitel, and Alicia M. Sintes. "Search Methods for Continuous Gravitational-Wave Signals from Unknown Sources in the Advanced-Detector Era". In: *Universe* 7.12 (2021).

[73] The LIGO Collaboration. "Setting upper limits on the strength of periodic gravitational waves from PSR $\mathrm{J1939} + 2134$ using the first science data from the GEO 600 and LIGO detectors". In: *Phys. Rev. D* 69 (8 2004), p. 082004.

[74] L. Sun et al. "Hidden Markov model tracking of continuous gravitational waves from young supernova remnants". In: *Phys. Rev. D* 97 (4 2018), p. 043013.

[75] Paola Leaci. "Searching for continuous gravitational wave signals using LIGO and Virgo detectors". In: *Journal of Physics: Conference Series* 354 (2012), p. 012010.

[76] Piccinni Ornella Juliana. "Status and perspectives of Continuous Gravitational Wave searches". In: *arXiv e-prints*, arXiv:2202.01088 (2022), arXiv:2202.01088.

[77] Surabhi Sachdev et al. *The GstLAL Search Analysis Methods for Compact Binary Mergers in Advanced LIGO's Second and Advanced Virgo's First Observing Runs*. 2019.

[78] Piotr Jaranowski and Andrzej Królak. "Searching for gravitational waves from known pulsars using the $\mathcal{F}$ and $\mathcal{G}$ statistics". In: *Classical and Quantum Gravity* 27.19 (2010), p. 194015.

[79] Xilong Fan, Yanbei Chen, and Chris Messenger. "Method to detect gravitational waves from an ensemble of known pulsars". In: *Physical Review D* 94 (2016).

[80] Curt Cutler and Bernard F. Schutz. "Generalized $\mathcal{F}$-statistic: Multiple detectors and multiple gravitational wave pulsars". In: *Phys. Rev. D* 72 (6 2005), p. 063006.

[81] M. Pitkin, C. Messenger, and X. Fan. "Hierarchical Bayesian method for detecting continuous gravitational waves from an ensemble of pulsars". In: *Phys. Rev. D* 98.6 (2018), p. 063001.

[82] G. Ashton and R. Prix. "Hierarchical multistage MCMC follow-up of continuous gravitational wave candidates". In: *Phys. Rev. D* 97 (10 2018), p. 103020.

[83] Matthew Pitkin et al. *A nested sampling code for targeted searches for continuous gravitational waves from pulsars*. 2017. URL: `https://arxiv.org/abs/1705.08978`.

[84] The LIGO Scientific Collaboration and the Virgo Collaboration and the KAGRA Collaboration. "Searches for Gravitational Waves from Known Pulsars at Two Harmonics in the Second and Third LIGO-Virgo Observing Runs". In: *The Astrophysical Journal Letters* 935.1 (2022).

[85] C. Brans and R. H. Dicke. "Mach's Principle and a Relativistic Theory of Gravitation". In: *Phys. Rev.* 124 (3 1961), pp. 925–935.

[86] The LIGO and Virgo Collaboration. "Searches for Gravitational Waves from Known Pulsars at Two Harmonics in 2015-2017 LIGO Data". In: *The Astrophysical Journal* 879.1 (2019), p. 10.

[87] The LIGO and Virgo Collaboration. "Diving below the Spin-down Limit: Constraints on Gravitational Waves from the Energetic Young Pulsar PSR J0537-6910". In: *The Astrophysical Journal Letters* 913.2 (2021), p. L27.

[88] The LIGO and Virgo Collaboration. "Narrowband Searches for Continuous and Long-duration Transient Gravitational Waves from Known Pulsars in the LIGO-Virgo Third Observing Run". In: *The Astrophysical Journal* 932.2, 133 (2022), p. 133.

[89] Marek Cieś lar et al. "Detectability of continuous gravitational waves from isolated neutron stars in the Milky Way". In: *Astronomy & Astrophysics* 649 (2021), A92.

[90] K. Lazaridis et al. "Generic tests of the existence of the gravitational dipole radiation and the variation of the gravitational constant". In: *MNRAS* 400.2 (2009), pp. 805–814.

[91] Ornella Juliana Piccinni et al. "A new data analysis framework for the search of continuous gravitational wave signals". In: *Classical and Quantum Gravity* (2018).

[92] P Astone, S Frasca, and C Palomba. "The short FFT database and the peak map for the hierarchical search of periodic sources". In: *Classical and Quantum Gravity* 22.18 (2005), S1197–S1210.

[93] Piotr Jaranowski, Andrzej Królak, and Bernard F. Schutz. “Data analysis of gravitational-wave signals from spinning neutron stars: The signal and its detection”. In: *Phys. Rev. D* 58 (6 1998), p. 063001.

[94] The LIGO and Virgo Collaboration. “Beating the spin-down limit on gravitational wave emission from the Vela pulsar”. In: *The Astrophysical Journal* 737.2 (2011), p. 93.

[95] P. Astone et al. “A method for detection of known sources of continuous gravitational wave signals in non-stationary data”. In: *Classical and Quantum Gravity* 27 (2010), p. 194016.

[96] Paola Leaci et al. “Novel directed search strategy to detect continuous gravitational waves from neutron stars in low- and high-eccentricity binary systems”. In: *Phys. Rev. D* 95 (12 2017), p. 122001.

[97] Réjean J. Dupuis and Graham Woan. “Bayesian estimation of pulsar parameters from gravitational wave data”. In: *Phys. Rev. D* 72 (10 2005), p. 102002.

[98] Avneet Singh, Maria Alessandra Papa, and Vladimir Dergachev. “Characterizing the sensitivity of isolated continuous gravitational wave searches to binary orbits”. In: *Phys. Rev. D* 100 (2 2019), p. 024058.

[99] Paola Leaci and Reinhard Prix. “Directed searches for continuous gravitational waves from binary systems: Parameter-space metrics and optimal Scorpius X-1 sensitivity”. In: *Phys. Rev. D* 91 (10 2015), p. 102003.

[100] P. Astone et al. “Coherent search of continuous gravitational wave signals: Extension of the 5-vectors method to a network of detectors”. In: *Journal of Physics: Conference Series* 363 (2012).

[101] Adalberto Giazotto, Silvano Bonazzola, and Eric Gourgoulhon. “Gravitational waves emitted by an ensemble of rotating neutron stars”. In: *Phys. Rev. D* 55 (4 1997), pp. 2014–2023.

[102] Dipongkar Talukder et al. “Measuring neutron-star ellipticity with measurements of the stochastic gravitational-wave background”. In: *Phys. Rev. D* 89 (12 2014), p. 123008.

[103] Federico De Lillo, Jishnu Suresh, and Andrew L. Miller. “Stochastic gravitational-wave background searches and constraints on neutron-star ellipticity”. In: *Mon. Not. Roy. Astron. Soc.* 513.1 (2022), pp. 1105–1114.

[104] Deepali Agarwal et al. “Targeted search for the stochastic gravitational-wave background from the galactic millisecond pulsar population”. In: *Phys. Rev. D* 106 (4 2022), p. 043019.

[105] Allan Birnbaum. “Combining Independent Tests of Significance”. In: *Journal of the American Statistical Association* 49.267 (1954), pp. 559–574.

[106] Shi Chen, Zhe Feng, and Xiaolian Yi. “A general introduction to adjustment for multiple comparisons”. In: *Journal of Thoracic Disease* 9.6 (2017).

[107] S. Won et al. “Choosing an optimal method to combine P-values”. In: *Statistics in Medicine* 28.11 (2009).

[108] R. Fisher. “Statistical Methods for Research Workers”. In: *Breakthroughs in Statistics: Methodology and Distribution*. Ed. by Samuel Kotz and Norman L. Johnson. New York, NY: Springer New York, 1992.

[109] Stephen Olejnik et al. “Multiple Testing and Statistical Power With Modified Bonferroni Procedures”. In: *Journal of Educational and Behavioral Statistics* 22.4 (1997), pp. 389–406.

[110] Thomas V Perneger. “What’s wrong with Bonferroni adjustments”. In: *BMJ* 316.7139 (1998), pp. 1236–1238.

[111] D. Zaykin et al. “Truncated product method for combining P-values.” In: *Genetic Epidemiology* 22.2 (2002).

[112] F. Dudbridge and BP. Koeleman. “Rank truncated product of P-values, with application to genomewide association scans.” In: *Genetic Epidemiology* 25.4 (2003).

[113] N A Heard and P Rubin-Delanchy. “Choosing between methods of combining p-values”. In: *Biometrika* 105.1 (2018), pp. 239–246.

[114] James A. Koziol and Michael D. Perlman. “Combining Independent Chi-Squared Tests”. In: *Journal of the American Statistical Association* 73.364 (1978), pp. 753–763.

[115] M. Pitkin, C. Messenger, and X. Fan. “Hierarchical Bayesian method for detecting continuous gravitational waves from an ensemble of pulsars”. In: *Phys. Rev. D* 98.6 (2018), p. 063001.

[116] Mauro Buono et al. “A method for detecting continuous gravitational wave signals from an ensemble of known pulsars”. In: *Classical and Quantum Gravity* 38 (2021).

[117] Luca D’Onofrio et al. “5n-vector ensemble method for detecting gravitational waves from known pulsars”. In: *Phys. Rev. D* 105.6 (2022), p. 063012.

[118] Khursheed Alam and K. T. Wallenius. “Distribution of a Sum of Order Statistics”. In: *Scandinavian Journal of Statistics* 6.3 (1979), pp. 123–126.

[119] Dmitri V. Zaykin et al. “Combining p-values in large-scale genomics experiments”. In: *Pharmaceutical Statistics* 6.3 (2007), pp. 217–226.

[120] Eric Thrane and Colm Talbot. “An introduction to Bayesian inference in gravitational-wave astronomy: Parameter estimation, model selection, and hierarchical models”. In: *Publications of the Astronomical Society of Australia* 36 (2019), e010.

[121] C. Biwer et al. “Validating gravitational-wave detections: The Advanced LIGO hardware injection system”. In: *Phys. Rev. D* 95 (6 2017), p. 062002.

[122] *O3 Continuous Wave Hardware Injections*. `https://www.gw-openscience.org/O3/o3_inj/`. Accessed: 2022-07-20.

[123] *ATNF Pulsar Catalogue, Catalogue Version 1.61*. `https://www.atnf.csiro.au/research/pulsar/psrcat/`.

[124] J. M. Yao, R. N. Manchester, and N. Wang. “A New Electron-density Model for Estimation of Pulsar and FRB Distances”. In: *Astrophysical Journal* 835.1, 29 (2017), p. 29.

[125] Michele Maggiore et al. “Science case for the Einstein telescope”. In: *Journal of Cosmology and Astroparticle Physics* 2020.03 (2020), pp. 050–050.

[126] Glen Cowan et al. “Asymptotic formulae for likelihood-based tests of new physics”. In: *Eur. Phys. J. C* 71 (2011). [Erratum: Eur.Phys.J.C 73, 2501 (2013)], p. 1554.

[127] Maximiliano Isi et al. “Establishing the significance of continuous gravitational-wave detections from known pulsars”. In: *Phys. Rev. D* 102 (12 2020), p. 123027.

[128] P.B. et al. Covas. “Identification and mitigation of narrow spectral artifacts that degrade searches for persistent gravitational waves in the first two observing runs of Advanced LIGO”. In: *Phys. Rev. D* 97.8, 082002 (2018), p. 082002.

[129] J. Weber. “Observation of the Thermal Fluctuations of a Gravitational-Wave Detector”. In: *Phys. Rev. Lett.* 17 (24 1966), pp. 1228–1230.

[130] H. A. David and H. N Nagaraja. “Order Statistics”. In: Wiley Series in Probability and Statistics, 2003.

[131] Richard Ruggles and Henry Brodie. “An Empirical Approach to Economic Intelligence in World War II”. In: *Journal of the American Statistical Association* 42.237 (1947), pp. 72–91.